KfK 5291
Dezember 1994

Contributions to the R-curve Behaviour of Ceramic Materials

T. Fett
Institut für Materialforschung

Kernforschungszentrum Karlsruhe

KERNFORSCHUNGSZENTRUM KARLSRUHE
Institut für Materialforschung

KfK 5291

Contributions to the R-curve Behaviour of Ceramic Materials

T. Fett

Kernforschungszentrum Karlsruhe GmbH, Karlsruhe

Kernforschungszentrum Karlsruhe GmbH
Postfach 3640, 76021 Karlsruhe

ISSN 0303-4003

Contributions to the R-curve behaviour of ceramic materials

Abstract

Several ceramic materials show an increase in crack growth resistance with increasing crack extension. Especially, in case of coarse-grained alumina this "R-curve effect" is caused by crack-face interactions in the wake of the advancing crack. Similar effects occur for whisker reinforced ceramics. Due to the crack-face interactions so-called "bridging stresses" are generated which transfer forces between the two crack surfaces. A second reason for an increase of crack-growth resistance are stress-induced phase transformations in zirconia ceramics with the tetragonal phase changing to the monoclinic phase. These transformations will affect the stress field in the surroundings of crack tips. The transformation generates a crack-tip transformation zone and, due to the stress balance, also residual stresses in the whole crack region which result in a residual stress intensity factor. This additional stress intensity factor is also a reason for the R-curve behaviour. In this report both effects are outlined in detail.

Beiträge zum R-Kurvenverhalten keramischer Materialien

Kurzfassung

Eine Reihe keramischer Werkstoffe zeigt einen "R-Kurveneffekt", d.h. einen Anstieg des Rißwiderstands bei Rißverlängerung. In grobkörnigem Aluminiumoxid ist dieser Anstieg auf Reibungseffekte und Rißflankenverhakungen im Bereich hinter der Rißspitze zurückzuführen. In umwandlungsverstärkten Keramiken treten spannungsinduzierte Phasenumwandlungen auf, deren Umwandlungsdehnungen zu einer Reduzierung des Spannungsfeldes im Rißspitzenbereich führen. Derartige Effekte treten insbesondere bei Zirkonoxid-Keramiken auf, wobei im singulären Spannungsfeld um die Rißspitze die tetragonale Phase in die monokline Phase umwandelt. Sowohl die Rißflankenverhakung wie auch die Phasenumwandlung führen zur Reduktion der Rißspitzenbelastung und damit zu einer Erhöhung der ertragbaren Belastung. Beide Effekte werden im Detail diskutiert.

Contents

1. Preface

In this report the author will give an overview of his present activities in the field of R-curve behaviour resulting either from bridging interactions in the wake of cracks or from phase transformations in the crack-tip region.
Several aspects were published in the last two years but have been examined in a wider context in the last months. The R-curves for growing natural cracks should be mentioned as an example (Section 14) which now also include subcritical crack growth.
Besides, the results of a number of completely new investigations have been incorporated. These are for example:

- A derivation of a bridging-stress relation, which combines elastic and frictional contributions (Section 4.2);
- the computation of phase-transformation zones for cracks in finite bodies (Section 5.1);
- the computation of shielding stress intensity factors for phase-transformation zones at the onset of stable crack propagation and during crack growth (Section 5.2);
- the applicability of the well-known Irwin relation between the stress intensity factor K_I and the energy release rate G, discussed for materials with R-curve behaviour and outlined in detail for the case of bridging interactions (Section 6);
- an experimental procedure for the determination of the stress intensity factor K_{I0}, which governs the onset of stable crack extension, proposed in section 12.4; and
- the possibility of determining the true R-curve from a load vs. displacement curve, discussed in Section 12.5,

Since this publication as a KfK-report will have a limited circulation only, the author is planning to publish single topics in international journals, too.

2. Introduction

Failure of ceramic materials often starts from cracks, which may originate at pores and inclusions or may be generated during surface treatment. Various failure modes are responsible for failure and finite lifetimes of ceramic materials. At moderate temperatures the most important of them are:

1. spontaneous failure,
2. subcritical crack growth under static load,
3. cyclic fatigue,
4. thermal shock and thermal fatigue.

Spontaneous failure occurs when the applied stress reaches the strength of the material or, in terms of fracture mechanics, when the stress intensity factor K_I of the most severe crack in a component reaches or exceeds the fracture toughness K_{Ic}. Therefore, K_{Ic} must be known for the spontaneous failure behaviour to be assessed.
Delayed failure at moderate temperatures may be caused either by subcritical crack growth governed by the actual stress intensity factor K_I or by crack propagation under cyclic load governed by the range of stress intensity factors ΔK and probably by the R-ratio defined as the quotient of minimum and maximum K-values.
Thermal fatigue features at least a combination of the failure modes mentioned before. Additional effects, for instance oxidation, may also have an influence.

The loading quantity in linear-elastic fracture mechanics which governs failure is the stress intensity factor K. The stress intensity factor K_I which is called the "mode-I" stress intensity factor and is caused by stresses normal to the crack area is of greatest importance to the strength- and failure behaviour. The stresses at a crack tip are directly related to K_I by the Sneddon equations, which are reported in most fracture-mechanics handbooks (e.g. [1]). Failure of a component occurs when the stress intensity factor of the most severe crack reaches a critical value K_{Ic}, the fracture toughness of the material. In case of ideally brittle materials the fracture toughness is independent of the crack extension and, consequently, identical with the stress intensity factor K_{I0} necessary for the onset of stable crack growth (fig.1)

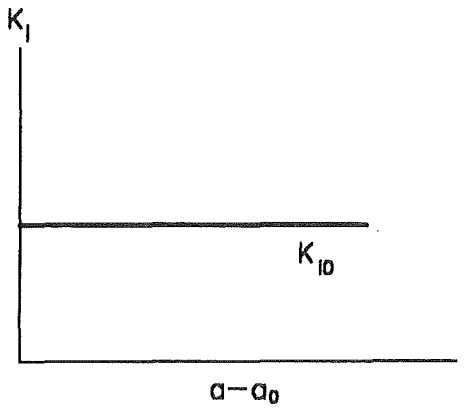

Figure 1. Flat crack-resistance curve. Crack-resistance for ideally brittle materials.

$$K_I = K_{I0} = K_{Ic} \qquad (2.0.1)$$

It is a well-known fact that the failure of several ceramics is influenced by an increasing crack-growth resistance curve. Three effects are responsible for this behaviour.

- In coarse-grained alumina the crack-growth resistance increases with increasing crack extension due to friction-like crack-border interactions in the wake of the advancing crack.
- In transformation-toughened ceramics the material undergoes a stress-induced martensitic transformation while the tetragonal material changes to the monoclinic phase (t- to m-ZrO_2). This transformation generates a crack-tip transformation zone and, due to the stress balance, also residual stresses in the whole crack region which result in a residual stress intensity factor. This stress intensity factor has to be added to the externally applied one.
- Further mechanisms are the generation of a micro-crack zone ahead of the crack tip and crack branching.

The effect of increasing crack resistance has consequences on many properties of ceramic materials. The following list contains only some of them:

- strength of components with natural cracks,
- delayed failure caused by subcritical crack growth,
- cyclic fatigue,
- thermal-shock resistance,
- fracture-toughness measurements by indentation tests.

In this report the author will make some contributions to the topic of R-curve behaviour.

3. Stable crack propagation and R-curves

3.1 Definition of the R-curve

In early measurements Hübner and Jillek [2] observed for alumina an increase in crack resistance with increasing crack extension. In fig.2 a crack-resistance curve is plotted. Crack propagation occurs when the applied stress intensity factor reaches the material property K_{I0}, which is responsible for the onset of crack growth. For further crack extension the externally applied load has to be increased. From the external load a characteristic stress σ^*_{appl} results and the applied stress intensity factor is given by

$$K_{I\,appl} = \sigma^*_{appl}\sqrt{a}\;Y \tag{3.1.1}$$

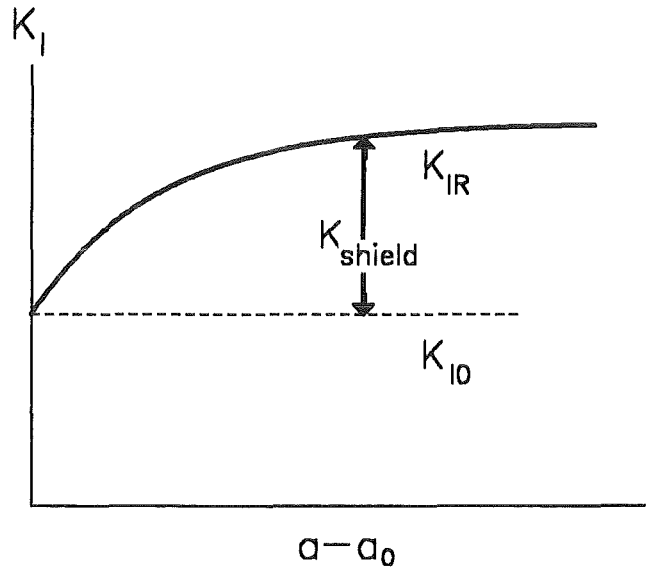

Figure 2. R-curve. Definition of an R-curve.

This stress intensity factor also increases during crack extension. $K_{I\,appl}$ is a loading quantity and the crack-resistance curve describes a material property. We have to distinguish between these quantities. Therefore, the material response to an applied load will be called K_{IR} below. The difference between the actual stress intensity factor $K_{I\,appl}$ and K_{I0} is called the shielding stress intensity factor.

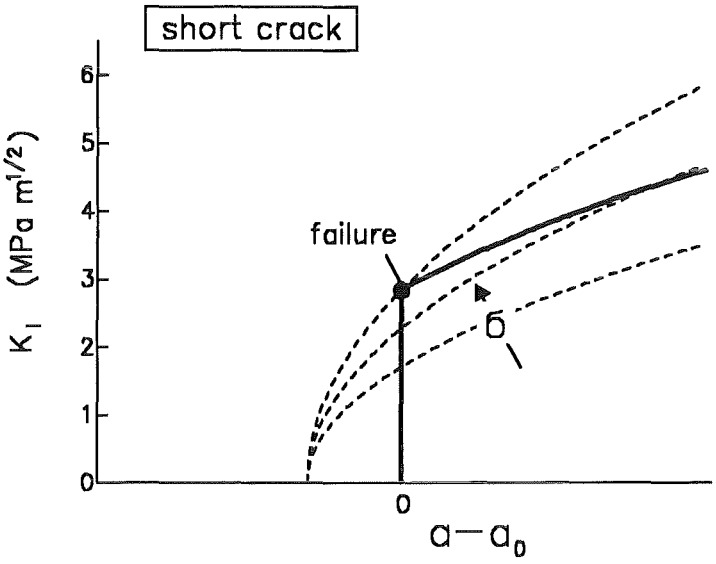

Figure 3. Failure behaviour. Influence of the R-curve on failure of a small crack; solid curve: K_{IR}, dashed curves: $K_{I\,appl}$.

3.2 Influence of R-curves on the failure of components with macro cracks and natural cracks

A first - and perhaps the most important - consequence of a rising crack-resistance curve is its influence on the strength. The principal strength behaviour in the presence of an R-curve effect is explained in figs.3 and 4. In case of a short crack (fig.3) the applied stress is increased. The lower dashed line intersects the R-curve (solid line in fig.3) at $\Delta a = a - a_0 = 0$, and also for the second dashed curve, which represents a state with increased loading, no crack growth is found. The upper curve represents the critical state where the applied stress intensity factor reaches the onset-value K_{I0} of stable crack growth. Since for the propagating crack always the condition $K_{I\,appl} > K_{I0}$ is fulfilled, catastrophic failure must occur at this point.
In fig.4 a longer crack is considered. Also in this case no crack propagation occurs for the two lowest dashed curves. At the moment when the condition $K_{I\,appl} = K_{I0}$ is fulfilled, the crack may extend. With increasing crack length a, the crack resistance as well as the applied stress intensity factor $K_{I\,appl}$ increase. In the first part of crack propagation the crack extension is stable since for all stresses an intersection of the curves for the applied stress intensity factor and the R-curve is found. This is possible until the failure point is reached which is given by the condition that the applied stress intensity factor curve is a tangent to the R-curve:

$$K_{I\,appl} = K_{IR} \quad , \quad \frac{\partial K_{I\,appl}}{\partial a} = \frac{\partial K_{IR}}{\partial a} \tag{3.2.1}$$

It becomes obvious that for longer cracks failure occurs at a higher applied stress intensity factor $K_{I\,appl}$. From these two examples we can conclude that R-curve effects may influence the strength of components with large cracks, but may have no significant effect on specimens with small defects. This is - of course - only a question of the initial steepness of the rising R-curve, i.e. for very steep R-curves also the small-crack behaviour must be affected.
The influence of an R-curve on the strength distribution has been discussed in [3]-[6] and the tendency has become evident that the R-curve behaviour will result in a reduced scatter of strength.

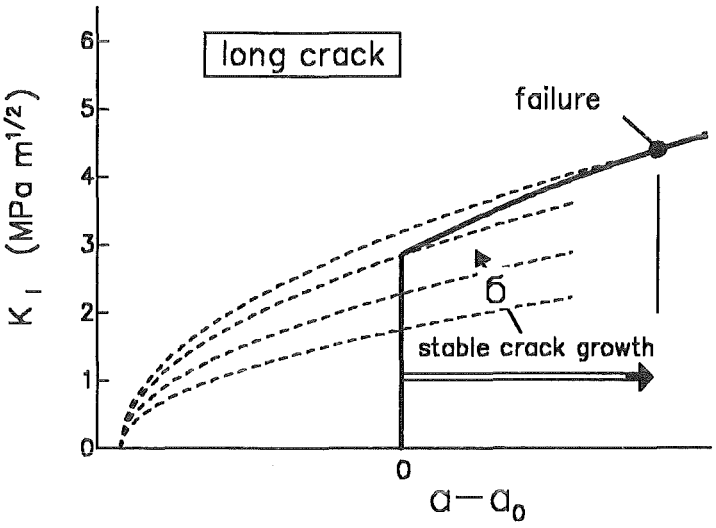

Figure 4. Failure behaviour. Influence of the R-curve on failure of a large crack; solid curve: K_{IR}, dashed curves: $K_{I\ appl.}$

From these schematic considerations it has to be expected that the influence of R-curve behaviour on failure is more pronounced for macro-cracks. But in case of a very steep R-curve also the strength of small, natural cracks can be affected.
In recent papers [7] [8] strength measurements for coarse-grained alumina have been described. In a Weibull-plot of inert bending strength a non-linear behaviour was observed as can be seen from fig.5. Such a behaviour can be caused, in principle, by a specific flaw population. But a second way of explaining it is provided by the R-curve effect. Since specimens with longer cracks (i.e. specimens with low strengths) may be more affected by the R-curve behaviour, devi-

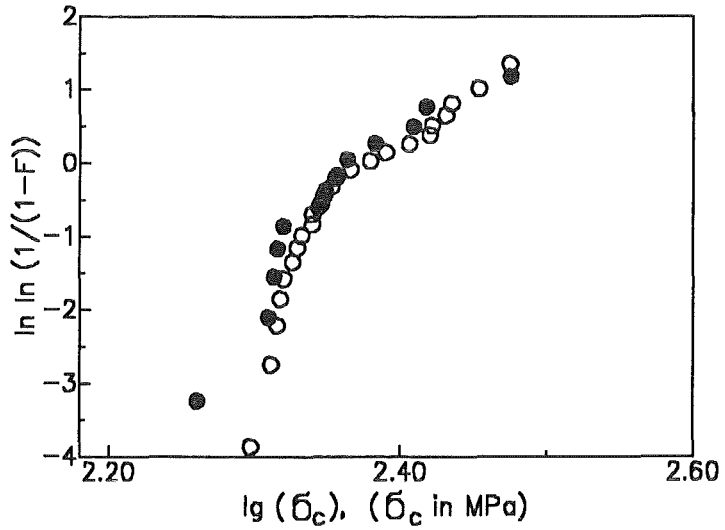

Figure 5. Strength of coarse-grained alumina. Four-point-bending strength of two batches of coarse-grained 99.6%-Al_2O_3.

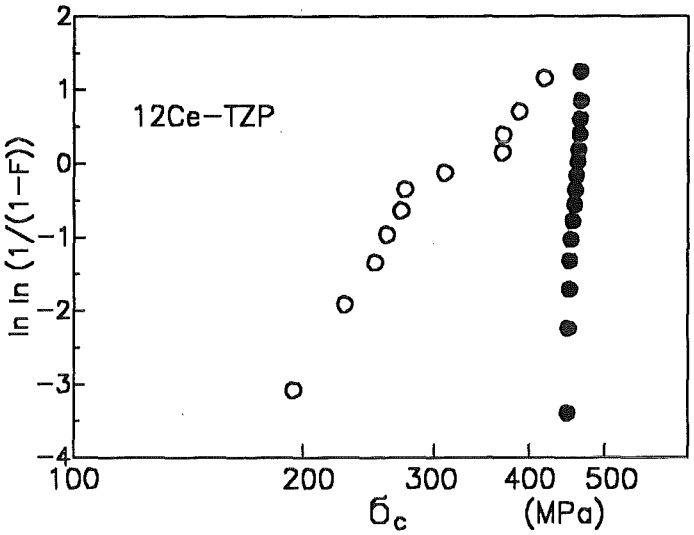

Figure 6. Strength of TZP-zirconia. Bending strength of 12Ce-TZP at room temperature (closed circles) and 600°C (open circles) reported by Proß [9].

ations from a linear Weibull distribution have to be expected. Details of the fracture-mechanics analysis will be outlined in Section 7.1. A very impressive result indicating R-curve effects on strength has been reported by Proß [9] for zirconia. Strength measurements (fig.6) performed with 12Ce-TZP showed a very high Weibull modulus of $m=92$ at room temperature and a strongly reduced value of $m=9$ at 600°C. Under the assumption of an identical flaw population at both temperatures, the difference in strength behaviour should only be the consequence of a strong R-curve effect:

- At room temperature, stress-induced martensitic transformation at the crack tips might occur which yields the shielding effect.
- At 600°C no martensitic transformation is possible and the material exhibits a Weibull modulus as usually found for ceramic materials

THEORETICAL CONSIDERATIONS ON R-CURVES

4. R-curves caused by crack-face bridging

4.1 Bridging stresses

Coarse-grained Al_2O_3 shows an R-curve behaviour which is characterised by an increase in crack growth resistance with increasing crack extension [2]-[21]. It was demonstrated experimentally [10],[11] that this effect is caused by crack-border interactions in the wake of the advancing crack. Recently, the crack-surface interactions have been detected in-situ under the electron microscope [22],[23]. The bridging interactions were observed mainly on large grains.

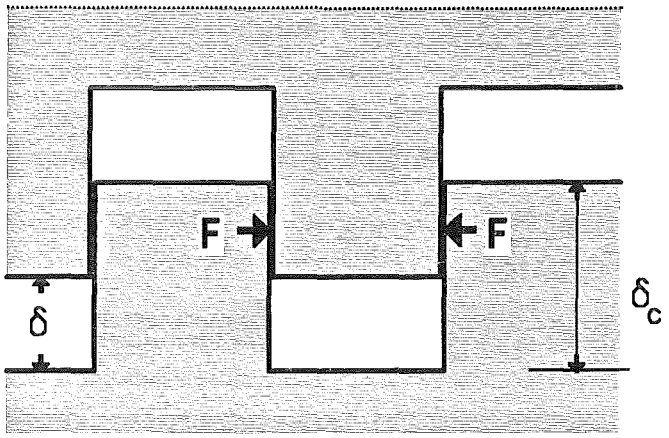

Figure 7. Bridging stress. Crack surface interaction due to friction forces (schematic).

In fig.7 such a bridging interaction influenced by a friction stress F is schematically illustrated. The crack face interactions localised at single grains can transfer loads which can be modelled in a more homogeneous way by so-called bridging stresses σ_{br} which depend only on the crack opening displacement δ. The bridging stresses shield the crack tip from the external loads as illustrated in fig.8 schematically.

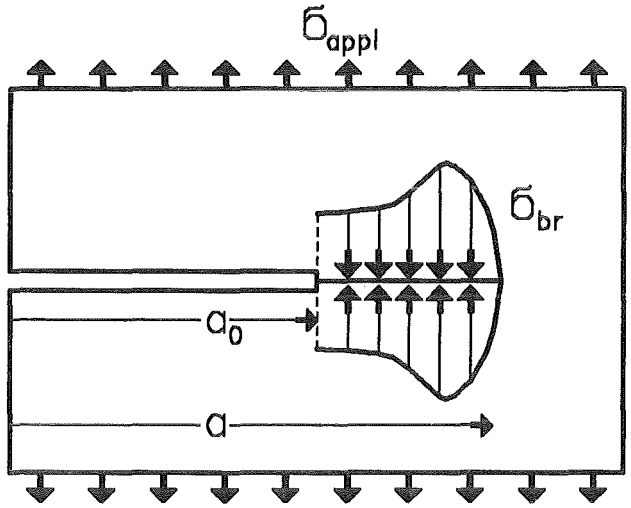

Figure 8. Bridging stress. Modelling of crack surface interactions by homogeneously distributed bridging stresses.

4.1.1 Bridging relations for friction induced stresses

For bridging stresses which are caused by friction effects Mai and Lawn [24] proposed a relation

$$\sigma_{br,grain} = \left\{ \begin{array}{ll} \sigma_0(1-\delta/\delta_c)^m & \text{for } \delta/\delta_c < 1 \\ 0 & \text{for } \delta/\delta_c > 1 \end{array} \right\} , \; m = 0,1,2,... \qquad (4.1.1)$$

that is shown in fig.9.
It is assumed that the characteristic displacement for which the bridging stresses vanish is proportional to the grain size. On account of grain size distribution, also the characteristic displacement is distributed.
It is assumed that the distribution density of δ_c is a Γ-distribution, as represented in fig.10.

$$f(\delta_c) = \frac{1}{\delta_0}\frac{\delta_c}{\delta_0}\exp(-\delta_c/\delta_0) \qquad (4.1.2)$$

Other Γ-distributions are considered in [18].
The macroscopically averaged bridging stresses result from

$$\sigma_{br,aver} = \int_0^\infty \sigma_{br,grain}\, f(\delta_c)\, d\delta_c \qquad (4.1.3)$$

For the most appropriate Γ-distribution, eq.(4.1.2), the following averaged bridging stress relations result:

$$\sigma_{br,aver} = \sigma_0\, g(\delta/\delta_0) \qquad (4.1.4)$$

with

$$g(\delta/\delta_0) = (1 + \delta/\delta_0)\ \exp(-\delta/\delta_0) \qquad \text{for} \quad m = 0 \tag{4.1.5}$$

$$g(\delta/\delta_0) = \exp(-\delta/\delta_0) \qquad \text{for} \quad m = 1 \tag{4.1.6}$$

$$g(\delta/\delta_0) = (1 - \delta/\delta_0)\ \exp(-\delta/\delta_0) + (\delta/\delta_0)^2 \mathbf{Ei}(\delta/\delta_0) \qquad \text{for} \quad m = 2 \tag{4.1.7}$$

where **Ei** is the exponential integral defined by

$$\mathbf{Ei}(x) = \int_x^\infty \frac{e^{-t}}{t}\, dt \quad , \quad x > 0 \tag{4.1.8}$$

available in most computer libraries.

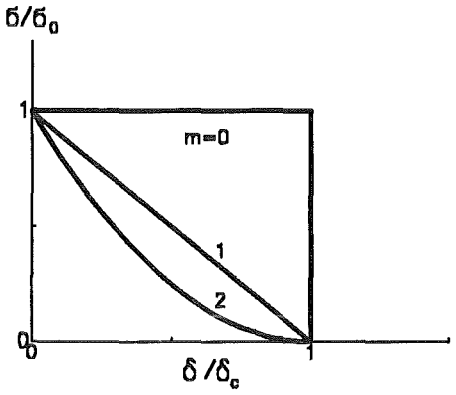

Figure 9. Bridging stresses. Stress-displacement relations for a single grain.

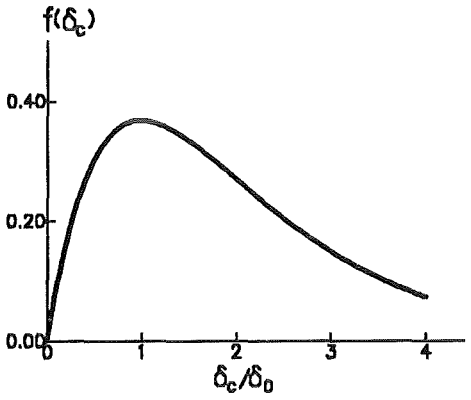

Figure 10. Bridging stresses. Distribution of the characteristic COD-value δ_c (abscissa normalised: δ_0/δ_0).

These bridging relations are shown in fig.11.
They ensure a continuously decreasing effect of crack-border interaction with decreasing displacement. Especially the mostly applied case $m = 1$ is used in the subsequent calculations.
Equation (4.1.6) describes friction-like bridging stresses in the wake of the propagating crack which step-like reach their maximum value directly at $\delta > 0$. In order to "smooth" this behaviour we propose a rewritten version

$$\sigma_{br} = \sigma_0 \exp(-\delta/\delta_0)\, h(\delta/\delta_0) \tag{4.1.9}$$

where $h(\delta/\delta_0)$ is a "switch-on" function for the bridging stresses which avoids that maximum stresses occur in the absence of any displacement. In eq.(4.1.6) a step function occurs with

$$h(\delta/\delta_0) = \begin{cases} 0 & \text{for} \quad \delta = 0 \\ 1 & \text{for} \quad \delta > 0 \end{cases} \tag{4.1.10}$$

The maximum bridging stress occurs at $\delta/\delta_0 = 0$:

$$\sigma_{max} = \sigma_0 \tag{4.1.11}$$

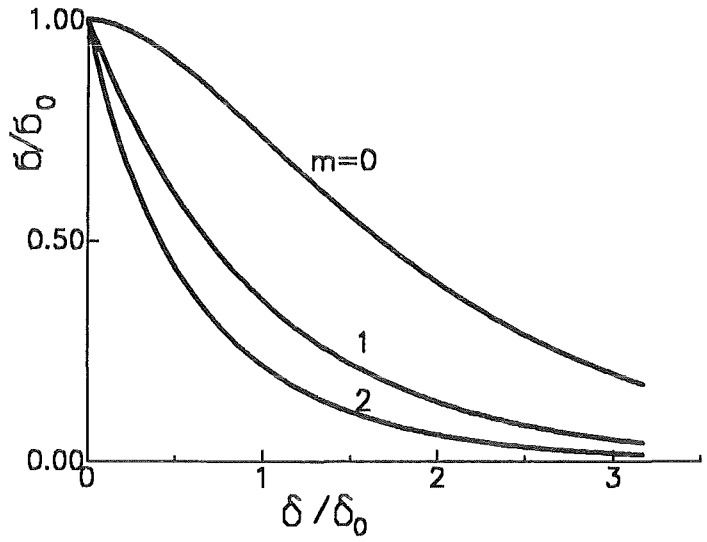

Figure 11. Bridging stresses. Influence of the parameter m in eq.(4.1.1) on the averaged bridging stress.

and the specific work necessary for dissolving the bridges is given as

$$W_{br} = \int_0^\infty \sigma_{br}(\delta)\, d\delta = \sigma_0\, \delta_0 \tag{4.1.12}$$

In this paper a continuous switch-on function is chosen

$$h(\delta/\delta_0) = 1 - \exp(-\lambda\, \delta/\delta_0) \tag{4.1.13}$$

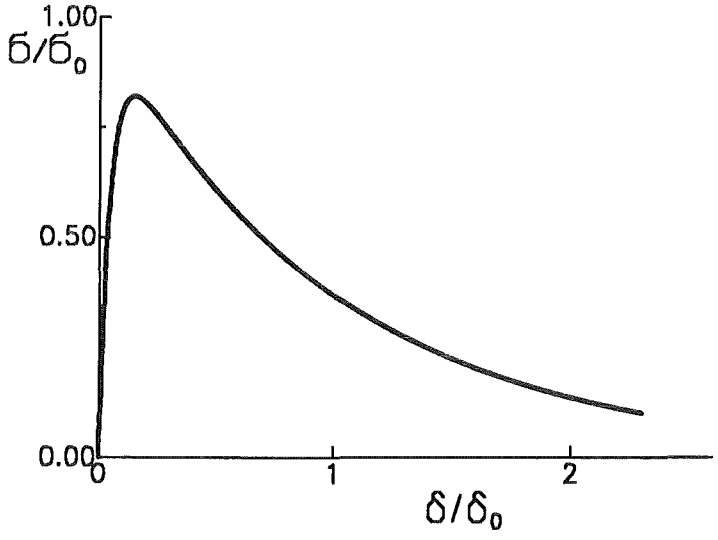

Figure 12. Bridging stresses. Stress-displacement relations for friction-like crack surface interactions according to eqs.(4.1.9) and (4.1.13).

This relation, initially only an assumption, will be justified in section 4.2. The relation is illustrated in fig.12 for $\lambda = 20$. The maximum bridging stresses are found for $\delta/\delta_0 = 0.1522$

$$\sigma_{max} = 0.8179\, \sigma_0 \tag{4.1.14}$$

and it results

$$W_{br} = \int_0^\infty \sigma_{br}(\delta)\, d\delta = \frac{20}{21}\, \sigma_0\, \delta_0 \tag{4.1.15}$$

4.1.2 Springs with limited extensions

In case of spring-like stresses the bridging stresses in a single bridge may be expressed by

$$\sigma_{br,spring} = \left\{ \begin{array}{ll} \sigma_0 \delta/\delta_c & \text{for } \delta/\delta_c < 1 \\ 0 & \text{for } \delta/\delta_c > 1 \end{array} \right\} \tag{4.1.16}$$

with maximum extension δ_c and maximum stress σ_0, shown in fig.13.

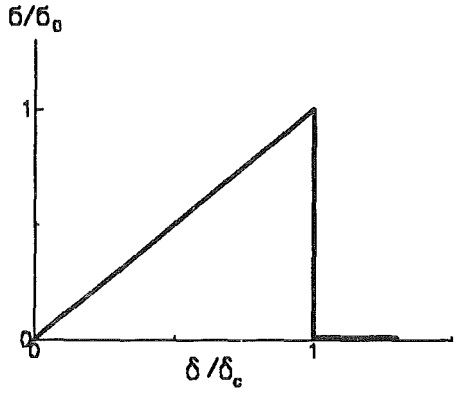

Figure 13. Local bridging stresses. Stress-displacement relations for a single spring $\sigma_{br}/\sigma_0 = f(\delta/\delta_0)$, eq.(4.1.19).

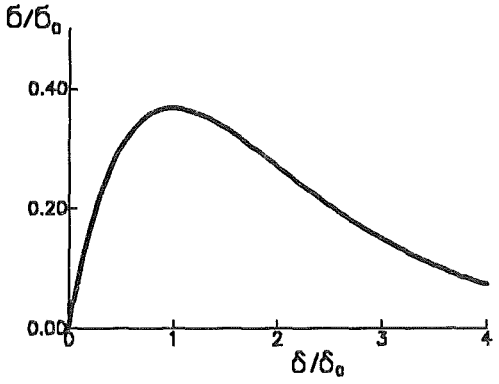

Figure 14. Global bridging stresses. Stress-displacement relations for spring-like crack surface interactions.

Similar to [19] it is assumed that the characteristic displacement δ_c for which the bridging stresses vanish is also Γ-distributed

$$f(\delta_{c,spring}) = \frac{1}{\delta_0}\, \frac{\delta_{c,spring}}{\delta_0}\, \exp(-\delta_{c,spring}/\delta_0) \tag{4.1.17}$$

with a characteristical displacement value δ_0 characterising the "width" of the distribution. Figure 10 illustrates eq.(4.1.17). The macroscopically averaged bridging stresses result from

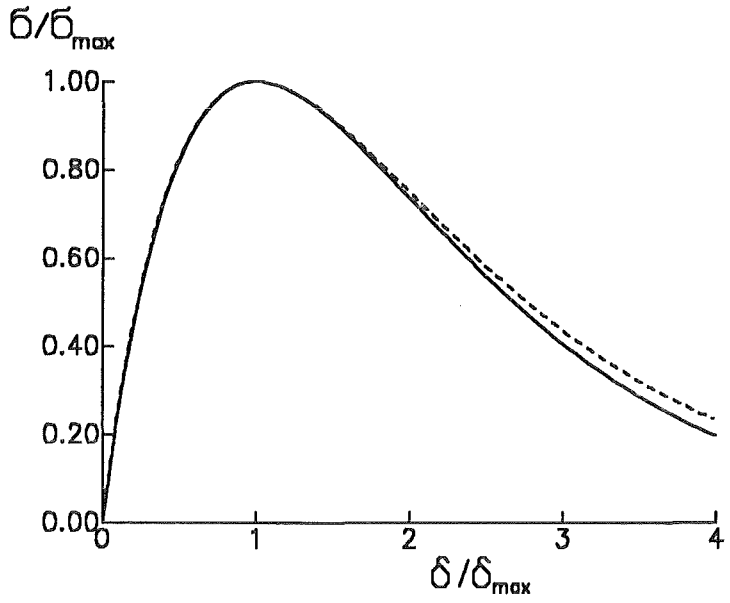

Figure 15. Bridging stresses. Intercomparison of stress-displacement relations; solid curve: eq.(4.1.19); dashed curve: eq.(4.1.22).

$$\sigma_{br} = \int_0^\infty \sigma_{br,spring}\, f(\delta_{c,spring})\, d\delta_{c,spring} \tag{4.1.18}$$

and we obtain by integration

$$\sigma_{br} = \sigma_0 \frac{\delta}{\delta_0} \exp(-\delta/\delta_0) \tag{4.1.19}$$

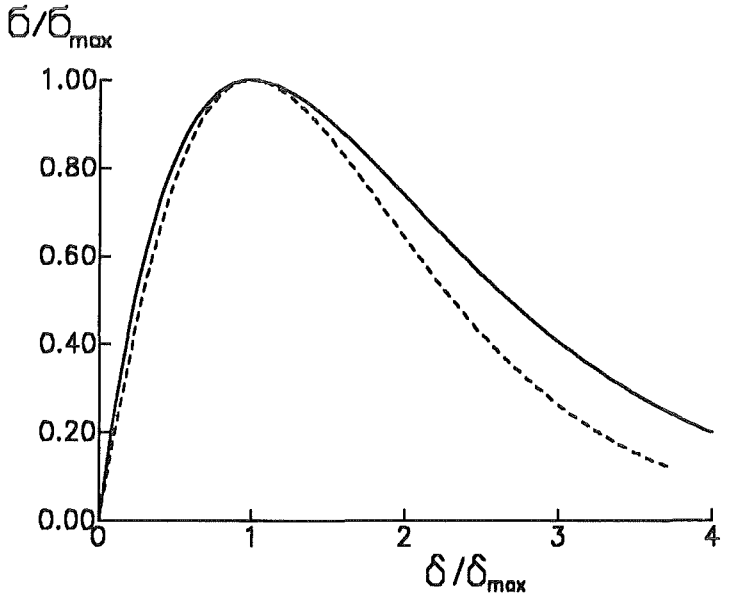

Figure 16. Bridging stresses. Intercomparison of stress-displacement relations; solid curve: eq.(4.1.19); dashed curve: eq.(4.1.26).

In this case one obtains at $\delta/\delta_0 = 1$:

$$\sigma_{max} = \sigma_0/e = 0.3679\,\sigma_0 \tag{4.1.20}$$

and

$$W_{br} = \int_0^\infty \sigma_{br}(\delta)\,d\delta = \sigma_0\,\delta_0 \tag{4.1.21}$$

In [25] the authors used a Morse-like bridging relation

$$\sigma_{br} = \sigma_0[\,\exp(-\delta/\delta_0) - \exp(-2\delta/\delta_0)] \tag{4.1.22}$$

with a maximum bridging stress at $\delta/\delta_0 = \ln(2)$:

$$\sigma_{max} = \frac{1}{4}\,\sigma_0 \tag{4.1.23}$$

and

$$W_{br} = \int_0^\infty \sigma_{br}(\delta)\,d\delta = \frac{1}{2}\,\sigma_0\,\delta_0 \tag{4.1.24}$$

The relation eq.(4.1.22) is a special case of eqs.(4.1.9) and (4.1.13) with $\lambda = 2$. Equation (4.1.22) is plotted in fig.15 together with eq.(4.1.19) in a normalised representation. There is a quite good agreement obvious. From this point of view both relations are appropriate to describe spring-like bridging interactions. If we now assume a more narrow distribution of the δ_c's we can use the next higher order Γ-distribution, namely

$$f(\delta_c) = \frac{1}{\delta_0}\left(\frac{\delta_c}{\delta_0}\right)^2 \exp(-\delta_c/\delta_0) \tag{4.1.25}$$

and we obtain for the bridging-relation

$$\sigma_{br}/\sigma_0 = \frac{\delta}{\delta_0}\left(1 + \frac{\delta}{\delta_0}\right)\exp(-\delta/\delta_0) \tag{4.1.26}$$

A comparison between the bridging relations for the first and second order Γ-distributions is made in fig.16.

4.2 A model for bridging-stress relations

The bridging effect is modelled as a two-dimensional problem for an internal crack in an infinite body, which is bridged by a single grain. This grain is assumed to be rigid ($E \to \infty$). Between the bridging grain and the surrounding material a residual stress acts due to mismatch of thermal expansion which creates the force F. This configuration is loaded by a remote stress σ_{appl}. It is the aim of the following considerations to calculate the displacements at a remote location $y = y_0$ as a function of the applied stress. Figure 17 illustrates the geometry in the absence of externally applied stresses.

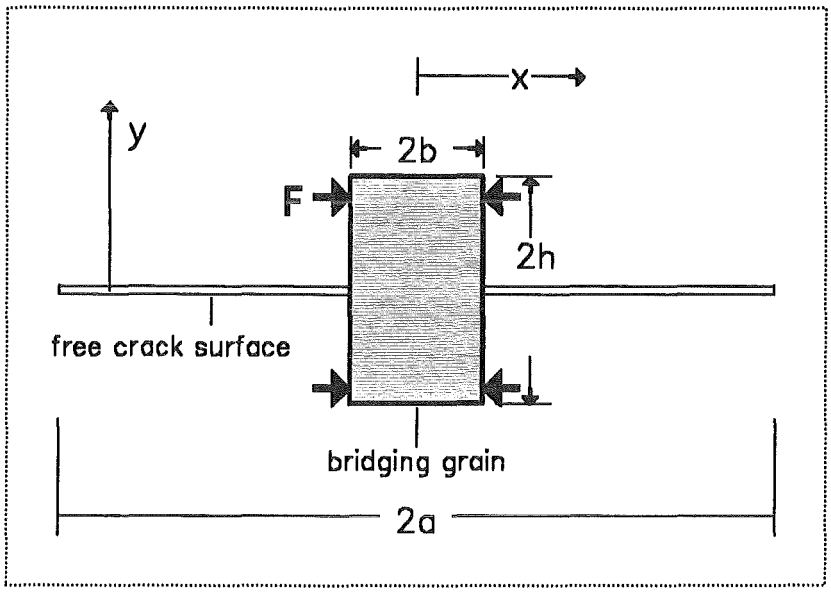

Figure 17. Bridged crack. Model of a bridged crack (unloaded).

For small, externally applied remote stresses σ_{appl} (fig.18) the stresses and displacements are governed by the mixed boundary problem

$$\begin{aligned} \delta &= 0 \quad \text{for} \quad |x| \leq b \\ \sigma &= 0 \quad \text{for} \quad |d| < |x| < |a| \end{aligned} \tag{4.2.1}$$

These conditions are valid until the load carried by the grain reaches the maximum friction force μF_0 between the bridging grain and its surroundings, i.e. for

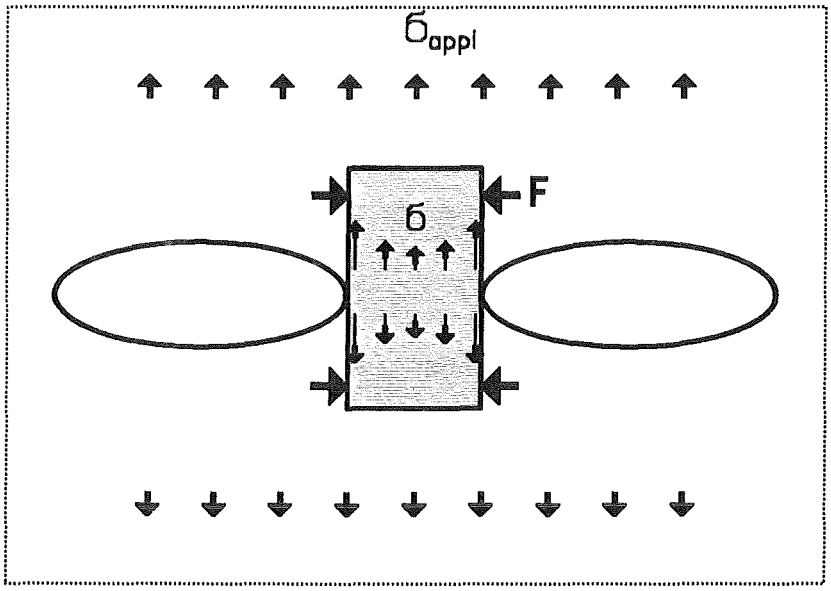

Figure 18. Bridged crack. Stresses and displacements for low remote loadings (schematic).

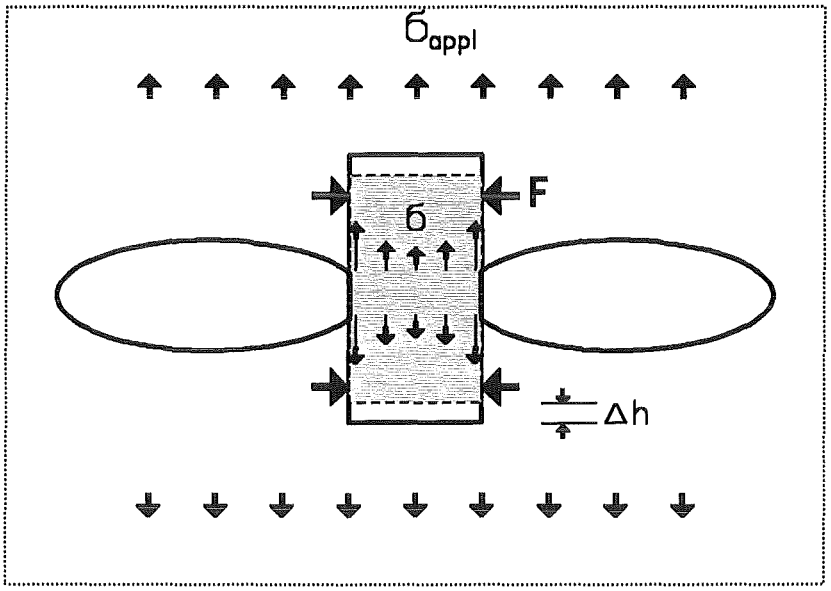

Figure 19. Bridged crack. Stresses and displacements for high remote loadings (schematic).

$$2\int_0^d \sigma(x)\,dx \leq \mu F_0 \tag{4.2.2}$$

If the load carried by the grain exceeds μF_0, sliding between the bridging grain and the surroundings, with an amount Δh, occurs (fig.19), the interaction force reduces to

$$F = F_0 \frac{h - \Delta h}{h} \tag{4.2.3}$$

and the equilibrium condition of forces reads

$$2\int_0^b \sigma(x)\,dx = \mu F_0 \frac{h - \Delta h}{h} \tag{4.2.4}$$

In this case, the boundary problem can be expressed by

$$\begin{aligned} \delta &= \Delta h \quad \text{for} \quad |x| \leq b \\ \sigma &= 0 \quad \text{for} \quad |d| < |x| < |a| \end{aligned} \tag{4.2.5}$$

4.2.1 Calculation of displacements

Due to the symmetry of the problem with respect to $x = 0$, the computations can be restricted to positive values of x. Using the relation between stresses and displacements, see eq.(4.3.4) in section 4.3, the mixed boundary problem can be written

$$\frac{1}{E'}\int_0^a\int_{\max(x,x')}^a h(a',x)h(a',x')\sigma(x')da'dx' = \Delta h \quad \text{for} \quad x \le b$$
$$\sigma = 0 \quad \text{for} \quad b < x < a \tag{4.2.6}$$

The weight function for an internal crack in an infinite body under symmetrical load is ([1])

$$h(x,a) = \frac{1}{\sqrt{\pi a}}\left[\left(\frac{a+x}{a-x}\right)^{1/2} + \left(\frac{a-x}{a+x}\right)^{1/2}\right] = \frac{2}{\sqrt{\pi a}}\frac{a}{\sqrt{a^2-x^2}} \tag{4.2.7}$$

In the absence of a bridging interaction the crack opening displacement field is given by

$$\delta_0(x) = \frac{2\sigma_{appl}}{E'}\sqrt{a^2-x^2} \tag{4.2.8}$$

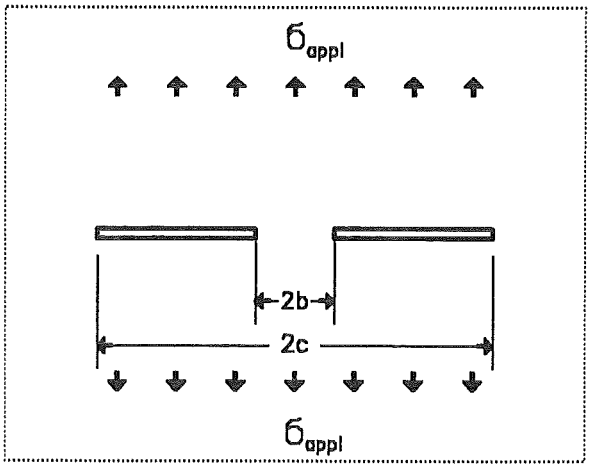

Figure 20. Partial crack problem. Case 1: Pair of collinear cracks.

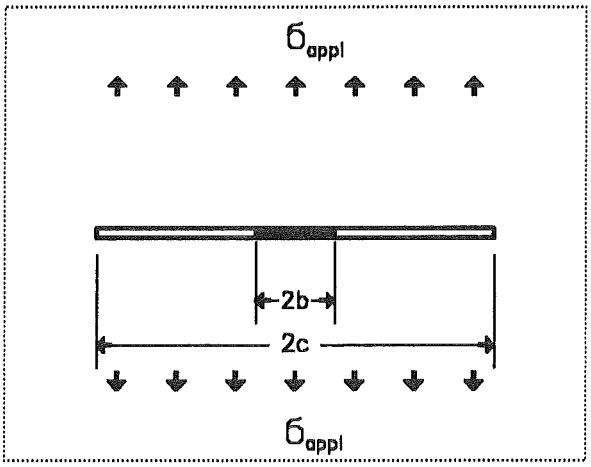

Figure 21. Partial crack problem. Case 2: Single crack opened by a wedge of constant thickness.

The stresses in the grain have to balance these crack opening displacements in the range $|x| \le b$. So we have to solve

$$\frac{4}{E'\pi}\int_x^a \frac{t}{\sqrt{t^2-x^2}}\left(\int_0^t \frac{\sigma(x)\,dx}{\sqrt{t^2-x^2}}\right)dt = -\frac{2}{E'}\sigma_{appl}\sqrt{a^2-x^2} + \Delta h \tag{4.2.9}$$

There are different possibilities of proceeding:

- Equation (4.2.9) can be solved numerically.
- The displacement field can be superimposed by solutions existing for partial problems.

We will choose the second way here. As a first partial problem we compute the crack opening displacements for two neighbouring single cracks, fig.20, ensuring zero displacements within $|x| \leq b$. The crack opening displacements are (see for instance [1])

$$\delta_1(x) = \frac{2\,a\,\sigma_{appl}}{E'\,\mathbf{K}(k)}\,[\mathbf{K}(k)\,E(\varphi, k) - \mathbf{E}(k)\,F(\varphi, k)] \tag{4.2.10}$$

where $F(\varphi, k)$ and $E(\varphi, k)$ are the first and second elliptical integrals to the modulus k with

$$k = \sqrt{1-(b/a)^2} \quad , \quad \varphi = arc\,sin\sqrt{\frac{a^2-x^2}{a^2-b^2}} \tag{4.2.11}$$

and $\mathbf{K}(k)$, $\mathbf{E}(k)$ are the complete elliptical integrals. In this context, it should be mentioned that in [1] the elliptical integral $\mathbf{K}$ is missing in the denominator of eq.(4.2.10). Equation (4.2.10) represents the displacement field for $\Delta h = 0$. In order to satisfy the constant displacements $\Delta h > 0$ in $-b < x < b$, we have to add the displacement field for a parallel rigid wedge of thickness $2\Delta h$ within $-b < x < b$. In order to avoid a separation of the contact surfaces, we assume the wedge to be welded with the surrounding material along the interfaces. The displacements are also given in handbooks (e.g. [1]). It holds

$$\delta_2(x) = \frac{F(\varphi, k)}{\mathbf{K}(k)}\,\Delta h \tag{4.2.12}$$

and, finally, the total solution for the displacements is given by

$$\delta(x) = \frac{2\,a\,\sigma_{appl}}{E'\mathbf{K}(k)}\,[\mathbf{K}(k)\,E(\varphi, k) - \mathbf{E}(k)\,F(\varphi, k)] + \frac{F(\varphi, k)}{\mathbf{K}(k)}\,\Delta h \tag{4.2.13}$$

The crack opening displacement field resulting from eq.(4.2.13) is shown in fig.22.

4.2.2 Calculation of stresses in the bridging element

The corresponding stresses $\sigma(x)$ in the grain can be calculated numerically with eq.(4.2.9). In order to solve eq.(4.2.9) we will first calculate as a partial problem the stress distribution for a crack of length $2a$ which is opened by a parallel wedge of length $2b$ and thickness Δh (see fig.21). The Westergaard stress function for this problem is given in [1] as

$$Z(z) = \frac{E'\,h\,a}{2\mathbf{K}(k)}\,\frac{1}{\sqrt{z^2-a^2}\,\sqrt{z^2-b^2}} \quad , \quad k = \sqrt{1-(b/a)^2} \tag{4.2.14}$$

from which the normal stress σ_y results by

$$\sigma_y = Re\{Z(z)\} - y\,Im\{Z'(z)\} \tag{4.2.15}$$

For $y = 0$ one obtains

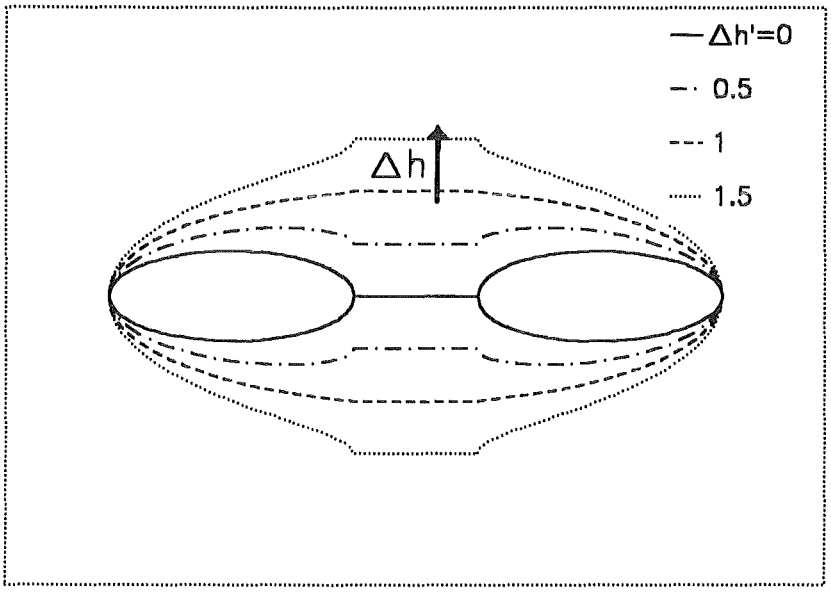

Figure 22. Bridged crack. Displacements calculated with eq.(4.2.13), $b/a=0.2$ and σ_{appl}=constant, $\Delta h' = E'\Delta h/(2\sigma_{appl}a)$.

$$\sigma_y = Re\{Z(z)\} \quad \rightarrow \quad \sigma_y = \frac{E'\,\Delta h\,a}{2\mathbf{K}(k)} \frac{1}{\sqrt{a^2-x^2}\sqrt{b^2-x^2}} \tag{4.2.16}$$

For the pair of collinear cracks - which result for $\Delta h=0$ - the stresses in the range $-b \le x \le b$ caused by the remote applied stress σ_{appl} are (see [26])

$$\sigma_y = \frac{\sigma_{appl}}{\mathbf{K}(k)} \frac{a^2\mathbf{E}(k) - x^2\mathbf{K}(k)}{\sqrt{(a^2-x^2)(b^2-x^2)}} \tag{4.2.17}$$

Superposition of the two partial crack problems yields

$$\sigma_y = \frac{1}{\mathbf{K}(k)} \frac{\sigma_{appl}\left[a^2\mathbf{E}(k) - x^2\mathbf{K}(k)\right] - a\Delta hE'/2}{\sqrt{(a^2-x^2)(b^2-x^2)}} \tag{4.2.18}$$

The total force P carried by the bridging element is then

$$P = 2\int_0^b \sigma_y\,dx = 2\sigma_{appl}a[2\mathbf{E}(k') - \mathbf{K}(k')] - E'\Delta h \tag{4.2.19}$$

$$k' = \sqrt{1-k^2} = b/a \tag{4.2.20}$$

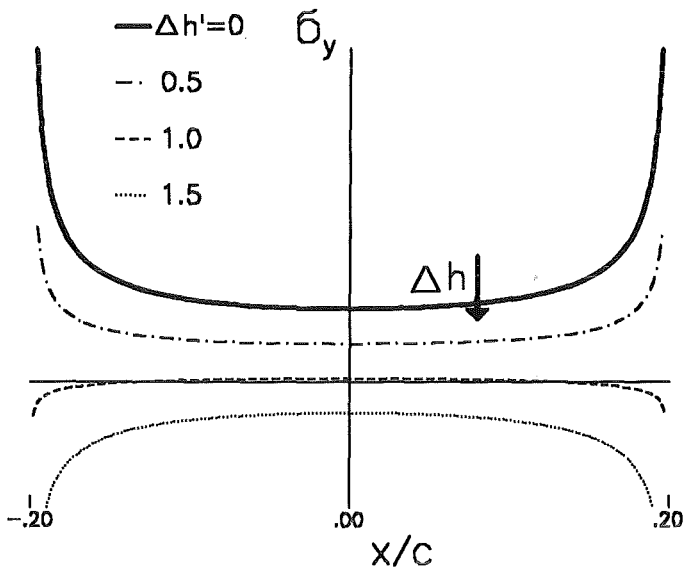

Figure 23. Stresses in the bridging grain. Stresses calculated with eq.(4.2.9), $b/a = 0.2$, $\sigma_{appl} = \text{const.}$, $\Delta h' = E'\Delta h/(2\sigma_{appl}a)$.

4.2.3 Load-displacement curve

The total volume V resulting from the local crack opening displacements

$$V = 4b\Delta h + 4\int_{x=b}^{x=a} \delta(x)\, dx \tag{4.2.21}$$

is a measure of the externally recorded loading-point displacements. From eqs.(4.2.2) and (4.2.19) we find the applied stress at which the maximum friction force F_0 is reached

$$\sigma_{appl,0} = \frac{\mu F_0}{2a[2\mathbf{E}(k') - \mathbf{K}(k')]} \tag{4.2.22}$$

The volume at $\sigma_{appl} = \sigma_{appl,0}$ is

$$V_0 = \frac{8a\sigma_{appl,0}}{E'\mathbf{K}(k)}\left[\mathbf{K}(k)\int_b^a E(\varphi, k)\, dx - \mathbf{E}(k)\int_b^a F(\varphi, k)\, dx\right] \tag{4.2.23}$$

For stresses below this limit the volume is

$$V = V_0 \frac{\sigma_{appl}}{\sigma_{appl,0}} \tag{4.2.24}$$

and for higher stresses applied one obtains

$$V = V_0 \frac{\sigma_{appl}}{\sigma_{appl,0}} + 4b\Delta h + \frac{4\Delta h}{\mathbf{K}(k)}\int_b^a F(\varphi,k)\, dx \tag{4.2.25}$$

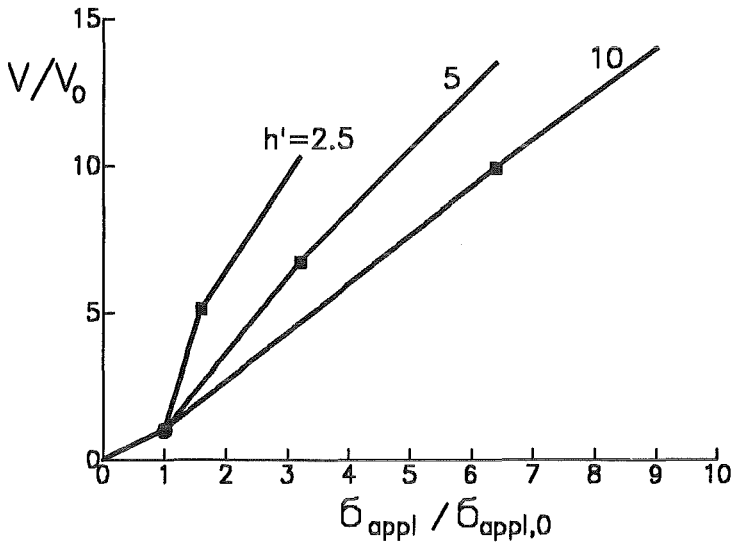

Figure 24. Volume of the opened crack. Volume of the opened crack as a measure of the "loading-point displacements". Geometrical data: specimen thickness = 1 (i.e. crack-opening area = crack-opening volume), $b/a = 0.2$, different values of h' as defined by eq.(4.2.27).

with Δh given as

$$\Delta h = h \frac{2\mathbf{E}(k') - \mathbf{K}(k')}{h' - [2\mathbf{E}(k') - \mathbf{K}(k')]} \left(\frac{\sigma_{appl}}{\sigma_{appl,0}} - 1 \right) \tag{4.2.26}$$

$$h' = \frac{hE'}{2a\sigma_{appl,0}} \tag{4.2.27}$$

The volume - standing for the remote displacement at a given point - as a function of the applied remote stress is shown in fig.24. We can identify three regions:

1. For $\sigma_{appl} \leq \sigma_{appl,0}$ the displacements are proportional to the applied load as expressed by eq.(4.2.24).

2. At $\sigma_{appl,0}$ the applied stress overcomes the friction forces μF_0. For $\sigma_{appl,0} < \sigma_{appl} \leq \sigma_{appl,max}$ the increase in displacements is steeper than in the range $\sigma_{appl} < \sigma_{appl,0}$.

3. At $\sigma_{appl,max}$ the bridging element is completely pulled out, equivalent to $\Delta h = h$,

$$\frac{\sigma_{appl,max}}{\sigma_{appl,0}} = \frac{h'}{2\mathbf{E}(k') - \mathbf{K}(k')} \tag{4.2.28}$$

and the subsequent curve follows according to

$$V = \frac{\sigma_{appl}}{\sigma_{appl,max}} V_{appl,max} \tag{4.2.29}$$

Dauskardt [27] reports load-COD-curves which are very similar to those represented in fig.24. A typical P-COD-curve is schematically shown in fig.25 for one cycle of a cyclic test. Dauskardt calls the first steep part (corresponding to the initial flat parts of fig.24) "elastic bridging" and the

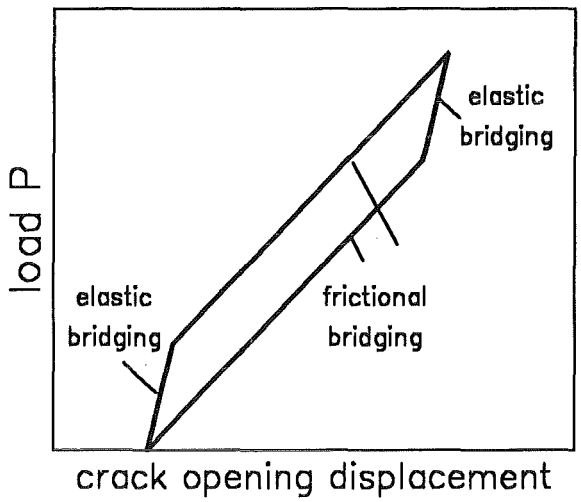

Figure 25. COD-behaviour. Applied load, P, versus crack opening displacement curves for Al_2O_3, as obtained by Dauskardt [27] (schematic).

following phase "frictional bridging". Having in mind the COD-calculations made in this section, we can interpret the displacements during *elastic bridging* as the displacements occurring in the crack regions outside the actual bridging element (no elastic strain of the bridging element itself). Obviously, the displacements in [27] were not large enough ($K_I = K_{Ic}$ may be reached before) to exhibit the third part of the curve, i.e. the unbridged state.
The bridging stresses result from the difference between the curve plotted in fig.24 and that curve which is obtained by prolongation of the line for $\sigma_{appl} \geq \sigma_{appl,max}$ to the origin (representing the completely unbridged state) as symbolised by the insert in fig.26. The result looks like the bridging relations proposed in fig.12. Considering the statistical distribution of the bridging-element lengths h, one obtains a smoother curve. If δ_{c1} is the displacement corresponding to $\sigma_{appl,0}$ and δ_c is the displacement at $\sigma_{appl,max}$, we can write the local bridging stresses as

$$\frac{\sigma}{\sigma_0} = \begin{cases} \delta/\delta_{c1} & \text{for} \quad \delta < \delta_{c1} \\ \dfrac{\delta_c - \delta}{\delta_c - \delta_{c1}} & \text{for} \quad \delta_{c1} < \delta < \delta_c \\ 0 & \text{for} \quad \delta > \delta_c \end{cases} \tag{4.2.30}$$

In the most general case one may consider the two typical displacements to be distributed independent of each other. But since the maximum friction force F_0 characterising the onset of sliding, $\delta = \delta_{c1}$, is proportional to the length h of the bridging element and also the characteristic displacement of complete pull-out is identical to h, it is sufficient to consider the distribution of δ_c by introducing the ratio

$$\lambda = \delta_c/\delta_{c1} = constant \tag{4.2.31}$$

Replacing δ_{c1} in eq.(4.2.30) by λ and δ_c and introducing this local bridging relation into eq.(4.1.3) yields for a Γ-distributed δ_c according to eq.(4.1.2) the averaged bridging relation

$$\sigma_{br} = \frac{\lambda}{\lambda - 1}\left[\exp(-\delta/\delta_0) - \exp(-\lambda\,\delta/\delta_0)\right] \tag{4.2.32}$$

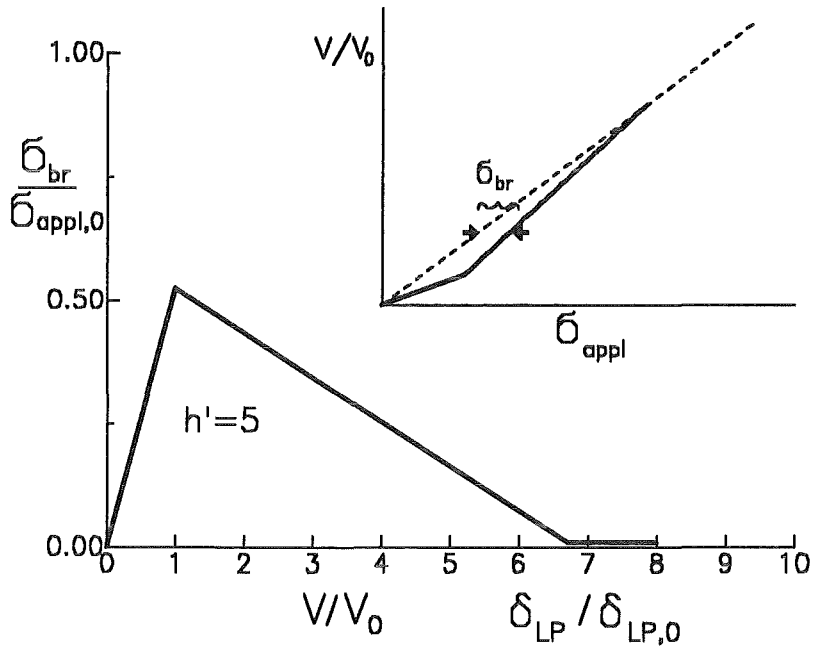

Figure 26. Bridging stress relation. Bridging stress resulting from fig.24.

which is identical with the estimated relation described by eqs.(4.1.9) and (4.1.13).

4.3 Calculation of the bridging stress intensity factor for one-dimensional cracks

A test specimen with a crack may be loaded by an external load, which leads to a stress distribution $\sigma_{appl}(x)$ at the location of the crack in the uncracked component. The geometrical quantities of such a crack are explained in fig.27. In case the material exhibits a bridging zone with crack-surface interactions, the total stress is the sum of the applied stress and the bridging stress σ_{br}, i.e.

$$\sigma_{total}(x) = \sigma_{appl}(x) + \sigma_{br}(x) \tag{4.3.1}$$

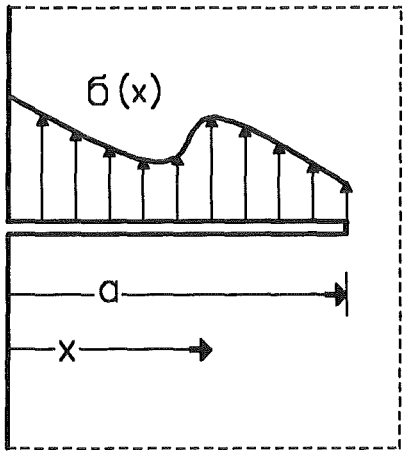

Figure 27. Weight function method. Crack with arbitrary crack face loading $\sigma(x)$.

These stresses are responsible for the stress intensity factor, which is given in the representation of the weight function [28]

$$K_I = \int_0^a h(\frac{x}{a}, \frac{a}{W})\sigma(x)\, dx \tag{4.3.2}$$

The total displacements of the crack surface can be easily derived by the relation existing between crack surface displacements, weight function and stress intensity factor as proposed by Rice [29]

$$h(x,a) = \frac{E'}{K_I}\frac{\partial\delta(x,a)}{\partial a} \tag{4.3.3}$$

with $E' = E/(1-\nu^2)$ for plane strain.
Integration of this formula yields the crack-surface displacements δ caused by the stress σ [30]

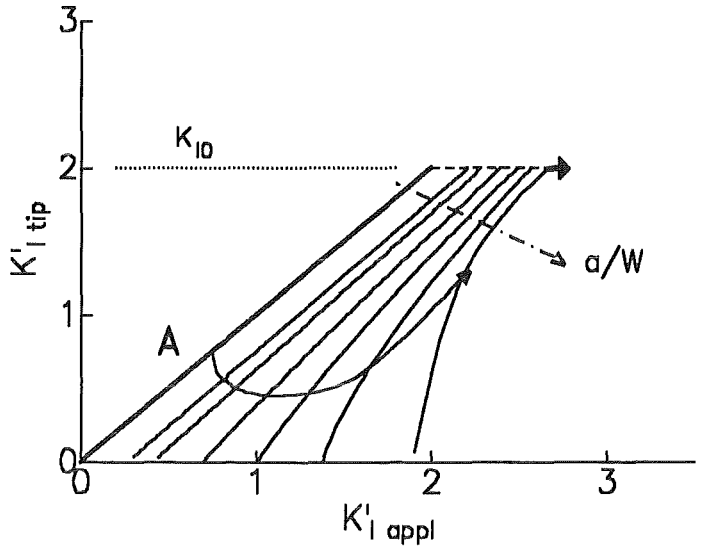

Figure 28. Stress intensity factors during crack extension. Normalised stress intensity factor K'_{tip} as a function of the applied stress intensity factor K'_{appl} for bending ($\delta'_0 = 1$, $a_0/W = 0.5$); dashed curve: stable crack growth, solid curve: subcritical crack growth.

$$\delta(x) = \frac{1}{E'} \int_0^a \int_{\max(x,x')}^a h(a',x)h(a',x')\sigma(x')da'dx' \tag{4.3.4}$$

where x is the coordinate with the displacement computed and x' is the location where the stress σ acts. Equation (4.3.4) can also be derived from the procedure of Paris [31] based on Castiglianos Theorem. A detailed description is given in the Appendix of Tadas' Handbook [1].
The stress intensity factors describing the R-curve behaviour can be obtained in the following way:

1. The total crack surface displacements according to the total stress, eq.(4.3.1), result as the solution of the integral equation

$$\delta = \frac{1}{E'} \int_0^a \int_{\max(x,x')}^a h(a',x)h(a',x')(\sigma_{appl} + \sigma_{br}(\delta))da'dx' \tag{4.3.5}$$

   The solution of the integral equation (4.3.5) provides the distribution of the bridging stresses as a function of the stresses applied.

2. The related bridging stress intensity factor $K_{I\,br}$ results from eq.(4.3.2) as

$$K_{I\,br} = \int_0^a h\left(\frac{x}{a}, \frac{a}{W}\right)\sigma_{br}(x)\,dx \tag{4.3.6}$$

3. and the applied stress intensity factor $K_{I\,appl}$ as

$$K_{I\,appl} = \int_0^a h\left(\frac{x}{a}, \frac{a}{W}\right)\sigma_{appl}(x)\,dx \tag{4.3.7}$$

4. Finally, the crack tip stress intensity factor $K_{I\,tip}$ is given by [32]

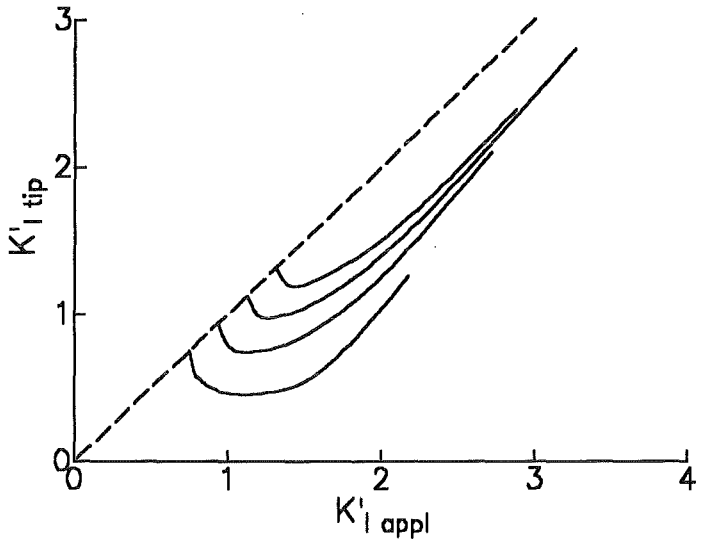

Figure 29. Subcritical crack extension. Development of the crack-tip stress intensity factor during subcritical crack growth with different initial stress intensity factors.

$$K_{I\,tip} = K_{I\,appl} + K_{I\,br} \tag{4.3.8}$$

The solution of the integral equation (4.3.5) can be determined by several methods. The simplest one is the iterative approximation. In the first step, the applied stress σ_{appl} is introduced in the integrand of eq.(4.3.5) yielding the crack surface displacement field δ_{appl}. A first approximation of the bridging stresses is obtained by introducing δ_{appl} in the bridging stress law. The bridging stresses obtained are then introduced once more in eq.(4.3.5) and the procedure is repeated as long as the bridging displacements are constant.

4.3.1 General results

In fig.28 results of calculations for a crack with an initial relative crack size (e.g. a saw notch) of $a_0/W = 0.5$ ($m = 1$, $\delta'_0 = 1$) under bending are represented as $K_{I\,tip}$ vs. $K_{I\,appl}$ for several actual crack lengths a/W using the weight function proposed in [33]. In this figure, the stress intensity factors are normalised with respect to the maximum bridging stress σ_0 and the specimens width W as

$$K'_I = \frac{K_I}{\sigma_0\sqrt{W}} \tag{4.3.9}$$

The displacements can be normalised by

$$\delta' = \frac{E'}{\sigma_0 W}\,\delta \tag{4.3.10}$$

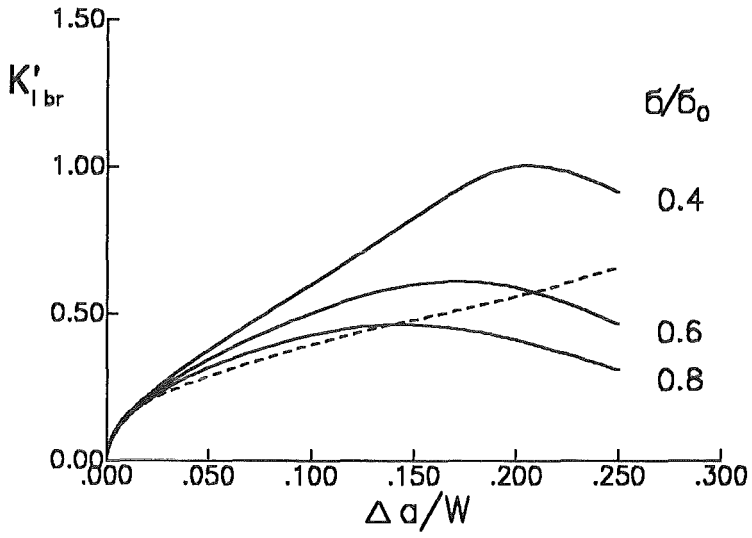

Figure 30. R-curves. Development of the bridging stress intensity factor during crack extension; dashed curve: stable crack growth, solid curves: subcritical crack growth for different loads.

4.3.2 Constant load tests

The representation of the stress intensity factor, fig.28, allows to describe crack extension tests under different loading conditions. In fig.28 crack propagation in a constant load test under subcritical crack growth conditions is illustrated by the solid line for $\sigma/\sigma_0 = 0.4$ and $\delta'_0 = 1$. The curve starts at point A corresponding to $K_{I\,appl} = K_{I\,tip} = \sigma\sqrt{a_0}\,Y$. With increasing crack length, first the crack-tip stress intensity factor $K_{I\,tip}$ decreases and after reaching a minimum value, $K_{I\,tip}$ increases monotonically. The resulting R-curve is plotted in fig.30. The curve first starts with a square-root shape, passes a maximum and decreases for large crack extension.
Constant load tests for several initial stress intensity factors K_{Ii} are shown in fig.29. The influence of the initial stress intensity factor on the R-curve can be seen from fig.30. It is evident that the R-curve is more pronounced for low values of applied stress.

4.3.3 Controlled fracture test

In this section tests with constant stress intensity factor $K_{I\,tip}$ are considered. Such tests are difficult to perform under subcritical crack growth conditions. One possibility would be to perform tests with constant crack growth rate. A much simpler possibility is to consider stable crack propagation, i.e. crack growth at $K_{I\,tip} = K_{I0}$ in a controlled fracture test. This type of test is represented in fig.28 by the dashed horizontal line. The related $K_{I\,appl}$-vs. Δa-curve is also entered in fig.30 as dashed line. At the beginning of crack extension, also this curve is approximately square-root shaped. For small crack extension this curve deviates hardly from the curve obtained under constant load conditions. Significant differences in the shapes of the R-curves become obvious for large crack extensions.
From the curves in fig.30 it becomes obvious that the R-curve depends

- on the special type of crack propagation (stable crack propagation or subcritical crack growth)
- and in case of subcritical crack growth on the level of applied stress.

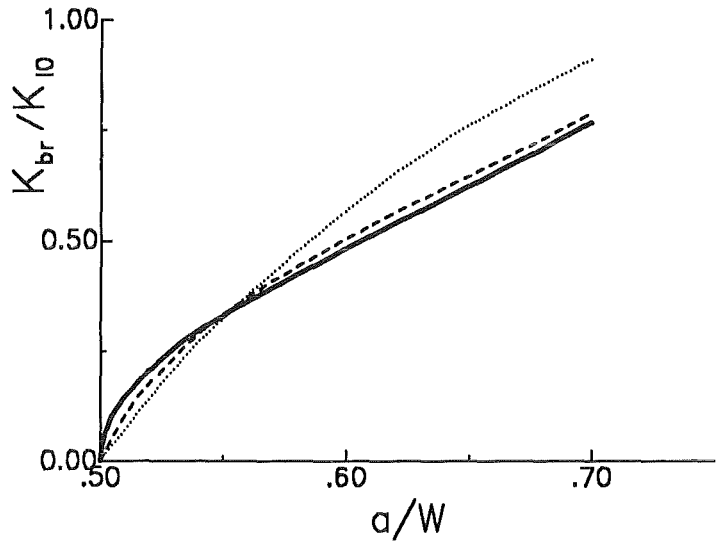

Figure 31. Influence of the bridging stress relation. Comparison of the R-curves ($K_{I\,br} = f(\Delta a)$ for different bridging stress relations; solid line: ((4.1.9) and (4.1.10)), dashed line: ((4.1.9) and (4.1.13)), dotted line: (4.1.19)).

4.3.4 Influence of bridging relations on the shape of the R-curve

From the solution of eq.(4.3.5) the bridging stresses along the crack can be computed for a given applied stress σ_{appl}, and eq.(4.3.2) provides the related stress intensity factors $K_{I\,appl}$ and $K_{I\,br}$. Since in a controlled frature test the crack-tip stress intensity factor $K_{I\,tip} = K_{total}$ is constant, namely $K_{I\,tip} = K_{I0}$, the R-curve $K_{I\,appl} = f(a - a_0)$ results from eq.(4.3.8) as

$$K_{I\,appl} = K_{I0} + |K_{I\,br}| \tag{4.3.11}$$

This correctly derived applied stress intensity factor $K_{I\,appl}$ will be denoted below as the real one. In fig.32 the entire R-curve is plotted for the bridging relation eqs.(4.1.9) and (4.1.13). Since K_{I0} is constant, $K_{I\,br}$ reflects all further information on the R-curve behaviour.
In order to allow a comparison to be made with the influence of the shape of the bridging-stress relation, we will choose the parameters σ_0 and δ_0 in such a way that the maximum bridging stresses as well as the separation energies are identical in all cases. Figure 31 shows the bridging stress intensity factor $K_{I\,br}$ as a function of the crack extension Δa in a normalised representation for the bridging relation eqs.(4.1.9) and (4.1.10) as solid curve, for relation (4.1.9) and (4.1.13) as dashed curve, and for eq.(4.1.19) as dotted line.
It is obvious that the dependency of (4.1.9) and (4.1.10) is square-root shaped at the beginning of crack extension. Also (4.1.9) and (4.1.13) shows a strong increase at $\Delta a = 0$. The initial slope for spring-like bridging stresses eq.(4.1.19) is much less steep.

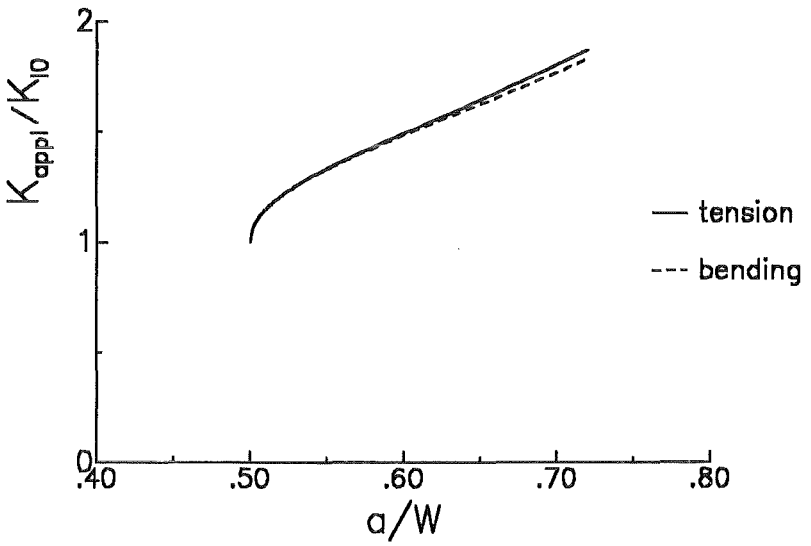

Figure 32. Influence of loading case on the R-curve. R-curve for a crack of initial crack depth $a_0/W=0.5$ computed with eqs.(4.3.5) to (4.3.8) for the bridging stress relation ((4.1.9) and (4.1.10)); Loading cases: bending (dashed curve), tension (solid curve).

4.4 Calculation of the bridging stress intensity factor for embedded circular cracks

Very often the R-curves are determined from specimens with macro-cracks, especially from through-the-wall cracks in plates. Sometimes these R-curves have to be transformed into small natural cracks. In this section simplified relations are derived for real cracks.
The R-curve behaviour has consequences on the strengths and lifetimes of ceramics.
In order to allow a simple analysis to be made, the natural cracks in ceramics are modelled by one half of a circular embedded crack (fig.33). For such a crack, loaded by a stress $\sigma(r)$, the related stress intensity factor is given by

$$K_I = \frac{2}{\sqrt{\pi a}} \int_0^a \frac{r\,\sigma(r)\,dr}{\sqrt{a^2 - r^2}} \tag{4.4.1}$$

where a is the crack size and r is the distance from the origin.

The COD-field exposed to combined loading by externally applied stresses and internal bridging stresses can be expressed in a power series representation with respect to $\sqrt{1-(r/a)^2}$ as

$$\delta = \sum_{n=0}^{\infty} C_n (1 - r^2/a^2)^{n+1/2} \quad , \quad C_0 = \frac{2}{\sqrt{\pi}} \sqrt{a}\, \frac{1-\nu^2}{E} K_{I\,tip} \tag{4.4.2}$$

In order to describe the characteristic features of the stress intensity factor solution only the dominating term of eq.(4.4.2) is considered. For an arbitrary bridging stress relation

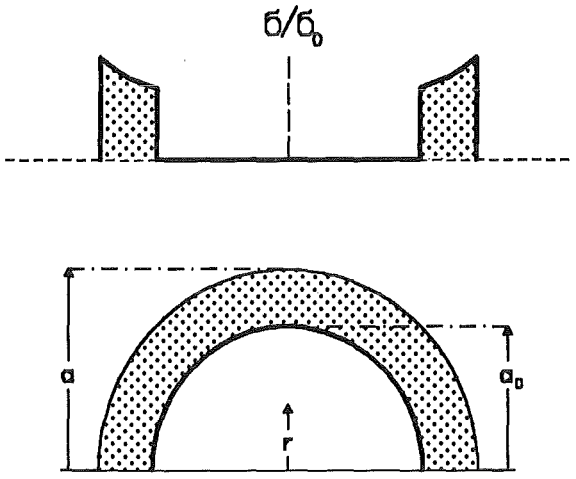

Figure 33. Semi-circular crack. A semi-circular crack with the total crack size a and the initially interaction free region $0 < r < a_0$.

$$\sigma_{br} = \sigma_0 f(\delta/\delta_0) \tag{4.4.3}$$

the bridging stress intensity factor $K_{I\,br}$ results from eq.(4.4.1)

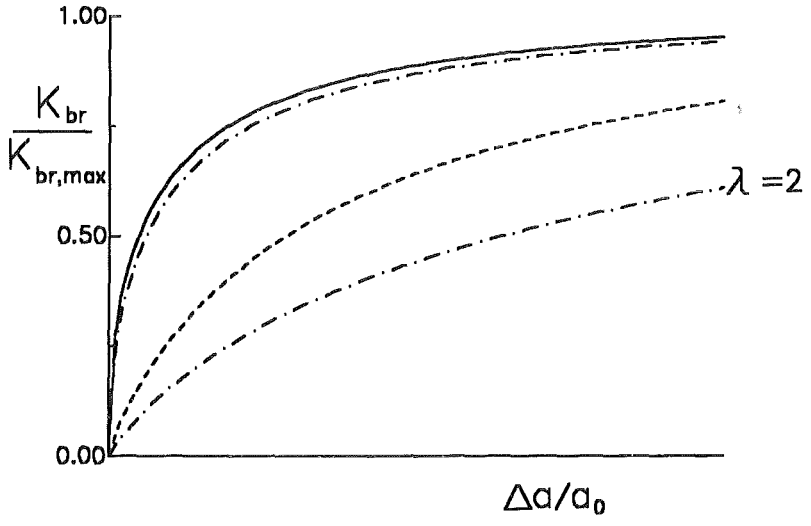

Figure 34. Bridging stress intensity factors for embedded circular cracks. Bridging stress intensity factor normalised on the maximum value for the bridging stress relations eq.(4.4.6) (solid curve), (4.4.10) (dash-dotted lines), and (4.4.14) (dashed line); relation (4.4.10) is plotted for $\lambda = 2$ (Morse law) and $\lambda = 20$ (this curve is very closed to the solid line).

$$K_{I\,br} \simeq \frac{2}{\sqrt{\pi}} \sqrt{a}\, \sigma_0 \int_{a_0/a}^{1} \frac{\rho}{\sqrt{1-\rho^2}}\, f\left(\frac{C_0}{\delta_0} \sqrt{1-\rho^2} \right) d\rho \tag{4.4.4}$$

or after substituting

$$y = \sqrt{1-\rho^2}$$

$$K_{I\,br} \simeq \frac{2}{\sqrt{\pi}} \sqrt{a}\, \sigma_0 \int_{0}^{\sqrt{1-(a_0/a)^2}} f\left(\frac{C_0}{\delta_0}\, y \right) dy \tag{4.4.5}$$

This relation can be integrated analytically for all bridging relations considered in section 4.1. we find for:

•

$$\sigma_{br} = \sigma_0 \exp(-\delta/\delta_0) \tag{4.4.6}$$

$$K_{I\,br} \simeq \frac{E'\sigma_0\delta_0}{K_{I\,tip}} \left[1 - \exp\left(-\frac{2}{\sqrt{\pi}} \frac{K_{I\,tip}\sqrt{a}}{E'\delta_0} \sqrt{1-(a_0/a)^2} \right) \right] \tag{4.4.7}$$

If we consider (formally) the limit case $a \to \infty$, we obtain from eq.(4.4.7) a maximum stress intensity factor

$$K_{I\,br,max} = \frac{E'\sigma_0\delta_0}{K_{I\,tip}} \tag{4.4.8}$$

and eq.(4.4.7) can be expressed by

$$K_{I\,br} \simeq K_{I\,br,max} \left[1 - \exp\left(-\frac{2}{\sqrt{\pi}} \frac{\sigma_0\sqrt{a}}{K_{I\,br,max}} \sqrt{1-(a_0/a)^2} \right) \right] \tag{4.4.9}$$

In this context it should be mentioned once more that the displacement field described by eq.(4.4.2) is an approximation, which is valid especially for small crack opening displacements. Nevertheless, numerical computations using the correct crack opening displacement field result in a similar relation [34].

•

$$\sigma_{br} = \sigma_0 [1 - \exp(-\lambda\delta/\delta_0)] \exp(-\delta/\delta_0) \tag{4.4.10}$$

$$K_{I\,br} \simeq \frac{E'\sigma_0\delta_0}{K_{I\,tip}}\left[\frac{\lambda}{1+\lambda} - \exp\left(-\frac{2}{\sqrt{\pi}}\frac{K_{I\,tip}\sqrt{a}}{E'\delta_0}\sqrt{1-(a_0/a)^2}\right)\right.$$
$$\left. + \frac{1}{\lambda+1}\exp\left(-(\lambda+1)\frac{2}{\sqrt{\pi}}\frac{K_{I\,tip}\sqrt{a}}{E'\delta_0}\sqrt{1-(a_0/a)^2}\right)\right] \tag{4.4.11}$$

(For Morse-like bridging stresses we have to introduce $\lambda = 1$). Or, with the maximum value

$$K_{I\,br,max} = \frac{E'\sigma_0\delta_0}{K_{I\,tip}}\frac{\lambda}{1+\lambda} \tag{4.4.12}$$

$$K_{I\,br} \simeq K_{I\,br,max}\left[1 - \frac{1+\lambda}{\lambda}\exp\left(-\frac{2}{\sqrt{\pi}}\frac{\sigma_0\sqrt{a}}{K_{I\,br,max}}\frac{\lambda}{1+\lambda}\sqrt{1-(a_0/a)^2}\right)\right.$$
$$\left. + \frac{1}{\lambda}\exp\left(-\frac{2}{\sqrt{\pi}}\frac{\sigma_0\sqrt{a}}{K_{I\,br,max}}\lambda\sqrt{1-(a_0/a)^2}\right)\right] \tag{4.4.13}$$

$$\sigma_{br} = \sigma_0\frac{\delta}{\delta_0}\exp(-\delta/\delta_0) \tag{4.4.14}$$

$$K_{I\,br} \simeq \frac{E'\sigma_0\delta_0}{K_{I\,tip}}\left[1 - \left(1 + \frac{2}{\sqrt{\pi}}\frac{K_{I\,tip}\sqrt{a}}{E'\delta_0}\sqrt{1-(a_0/a)^2}\right)\cdot\right.$$
$$\left.\cdot\exp\left(-\frac{2}{\sqrt{\pi}}\frac{K_{I\,tip}\sqrt{a}}{E'\delta_0}\sqrt{1-(a_0/a)^2}\right)\right] \tag{4.4.15}$$

and with the same maximum value as given by eq.(4.4.8)

$$K_{I\,br} \simeq K_{I\,br,max}\left[1 - \left(1 + \frac{2}{\sqrt{\pi}}\frac{\sigma_0\sqrt{a}}{K_{I\,br,max}}\sqrt{1-(a_0/a)^2}\right)\cdot\right.$$
$$\left.\cdot\exp\left(-\frac{2}{\sqrt{\pi}}\frac{\sigma_0\sqrt{a}}{K_{I\,br,max}}\sqrt{1-(a_0/a)^2}\right)\right] \tag{4.4.16}$$

In fig.34 the bridging stress intensity factors normalised to the maximum values are plotted for the bridging relations considered before. Whilst for eq.(4.4.6) the increase in the bridging stress intensity factor is square-root shaped, the initial part is linear for the other bridging relations. In the case of eq.(4.4.10) with $\lambda = 20$, the bridging stress intensity factor is very close to that for eq.(4.4.6). This becomes obvious from fig.34 where only for small displacements a deviation from the exponential behaviour can be detected. The other relations which exhibit a more pronounced linear initial part in the $\sigma_{br} - \delta$ –curve yield rather linear R-curves.

5. R-curves caused by phase transformations

5.1 Phase-transformation zone at the crack tip

Due to the singular stress field near the crack tip in transformation-toughened ceramics, the material undergoes a stress-induced martensitic transformation and the tetragonal material changes to the monoclinic phase (t- to m-ZrO_2). This transformation occurs when the local stresses reach a critical value and the result is a crack-tip transformation zone. In the following considerations it is assumed according to the analysis of McMeeking and Evans [35] that the transformation is initiated when the hydrostatic tensile stress reaches a characteristic value σ_{hyd}^{ξ}. For the special case of a crack in an infinite body McMeeking and Evans [35] and Budiansky et al. [36] computed the transformation zone ahead of a crack tip under conditions of small-scale phase transformation (zone size $\ll$ crack size) neglecting the pertubation of the stress field due to the transformation.

5.1.1 Weak phase transformations

In the next sections it is assumed that the influence of the dilatation stresses on the shape and the size of the zone is negligible, i.e. we will restrict the considerations to the limit case $p/\sigma_{hyd}^{\xi} \to 0$, i.e. the case of weak transformation. The quantity p is given by

$$p = \frac{\varepsilon^T f E}{3(1-2\nu)} \tag{5.1.1}$$

where ε^T is the volumetric phase transformation strain, f the volume fracture of transformed material, E Young's modulus and ν Poisson's ratio.

5.1.1.1 Small-scale transformation zones

For the special case of a crack in an infinite body McMeeking and Evans [35] computed the transformation zone ahead of a crack tip under conditions of small-scale phase transformation (zone size $\ll$ crack size). In this limit case the stresses ahead of a crack tip are given in polar coordinates with the origin at the tip by

$$\sigma_r = \frac{K_I}{\sqrt{2\pi r}} \cos(\varphi/2)\left(1 + \sin^2(\varphi/2)\right)$$
$$\sigma_\varphi = \frac{K_I}{\sqrt{2\pi r}} \cos(\varphi/2)\cos^2(\varphi/2) \tag{5.1.2}$$

where K_I is the mode-I crack-tip stress intensity factor. From the sum of stress components, eq.(5.1.2), the hydrostatic stress σ_{hyd} results for plane strain conditions

$$\sigma_{hyd} = \frac{1+\nu}{3}(\sigma_r + \sigma_\varphi) = \frac{1+\nu}{3}(\sigma_x + \sigma_y) \tag{5.1.3}$$

yielding

$$\sigma_{hyd} = \frac{2(1+\nu)}{3}\frac{K_I}{\sqrt{2\pi r}}\cos(\varphi/2) \tag{5.1.4}$$

In the special case of phase transformation activated by hydrostatic stress the size and shape of the zone results from the condition

$$\sigma_{hyd} = \sigma^c_{hyd} \tag{5.1.5}$$

when the hydrostatic stress reaches the characteristic value σ^c_{hyd}. Combination of eqs.(5.1.4) and (5.1.5) gives the transformation zone as

$$r = \frac{2}{9\pi}(1+\nu)^2(K_I/\sigma^c_{hyd})^2\cos^2(\varphi/2) \tag{5.1.6}$$

If we introduce the width of the transformation zone ω, which is obtained for $\varphi = \pi/3$, we can write

$$\omega = \frac{(1+\nu)^2}{4\sqrt{3}\,\pi}(K_I/\sigma^c_{hyd})^2 \quad , \quad r = \frac{8}{3\sqrt{3}}\,\omega\,\cos^2(\varphi/2) \tag{5.1.7}$$

This formula has been derived at an early stage by McMeeking and Evans [35]. Figure 35 shows the geometrical data occurring in eq.(5.1.7). It should be mentioned once more that this relation is only valid if the boundaries of the body are far away from the crack tip.

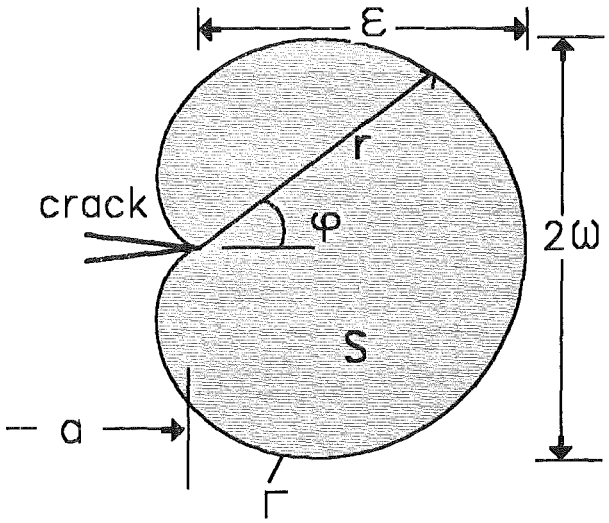

Figure 35. Transformation zone ahead of a crack tip. Geometrical data.

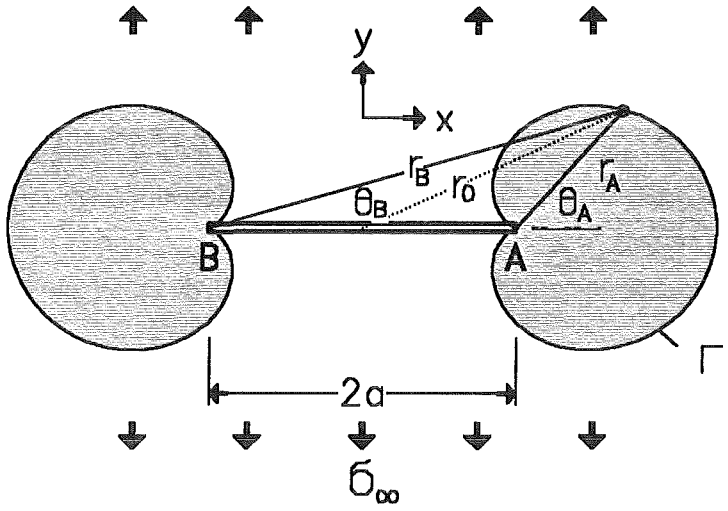

Figure 36. Transformation zone in front of an internal crack. Geometrical data.

5.1.1.2 Transformation zones for internal cracks in infinite bodies

To show the effect of the crack length on the phase transformation zone, we will consider an infinite body containing an internal "through-the-thickness" crack of total length 2a under remote tension loading. Figure 36 shows the relevant geometrical data.
The stresses acting on this type of crack are exactly known (see e.g. [26]), and we obtain the sum $\sigma_x + \sigma_y$ as

$$\sigma_x + \sigma_y = \sigma_\infty \left[\frac{2\,r_0}{\sqrt{r_A r_B}} \cos\left(\theta_0 - \frac{\theta_A + \theta_B}{2} \right) - 1 \right] \tag{5.1.8}$$

with the radii

$$\begin{aligned} r_0 &= \sqrt{r_A^{\,2} + a^2 + 2 a r_A \cos\theta_A} \\ r_B &= \sqrt{r_A^{\,2} + 4a^2 + 4 a r_A \cos\theta_A} \end{aligned} \tag{5.1.9}$$

and the angles

$$\begin{aligned} \theta_0 &= \arctan\left(\frac{r_A \sin\theta_A}{a + r_A \cos\theta_A} \right) \\ \theta_B &= \arctan\left(\frac{r_A \sin\theta_A}{2a + r_A \cos\theta_A} \right) \end{aligned} \tag{5.1.10}$$

Also in this case, the size and shape of the transformation zone result from the condition

$$\sigma_{hyd} = \sigma_{hyd}^{c}$$

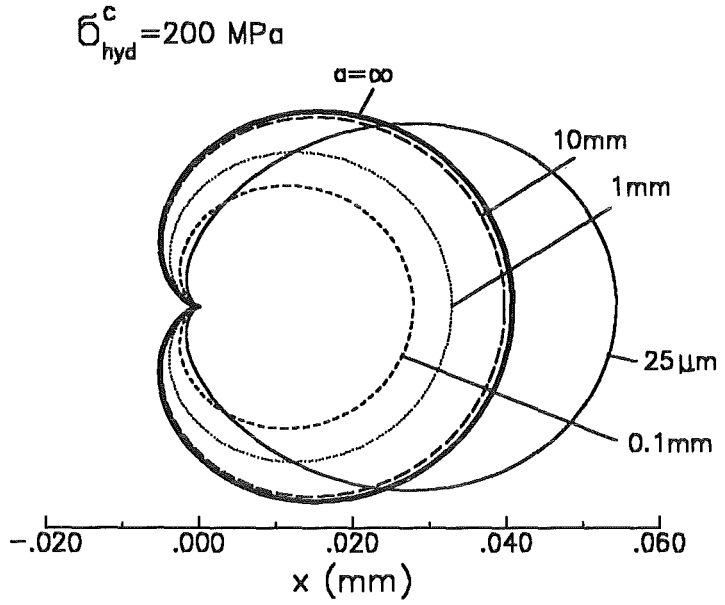

Figure 37. Transformation zone in front of an internal crack. Change of the transformation zone with the initial crack length a for a hydrostatic stress σ^c_{hyd}=200 MPa and a crack-tip stress intensity factor K_{tip}=4 MPa $\sqrt{m}$).

The influence of this characteristic stress and the influence of the initial crack size on the phase-transformation zone are shown in fig.37. Other than for the limit case of small-scale transformation zones, we conclude that the zone size is dependent on the crack length. For large cracks the size of the zone increases monotonically with increasing initial crack length. In case of a small crack the applied tensile stress has to be increased considerably to reach the same K_{I0} as obtained for a long crack under lower stress. If the crack is very small (or the critical phase-transformation stress is low), a large transformation zone will result.
From eqs.(5.1.8)-(5.1.10) we can conclude that the hydrostatic stress can be written as

$$\sigma_{hyd} = \frac{1+\nu}{3\sqrt{a\,\pi}} K_I \cdot f(r_A/a, \theta_A) \tag{5.1.11}$$

where the stress intensity factor is given by

$$K_I = \sigma_\infty \sqrt{\pi a} \tag{5.1.12}$$

The size and shape of the transformation zone result from eq.(5.1.5) and the zone contour represented implicitly by

$$f(r_A/a, \theta_A) = \frac{3}{1+\nu} \sqrt{\pi a}\, \frac{\sigma^c_{hyd}}{K_I} \tag{5.1.13}$$

from which we conclude that a normalised representation

$$r_A/a = g\left(\theta_A, \frac{K_I}{\sigma^c_{hyd}\sqrt{a}}\right) \tag{5.1.14}$$

is possible. Figure 38 shows the results of fig.37 in this representation. If we now consider a very long crack with $a \gg \omega$, it results for the quantities of eqs.(5.1.8)-(5.1.10):

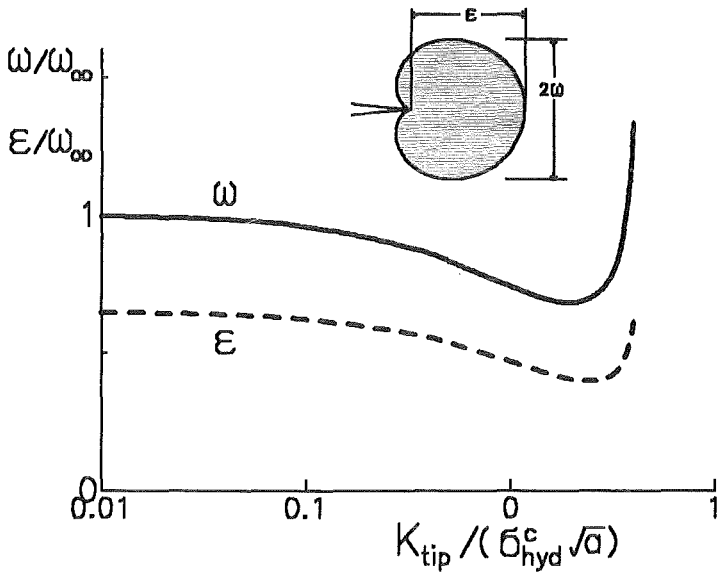

Figure 38. Transformation zone in front of an internal crack. Change of the transformation zone in a normalised representation.

$$r_0 \to a \ , \ r_B \to 2a \ , \ \theta_0 \to 0 \ , \ \theta_B \to 0$$

and after introducing these limit values in eq.(5.1.8) we get

$$r_A = \frac{2a \cos^2(\theta_A/2)}{\left(1 + \frac{3}{1+\nu}\sqrt{\pi a}\,\frac{\sigma^c_{hyd}}{K_I}\right)^2} \tag{5.1.15}$$

In case of an infinite crack length the term 1 in the denominator can be neglected and eq.(5.1.7) results as a first-order approximation.

5.1.1.3 Transformation zones for finite cracks in finite bodies

No exact stress solution is known for finite bodies. The transformation zone can be calculated from the Airy stress function Φ, which satisfies the bi-potential equation

$$\Delta\Delta\Phi = 0 \tag{5.1.16}$$

If this function is known for a given crack in a component, the stresses result as

$$\sigma_r = \frac{1}{r}\frac{\partial\Phi}{\partial r} + \frac{1}{r^2}\frac{\partial^2\Phi}{\partial\varphi^2}$$

$$\sigma_\varphi = \frac{\partial^2\Phi}{\partial r^2} \tag{5.1.17}$$

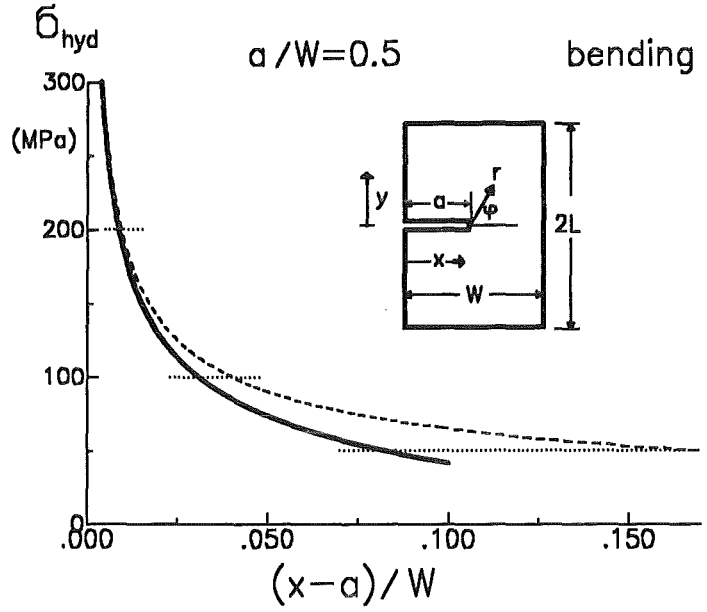

Figure 39. Hydrostatic stresses ahead of an edge-crack in a bending bar. Comparison between the total stresses (solid curve) and the singular stress term (dashed curve).

$$\tau_{r\varphi} = \frac{1}{r^2}\frac{\partial \Phi}{\partial \varphi} - \frac{1}{r}\frac{\partial^2 \Phi}{\partial r \partial \varphi}$$

The symmetric part of the stress function - the only part of interest here - reads [37]

$$\Phi_s = \sum_{n=0}^{\infty} r^{n+3/2} A_n \left[\cos(n+3/2)\varphi - \frac{n+3/2}{n-1/2}\cos(n-1/2)\varphi \right] \qquad (5.1.18)$$

$$+ \sum_{n=0}^{\infty} r^{n+2} A_n^* [\cos(n+2)\varphi - \cos n\varphi]$$

For practical application of eq.(5.1.18), the infinite series must be truncated after the Nth term for which an adequate value must be chosen.
The still unknown coefficients in eq.(5.1.18) can be determined using the Boundary Collocation Method (BCM). For the special case of an edge crack in a bending bar the coefficients for (5.1.18) were determined and tabulated in [38].
The series representation of the stress function leads to the hydrostatic stress

$$\sigma_{hyd} = -4\frac{1+\nu}{3}\sum_{n=0}^{\infty}\left[A_n r^{n-1/2}\frac{(n+3/2)(n+1/2)}{n-1/2}\cos(n-1/2)\varphi \right. \qquad (5.1.19)$$

$$\left. + A_n^* r^n (n+1)\cos n\varphi \right]$$

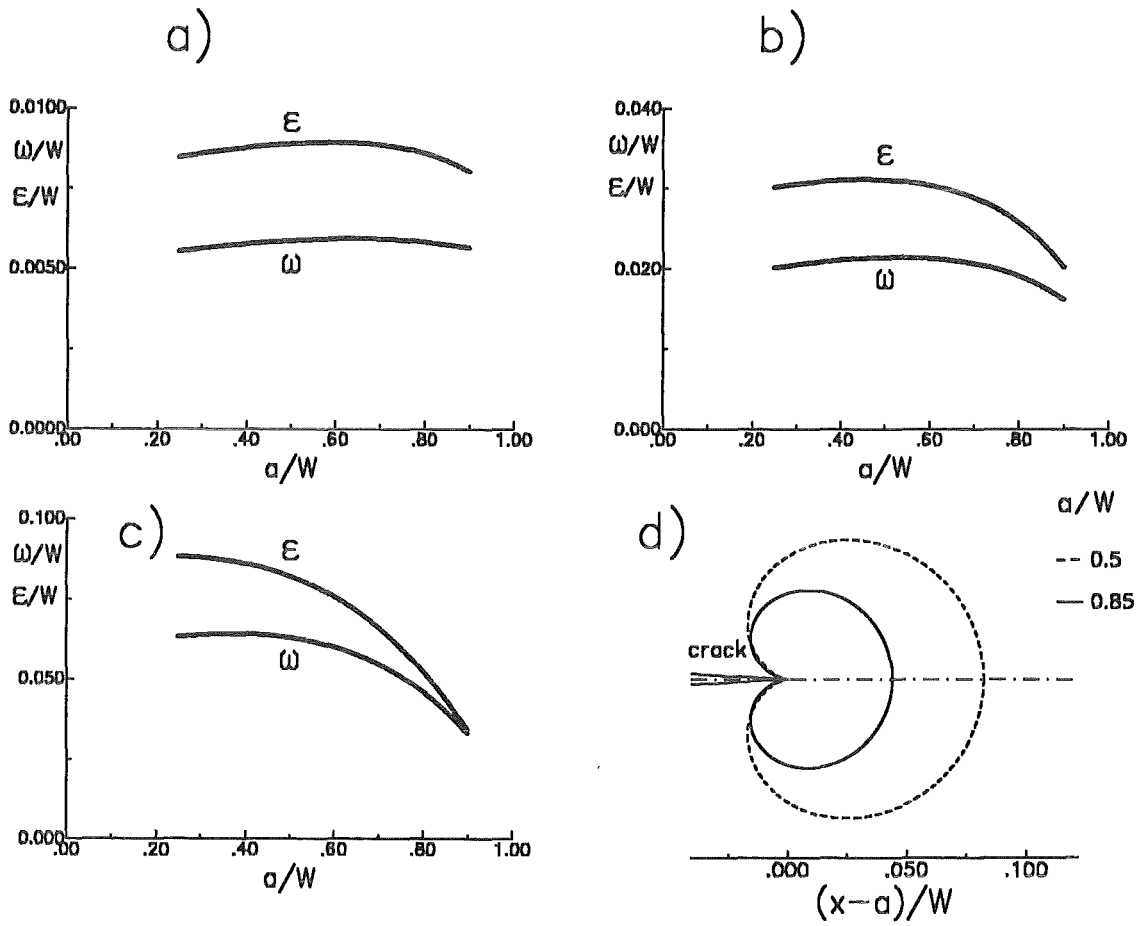

Figure 40. Transformation zone. Influence of the initial crack size on the size of the transformation zone; $W = 4.5$mm, $a = 2.25$mm, $K_I = 4$MPa $\sqrt{m}$, a) $\sigma_{hyd} = 200$MPa, b) $\sigma_{hyd} = 100$MPa, c) $\sigma_{hyd} = 50$MPa (for ε and ω see fig.35), d) Shape of zones for $W = 4.5$mm, $K_I = 4$MPa $\sqrt{m}$, $\sigma_{hyd} = 50$MPa.

In fig.39 the hydrostatic stress ahead of a crack in a bending bar with $a/W = 0.5$ is plotted for the situation $K_I = 4$ MPa $\sqrt{m}$ with $\nu = 0.2$ and $W = 4.5$mm. Whereas the solid curve represents the complete stress solution, the dashed curve only represents the first (singular) term of the series. It becomes obvious that for $\sigma_{hyd} > 300$ MPa the hydrostatic stresses are sufficiently represented by the singular stress term. For stresses $\sigma_{hyd} < 100$ MPa the deviations from the correct solution are strong.

Figure 40 shows the influence of the transformation stress, σ^c_{hyd}, on the width ω and the length ε of the transformation zone for the limit case $p/\sigma^c_{hyd} \to 0$. The influence of transformation on the shape of the zone is neglected. With increasing a the width ω of the transformation zone at $K_I = K_{I0}$ increases and, after passing a maximum at about $a/W = 0.6$, ω decreases again. The same dependency can be observed for the "length" of the transformation zone, i.e. for the distance ahead of the crack where the material changes from the transformed to the original state. Part d) gives an impression of the changes in size and shape for a low critical transformation stress.

Figure 41 illustrates the change of size of the transformation zone as a function of the critical hydrostatic stress in a normalised representation

$$\omega^* = \omega(\sigma^c_{hyd}/K)^2 4\sqrt{3}\,\pi/(1+\nu)^2 \quad , \quad \varepsilon^* = \varepsilon(\sigma^c_{hyd}/K)^2 4\sqrt{3}\,\pi/(1+\nu)^2 \qquad (5.1.20)$$

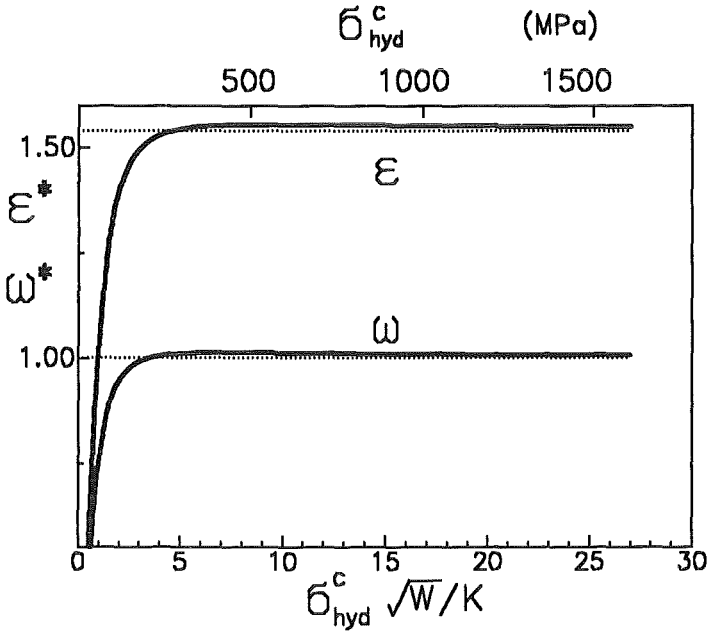

Figure 41. Transformation zone. Change of size of transformation zone with critical hydrostatic stress in a normalised representation; $a/W=0.5$, upper scale valid for $W=4.5$mm and $K_I=4$ MPa$\sqrt{\text{m}}$; solid curve: complete stress solution, dotted lines: singular stress term eq.(5.1.7); (for ε^* and ω^* see eq.(5.1.20)).

$\sigma^c_{hyd}\sqrt{W}/K$	ν	a/W=0.25	0.4	0.5	0.6	0.7	0.85
0.5	0.2	0.478	0.457	0.434	0.399	0.348	0.232
	0.3	0.448	0.423	0.400	0.365	0.317	0.209
1.0	0.2	0.728	0.748	0.744	0.719	0.666	0.510
	0.3	0.703	0.718	0.710	0.683	0.628	0.472
1.5	0.2	0.832	0.872	0.881	0.873	0.839	0.708
	0.3	0.815	0.852	0.859	0.847	0.809	0.669
2.0	0.2	0.884	0.928	0.943	0.945	0.926	0.832
	0.3	0.871	0.915	0.929	0.928	0.905	0.800
3.0	0.2	0.931	0.972	0.990	0.999	0.996	0.955
	0.3	0.923	0.966	0.984	0.992	0.987	0.936
5.0	0.2	0.964	0.995	1.010	1.020	1.024	1.022
	0.3	0.960	0.993	1.008	1.018	1.023	1.016
10.	0.2	0.984	1.002	1.011	1.018	1.023	1.032
	0.3	0.982	1.002	1.011	1.018	1.024	1.033
15.	0.2	0.990	1.002	1.009	1.014	1.018	1.026
	0.3	0.989	1.002	1.009	1.014	1.019	1.028

Table 1. Phase-transformation zone. Normalised zone width ω^* according to eq.(5.1.20).

For very high transformation stresses the curves tend towards 1 for ω^* and towards $8/\sqrt{27}$ for ε^*. We can conclude from this plot that small-scale transformation conditions are fulfilled for

$\sigma_{hyd}^{f}\sqrt{W}\,/K_I > 5$. The zone width has been computed for a field of parameters and the normalised data have been entered in Table 1.

5.1.2 Phase transformation zones for strong transformations

Under conditions of small-scale transformation, the influence of the dilatation stresses on the zone size and zone shape was studied by Stump and Budiansky [40] and Amazigo and Budiansky [41] using Hutchinson's [42] analytical solution for a stress field of pairs of small circular spots of dilatation. Their procedure leads to an integral equation that has to be solved numerically. The result is a relation which contains eq.(5.1.3) as the principal term and provides an additional term representing the influence of the phase-transformation stresses on the total hydrostatic stress

$$\sigma_{hyd} = \frac{2(1+\nu)}{3}\frac{K_I}{\sqrt{2\pi r}}\cos(\varphi/2) + \\ + \frac{p(1-2\nu)}{6\pi}\frac{1+\nu}{1-\nu}\int_S Re\left\{\frac{1}{\sqrt{zz_0}\left(\sqrt{z}+\sqrt{z_0}\right)^2}+\frac{1}{\sqrt{z\bar{z}_0}\left(\sqrt{z}+\sqrt{\bar{z}_0}\right)^2}\right\}dS_0 \tag{5.1.21}$$

where

$$z = r\exp(i\varphi) \quad , \quad \bar{z} = r\exp(-i\varphi) \tag{5.1.22}$$

z describes the location where the stresses are evaluated and z_0 are the locations of the dilatation spots.
A different approach to determine the initial phase transformation zone is the use of the fracture mechanics weight function.

5.1.2.1 Calculation of crack-tip stress fields with the weight function

A crack of length a in a body may be loaded by tractions $\mathbf{T}(s)$ acting normal to a curve Γ (fig.42). The tractions are responsible for a stress field at the crack tip which can be characterised by a stress intensity factor K^T where the supscript "T" refers to the loading system. One can write

$$K^T = \int_\Gamma \mathbf{T}\cdot\mathbf{h}\,dS \tag{5.1.23}$$

where $\mathbf{h}$ is the vector of the weight function $\mathbf{h} = (h_y, h_x)^T$ and $\mathbf{T} = (T_y, T_x)^T$. In the following considerations only loading cases symmetrical to the x-axis will be taken into account, i.e. only mode-I stress intensity factors will occur.
Rice [29] has shown that the weight function is related to the displacement field $\mathbf{u} = (u_y, u_x)^T$ by

$$\mathbf{h} = \frac{E'}{K_r}\frac{\partial \mathbf{u}}{\partial a} \tag{5.1.24}$$

where K_r is the stress intensity factor for an arbitrary reference loading case. Subsequently, this reference loding case is identified with the loadings by the tractions $\mathbf{T}$, i.e. $K_r = K^T$. Equations (5.1.24) then enable the displacements to be determined at an arbitrary location characterised by the coordinates x,y. In order to avoid confusions, the location where the tractions act may be described by $\tilde{x}, \tilde{y}$. The weight functions are distinguished in the same way ($\tilde{h} = h(\tilde{x}, \tilde{y})$). The displacements result from eq.(5.1.24) as

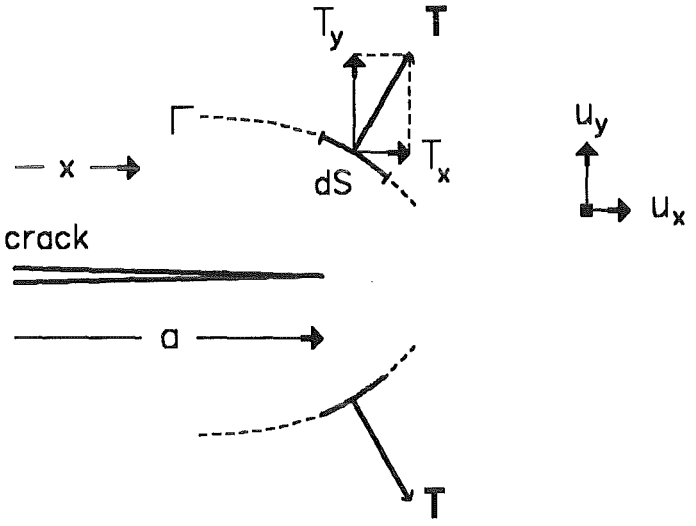

Figure 42. Crack loaded by tractions. Geometrical data.

$$u_y = \frac{1}{E'} \int_0^a \left[\int_\Gamma \tilde{\mathbf{h}} \cdot \mathbf{T}\, dS \right] h_y(a')\, da' + u_{y0} \tag{5.1.25}$$

$$u_x = \frac{1}{E'} \int_0^a \left[\int_\Gamma \tilde{\mathbf{h}} \cdot \mathbf{T}\, dS \right] h_x(a')\, da' + u_{x0} \tag{5.1.26}$$

where u_{y0} and u_{x0} are the displacements in the absence of a crack. The strains are obtained from

$$\varepsilon_y = \frac{1}{E'} \frac{\partial}{\partial y} \int_0^a \left[\int_\Gamma \tilde{\mathbf{h}} \cdot \mathbf{T}\, dS \right] h_y(a')\, da' + \varepsilon_{y0} \tag{5.1.27}$$

$$\varepsilon_x = \frac{1}{E'} \frac{\partial}{\partial x} \int_0^a \left[\int_\Gamma \tilde{\mathbf{h}} \cdot \mathbf{T}\, dS \right] h_x(a')\, da' + \varepsilon_{x0} \tag{5.1.28}$$

Finally, the stresses result from Hooke's law

$$\sigma_y = \frac{1-\nu}{1-2\nu} \int_0^a \left[\int_\Gamma \tilde{\mathbf{h}} \cdot \mathbf{T}\, dS \right] \left((1-\nu) \frac{\partial h_y(a')}{\partial y} + \nu \frac{\partial h_x(a')}{\partial x} \right) da' + \sigma_{y0} \tag{5.1.29}$$

$$\sigma_x = \frac{1-\nu}{1-2\nu} \int_0^a \left[\int_\Gamma \tilde{\mathbf{h}} \cdot \mathbf{T}\, dS \right] \left(\nu \frac{\partial h_y(a')}{\partial y} + (1-\nu) \frac{\partial h_x(a')}{\partial x} \right) da' + \sigma_{x0} \tag{5.1.30}$$

The hydrostatic stresses in a phase transformation zone at a crack tip will be considered as a practical example. In order to be able to compute the size of the transformation zone, we are interested in the hydrostatic tension stress ([35]). For plane strain conditions it holds

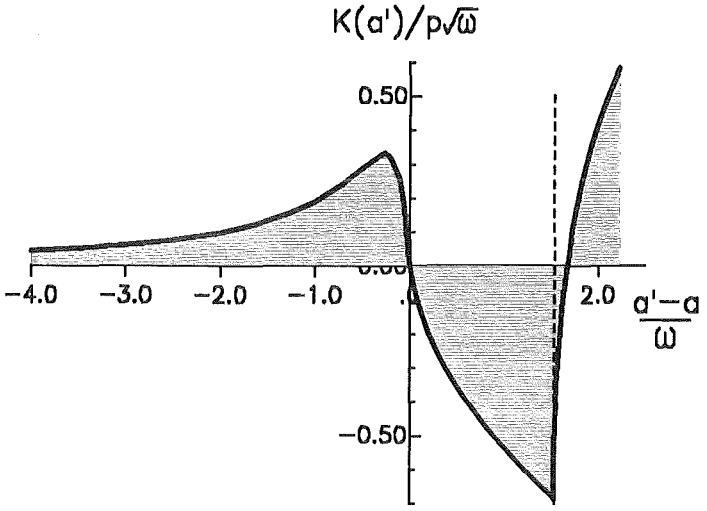

Figure 43. Stress intensity factor caused by the transformation zone. Value of the integral $K^T(a')$ in eq.(5.1.33) (first approximation).

$$\sigma_{hyd} = \frac{1+\nu}{3}(\sigma_x + \sigma_y) = \frac{E}{3(1-2\nu)}(\varepsilon_x + \varepsilon_y) \tag{5.1.31}$$

$$\sigma_{hyd} = \frac{1-\nu^2}{3(1-2\nu)} \int_0^a \left[\int_\Gamma \tilde{\mathbf{h}} \bullet \mathbf{T}\, dS \right] \left(\frac{\partial}{\partial x} h_x(a') + \frac{\partial}{\partial y} h_y(a') \right) da' + \sigma_{hyd,0} \tag{5.1.32}$$

written in the short form as

$$\sigma_{hyd} = \frac{1-\nu^2}{3(1-2\nu)} \int_0^a K^T(a')\, \nabla \bullet \mathbf{h}(a')\, da' + \sigma_{hyd,0} \tag{5.1.33}$$

where $\sigma_{hyd,0}$ is the hydrostatic stress in the absence of the crack. It can be concluded from general principles that for an inclusion (and also for a phase transformation zone) in an infinite body the hydrostatic stress is ([39],[43])

$$\sigma_{hyd,0} = \begin{cases} -\frac{2}{3}\frac{1-2\nu}{1-\nu} p & \text{for } x,y \in S \\ 0 \quad \text{for} & x,y \notin S \end{cases} \tag{5.1.34}$$

For the numerical evaluation of eq.(5.1.33) in the limit case of small-scale transformation zones we will use the weight function for a long crack in an infinite body as given by Tada et al. [1]

$$h_x = \frac{1}{\sqrt{8\pi r}\,(1-\nu)} \left[2\nu - 1 + \sin\left(\frac{\varphi}{2}\right) \sin\left(\frac{3}{2}\varphi\right) \right] \cos\left(\frac{1}{2}\varphi\right) \tag{5.1.35}$$

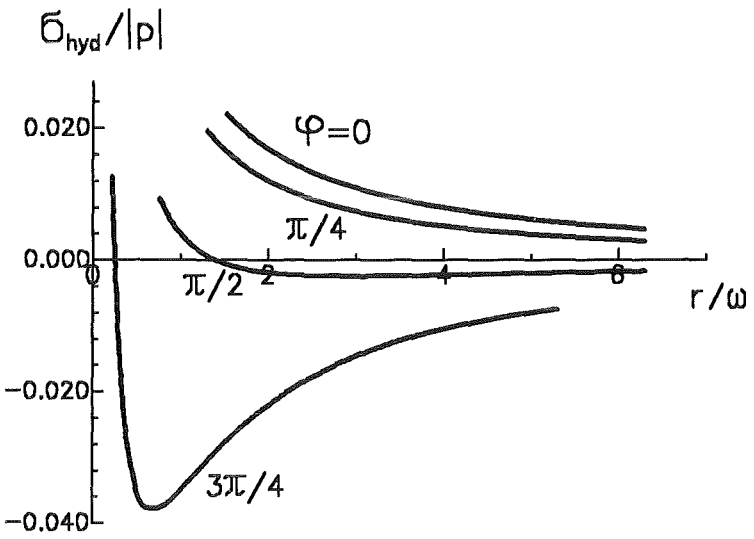

Figure 44. Hydrostatic stress around the transformation zone. σ_{hyd} caused by the first-order transformation zone.

$$h_y = \frac{1}{\sqrt{8\pi r}\,(1-\nu)}\left[2 - 2\nu - \cos\left(\frac{\varphi}{2}\right)\cos\left(\frac{3}{2}\varphi\right)\right]\sin\left(\frac{1}{2}\varphi\right) \tag{5.1.36}$$

where r and φ are polar coordinates with the origin at the crack tip. We will use the result of McMeeking and Evans [35] as a first approximation. Starting with the transformation zone given by eq.(5.1.7), the second approximation of the transformation zone was determined. For the numerical evaluation $\nu = 0.2$ was chosen. Since the value $K(a')$ at $a' = a$ disappears, we see that the transformation zone in the first approximation does not create a shielding stress intensity factor. Figure 43 represents the stress intensity factor $K(a')$ which is necessary to evaluate eq.(5.1.33). As a result of eq.(5.1.33), fig.44 shows the hydrostatic stress component outside the first estimation transformation zone as a function of the distance from the crack tip. An arbitrary hydrostatic stress σ_{hyd} caused by the externally applied load is reached at the distance r

$$r = r_c\left(\frac{\sigma^c_{hyd}}{\sigma_{hyd}}\right)^2 \tag{5.1.37}$$

Introducing eq.(5.1.7) yields

$$\sigma_{hyd}(r, \varphi) = \sigma^c_{hyd}\,\frac{4}{3^{3/4}\sqrt{2}}\,\frac{\cos(\varphi/2)}{\sqrt{r/\omega}} \tag{5.1.38}$$

The size of the phase tansformation zone in the second approximation results from the condition

$$\sigma_{hyd} = \sigma_{hyd,appl} + \sigma_{hyd,transf\,zone} = \sigma^c_{hyd} \tag{5.1.39}$$

leading to the relation

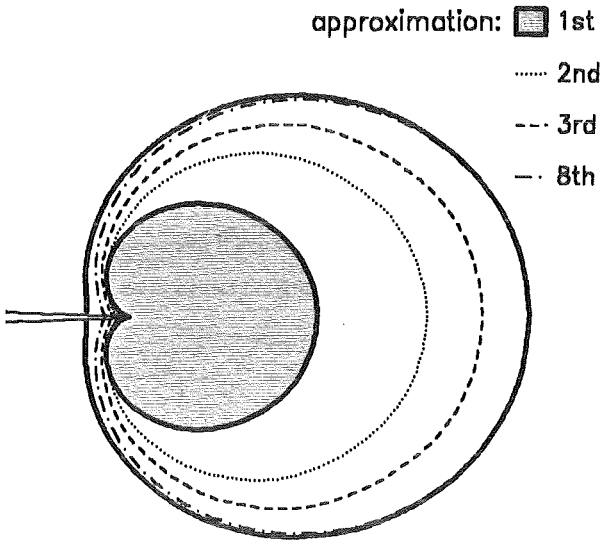

Figure 45. Phase transformation zone. Change of the transformation zone by the hydrostatic stress portion caused by the transformation zone itself, outer solid line: final zone size ($p/\sigma^{c}_{hyd} = 15$).

$$\frac{4}{3^{3/4}\sqrt{2}} \frac{\cos(\varphi/2)}{\sqrt{r/\omega}} + \frac{\sigma_{hyd}(r/\omega)}{p} \cdot \frac{p}{\sigma^{c}_{hyd}} = 1 \qquad (5.1.40)$$

from which the radius of the zone can be obtained using a zero routine. The phase transformation zone resulting as the second approximation was chosen as the input to determine the zone in a third approximation. The change in size of the zone with the number of iterations is given in fig.45. Whereas the zone for $\varphi < 0.7$ reaches its limit of saturation early, the minimum dimension attains it later. The shape of the transformation zone tends more and more to become a circle with the crack tip inside. The shielding stress intensity factor is also plotted as a function of the number of iterations (fig.46). With increasing number of iterations, $K(a')$ first increases and having passed a maximum this stress intensity factor decreases continuously towards zero.
In order to avoid a great number of additional iteration steps demanding much expenditure in computer time, we will use an accelerated procedure for the further computations. The final shape of the zone can be estimated from a plot $r(\varphi)$ versus $1/N$ and from extrapolating to $1/N=0$. In this way, the contour of the final zone can be determined with sufficient accuracy in the range $0 \leq \varphi \leq 0.6\pi$. This estimated zone contour is now considered as a first approximation to the procedure described before. The change of zone size from the first approximation to the second is very small. A comparison of the second approximation with the third showed that no further change in zone size had occurred, i.e. the final zone was determined with sufficient accuracy. The final contour is plotted as the outer solid line in fig.45. The shielding stress intensity factor corresponding to the last iteration was found to be (for $p/\sigma^{c}_{hyd} = 15$) $K/(p\sqrt{\omega}) = 0.00055$ and $K/(p\sqrt{\omega}) = 0.0025$ in the step before. These results (entered in fig.46 as circles) ensure that the final shielding stress intensity factor is zero within the accuracy of the numerical analysis. This is in good agreement with the general proof by Budiansky et al. [36]. They showed by application of the J-integral that in case of small-scale transformation zones the shielding stress intensity factor vanishes for a non-extending crack. The influence of the ratio p/σ^{c}_{hyd} is shown in fig.47. An agreement with the results of Stump and Budiansky [40] is evident.

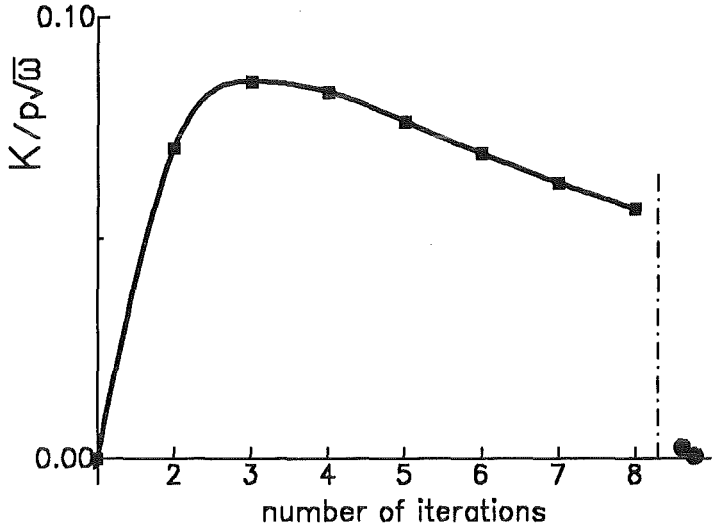

Figure 46. Convergence of the computations. Shielding stress intensity factor $K(a' = a)$ for $(p/\sigma_{hyd} = 15)$; circles: results for the additional iterations using the accelerated procedure.

5.2 Calculation of R-curves

5.2.1 Stress intensity factor

In this section a stress intensity factor analysis will be made similar to the investigation of McMeeking and Evans [35] who used an Eshelby technique [39]. Therefore, we assume the transformation zone ahead of the crack tip (see Section 5.1) to be removed from the original material. The transformed material which under unconstrained transformation exhibits a strain ε^T is assumed to be restored to the original shape of the non-transformed material by applying surface tractions **T** to the transformation zone. The zone now fits again into the body and equilibrium can be obtained by nullifying the surface tractions with a layer of body forces. The surface tractions then result in a residual stress intensity factor K^T. Since this stress intensity factor is caused by the residual stresses caused by the phase transformations it may be denoted in the following as K_{Ires}

$$K_{Ires} = \int_{S_T} \mathbf{T} \cdot \mathbf{h}\, dS \tag{5.2.1}$$

where S_T is the line describing the contour of the transformation zone and **h** is the vector of the weight function $\mathbf{h} = (h_y, h_x)^T$. Also for calculating stress intensity factors it is assumed that the change of shape of the zone by the transformation is negligible.
In the special case of a dilatational transformation the surface tractions are given by the normal pressure p defined by eq.(5.1.1), and the residual stress intensity factor K_{Ires} results

$$K_{Ires} = p \int_{S_p} \mathbf{n} \cdot \mathbf{h}\, dS \tag{5.2.2}$$

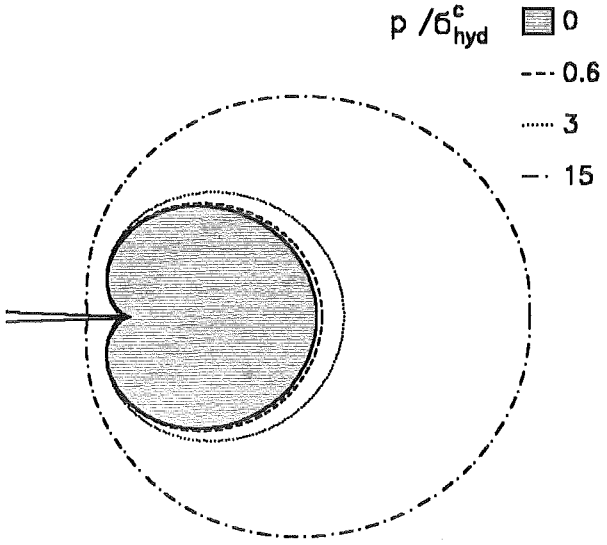

Figure 47. Final phase transformation zone. Shape of zone for several values of p/σ^c_{hyd}.

where **n** is the outward surface normal along the contour of the transormation zone. For numerical computations we rewrite eq.(5.2.2)

$$K_{Ires} = p\int_{S_p} (h_x dy - h_y dx) \tag{5.2.3}$$

where the x-axis corresponds to the axis of the crack. The components h_x and h_y of the weight function are given by eqs.(5.1.35) and (5.1.36) for infinite bodies and by the relations in Section A.1 for rectangular plates and bars of finite dimensions.

5.2.2 Stress intensity factor at the onset of crack extension

If a cracked body undergoes growing external loading, the transformation zone increases simultaneously and at the onset of crack extension it reaches its charcteristic size. A first question is whether this zone with its stress field leads to a shielding stress intensity factor before crack growth starts. Therefore, it is necessary to calculate the stress intensity factor which is caused by the tractions needed to restore the initial shape of the zone.
The weight function procedure is appropriate to solve the problem. This will be outlined in two steps:

1. First, the transformation zone is assumed to be small compared with the crack length and with the specimen width, i.e. $\omega \ll a, W$. In this limit case the exact weight function is known.

2. Then, the transformation zone and the crack size are assumed to be small compared with the specimen size, but may be of the same order of magnitude, i.e. $\omega \simeq a \ll W$. This special case will be considered for an internal crack for which the exact weight function is known, too.

5.2.2.1 Small-scale transformation zones

The weight function method was used by McMeeking and Evans [35] at an early stage already. For transformation activated by hydrostatic stress the shape of the zone has been computed analytically (see eq.(5.1.7)).

$$r = \frac{8}{3\sqrt{3}}\,\omega\,\cos^2(\varphi/2)$$

In [35] the dominating term of the weight function was used as described by eqs.(5.1.35) and (5.1.36). It was shown that the resulting stress intensity factor is $K_{Ires}=0$.
This important result could also be confirmed by an analysis on the basis of the J-integral as has been shown by Budiansky et al. [36]. On the other hand, it is not self-evident that

- also the higher terms of the correct weight function will not make a contribution to the stress intensity factor K_{Ires}, and
- $K_{Ires}=0$, especially for shapes of zones deviating from that in infinite bodies (eq.(5.1.7)).

5.2.2.2 Internal crack with transformation zones at both ends

The weight function for an **internal crack** in an **infinite body** loaded with symmetrical remote tractions (symmetrical with respect to $x=0$ and $y=0$) is given by [45]

$$h_x = \frac{1}{2\sqrt{\pi a}}\left\{\frac{\kappa-1}{\kappa+1}\left(\sqrt{\frac{r_A}{r_B}}-\sqrt{\frac{r_B}{r_A}}\right)\cos\frac{\theta_A-\theta_B}{2}+\right. \tag{5.2.4}$$

$$\left.+\frac{2}{\kappa+1}\sqrt{\frac{r_A}{r_B}}\,\sin\theta_A\left[\frac{r_B}{r_A}\sin\frac{3\theta_A-\theta_B}{2}-\frac{r_A}{r_B}\sin\frac{3\theta_B-\theta_A}{2}-\frac{a}{r_A}\sin\frac{3\theta_A+\theta_B}{2}\right]\right\}$$

$$h_y = \frac{1}{\sqrt{\pi a}}\left\{\left(\sqrt{\frac{r_B}{r_A}}+\sqrt{\frac{r_A}{r_B}}\right)\sin\frac{\theta_A-\theta_B}{2}+\right. \tag{5.2.5}$$

$$\left.+\frac{2}{\kappa+1}\sqrt{\frac{r_A}{r_B}}\,\sin\theta_A\left[\frac{r_A}{r_B}\cos\frac{3\theta_B-\theta_A}{2}-\frac{r_B}{r_A}\cos\frac{3\theta_A-\theta_B}{2}+\frac{a}{r_B}\cos\frac{3\theta_B+\theta_A}{2}+\frac{a}{r_A}\cos\frac{3\theta_A+\theta_B}{2}\right]\right.$$

with

$$r_B = \sqrt{r_A^2+4a^2+4ar_A\cos\theta_A} \tag{5.2.6}$$

and the angle

$$\theta_B = \arccos\left(\frac{2a+r_A\cos\theta_A}{r_B}\right) \tag{5.2.7}$$

where the subscript A refers to the crack tip A (see fig.36). The quantity κ is defined as

$$\kappa = \begin{Bmatrix}(3-\nu)/(1+\nu) & \text{for plane stress}\\ 3-4\nu & \text{for plane stress}\end{Bmatrix} \tag{5.2.8}$$

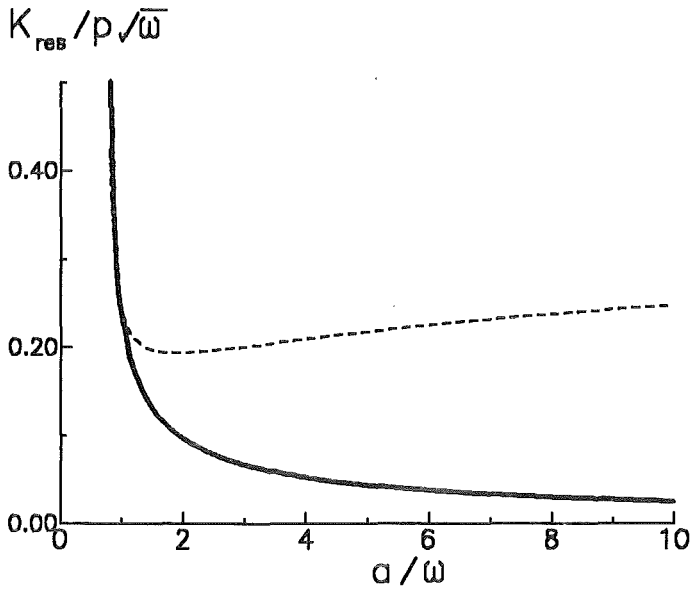

Figure 48. Residual stress intensity factor. Influence of ratio "crack length/zone size", solid curve: $K_{res}/p\sqrt{\omega}$, dashed curve: $K_{res}/p\sqrt{\omega} \cdot (a/\omega)$.

Introducing the contour of the phase-transformation zone into eq.(5.2.2) and applying the weight function, eq.(5.2.4) and (5.2.5), allows the residual stress intensity factor K_{res} to be determined. The result of such computations has been entered in fig.48. It is obvious that the residual or shielding stress intensity factor does not vanish at the onset of crack extension.

5.2.3 The crack-extension phase

5.2.3.1 Repetition of the analysis made by McMeeking and Evans

In [35] McMeeking and Evans considered the stress intensity factor of a transformation zone after a crack propagation Δa (see fig.49). In their analysis it was assumed that the transformation zone is negligible compared with the crack length and the ligament, i.e. $\omega \ll a, W-a$. In this special case, the leading term of the crack-tip stress field governs the transformation zone, and the crack-tip displacement field is sufficient for the derivation of the weight function. First, the analysis of McMeeking and Evans will be repeated here.
After a crack extension of Δa (fig.49) the transformation zone is described by

$$r = \frac{8}{3\sqrt{3}}\,\omega\,\cos^2(\varphi/2) \qquad \text{for} \quad \varphi \leq \pi/3 \tag{5.2.9}$$

$$r = \frac{\omega}{\sin\varphi} \qquad \text{for} \quad \pi/3 \leq \varphi \leq \varphi_L \tag{5.2.10}$$

and

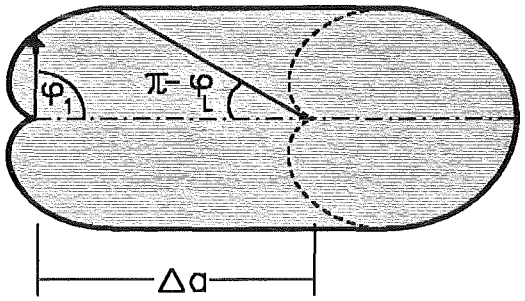

Figure 49. Phase-transformation zone during crack propagation. Shape of zone after a crack extension Δa. Definition of the limit angle φ_L and the polar angle φ_1.

$$\varphi = arc\ \tan \frac{r_1 \sin \varphi_1}{r_1 \cos \varphi_1 - \Delta a} \qquad \text{for} \quad \varphi > \varphi_L \tag{5.2.11}$$

$$r = \sqrt{r_1^2 - 2r_1 \Delta a \cos \varphi_1 + (\Delta a)^2}$$

with

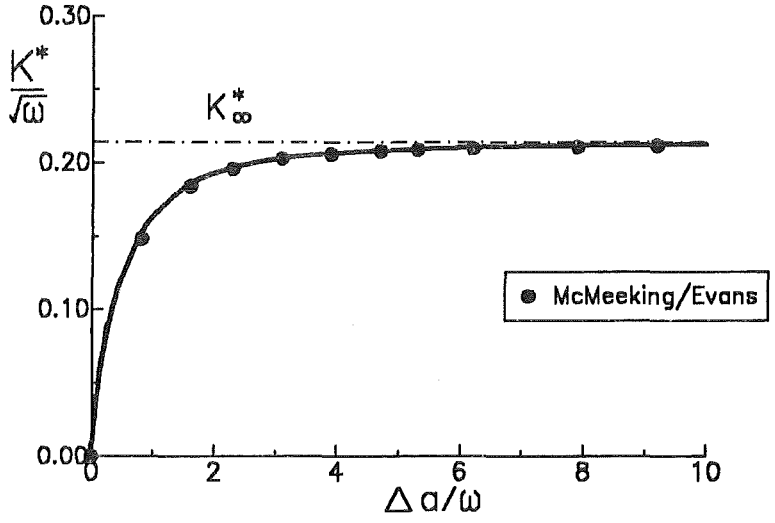

Figure 50. Normalised shielding stress intensity factor. $K^* = K(1 - \nu)/3p\ (1 - 2\nu)$; results compared with data tabulated in [35].

$$\varphi_L = \pi - arc\ \tan \frac{\omega \tan(\pi/3)}{\omega - \Delta a \tan(\pi/3)} \tag{5.2.12}$$

The coordinates (r_1, φ_1) describe points at the boundary of the transformation zone for $\varphi > \varphi_L$. These coordinates are the polar coordinates with the origin at the initial location of the crack tip before crack extension occurred.
The result of the calculations is shown in fig.50. In addition to the own results the data tabulated in [35] are entered. A saturation behaviour of the stress intensity factor is obvious.

5.2.3.2 Relation between shielding and applied stress intensity factor

For small-scale transformation zones a simple expression between the shielding and the applied stress intensity factors can be derived for steady-state conditions, i.e. after a sufficiently long crack extension phase. From the width ω of the phase transformation zone provided by eq.(5.2.15)

$$\omega = \frac{(1+\nu)^2}{4\sqrt{3}\,\pi} \left(K_{I\,tip}/\sigma^c_{hyd}\right)^2$$

and the steady-state value of the shielding stress intensity factor

$$K_{sh,steady-state} = 0.66 p \sqrt{\omega}\ \frac{1-2\nu}{1-\nu} \tag{5.2.13}$$

we obtain

$$K_{sh,steady-state} = \frac{0.44}{3^{1/4}\sqrt{\pi}} \frac{(1+\nu)(1-2\nu)}{1-\nu} \frac{p}{\sigma^c_{hyd}} K_{I\,tip} \tag{5.2.14}$$

5.2.3.3 Calculation of stresses along the crack line

The phase-transformation zone generates tensile stresses in the surrounding non-transformed material. These stresses act in the body when the externally applied surface tractions **T** are removed. Of special interest for weight function applications is the stress distribution along the crack-propagation line in the uncracked body.
We imagine that a virtual crack is introduced into the body with the tip embedded in the transformation zone. Its length a' is assumed to be different from the real crack of length a that has produced the transformation zone, i.e. $a' \neq a$. This virtual crack is used as a sensor for the residual stress field (fig.51).
The residual stress field $\sigma_{res}(x)$ gives rise to the residual stress intensity factor K_{res}

$$K_{res}(a') = \int_0^{a'} \sigma_{res}(x)\, h(x,a)\, dx \tag{5.2.15}$$

where $h(x, a')$ is the crack-surface weight function, i.e. the weight function for $\varphi = \pi$. Since the stress intensity factor $|K_{res}|$ can be computed with the weight function procedure of Sections 5.2.2.1 and 5.2.3.1, the left-hand side of eq.(5.2.15) is known. In this case one has to solve eq.(5.2.15), which is a Volterra integral equation of the first kind.
In order to demonstrate the procedure, the near-tip weight function (eqs.(5.1.35) and (5.1.36)) is used. For $\varphi = \pi$ one obtains the simple expression

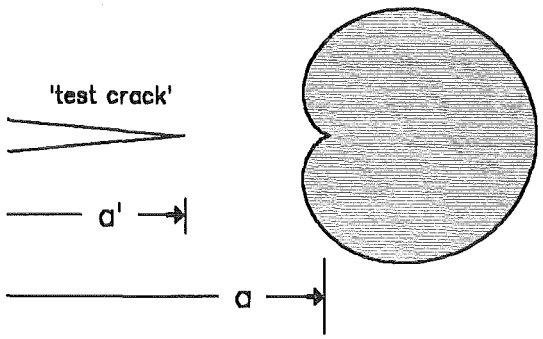

Figure 51. Determination of the stresses near a transformation zone. A fracture mechanical approach for the determination of stresses at the crack propagation line by computation of stress intensity factors for virtual 'test cracks'.

$$h(x, a') = \sqrt{\frac{2}{\pi(a' - x)}} \tag{5.2.16}$$

Introducing eq.(5.2.16) into (5.2.15) yields the Abel integral equation

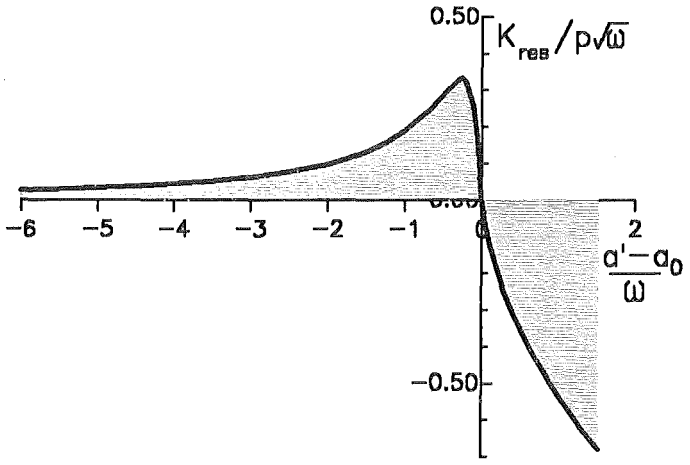

Figure 52. Stress intensity factors for test cracks. Influence of crack length on the stress intensity factor K_{res} caused by the residual stresses on the crack propagation line of a real physical crack.

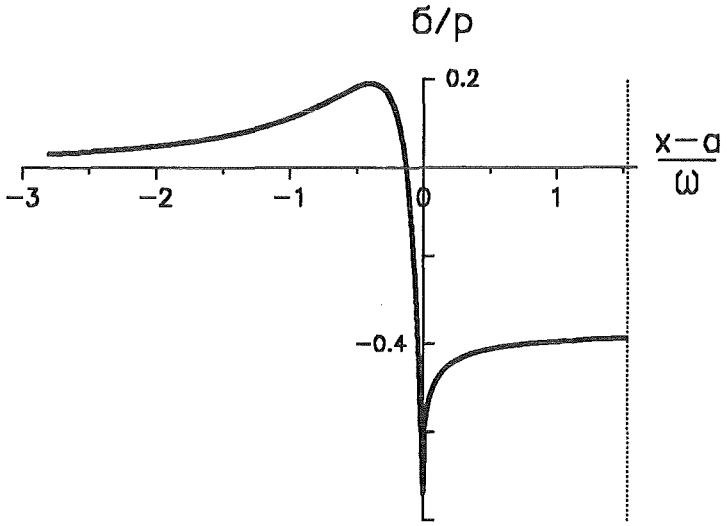

Figure 53. Stresses caused by the transformation zone. Stress distribution in the uncracked component along the crack and in the transformation zone.

$$\int_0^{a'} \frac{\sigma(x)}{\sqrt{a'-x}}\,dx = \sqrt{\frac{\pi}{2}}\,K(a') \tag{5.2.17}$$

with the well-known solution

$$\sigma(x) = \frac{1}{\sqrt{2\pi}}\frac{d}{dx}\left[\int_0^{x} \frac{K(a')}{\sqrt{x-a'}}\,da'\right] \tag{5.2.18}$$

As an example, the procedure is now applied to the initial transformation zone at the onset of crack propagation, i.e. at $K_I = K_{I0}$. The stress intensity factor $K(a')$ has been determined for differently chosen virtual crack lengths a'. The values - normalised to the pressure p - are plotted in fig.52. The stress distribution resulting from eq.(5.2.18) is shown in fig.53.

5.3 Crack opening displacements

Knowledge of the stresses in the uncracked body containing the phase-transformation zone allows the corresponding crack opening displacements to be determined by evaluation of eq.(4.3.4), which reads in case of the residual stress field $\sigma_{res}(x)$

$$\delta_{res}(x) = \frac{1}{E'}\int_0^a \int_{\max(x,x')}^a h(a',x)h(a',x')\sigma_{res}(x')da'dx' \tag{5.3.1}$$

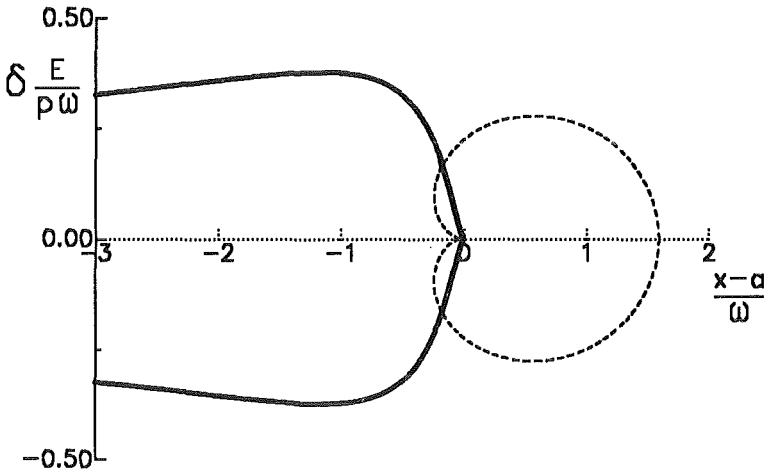

Figure 54. Crack-opening displacements caused by the transformation zone. Normalised displacements for a large crack $a \gg \omega$; (note the absence of a square-root shaped crack opening displacement at the crack tip).

It should be noted that the notation δ is used for the crack-face displacements ($x \leq a$, $y = 0$) as a special case of the displacement component u_y. The displacements can, in principle, be computed by evaluating this double integral using the stresses σ_{res}. The numerical evaluation becomes much simpler if eq.(5.3.1) is rewritten

$$\delta_{res}(x) = \frac{1}{E'} \int_x^a h\left(\frac{x}{a'}, \frac{a'}{W}\right) \left[\int_0^{a'} h\left(\frac{x'}{a'}, \frac{a'}{W}\right) \sigma_{res}(x')dx'\right] da' \tag{5.3.2}$$

where the inner integral is identical with $K(a')$ represented in fig.52. Consequently, one obtains

$$\delta_{res}(x) = \frac{1}{E'} \int_x^a h\left(\frac{x}{a'}, \frac{a'}{W}\right) K_{res}(a')\, da' \tag{5.3.3}$$

The evaluation of eq.(5.3.3) needs the evaluation of cracks with $a' \leq a$. The numerical effort may be drastically reduced by introducing the Green's function which reduces the evaluation to a fixed crack length a and one single integration. With the Green's function the displacements at any location of a body can be determined. In the following we will compute this function for crack opening displacements in case of loadings acting on the crack faces. The Green's function $G(x,x')$ describes the displacement at a point x for a pair of single forces acting at the point x'. Consequently, the crack opening displacement for a distributed stress results as

$$\delta(x) = \frac{1}{E'} \int_0^a G(x,x')\, \sigma(x')\, dx' \tag{5.3.4}$$

Comparing eqs.(5.3.2) and (5.3.4) gives

$$G(x,x') = \int_{\max(x,x')}^a h(a',x)h(a', x')\, da' \tag{5.3.5}$$

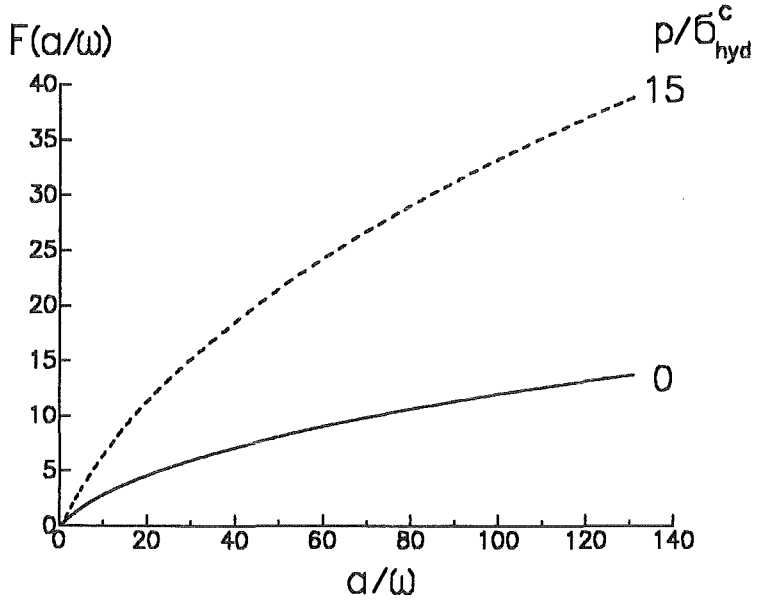

Figure 55. Area or volume caused by crack opening due to the transformation zone. The ordinate represents the integral explained by eq.(5.3.15).

The main advantage of the Green's function becomes obvious for the case that eq.(5.3.5) can be integrated analytically. If we are interested in the near-tip crack opening displacement field we have to introduce the singular term of the weight function resulting in

$$G(x,x') = \frac{2}{\pi}\int_{\max(x,x')}^{a} \frac{da'}{\sqrt{a'-x}\,\sqrt{a'-x'}} = \frac{4}{\pi}\ln\frac{\sqrt{a-x}+\sqrt{a-x'}}{\sqrt{|x-x'|}} \qquad (5.3.6)$$

If the displacements at any other location has to be computed this can be done by application of eqs.(5.1.25) and (5.1.26). Greens functions for crack opening displacements can be derived for tractions at any location of a component. If we write eqs.(5.1.25) and (5.1.26) in the form

$$u_y = \frac{1}{E'}\int_\Gamma \left[T_y\, G_{yy}(x,y,\tilde{x},\tilde{y}) + T_x\, G_{yx}(x,y,\tilde{x},\tilde{y})\right] dS \;+\; u_{y0} \qquad (5.3.7)$$

$$u_x = \frac{1}{E'}\int_\Gamma \left[T_y\, G_{xy}(x,y,\tilde{x},\tilde{y}) + T_x\, G_{xx}(x,y,\tilde{x},\tilde{y})\right] dS \;+\; u_{x0} \qquad (5.3.8)$$

we obtain the Green's functions (notation see fig.42) as

$$G_{yy}(x,y,\tilde{x},\tilde{y}) = \int_0^a \tilde{h}_y(a')\,h_y(a')\,da' \quad , \quad G_{xy}(x,y,\tilde{x},\tilde{y}) = \int_0^a \tilde{h}_y(a')\,h_x(a')\,da' \qquad (5.3.9)$$

$$G_{yx}(x,y,\tilde{x},\tilde{y}) = \int_0^a \tilde{h}_x(a')\, h_y(a')\, da' \quad , \quad G_{xx}(x,y,\tilde{x},\tilde{y}) = \int_0^a \tilde{h}_x(a')\, h_x(a')\, da' \tag{5.3.10}$$

In matrix representation we can abbreviate the last relations

$$\mathbf{u} = \int_\Gamma \underline{G}\, \mathbf{T}\, dS + \mathbf{u}_0 \tag{5.3.11}$$

with $\mathbf{u} = (u_y, u_x)^T$, $\mathbf{u}_0 = (u_{y0}, u_{x0})^T$, $\mathbf{T} = (T_y, T_x)^T$, and

$$\underline{G} = (G_{ij}) = \begin{pmatrix} G_{yy} & G_{yx} \\ G_{xy} & G_{xx} \end{pmatrix} \tag{5.3.12}$$

$$G_{ij} = \int_0^a \tilde{h}_i\, h_j\, da' \tag{5.3.13}$$

In the same way we can derive Green's functions for the stress components σ_y, σ_x (eqs.(5.1.29) and (5.1.30)) and for the hydrostatic stress ((5.1.32)).

5.3.1 Crack opening displacements for nonpropagated cracks

5.3.1.1 Small-scale transformations

The resulting crack opening displacements for a crack with $a \gg \omega$ resulting from application of the near-tip weight function, eqs.(5.1.35) and (5.1.36), are plotted in fig.54. It can be seen that no square-root shaped displacements occur directly at the crack tip ($x \to a$). This confirms the fact, $K_{res} = 0$, resulting from the stress intensity factor calculations. The volume (or the area) due to the crack opening is given by

$$V = 2\frac{p\omega^2}{E'} F(a/\omega) \tag{5.3.14}$$

with

$$F(a/\omega) = \int_0^{a/\omega} \left(\delta_{res} \frac{E'}{p\omega}\right) d\frac{x}{\omega} \tag{5.3.15}$$

The integral has been evaluated numerically and the result is plotted in fig.55. For $a/\omega > 1$ we can approximate the function F by

$$F(a/\omega) = \frac{1.22\gamma^2}{\sqrt{\gamma\, \omega/a}} \exp\left[-1.52\left(\gamma\, \frac{\omega}{a}\right)^{0.63}\right] \tag{5.3.16}$$

with

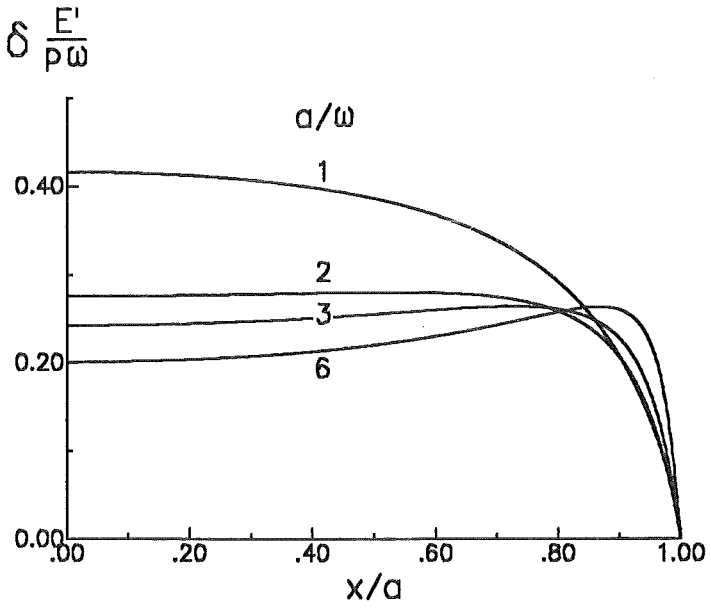

Figure 56. Crack opening displacements caused by phase transformation zones.

$$\gamma = \begin{cases} 1 & \text{for} \quad p/\sigma^c_{hyd} = 0 \\ 2 & \text{for} \quad p/\sigma^c_{hyd} = 15 \end{cases} \tag{5.3.17}$$

It should be noted that the quantity γ can approximatively be described by the height of the phase-transformation zone

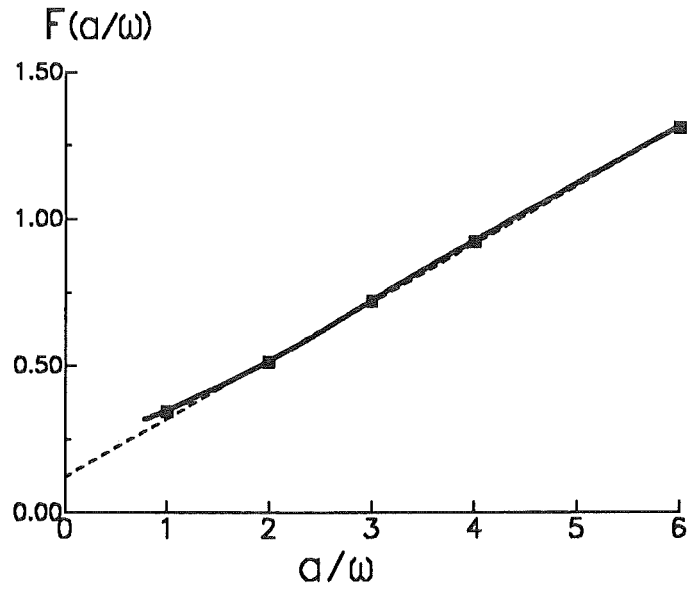

Figure 57. Area or volume caused by crack opening due to the transformation zone. The ordinate represents the integral explained by eq.(5.3.15).

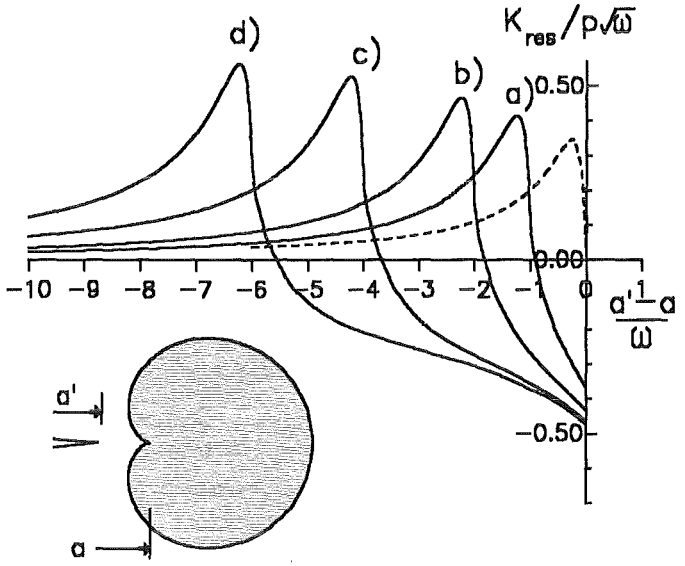

Figure 58. Stress intensity factor for propagated cracks caused by the phase-transformation zone. Crack extensions: a) $\Delta a/\omega = 1$, b) $\Delta a/\omega = 2$, c) $\Delta a/\omega = 4$, d) $\Delta a/\omega = 6$, dashed curve: $\Delta a = 0$.

$$\gamma \simeq \frac{\text{zone height for } p/\sigma^c_{hyd}}{\text{zone height for } p/\sigma^c_{hyd} = 0} \tag{5.3.18}$$

5.3.1.2 Finite internal crack

The crack opening displacements resulting from application of the weight function eq.(5.2.5), which reads for $\varphi = \pi$ and symmetric loading

$$h_y = \frac{2}{\sqrt{\pi a}} \frac{1}{\sqrt{1-(x/a)^2}} \tag{5.3.19}$$

are plotted in fig.56 for $\nu = 0.2$.
The volume (or the area) of the crack can be determined from the displacements as

$$V_{res} = 4\omega^2 \frac{p}{E'} F(a/\omega) \tag{5.3.20}$$

with F defined by eq.(5.3.15). The integral $F(a/\omega)$ is shown in fig.57. For $1 < a/\omega < 6$ the function $F(a/\omega)$ may be approximated by the straight line

$$F(a/\omega) \simeq 0.12 + 0.2\frac{a}{\omega} \tag{5.3.21}$$

which is represented in fig.57 by the dotted line. The residual crack opening displacements may be important in investigations of components compliances since total crack closure of present micro-cracks only takes place under external compressive stresses.

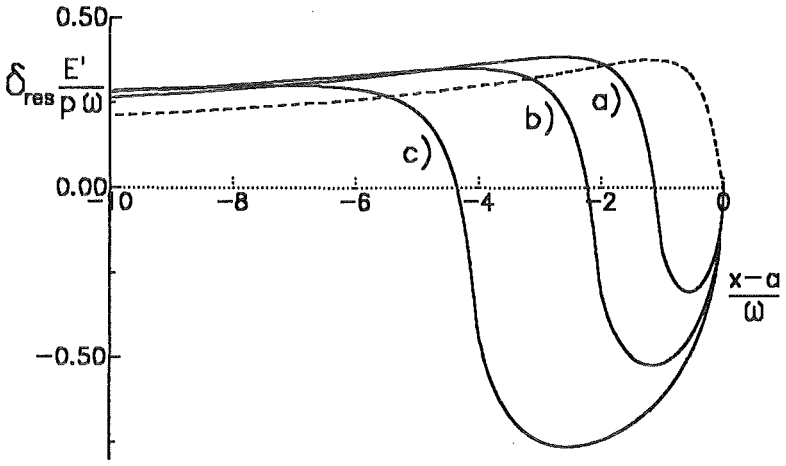

Figure 59. Crack opening displacements caused by phase transformation zones. Near-tip behaviour; crack extensions as fig.58.

5.3.2 Crack opening displacements for propagated cracks

For the numerical evaluation of crack opening for propagated cracks we will restrict the computations again to the limit case of small-scale transformations. The stress intensity factor $K_{res}(a')$ for a crack length $a' \leq a$ - but fixed location of the phase transformation zones - can be computed with eq.(5.1.23). Now we are interested in the crack opening displacement field for a disappearing crack-tip stress intensity factor. In order to compensate the negative residual stress intensity factor K_{res} of the propagated cracks and to get $K_{I\,tip}=0$ we have to apply an external

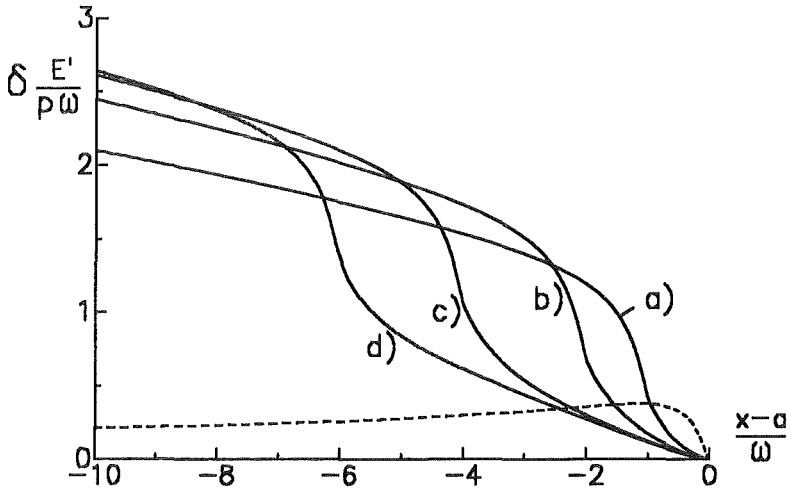

Figure 60. Crack opening displacements at $K_{I\,tip}=0$. Combination of loading by residual stresses and external load.

load which causes a stress σ_{appl} along the crack line. In case of pure tensile loading this stress must be

$$\sigma_{appl} = \frac{K_{res}}{\int_0^a h(x,a)\,dx} \tag{5.3.22}$$

and the corresponding crack opening displacement field results as

$$\delta_{appl}(x) = \frac{\sigma_{appl}}{E'} \int_x^a h(x, a')\left[\int_0^{a'} h(x', a')dx'\right]da' \tag{5.3.23}$$

The residual stress intensity factors $K_{res}(a')$ are plotted in fig.58 for several grown cracks. The related crack opening displacements δ_{res} resulting by application of the near-tip weight function, eq.(5.1.36), which reads for $\varphi = \pi$ and symmetric loading

$$h = \sqrt{\frac{2}{\pi(a-x)}} \tag{5.3.24}$$

are plotted in fig.59 for $\nu = 0.2$. It can be seen that in case of $\Delta a = 0$ no square-root shaped displacements occur directly at the crack tip ($x \to a$). This confirms the fact, $K_{res} = 0$, resulting from the stress intensity factor calculations.
Introducing eq.(5.3.19) into eqs.(5.3.22) and eq.(5.3.23) yields for a constant applied stress and for $K_{I\,tip} = 0$

$$\delta_{total} = \frac{2K_{res}}{E'\sqrt{2\pi a}}\left(\sqrt{a(a-x)} + x\,\ln\frac{\sqrt{x}}{\sqrt{a}+\sqrt{a-x}}\right) + \delta_{res} \tag{5.3.25}$$

Figure 60 shows the total displacements for $K_{I\,tip} = 0$. It can be seen that in the case of small-scale transformation at all locations along the crack the condition $\delta_{total} > 0$ is fulfilled, i.e. a crack opens exactly at $K_{I\,tip} = 0$. The equivalence

$$\delta_{total} \geq 0 \;\forall\; x < a \quad \Leftrightarrow \quad K_{I\,tip} \geq 0 \tag{5.3.26}$$

- self-evident for the near-tip crack opening displacements - can consequently be used also for the far-tip crack opening displacements which reduces considerations of crack closure to the consideration of residual stress intensity factors.

6. Energy release rate, stress intensity factors and compliance

6.1 Basic relations

The bridging stresses in ceramics are extremely non-linear and their range of extension is not negligible compared with the crack length. The consequences of the bridging interactions on fracture-mechanical considerations may become very serious.
Some special questions are:

1. R-curves are often expressed in terms of energy release rates instead of stress intensity factors using the well-known Irwin-relation

$$G_I = K_I^2/E' \tag{6.1.1}$$

   with $E' = E/(1-\nu^2)$, E=Youngs modulus and ν=Poisson ratio. This relation was proposed for linear-elastic material behaviour. Now the question arises whether or not this relation can be also applied in presence of R-curve behaviour for the applied stress intensity factors $K_{I\,appl}$.
2. What is the meaning of the compliance in presence of non-linear bridging interactions and is the crack-length measurement via compliance correct?

These two questions will be considered here, following the analysis given in [47].
Let us consider a specimen (fig.61) of width W, thickness B, and length $2L$ which contains a crack of depth a_0 with completely separated crack surfaces (produced, e.g., by a very narrow saw-cut with negligible notch-root radius). Starting from this initial crack size, a crack may propagate under increasing external loads, and in case of coarse-grained materials bridging interactions occur which result in bridging stresses depending on the actual crack opening displacements δ.
The externally applied load P is related to σ_{appl} by

$$P = \sigma_{appl}\, WB \tag{6.1.2}$$

where B is the thickness of the plate.
For the description of crack opening and crack propagation in terms of energy we consider a crack of total length a with crack surface interactions in the range $a_0 < x < a$ in the unloaded state ($\delta = 0$).
The specimen is exposed to increasing externally applied stresses σ_{appl} at the free ends of the specimen. For reasons of simplicity, this stress is assumed to be constant, i.e. independent of the coordinate x. In eq.(4.3.4) x is the coordinate where the displacement is computed and x' is the location where the stress σ acts. If the applied stress σ_{appl} as well as bridging stresses σ_{br} act on the crack surfaces, the total stress is

$$\sigma_{total} = \sigma_{appl} + \sigma_{br} \quad ; \quad \sigma_{br} < 0 \tag{6.1.3}$$

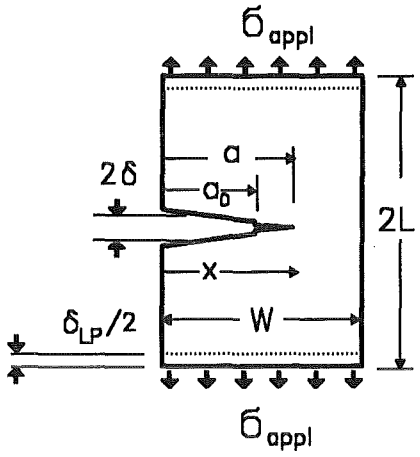

Figure 61. Edge-cracked plate. Geometrical data of an edge-cracked plate under tensile load.

and the total crack opening displacements result as

$$\delta_{total}(x) = \delta_{appl} + \delta_{br} = \frac{1}{E'} \int_0^a \int_{max(x,x')}^a h(a',x)\, h(a', x')\, [\sigma_{appl}(x') + \sigma_{br}(x')]\, da'dx' \qquad (6.1.4)$$

where δ_{appl} is the displacement caused by the applied stress. $\sigma_{appl}(x')$ is the stress in the uncracked component at the location of the crack. For the plate under uniform tension $\sigma_{appl}(x)$ is identical with the externally applied stress. Note that δ_{total} is the crack opening displacement of one crack border, whereas δ_{LP} is the total load point displacement (see fig.61).
Far away from the crack, the crack opening displacements δ_{total} lead to displacements δ_{LP} which will be called the "loading point displacements". It holds for tensile loading

$$\delta_{LP} = \frac{\sigma_{appl}}{E} 2L + \frac{2}{W} \int_0^a \delta_{total}(x)\, dx \qquad (6.1.5)$$

A similar relation for bending is given by eq.(12.5.6). The first term in (6.1.5) represents the displacements of the uncracked structure in pure tension and the second term is the contribution of the crack. If a minimum length of $L > W$ is ensured the stress intensity factor and δ_{total} are independent of L. In all further equations the first term in (6.1.5) is omitted.
Under loading conditions different from pure tension ($\sigma_{appl} \neq constant$) (6.1.5) has to be replaced by

$$P\, d\delta_{LP} = +\, 2B \int_0^a \sigma_{appl}\, d\delta_{total}(x)\, dx \qquad (6.1.6)$$

6.2 Energy considerations

6.2.1 Definition of the crack driving force

6.2.1.1 Linear-elastic material behaviour

In case of linear-elastic fracture mechanics the energy release rate G - called the crack driving force - is defined as the virtual change of potential energy δU_p available for a virtual crack-area increment $B\,\delta a$ and is directly related to the stress intensity factor by

$$G_I = -\frac{\delta U_p}{B\,\delta a} = \frac{K_I^2}{E'} \tag{6.2.1}$$

In order to separate loading quantities which are related to *virtual* crack extensions from energy consumptions during real crack extensions we will use in this section as a special notation for the virtual crack changes the symbol δ.
The potential energy consists on the virtual work δA done by the external load and the virtual change of the elastically stored energy in the component δU:

$$\delta U_p = \delta U - \delta A \quad , \quad \delta A = P\,\delta\delta_{LP} \tag{6.2.2}$$

In the sense of eq.(6.2.1) G is a loading quantity (not a material property) and up to now not related to real crack extensions da. In case of a real crack extension the energy dW_{crack} is necessary to create the new crack increment Bda. The energy per crack area increment defines the material property called "crack resistance" R

$$R = \frac{1}{B}\frac{dW_{crack}}{da} \tag{6.2.3}$$

The condition for maintaining crack propagation is expressed by

$$G = R \tag{6.2.4}$$

where G_0 is a characteristical value of G that governs onset of stable crack growth. The left-hand side describes the available energy and the right-hand side the necessary energy.

6.2.1.2 Nonlinear-elastic material behaviour

If nonlinear material behaviour plays a role - this is the case in the presence of strongly nonlinear bridging stresses - the relations of linear-elastic fracture mechanics have to be replaced by the J-integral concept. In order to apply J-integral we have to consider that the energy storaged in the bridges W_{br} is **elastically stored energy** and therefore completely reversible. In this state it is not of importance what the real material response during unloading as long as no real displacement reversals occur. Here it should be emphasized once more that the J-integral is a loading quantity and not influenced by real material behaviour. Under these circumstances the virtual change of potential energy is

$$\delta U_p = \delta U + \delta W_{br} - \delta A \quad , \quad \delta A = P\,\delta\delta_{LP} \tag{6.2.5}$$

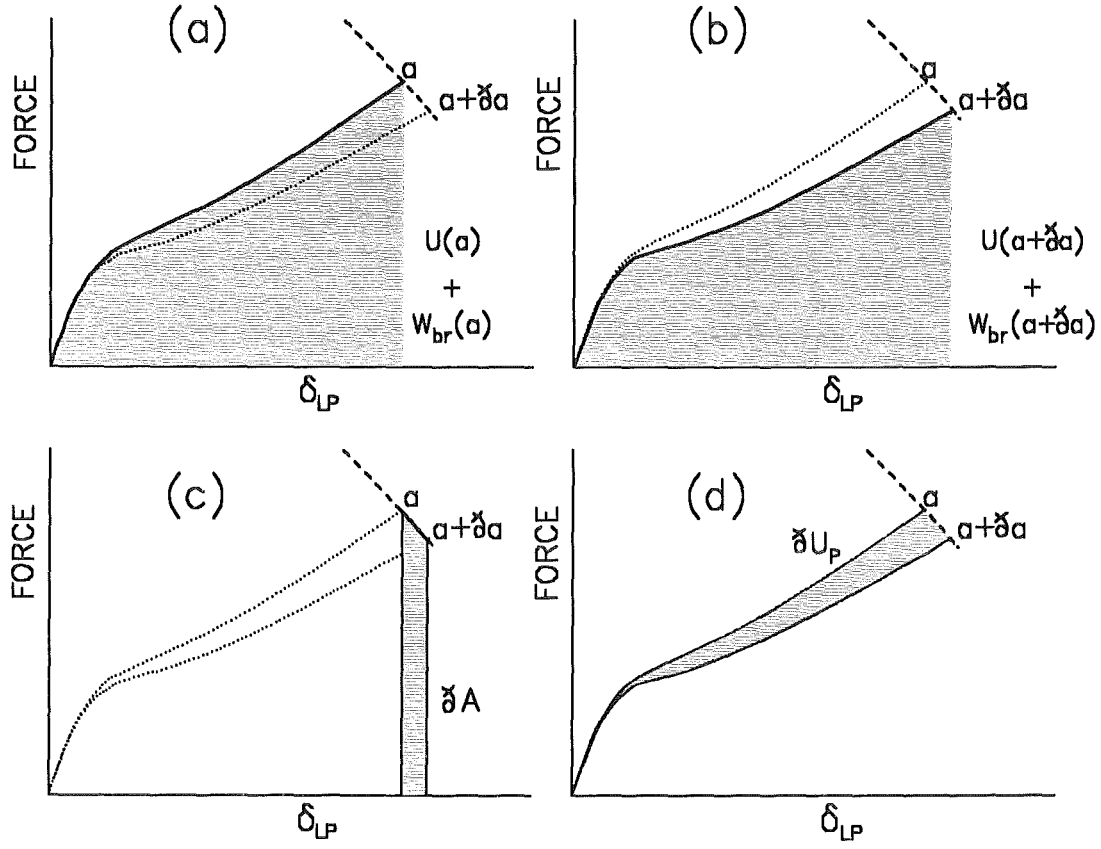

Figure 62. Change of energies. Energy portions for specimens with crack lengths a and $a + da$: a) elastically stored energy for a crack of length a; b) elastically stored energy for a crack of length $a + da$; c) work increment done by the external load; d) increment of potential energy.

The virtual energy contributions are illustrated in fig.62. Because of the lack of the special differential sign for virtual increments in the computer chart program the symbol d is used in fig.62. For nonlinear elastic material behaviour the loading quantity is

$$J = -\frac{\delta U_p}{B\,\delta a} \tag{6.2.6}$$

and by definition $G = J = K_I^2/E'$ for the linear elastic case.
From eq.(6.2.1) and (6.2.5) it results for the J-integral [48]

$$J = -\int_0^{\delta_{LP}} \left(\frac{\delta P}{\delta a}\right)_{\delta'_{LP}} d\delta'_{LP} \tag{6.2.7}$$

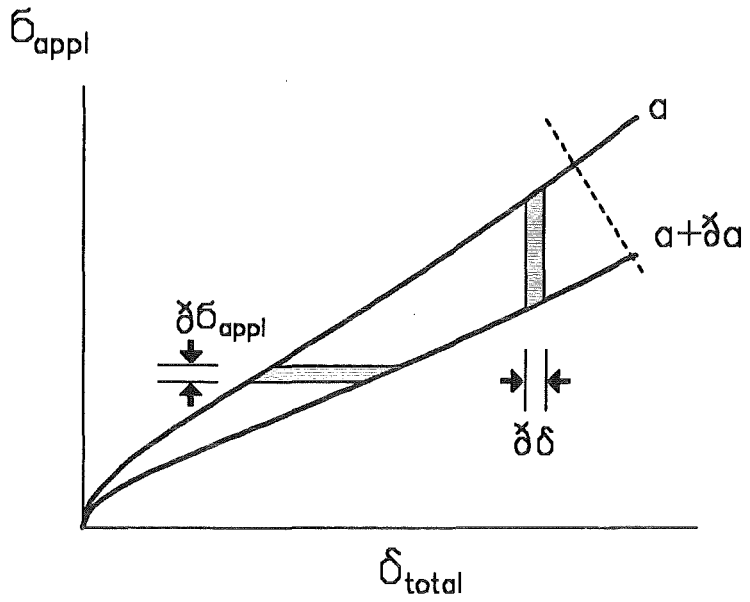

Figure 63. Integration increments. Energy increments according to eqs.(6.2.9) and (6.2.10).

$$J = \int_0^P \left(\frac{\eth \delta'_{LP}}{\eth a} \right)_{P'} dP' \tag{6.2.8}$$

and by using eq.(6.1.5)

$$J = -2\int_0^a dx \int_0^{\delta_{total}} \left(\frac{\eth \sigma'_{appl}}{\eth a} \right)_{\delta'_{total}} d\delta'_{total} \tag{6.2.9}$$

$$J = 2\int_0^a dx \int_0^{\sigma_{appl}} \left(\frac{\eth \delta'_{total}}{\eth a} \right)_{\sigma'_{appl}} d\sigma'_{appl} \tag{6.2.10}$$

Figure 63 shows the related potential energy dU_p.

6.2.1.3 Stress intensity factors, J-integral and energy release rate

If we introduce $\delta_{total} = \delta_{appl} + \delta_{br}$ in eq.(6.2.10)

$$J = 2\int_0^a dx \int_0^{\sigma_{appl}} \left[\left(\frac{\eth \delta'_{appl}}{\eth a} \right)_{\sigma'_{appl}} + \left(\frac{\eth \delta'_{br}}{\eth a} \right)_{\sigma'_{appl}} \right] d\sigma'_{appl} \tag{6.2.11}$$

and applying eq.(4.3.3) in the form

$$\frac{\partial \delta_{appl}}{\partial a} = \frac{K_{appl}\, h(x,a)}{E'} \tag{6.2.12}$$

we obtain

$$J = 2\int_0^a \frac{h(x,a)}{E'}\, dx \int_0^{\sigma_{appl}} K'_{appl}\, d\sigma'_{appl} + 2\int_0^a dx \int_0^{\sigma_{appl}} \left(\frac{\partial \delta'_{br}}{\partial a}\right)_{\sigma'_{appl}} d\sigma'_{appl} \tag{6.2.13}$$

Since

$$K'_{I\,appl} = \frac{K_{I\,appl}}{\sigma_{appl}}\, \sigma'_{appl} \tag{6.2.14}$$

the first term in (6.2.13) can be evaluated

$$J = \int_0^a \frac{h(x,a)}{E'}\, \sigma_{appl} K_{I\,appl}\, dx + 2\int_0^a dx \int_0^{\sigma_{appl}} \left(\frac{\partial \delta'_{br}}{\partial a}\right)_{\sigma'_{appl}} d\sigma'_{appl} \tag{6.2.15}$$

and after introduction of eq.(4.3.2) into the first term

$$J = \frac{1}{E'} K^2_{I\,appl} + 2\int_0^a dx \int_0^{\sigma_{appl}} \left(\frac{\partial \delta'_{br}}{\partial a}\right)_{\sigma'_{appl}} d\sigma'_{appl} \tag{6.2.16}$$

Since the second term in eq.(6.2.16) will vanish only in the case of cracks without bridging stresses we can conclude that the Irwin formula - written in terms of the applied stress intensity factor $K_{I\,appl}$ - is not generally valid

$$J \neq \frac{K^2_{I\,appl}}{E'} \tag{6.2.17}$$

This inequality holds for the general case without special assumptions made on the bridging stresses.

6.2.1.4 Special assumption on bridging stresses

Now a special assumption is made on the bridging stresses. It is physically meaningful to assume that the bridging stresses are only dependent on the actual crack opening diplacements (δ_{total})

$$\sigma_{br} = f(\delta_{total}) \tag{6.2.18}$$

and, for instance, not explicitly on the x-coordinate. Furthermore, it is assumed that this stress vs. displacement relation is a unique law for monotonically increasing displacements. The ques-

tion whether or not the bridging-stress relation may change in unloading situations, i.e. in situations where the displacements can decrease, is without importance to the present considerations, since in controlled fracture tests the crack opening displacements increase monotonocally during crack extension.
This fact can easily be concluded from the weight function relation (4.3.3). In controlled fracture tests crack propagation occurs at $K_{total}=K_{I\,tip}=K_{I0}$. From (4.3.3) we conclude that for any given value of x - since $h(x,a)>0$ - for all $0 \leq x < a$

$$\frac{\delta\delta_{total}}{\delta a}\Big|_{K_{total}=K_{I0}} = \frac{K_{I0}}{E'}\, h(x,a) > 0 \tag{6.2.19}$$

i.e. a monotonic increase in COD with increasing crack length.
Introducing eq.(6.1.3) into (6.2.9) gives

$$J = -2\int_0^a dx \int_0^{\delta_{total}} \left[\left(\frac{\delta\sigma'_{total}}{\delta a} \right)_{\delta'_{total}} - \left(\frac{\delta\sigma'_{br}}{\delta a} \right)_{\delta'_{total}} \right] d\delta'_{total} \tag{6.2.20}$$

If σ'_{br} is a unique function of δ'_{total}, one can write for the second term in brackets (since δ'_{total} is kept constant)

$$\left(\frac{\delta\sigma'_{br}}{\delta a} \right)_{\delta'_{total}} = 0 \tag{6.2.21}$$

and (6.2.20) reduces to

$$J = -2\int_0^a dx \int_0^{\delta_{total}} \left(\frac{\delta\sigma'_{total}}{\delta a} \right)_{\delta'_{total}} d\delta'_{total} \tag{6.2.22}$$

After integration by parts (see fig.63 and replace the vertical axis by σ_{total}) this reads

$$J = 2\int_0^a dx \int_0^{\sigma_{total}} \left(\frac{\delta\delta'_{total}}{\delta a} \right)_{\sigma'_{total}} d\sigma'_{total} \tag{6.2.23}$$

and with eq.(4.3.3), written in the form

$$\frac{\delta\delta_{total}}{\delta a} = \frac{K_{total}\, h(x,a)}{E'} \tag{6.2.24}$$

we obtain

$$J = 2\int_0^a dx \int_0^{\sigma_{total}} \frac{K'_{total}}{E'}\, h(x,a)\, d\sigma'_{total} \tag{6.2.25}$$

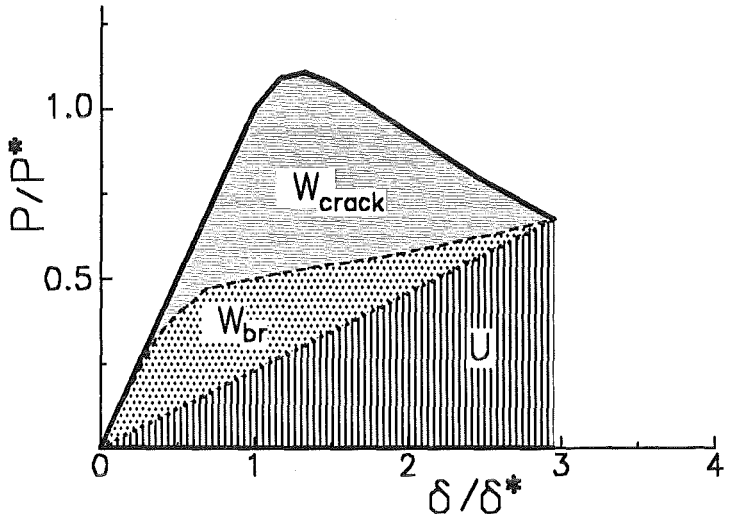

Figure 64. Energy balance. Global energies for a cracked component under tesion; Load and loading-point displacement normalised on the values at the onset of stable crack extension (*).

Changing the order of integration results in

$$J = \frac{2}{E'} \int_0^{K_{total}} K'_{total}\, dK'_{total} = \frac{K^2_{total}}{E'} = G \qquad (6.2.26)$$

Since during crack propagation the crack-tip stress intensity factor equals K_{I0}, we finally can write

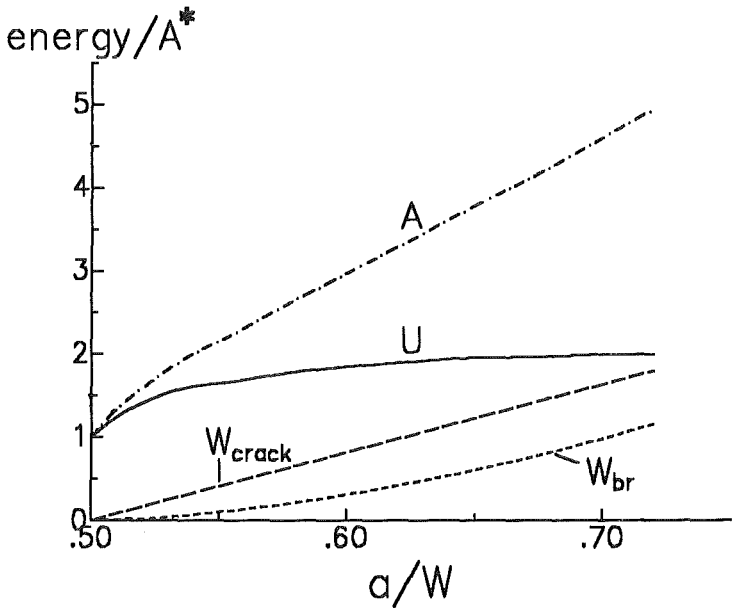

Figure 65. Energy balance. Energy contributions during stable crack propagation; $A^* = P^*\delta^*/2$, loading case: tension.

$$G_{I0} = J_0 = \frac{K_{I0}^2}{E'} \tag{6.2.27}$$

6.2.2 The crack resistance

6.2.2.1 Energy balance during crack propagation

During stable crack propagation the externally applied force P performs the mechanical work A, which is identical with the area under the load-displacement curve

$$A = \int_0^{\delta_{LP}} P' \, d\delta'_{LP} \tag{6.2.29}$$

This energy equals the sum of

- the elastically stored energy in the specimen U,
- the energy necessary to create a new fracture surface W_{crack}, and
- the energy deposit in the bridges W_{br},

i.e.

$$A = U + W_{crack} + W_{br} \tag{6.2.30}$$

The energy necessary to create a new crack surface is

$$W_{crack} = \frac{K_{I0}^2}{E'} (a - a_0) \tag{6.2.31}$$

and the energy consumed in the bridges is given by

$$W_{br} = -2B \int_0^a dx \int_0^{\delta_{total,c}} \sigma'_{br} \, d\delta'_{total} \quad ; \quad \sigma_{br} < 0 \tag{6.2.32}$$

In the special case of the exponential relation, eqs.(4.1.9) and (4.1.10), the inner integral can be evaluated and it results

$$W_{br} = -2B \, \sigma_0 \delta_0 \int_0^a [1 - \exp(-\delta_{total,c}/\delta_0)] \, dx \quad ; \quad \sigma_0 < 0 \tag{6.2.33}$$

The elastically stored energy U in the specimen is given by (see fig.64)

$$U = \frac{1}{2} P \, \delta_{LP} \tag{6.2.34}$$

in a simple way from the applied load and the loading point displacement. The different energy contributions are plotted in fig.65 versus the crack extension $\Delta a = a - a_0$ for tension as the loading case. Whilst the "bridging energy" W_{br} and the crack surface energy W_{crack} increase monotonically with crack extension, the elastic energy seem to reach a saturation. The incremental ener-

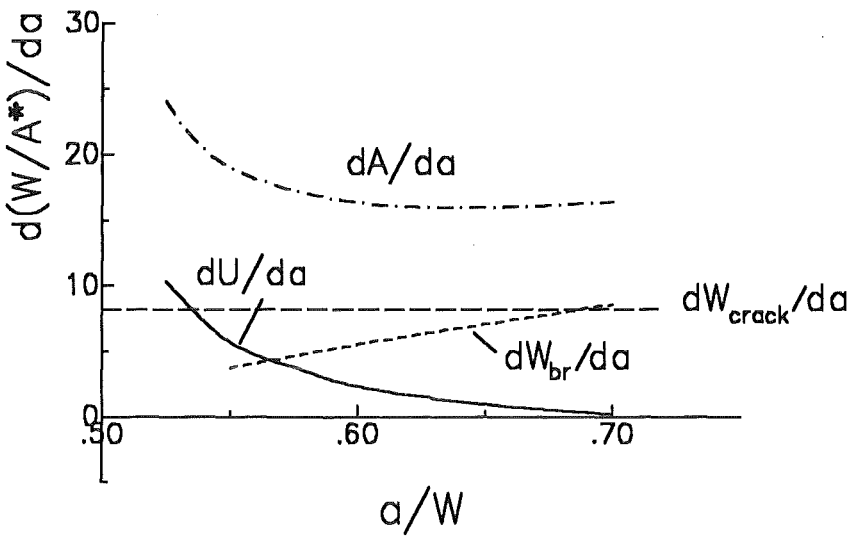

Figure 66. Energy rates. Energy rates according to fig.65.

gies dA/da, dW_{br}/da, dW_{crack}/da, and dU/da are plotted in fig.66. dU/da may change its sign at $a/W>0.7$.

In the linear-elastic case with unloaded crack faces the crack resistance was defined by the energy that has to be provided to create new crack surface. In the presence of bridging stresses an additional energy has to be provided to overcome the attracting bridging stresses. Consequently, the crack growth resistance now reads

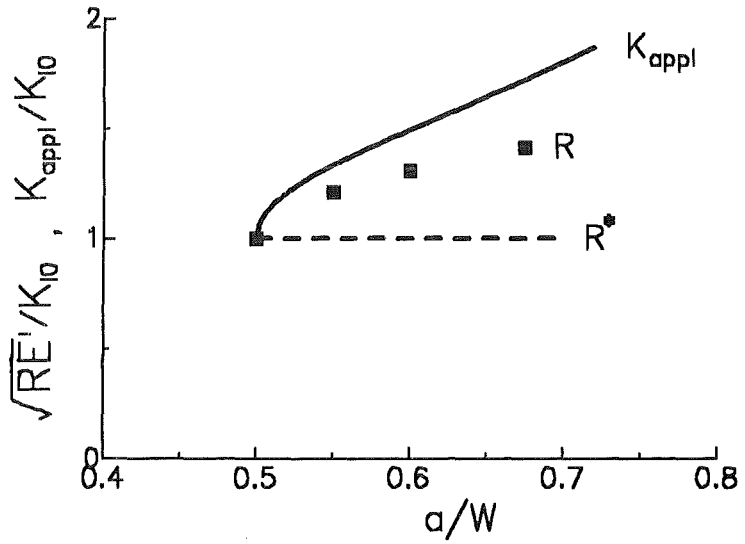

Figure 67. Applied stress intensity factor and crack resistance. Applied stress intensity factor $K_{I\,appl}$ and crack resistance R (expressed in terms of stress intensity factor) for the tensile loading case, computed with the bridging stress relation $\sigma_{br} = \sigma_0 \exp(-\delta/\delta_0)$.

$$R = \frac{1}{B}\left(\frac{dW_{crack}}{da} + \frac{dW_{br}}{da}\right)$$
$$= \frac{K_{I0}^2}{E'} + \frac{1}{B}\frac{dW_{br}}{da} \tag{6.2.35}$$

6.2.2.2 The crack resistance and the applied stress intensity factor

It can easily be shown that the applied stress intensity factor $K_{I\,appl}$ and the crack resistance R are not identical in the general case. For the further conclusions we consider the tensile loading case. We express the term $K_{I\,appl}^2/E'$ by definition of the weight function in the form

$$h(x,a) = \frac{E'}{K_{I\,appl}}\frac{\partial}{\partial a}\delta_{appl}(x,a) \tag{6.2.36}$$

as

$$\frac{1}{E'}K_{I\,appl}^2 = \frac{K_{I\,appl}}{E'}\int_0^a h(x,a)\sigma_{appl}\,dx = \int_0^a \sigma_{appl}\frac{\partial \delta_{appl}}{\partial a}\,dx \tag{6.2.37}$$

Introducing eq.(6.1.5) yields

$$\frac{1}{E'}K_{I\,appl}^2 = \frac{1}{2B}P\frac{\partial \delta_{LP,appl}}{\partial a} \tag{6.2.38}$$

The loading point displacements $\delta_{LP,appl}$ can be written

$$\delta_{LP,appl} = \delta_{LP,total} - \delta_{LP,br} = \delta_{LP,total} + |\delta_{LP,br}| \tag{6.2.39}$$

and consequently

$$\frac{1}{E'}K_{I\,appl}^2 \neq \frac{1}{2B}P\frac{\partial \delta_{LP,total}}{\partial a}$$
$$\frac{1}{E'}K_{I\,appl}^2 \neq R \tag{6.2.40}$$

In cases where the bridging zone increases with increasing crack length (before a saturation in R is reched) we will find

$$d(\delta_{LP,appl}) > d(\delta_{LP,total}) \quad \rightarrow \quad \frac{1}{E'}K_{I\,appl}^2 > R \tag{6.2.41}$$

As an example the applied stress intensity factor $K_{I\,appl}$ and the crack resistance R have been computed numerically for a component under tensile loading containing a crack of initial length $a/W = 0.5$ using the bridging stress relation $\sigma_{br} = \sigma_0 \exp(-\delta/\delta_0)$ with $\sigma_0 = K_{I0}/\sqrt{W}$ and $\delta_0 = 5/6 \cdot (\sigma_0 W/E')$. The results of R are formally expressed in terms of stress intensity factors and plotted in fig.67. The disagreement of the two quantities is clearly obvious.

6.3 Application of a Dugdale model by Evans and McMeeking

In a simple model Evans and McMeeking [49] considered the conversion of energy release rates in stress intensity factors in a special model. They studied a small scale bridging zone in a brittle material reinforced by fibers (see fig.68). In the following the nomenclature of [49] will be used. The crack surface stresses transferred by the fibres are considered to be homogeneously distributed in the bridged crack area. The maximum size of the bridging zone is D_c where the subscript refers to the critical situation at the crack tip, i.e. $K_{I\,tip}=K_{I0}$.
From the J-integral around the traction zone the critical value of the change in energy release rate $\Delta\mathbf{G}$ is derived as

$$\Delta\mathbf{G}_c = 2\sigma f u_c \tag{6.3.1}$$

with the tractions in the fibers σ, the area fraction of reinforcements on the crack plane and u_c the critical crack opening at the end of the bridging zone, given by

$$u_c = \frac{4(1-\nu)}{G}\left(\frac{f\sigma D_c}{\pi} + \frac{K_{I0}\sqrt{D_c}}{G\sqrt{2\pi}}\right) \tag{6.3.2}$$

where G is the shear modulus and K_{I0} is the critical crack-tip stress intensity factor.
The contribution of the bridging zone to the stress intensity factor results with the near-tip weight function as

$$\Delta K_I = -\sqrt{\frac{2}{\pi}}\, f \int_0^{D_c} \frac{\sigma(x)}{\sqrt{x}}\, dx \tag{6.3.3}$$

where x is the distance from the crack tip. The "change in fracture toughness" ΔK_c results from eq.(6.3.3) as

$$\Delta K_c = 2\sigma f\sqrt{2D_c/\pi} \tag{6.3.4}$$

The following *definitions* are introduced

$$\frac{2G\mathbf{G}_c}{1-\nu} = K_c^{\,2} \tag{6.3.5}$$

$$K_c = K_{I0} + \Delta K_c \tag{6.3.6}$$

$$\mathbf{G}_c = \mathbf{G}_0 + \Delta\mathbf{G}_c \tag{6.3.7}$$

In the opinion of the author eqs.(6.3.6) and (6.3.7) are definitions of the quantities K_c and $\mathbf{G}_c$. On the other hand there is no additional freedom to *define* a relation between the two quantities of type eq.(6.3.5). The validity of eq.(6.3.5) has to be proved.
If we assume eq.(6.3.5) would be correct, it results by combining eqs.(6.3.5) to (6.3.7) yielding

$$2G\Delta\mathbf{G}_c/(1-\nu) = (\Delta K_c)^2 + 2K_{I0}\Delta K_c \tag{6.3.8}$$

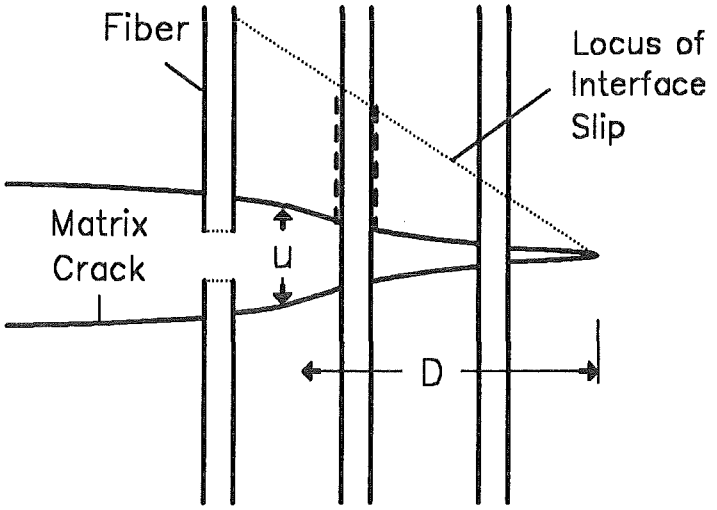

Figure 68. Bridging zone in reinforced materials. Bridging zone for slipping fibers according to Evans and McMeeking [49].

Introducing of eq.(6.3.1) and eq.(6.3.2) at the left side of (6.3.8) and eq.(6.3.4) at the right hand side it results that the left-hand side is twice the right-hand side.
The reason is a typing error in eq.(6.3.1) since

$$J = \sigma \cdot \mathrm{COD} \quad \rightarrow \quad \Delta G_c = \sigma f u_c \tag{6.3.9}$$

The analysis of Evans and McMeeking confirms the correctness of relation (6.3.5) for a special case, namely the **steady-state behaviour** of a growing crack in an infinite body with a small bridging zone of constant length behind the crack tip.
In this special case it holds (in notation of the previous sections)

$$\int_{(crack)} \delta_{br}(x)\, dx = const.$$

$$\rightarrow \quad \frac{d}{da}\int_{(crack)} \delta_{appl}(x)\, dx = \frac{d}{da}\int_{(crack)} \delta_{total}(x)\, dx \tag{6.3.10}$$

and from the considerations made in section 6.2.2.2 we can conclude

$$\left(\frac{1}{E'} K^2_{I\,appl}\right)_{steady-state} = R_{steady-state} \tag{6.3.11}$$

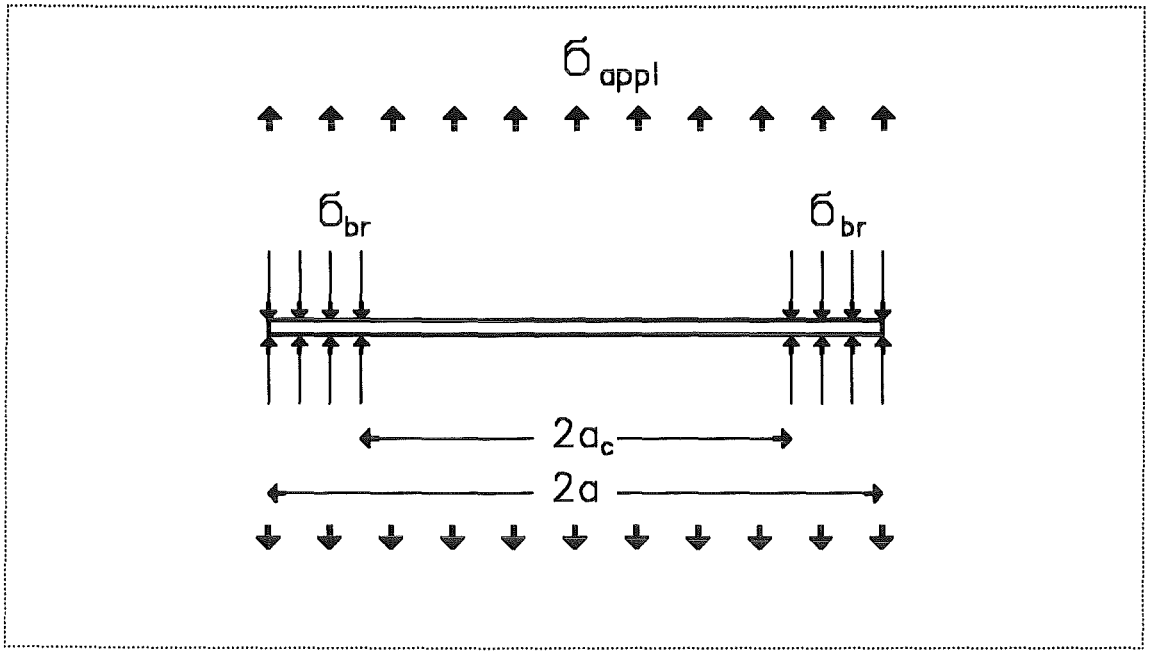

Figure 69. Griffith crack with bridging zone. Griffith crack with constant bridging stresses; loading situation and geometry.

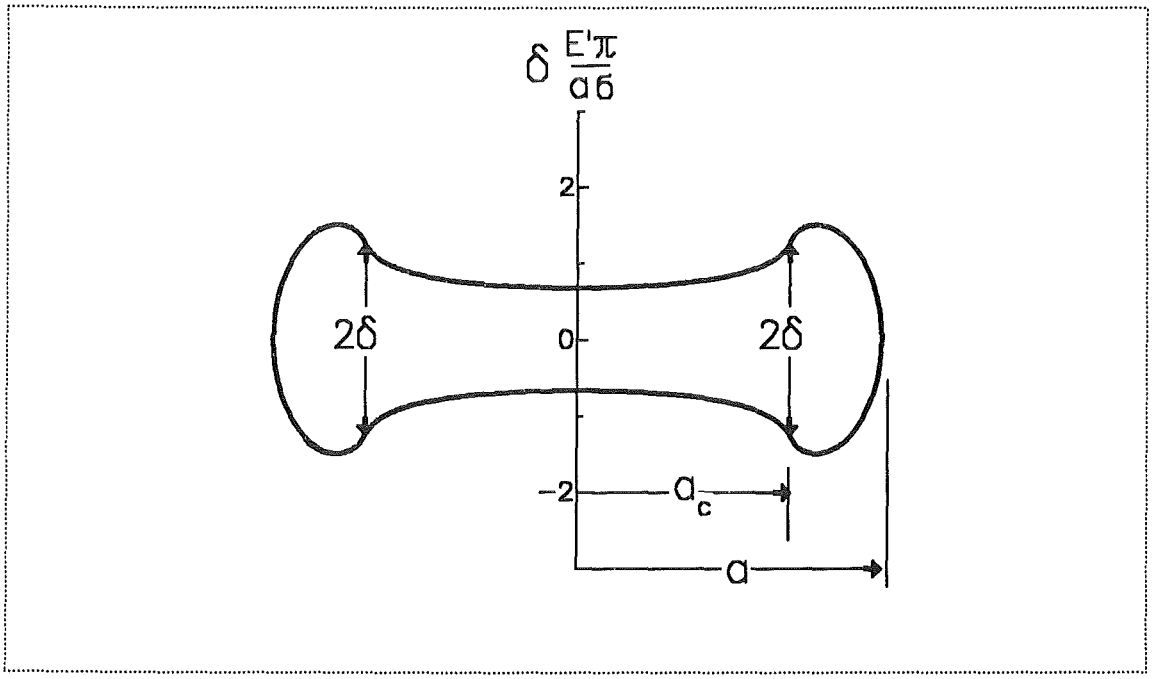

Figure 70. Bridging COD field. Griffith crack with constant bridging stresses; displacemet field caused by the strip load.

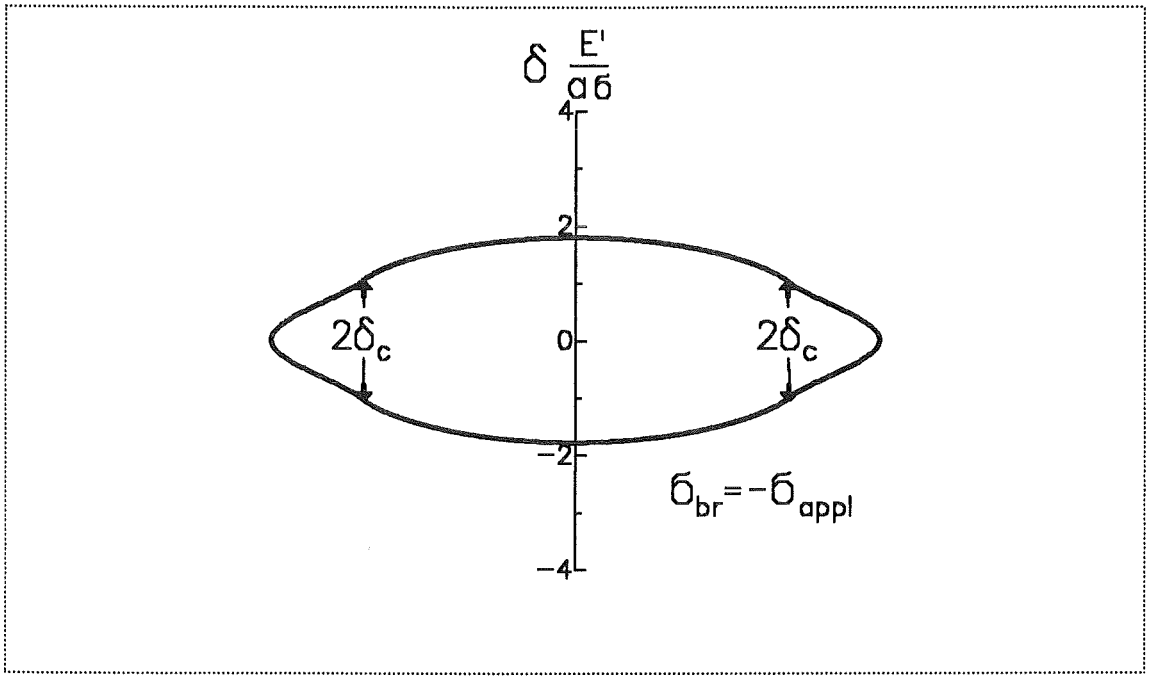

Figure 71. Total COD field. Griffith crack with constant bridging stresses; total displacemet field.

6.4 R-curve for a Griffith crack with constant bridging stresses

A restriction of the model used by Evans and McMeeking is that an approximate weight function has to be used which becomes correct only in the limit case of an infinitely large crack compared with the dimension of the bridging zone. In order to investigate the relation between crack resistance and applied stress intensity factor it is useful to apply an analytically exact solution.

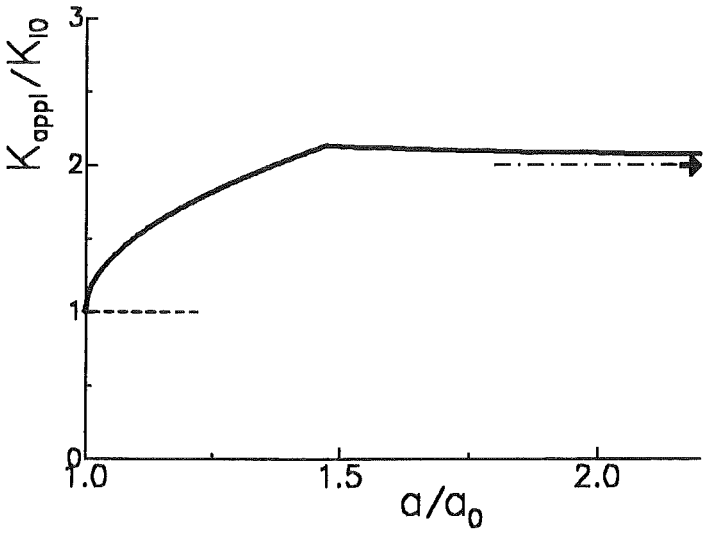

Figure 72. Applied stress intensity factor. R-curve for a Griffith crack with bridging stresses σ = constant.

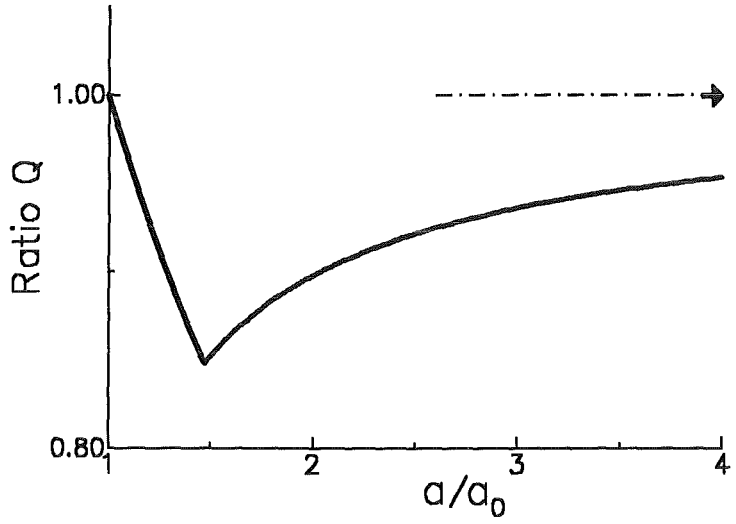

Figure 73. . Ratio of crack resistance and stress intensity factors according to eq.(6.4.10).

Let us consider a Griffith crack (a straight through-the-thickness crack) of size 2a in an infinite body which is symmetrically loaded in the range $a_c < |x| < a$ by a constant stress σ. Figure 69 illustrates geometry and loading conditions. The displacements under this strip load are given by eq.(4.3.4) and the weight function reads

$$h(x,a) = \frac{2}{\sqrt{\pi a}} \frac{a}{\sqrt{a^2 - x^2}} \tag{6.3.12}$$

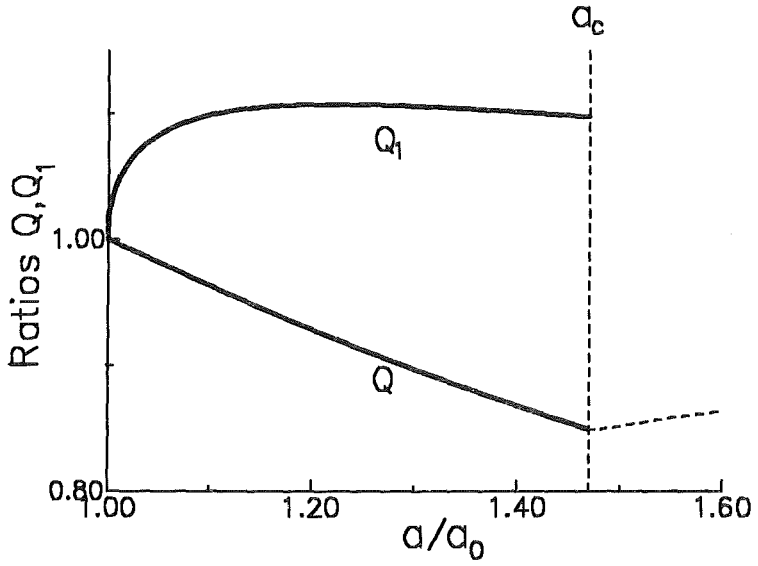

Figure 74. . Ratio of crack resistance and stress intensity factors according to eqs.(6.4.10) and (6.4.12) for the first phase of crack extension $a \leq a_c$.

We find for the crack opening displacement field according to [80]

$$\delta(x,a) = \frac{\sigma a}{E'\pi}\left[4\theta \sin\varphi - \cos\varphi \cdot \ln\frac{\sin^2(\theta-\varphi)}{\sin^2(\theta+\varphi)} - 2\cos\theta \cdot \ln\frac{\sin\theta+\sin\varphi}{\sin\theta-\sin\varphi}\right] \tag{6.4.1}$$

$$\theta = \arccos(a_0/a) \quad , \quad \varphi = \arccos(x/a) \tag{6.4.2}$$

as plotted in fig.70. The related bridging stress intensity factor results as

$$K_{I\,br} = \sigma 2\sqrt{a/\pi}\int_{a_c}^{a}\frac{dx}{\sqrt{a^2-x^2}} = 2\sigma\sqrt{\frac{a}{\pi}}\left[\frac{\pi}{2} - \arcsin(a_c/a)\right] \tag{6.4.3}$$

The crack opening displacement field caused by the applied stresses σ_{appl} is

$$\delta(x,a) = 2\frac{\sigma_{appl}}{E'}\sqrt{a^2-x^2} \tag{6.4.4}$$

and the applied stress intensity factor $K_{I\,appl}$ is given as

$$K_{I\,appl} = \sigma_{appl}\sqrt{\pi a} \tag{6.4.5}$$

The total crack opening displacement field follows from the superposition of eqs.(6.4.1) and (6.4.4), and the total stress intensity factor from superposition of eqs.(6.4.3) and (6.4.5). Figure 71 shows the total crack opening displacement field for $|\sigma|/\sigma_{appl}=1$.

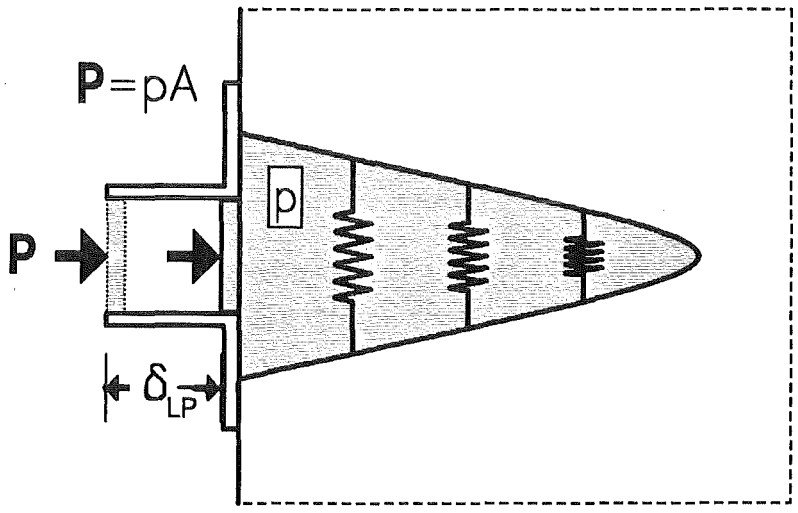

Figure 75. Crack surface loading. A crack loaded by a crack surface pressure p and by bridging stresses modelled by a system of non-linear springs.

For the calculation of the R-curve it is assumed that a critical crack opening displacement δ_c exists at which the bridging interactions become abruptly dissolved, i.e. $\sigma_{br} = 0$ for $\delta > \delta_0$. Now we can determine the R-curve numerically from the two conditions:

1. The total stress intensity factor must coincide with K_{I0}

$$\sigma_{appl}\sqrt{\pi a} - |\sigma_{br}|2\sqrt{\frac{a}{\pi}}\left[\frac{\pi}{2} - arcsin(a_c/a)\right] = K_{I0} \tag{6.4.6}$$

2. At the end of the bridging zone the critical crack opening displacement must be reached

$$2\frac{\sigma_{appl}}{E'}\sqrt{a^2 - x^2} - |\delta_{br}| = \delta_c \tag{6.4.7}$$

The solution of these two relations results in σ_{appl} and a_c for a given crack length a. From σ_{appl} the stress intensity factor $K_{I\,appl}$ can be calculated. An R-curve resulting for a crack of initial crack length a_0 is represented in fig.72. The calculation of the R-curve was performed in the following way. A crack of initially unbridged length $a = a_0$ is considered. The applied stress is increased up to a certain value that satisfies the condition for the onset of stable crack extension, namely

$$K_I = \sigma_{appl}\sqrt{\pi a_0} \tag{6.4.8}$$

Then a is increased as long as $\delta(x = a_0) < \delta_c$. The applied stress intensity factor results from eq.(6.4.6) as

$$K_{I\,appl} = K_{I0} + |\sigma_{br}|2\sqrt{\frac{a}{\pi}}\left[\frac{\pi}{2} - arcsin(a_0/a)\right] \tag{6.4.9}$$

During further crack extension it results $a_c > a_0$ and the solution of eqs.(6.4.6) and (6.4.7) can be found with a zero routine. The R-curve, resulting for $\delta_c E'/(|\sigma_{br}|a_0) = 1.5$ is plotted in fig.72. The R curve starts very steep like $K_{br} \propto \sqrt{a - a_0}$ and after δ_c is reached (in the plotted example at $a = 1.47a_c$) the applied stress intensity factor decreases slightly against the asymptotic value of $K_{I\,appl}/K_{I0} = 2$. The crack resistance obtained with eq.(6.3.1) has been plotted in fig.73 in a normalised representation according to eq.(6.3.8) as the ratio

$$Q = \frac{E'J}{K_{I\,br}^2 + 2|K_{I\,br}|\,K_{I0}} \tag{6.4.10}$$

This ratio should be $Q = 1$ if the Irwin equation would be valid in the presence of an R-curve behaviour. From fig.73 we find that at the onset of crack extension the ratio is $Q = 1$. In this situation the bridging zone is negligible in size compared with the initial crack length a_0. Then we detect a significant deviation from the value $Q = 1$ and after very long crack propagation, when the bridging zone of finite length is again small compared with the crack length, the ratio Q tends asymptotically against $Q = 1$.
If we consider the work done by the external load against the constant bridging stresses we can write for $a < a_c$

$$W_{br} = \sigma\int_{a_0}^{a} 2\delta(x)\,dx \tag{6.4.11}$$

that allows to define the ratio

$$Q_1 = \frac{dW_{br}/da}{K_{I\,br}^2 + 2|K_{I\,br}|\,K_{I0}} \tag{6.4.12}$$

Figure fig.74 illustrates the two ratios Q, Q_1 for $a \leq a_c$. This ratio also deviates from the value $Q=1$.

6.4.1 A simple model for the crack surface loadings

The main topic of this section was to prove the validity of the Irwin relation eq.(6.1.1) in presence of bridging stresses. If this is really a general relation it must be correct for any conceivable loading case. In the previous considerations the crack surface loading was a virtual pressure of same value as the tensile stresses σ_{appl} which are caused in uncracked body by the externally applied load. This load has been assumed to be a remote stress in a long tensile specimen. The loading situation becomes more clear when the principle of superposition - yielding the virtual crack surface loadings - is dropped and the virtual pressure is substituted by a real crack surface load.
In the simple model illustrated by fig.75 a crack is opened by an incompressible liquid with the directly applied pressure p and the bridging interactions are represented by non-linear springs. The externally applied load P results as the product of the actual pressure and the area A of the piston

$$P = pA \tag{6.4.13}$$

which squeezes the liquid into the crack. The volume caused by the crack surface displacements $\delta(x)$ is then given by the "loading-point displacement" δ_{LP} as

$$\begin{aligned} V &= 2B\int_0^a \delta(x)\,dx = A\delta_{LP} \\ \rightarrow \quad \delta_{LP} &= \frac{2B}{A}\int_0^a \delta(x)\,dx \end{aligned} \tag{6.4.14}$$

in agreement with eq.(6.1.5). The fracture mechanical treatment is then identical to that done before with the virtual stresses.

6.5 Compliance in presence of R-curve effects

In presence of bridging stresses at the crack faces also deviations in the compliance have to be expected [50].
Due to the bridging stresses, the specimens' stiffness is greater than that obtained for specimens with completely free crack surfaces, i.e. the crack length resulting from compliance measurements will be lower than the real physical crack length. Two special questions are:

- What is the meaning of the compliance in presence of non-linear bridging interactions?
- Is the crack-length measurement via compliance correct?

In fig.76 measurements of crack length based on compliance and on microscopic observations are compared [20]. For larger crack extension it is obvious that the compliance method underestimates the real crack length. These differences give rise for a detailed analysis of compliance behaviour.

6.5.1 Loading-point compliance

The compliance of a cracked specimen is defined as the relative displacement of the loading points δ_{LP} divided by the load applied

$$C = \frac{\delta_{LP}}{P} \tag{6.5.1}$$

The compliance is applied in fracture mechanics

- for the determination of the actual crack depth, and
- for the computation of energy release rates from load vs. displacement curves resulting in controlled fracture tests.

In case of a crack in a component with crack faces completely free of stresses the compliance is directly related to the crack depth. Under pure tensile loading it holds

$$C = C_0 + \frac{2}{BE'} \int_0^{\alpha} Y^2(\alpha')\, \alpha'\, d\alpha' \quad , \quad \alpha = a/W \tag{6.5.2}$$

where Y is the geometric function for the stress intensity factor calculation, defined by

$$K = \sigma_{appl}\, Y \sqrt{a} \tag{6.5.3}$$

which can be taken from handbooks.
Due to the bridging stresses, the specimens' stiffness is greater than that obtained for specimens with completely free crack surfaces, i.e. the crack length resulting from compliance measurements will be lower than the real physical crack length.
Equations (6.1.4) and (6.1.5) provide the possibility of computing a differential compliance C_{diff} which gives the increment of displacement for a given increment of load (or stress applied)

$$C_{diff} = \frac{d\delta_{LP}}{dP} \tag{6.5.4}$$

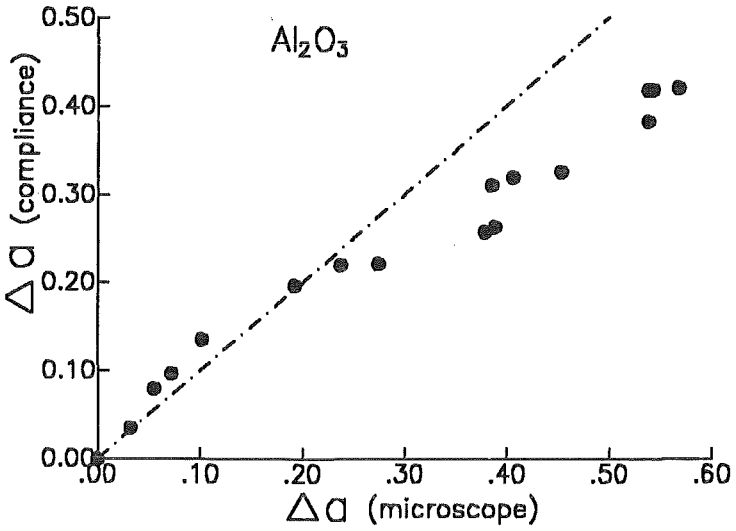

Figure 76. Crack-length measurements. Crack length measurements for a crack of initial depth $a_0 = 2.25$mm in a bending bar of $W = 4.5$mm thickness; material 99.6% Al_2O_3 (mean grain size $\simeq 20\mu$m).

whilst the global compliance C_{glob} is defined by eq.(6.5.1).
For numerical calculations the bridging stress relations given in section 4.1 are used in the following. In order to allow dimensionless computations to be made, the numerical results for the stress intensity factors and displacements are normalised by the characteristic bridging stress σ_0 and the specimen width W according to

$$K' = \frac{K}{\sigma_0\sqrt{W}} \quad , \quad \delta' = \frac{\delta E'}{\sigma_0 W} \tag{6.5.5}$$

In fig.77 the loading-point displacements are plotted as a function of the stress applied. The displacements are normalised on that value that is reached at $K'_{tip} = 1$. As can be seen from fig.77, most of the deviations between the loading-point displacements in the presence of bridging stresses and the displacements calculated ignoring these additional stresses (dash-dotted straight line) occur at lower loads. The higher the load, the smaller is the remaining bridging zone, and the influence of bridging stresses decreases. A lower limit of the displacements can be calculated by considering only the initial crack size $a = a_0$. This limit case is introduced in fig.77 as a dotted straight line.
In fig.78 the total compliance is shown for a crack of $a/W = 0.7$ and $a_0/W = 0.5$. As expected from the non-linear bridging stress, the comliance is not constant. Under low loads the compliance in the presence of bridging stresses tends towards the compliance of a crack of length a_0/W without bridging stresses. At high loads the compliance tends asymptotically to the compliance of a crack of depth a/W without bridging stresses.
The differential compliance resulting from the results given in fig.78 is shown in fig.79. Significant deviations between differential compliance and global compliance are evident.
The total compliance of the whole crack-containing component is then given by

$$C_{total} = C_{glob} + C_0 \quad , \quad C_0 = \frac{2L}{EWB} \quad \text{for tension} \tag{6.5.6}$$

where C_0 is the compliance of the uncracked component. In fig.80 the compliance of the specimen in the presence of bridging stresses is represented together with the compliance in the ab-

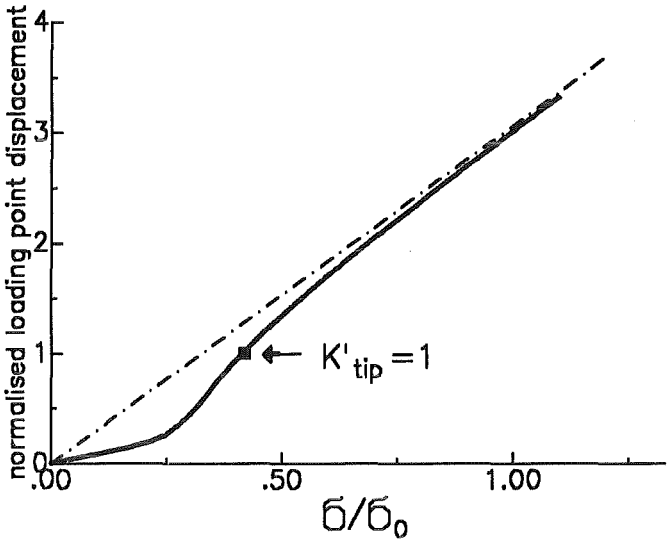

Figure 77. Loading-point displacements. Loading point displacements as a function of load, calculated with eq.(4.1.9) and (4.1.13) for $a/W = 0.7$; dash-dotted straight line: displacements for the elastic case with interaction free crack surfaces, dotted straight line: limit case for $a/W = 0.5$.

sence of bridging interactions versus the actual crack size. It is obvious that the specimens with bridging interactions react more rigidly than the ideal fracture-mechanics specimens with completely free crack faces. Two types of crack depth can be concluded from fig.81, namely the real physical crack depth a_{phys} and the apparent crack depth a_{compl} which can be concluded from the compliance by application of pure linear-elastic relations. In the representation fig.80 one can also see that the real crack size is larger than that obtained from the compliance.

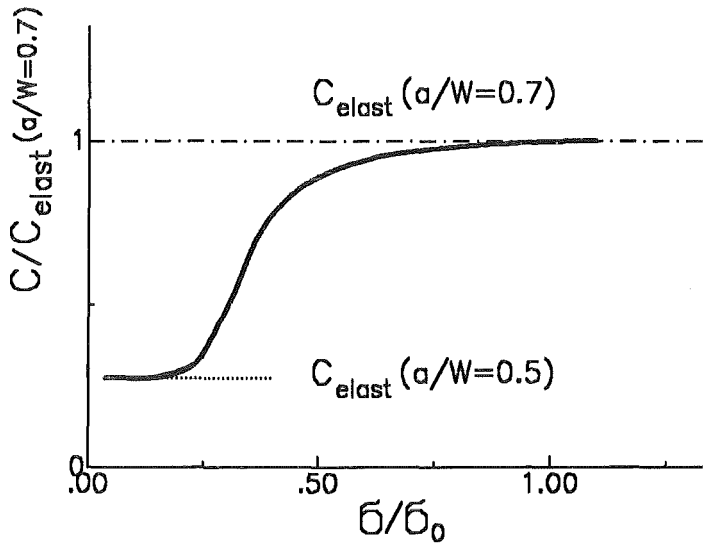

Figure 78. Global compliance. Global loading point compliance, calculated with eq.(4.1.9) and (4.1.13) for $a/W = 0.7$; dash-dotted straight line: limit case for interaction free crack with $a/W = 0.7$; dotted straight line: compliance of an interaction free crack with $a/W = 0.5$.

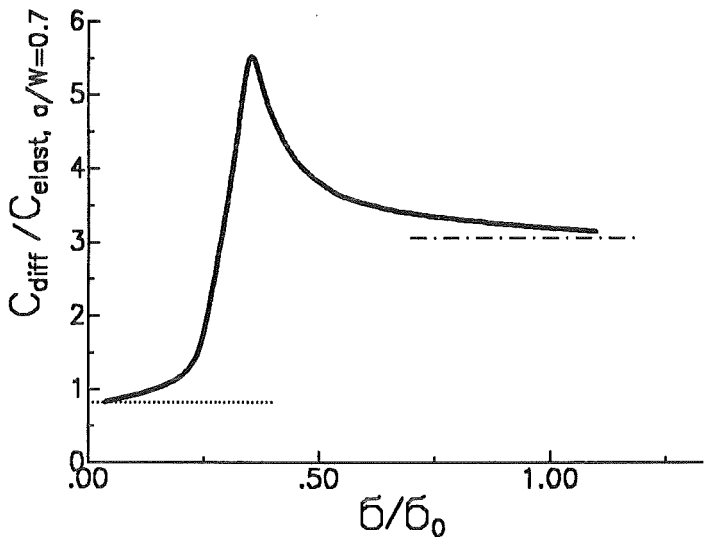

Figure 79. Differential compliance. Differential compliance according to eq.(6.5.4) derived from the data of fig.77.

6.5.2 Crack-mouth compliance

A very popular possibility of indirect determination of the crack depth is the measurement of crack-mouth opening. The related crack-mouth compliance C_{CM} can be derived from the displacements δ_{CM} at the location $x = 0$ and the actual load P as

$$C_{CM} = \frac{\delta_{CM}}{P} \tag{6.5.7}$$

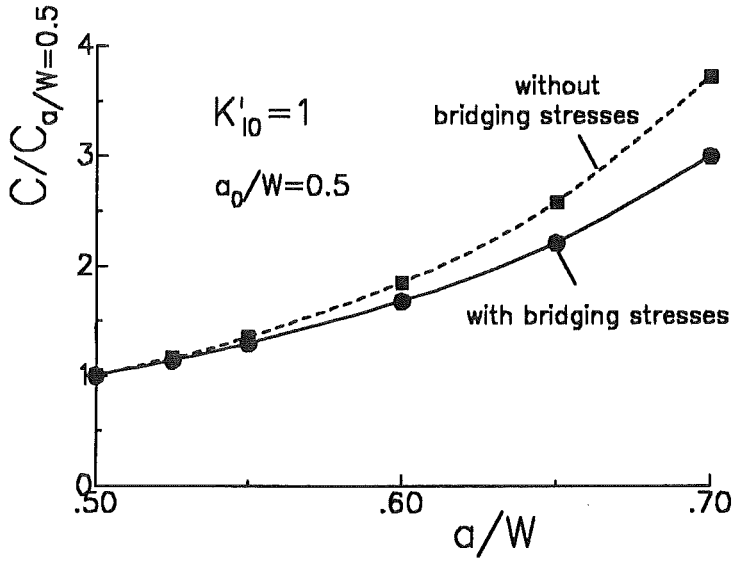

Figure 80. Global compliance. Global compliance as a function of crack length for $K'_{I0}=1$.

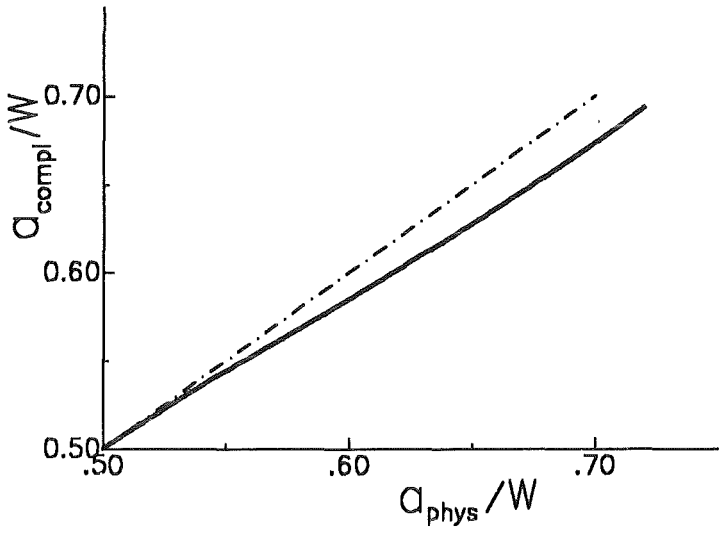

Figure 81. Crack length. Deviations between the physical crack depth a_{phys} and the apparent crack depth a_{compl} as resulting from the compliance.

where the crack-mouth displacements may be determined from eq.(6.1.4) as

$$\delta_{CM} = \frac{1}{E'} \int_0^a \int_{x'}^a h(a',0)h(a', x') \left[\sigma_{appl}(x') + \sigma_{br}(x')\right] da'dx' \tag{6.5.8}$$

Figure 82 shows the crack profiles under different loads for cracks with and without bridging interactions in the region $a_0 < x < a$ for a crack with $a_0/W = 0.5$, $a/W = 0.7$. In fig.83 the crack-mouth displacements resulting from (6.5.8) are plotted for $a_0/W = 0.5$, $a/W = 0.7$ and the bridging stress relations given by eqs.(4.1.9) and (4.1.13). A curve is obtained which is qualitatively identical to that for the loading-point displacements. Figure 84 represents the crack-mouth displacements for the three bridging relations used. In all cases the crack-mouth displacement underestimates the actual crack length, i.e. the curves run below the upper straight line.

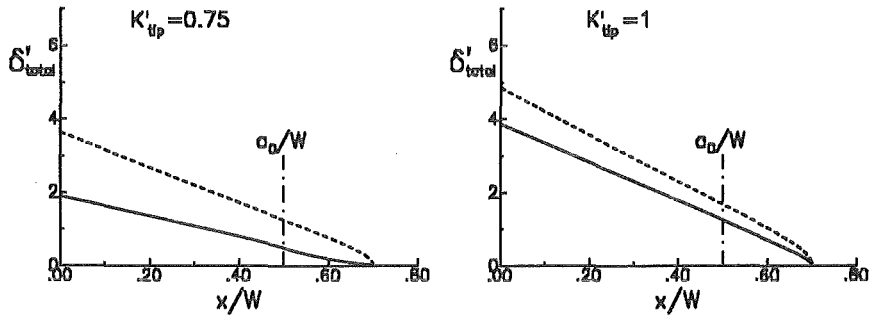

Figure 82. Crack profile. Crack profile for a crack (in a bent plate) with bridging stresses in the range $a_0/W < x/W < a/W$; dashed curves: crack profiles in the absence of bridging stresses (loaded by the same applied stress intensity factor K'_{appl}).

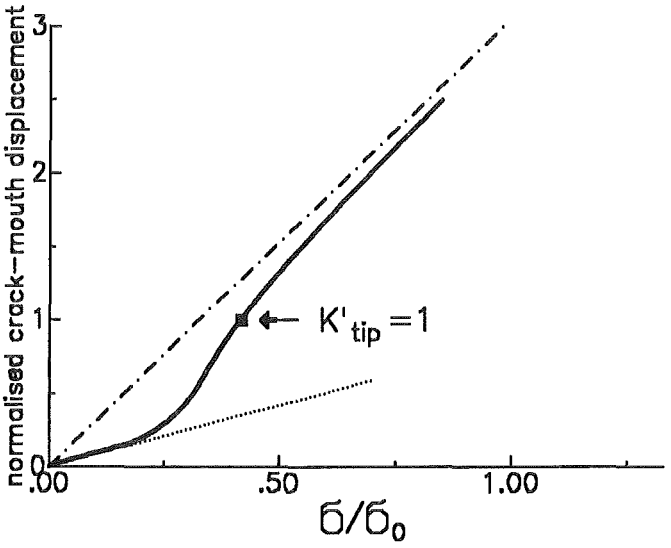

Figure 83. Crack-mouth displacement. Crack-mouth displacements as a function of load calculated with eqs.(4.1.9) and (4.1.13) for $a/W = 0.7$; straight line: displacements for the elastic case with interaction free crack surfaces.

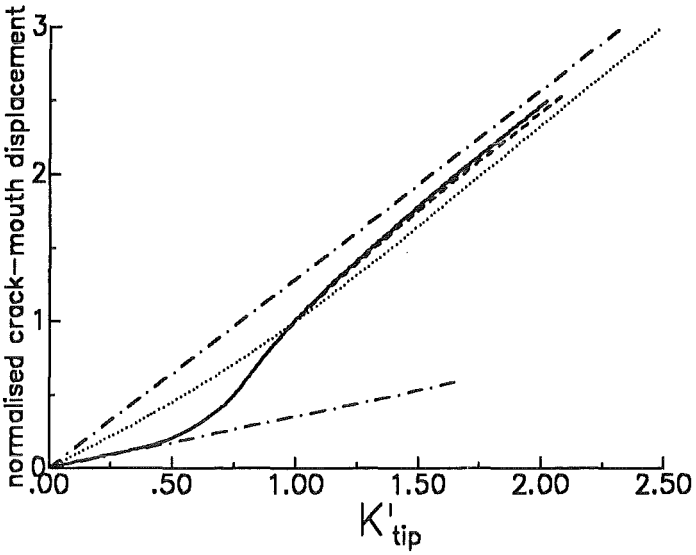

Figure 84. Influence of bridging relation. Crack-mouth openings for a crack with $a_0/W=0.5$, $a/W=0.7$, calculated with different bridging stress relations; solid line: eqs.(4.1.9) and (4.1.13), dashed line: eqs.(4.1.9) and (4.1.10), dotted line: eq.(4.1.19).

INFLUENCE OF R-CURVE EFFECTS ON MECHANICAL PROPERTIES

7. Influence of R-curve effects on the inert strength

7.1 R-curves due to bridging interactions

In the past R-curve effects were investigated mainly with specimens containing artificial macro-cracks. From section 3.2 it can be concluded that for very strongly rising R-curves also small natural cracks can be affected. An analysis of this topic is given in [51]
Due to the crack-surface interactions, the stress intensity factor acting at the crack tip $K_{I\,tip}$ deviates from the externally applied stress intensity factor $K_{I\,appl}$ according to eq.(4.3.8). This relation is the basis for understanding R-curve influences on the strength behaviour. To be able to evaluate it we need the applied stress intensity factor as well as the bridging stress intensity factor. In this section first relations are presented for $K_{I\,appl}$ and $K_{I\,br}$ for circular and elliptical cracks. Then the development of cracks in the presence of R-curve effects and their influence on bending strength is discussed and finally a procedure is described which allows the bridging stresses to be estimated.
The cracks in the surface region of ceramic materials caused by surface grinding which propagate under increasing load are assumed to be semi-elliptical in shape. The stress intensity factor caused by the externally applied stress σ results as

$$K_{I\,appl} = Y(a/c, a/W)\sigma\sqrt{a} \quad , \tag{7.1.1}$$

where Y is the so-called geometric function, depending on the aspect ratio a/c and the relative crack depth a/W. The geometrical quantities are explained in fig.85. Different types of stress intensity factors are available to solve two-dimensional crack problems. One possibility is to use local stress intensity factors which vary along the crack front. Such stress intensity factors are available for simple load cases. Newman and Raju provided solutions for semi-elliptical surface cracks under tension and bending [52].
Beside the local stress intensity factors also averaged stress intensity factors are currently used in fracture mechanics. These stress intensity factors are defined in terms of the 2-dimensional weight function as

$$\overline{K_I} = \frac{E'}{\overline{K_{Ir}}} \int_{(S)} \sigma \frac{\partial v_r}{\partial(\Delta S)}\, dS \tag{7.1.2}$$

where $E' = E/(1-\nu^2)$. ∂v_r is the virtual change of the crack opening displacements of a reference loading case (mostly tension) for a virtual extension $\partial(\Delta S)$ of the crack surface S, σ is the arbitrarily distributed normal stress in the uncracked structure, and $\overline{K_{Ir}}$ is the reference stress intensity factor defined by

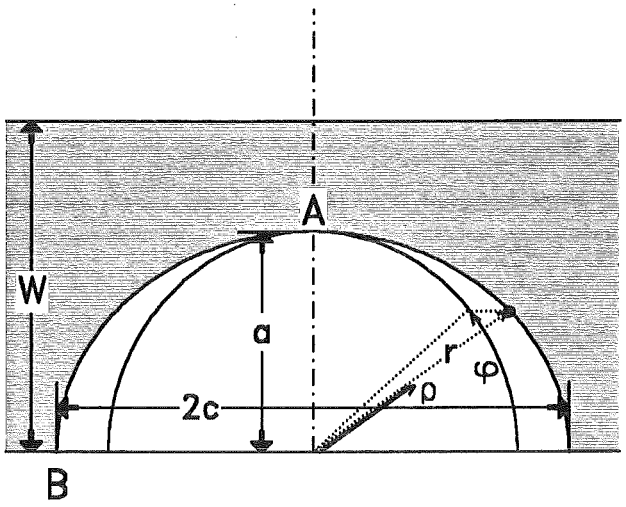

Figure 85. Geometry of a surface crack. Semi-elliptical surface crack in a ceramic specimen (not truely scaled).

$$\overline{K_{Ir}^2} = \frac{1}{\Delta S} \int K_{Ir}^2 d(\Delta S) \tag{7.1.3}$$

The main advantage of averaged stress intensity factors is their availability for arbitrary stress distributions. In order to reduce the infinite number of possible virtual crack extensions Cruse and Besuner [53] suggested for semi-elliptical surface cracks that a virtual crack extension should lead again to a semi-ellipse. Cruse and Besuner's proposal is expressed by

$$d(\Delta S_A) = \frac{1}{2} c\Delta a \sin^2\varphi \, d\varphi \qquad \Delta S_A = \frac{1}{2} \pi c \Delta a \tag{7.1.4}$$

describing a crack extension in direction of the semi-axis a and leading to the stress intensity factor $\overline{K_A}$, and

$$d(\Delta S_B) = \frac{1}{2} a\Delta c \cos^2\varphi \, d\varphi \qquad \Delta S_B = \frac{1}{2} \pi a \Delta c \tag{7.1.5}$$

describing a virtual crack extension in c-axis direction resulting in the stress intensity factor $\overline{K_B}$. The practical application of averaged stress intensity factors has been described in more detail in [54]. The reference crack opening displacement field for semi-elliptical surface cracks necessary for the evaluation of eq.(7.1.2) has been derived in [55].
Especially for the bending load case one obtains averaged stress intensity factors directly from eq.(7.1.3) by inserting the local bending solution in eq.(7.1.3). The resulting averaged stress intensity factors can be computed by

$$\overline{K}_{A,B} = \sigma_{bend} \overline{Y}_{A,B} \sqrt{a} \tag{7.1.6}$$

with

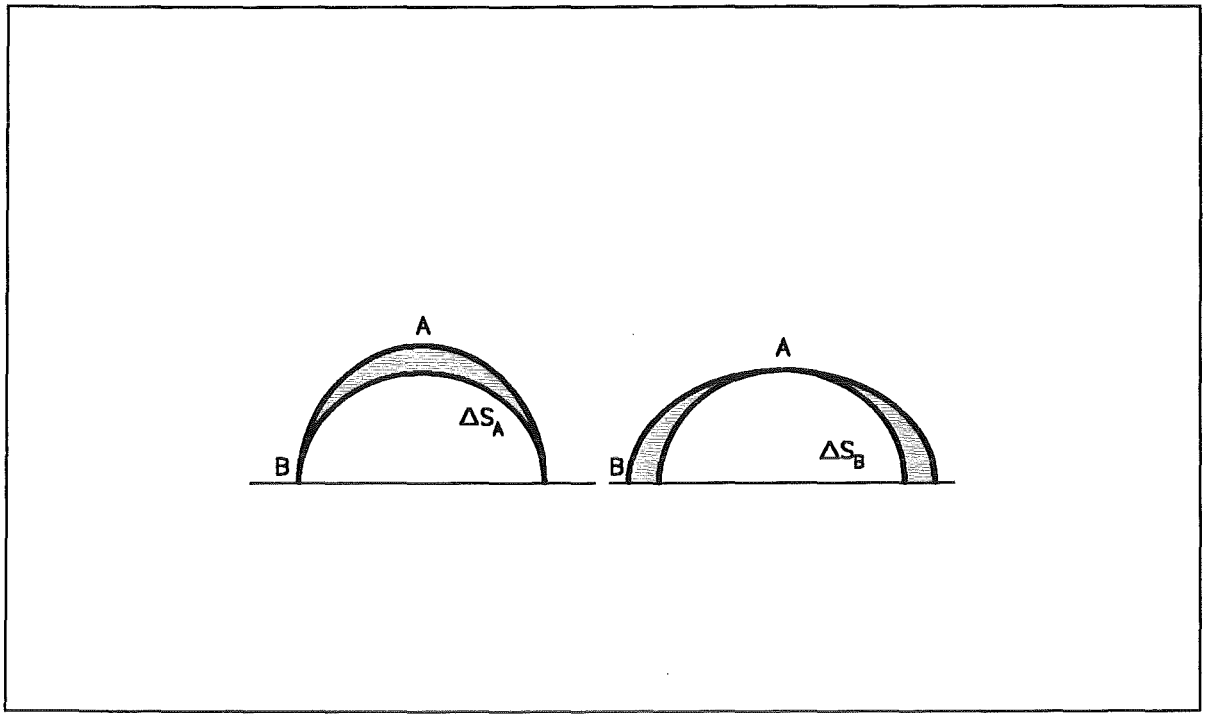

Figure 86. Virtual crack increments. Virtual crack extensions for weight function applications as proposed by Cruse and Besuner [53] (illustration restricted to one half of the embedded crack).

$$\bar{Y}_A = \left[\frac{4}{\pi} \int_0^{\pi/2} Y^2(\varphi) \sin^2\varphi \, d\varphi \right]^{1/2} \tag{7.1.7}$$

$$\bar{Y}_B = \left[\frac{4}{\pi} \int_0^{\pi/2} Y^2(\varphi) \cos^2\varphi \, d\varphi \right]^{1/2} \tag{7.1.8}$$

For the numerical calculations the bending solution of Newman and Raju [52] is recommended.

7.1.1 The bridging stress intensity factor

Bridging stress intensity factors are available only for a few types of crack, namely edge cracks and embedded circular cracks [18]. It will be shown in this section how the bridging stress intensity factor for an embedded elliptical crack can be estimated from the bridging stress intensity factor of an embedded circular crack by application of the weight function procedure for averaged stress intensity factors

In the subsequent considerations the additional assumption is made that bridging stress intensity factors for semi-elliptical surface cracks can be approximated by the bridging stress intensity factors of embedded elliptical cracks with the same aspect ratio.

Circular cracks:

The friction induced bridging stresses σ_{br} as a function of the crack opening displacement δ may be described by a number of relations. Here we use the exponential description

$$\sigma_{br} = \sigma_0 \exp(-\delta/\delta_0) \tag{7.1.9}$$

with a maximum stress σ_0 and a characteristic range δ_0.
The bridging stress intensity factor $K_{I\,br}$ for a penny-shaped embedded crack was calculated applying the weight function method [18]. According to [34] the results can be approximated by

$$K_{I\,br\,circle} = \frac{\sigma_0 Y\sqrt{a_0}}{C}\left\{1 - \exp\left(-C\sqrt{a/a_0 - a_0/a}\right)\right\} \tag{7.1.10}$$

with the abbreviation

$$C = \frac{4 \cdot 1.141(1-\nu^2)K_{I0}\sqrt{a_0}}{YE\pi\delta_0} \tag{7.1.11}$$

For bridging stresses with a large range of action ($\delta_0 \to \infty$) eq.(7.1.3) reduces to become

$$K_{I\,br\,circle}(\delta_0 \to \infty) = \sigma_0 Y\sqrt{a}\,\sqrt{1-(a_0/a)^2} \tag{7.1.12}$$

For numerical calculations the following parameters - characteristic of coarse-grained Al_2O_3 - were maintained constant:

$$E = 3.6 \cdot 10^5\ \text{MPa},\ \nu = 0.2,\ K_{I0} = 3\ \text{MPa}\sqrt{\text{m}}$$

and the bridging parameters were considered to be variable.

Elliptical cracks:
In order to take into account the influence of the elliptical crack shape we apply an estimative relation which is often used in fracture mechanics. Since the bridging stress intensity factors in elliptical cracks can be computed (at least in terms of averaged stress intensity factors) for the case of ($\delta_0 \to \infty$) one can approximate

$$\overline{K}_{br,\,ellipse}(\delta_0) \simeq \overline{K}_{br,\,circle}(\delta_0)\,\frac{\overline{K}_{br,\,ellipse}(\delta_0 \to \infty)}{\overline{K}_{br,\,circle}(\delta_0 \to \infty)} \tag{7.1.13}$$

In this context it should be mentioned that in case of a radial symmetrically loaded circular crack the local stress intensity factor and any averaged stress intensity factor are identical. The greater the parameter δ_0 is the better will be the approximation.
The averaged stress intensity factors for the elliptical crack with $\delta_0 \to \infty$, needed in eq.(7.1.13), are given in the Appendix. In the subsequent considerations the bars over the averaged stress intensity factors and related geometric functions will be dropped.

7.1.2 Crack development in bending strength tests

In the subsequent considerations two assumptions will be made:

- It is assumed that eq.(7.1.13) will also describe surface cracks.
- The width of bending bars is assumed to be large so that a finite width correction is neither necessary for the bridging stress intensity factor nor for the externally applied stress intensity factor.
- It is assumed that the initial cracks are semi-circular.

With increasing applied bending stress σ_b a semi-circular shaped surface crack ($a_0 = c_0$) starts to propagate at point B - where the geometric function $Y(a_0/W, a_0/c_0)$ reaches its maximum value - if the condition

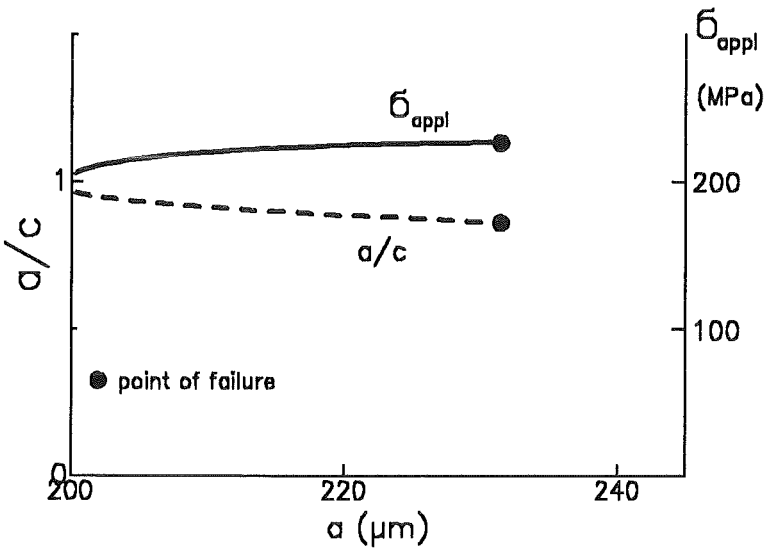

Figure 87. Stress and aspect ratio. Development of the aspect ratio under increasing applied stress in a strength test ($\delta_0 = 1\mu m$ $\sigma_0 = 100$ MPa.).

$$\sigma_b Y_B(a_0/c_0, a_0/W)\sqrt{a_0} = K_{I0} \tag{7.1.14}$$

is fulfilled. Crack propagation at point A occurs at a higher stress level where the two conditions

$$\begin{aligned} \sigma_b Y_A(a_0/c, a_0/W)\sqrt{a_0} - K_{Ibr,A}\Big|_{\Delta a = 0} &= K_{I0} \\ \sigma_b Y_B(a_0/c, a_0/W)\sqrt{a_0} - K_{Ibr,B}\Big|_{\Delta c = c - a_0} &= K_{I0} \end{aligned} \tag{7.1.15}$$

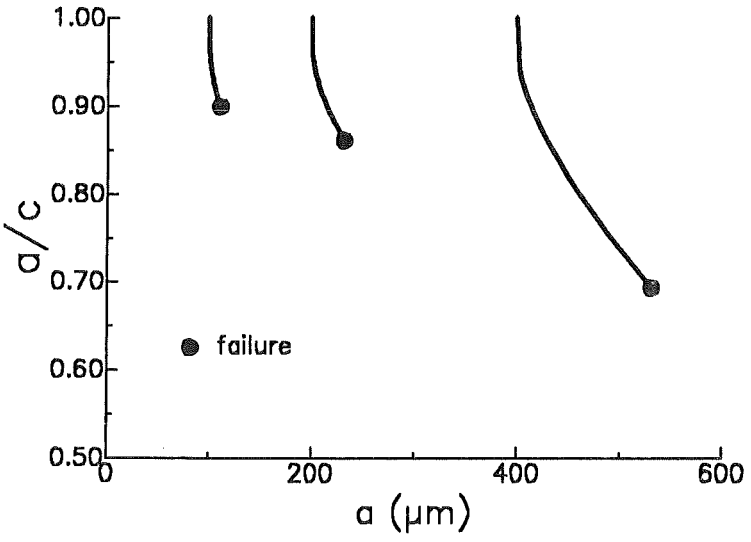

Figure 88. Crack shape. Development of the aspect ratio a/c as a function of the initial crack size a_0.

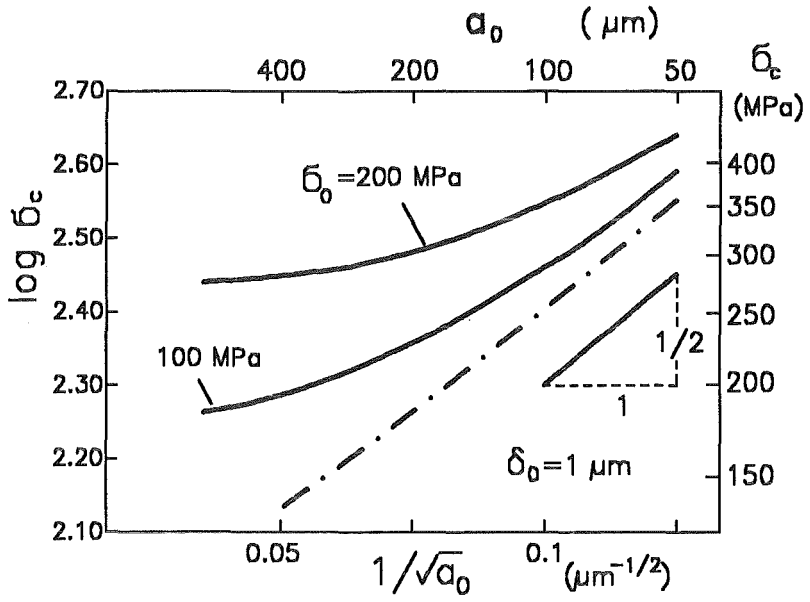

Figure 89. Strength. Strength σ_c for a material with $\delta_0 = 1\mu m$ (dash-dotted line: bending strength in the absence of bridging stresses).

are simultaneously fulfilled. The further crack development is then described by the equations

$$\sigma_b Y_A(a/c, a/W)\sqrt{a} - K_{I\,br,A}\Big|_{\Delta a = a - a_0} = K_{I0}$$
$$\sigma_b Y_B(a/c, a/W)\sqrt{a} - K_{I\,br,B}\Big|_{\Delta c = c - a_0} = K_{I0} \qquad (7.1.16)$$

After stepwise increased external bending stress σ_b failure can be observed at that stress value where for the first time no solution of eq.(7.1.16) is found. In eqs.(7.1.15) and eq.(7.1.16) the bridging term is introduced with a minus sign since the bridging stresses are acting against the stresses applied.

For numerical calculations the equations (7.1.16) were solved by use of two coupled zero-routines resulting in the crack data a, c for a given stress σ.

In fig.87 the applied stress for a crack of initial crack size $a_0 = 200\mu m$ is plotted as a function of the crack length. The calculations were carried out with $\sigma_0 = 100$MPa and $\delta_0 = 1\mu m$. Failure occurs at about $a = 240\mu m$. Additionally the aspect ratio a/c is shown. With increasing crack size the aspect ratio decreases and the initially semi-circular shaped crack becomes a semi-ellipse but the maximum deviations from the semi-circular shape are relatively small.

The development of the aspect ratio with crack extension is illustrated in fig.88 for three cracks of different initial crack sizes a_0. It is obvious that the strongest change of the aspect ratio occurs at the beginning of crack propagation.

Figure 89 shows the bending strength influenced by the bridging stresses (solid lines) as well as the bending strength in the absence of an R-curve effect (dash-dotted line) as a function of the initial crack size a_0 in a representation where the abscissa is scaled according to $\log(1/\sqrt{a_0})$. It can be seen that the bending strength deviates from the linear dependency, especially for relatively large cracks, i.e. for relatively low strength values. This behaviour is a consequence of the R-curve effect and the significantly deviating stress intensity factors in bending compared to pure tension.

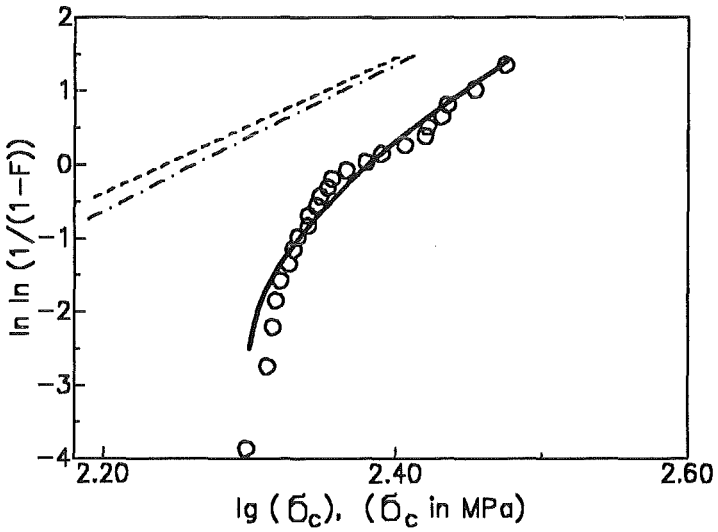

Figure 90. Strength calculation. Strength data of fig.5 compared with calculations using data-set (7.1.18); dash-dotted curve: bending strength in the absence of bridging stresses; dashed curve: tensile strength in the absence of bridging stresses.

7.1.3 Estimation of bridging parameters from strength measurements

Now the question arises whether strength data can provide information on the bridging parameters δ_0 and σ_0. For a determination of these parameters the bending strength data of fig.5 are used. The bending strength measurements were carried out on 3.5x4.5x50mm specimens made of coarse-grained 99.6% Al_2O_3 (Frialit/Degussit, Friedrichsfeld AG, Mannheim, FRG) with a mean grain size of 20μm. A strong R-curve behaviour has been found for this material by measurements performed with macro-cracks [18]. The bending bars were only roughly ground which resulted in a relatively low strength. Such a surface state can ensure that all specimens will fail due to only one flaw population, namely surface cracks. Before testing the specimens were annealed in the vacuum for 5 hours at 1200°C. The typical effect illustrated in fig.89 seems to be present. Under the assumption that the initial crack size distribution is given by a two-parametric Weibull distribution

$$F(a_0) = \exp\left[-\left(\frac{a_{00}}{a_0} \right)^m \right] \tag{7.1.17}$$

with the Weibull-parameters m, a_{00} one can determine the unknown parameters.
With a least-squares procedure the parameters σ_0, δ_0, a_{00}, m were determined in the following way:
For the parameter field $\delta_0 = (0/0.5/1/2/4\mu m)$, $m = (1.5/2/2.5/3)$, $\sigma_0 = (0/50/100/150/200MPa)$, and $a_{00} = (50/100/200/400/700\mu m)$ a field of related strength values has been determined. Application of cubic splines then allowed the data to be interpolated. A least-squares routine (the author used the Harwell Subroutine VA02A) yielded the best parameter set. In each step of the least-squares routine the strength distribution is calculated for the actual parameter set. The subroutine compares the calculated distribution with the measured one and changes the actual parameters systematically as long as the best parameter set is obtained. The resulting parameters for the data of fig.5 are:

$$\sigma_0 = 120MPa\,, \quad \delta_0 = 1\mu m\,, \quad a_{00} = 200\mu m\,, \quad m = 2 \tag{7.1.18}$$

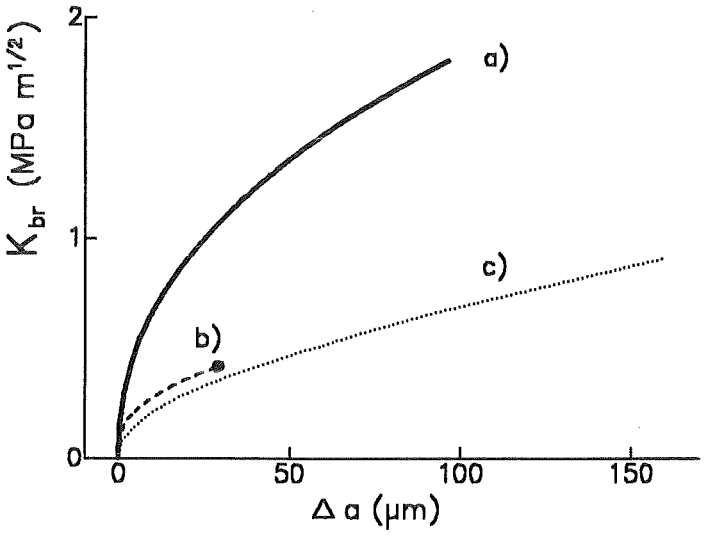

Figure 91. R-curves. a) R-curve for a semi-circular surface crack with initial crack size $a_0=400\mu m$ calculated with data set (7.1.18) based on bending strength results;
b) R-curve calculated for the same crack with bridging stress parameters derived from macro-cracks [18];
c) macro-crack R-curve obtained in [18] from subcritical crack growth tests with notched bending specimens.

Figure 90 shows the fitting curve together with the strength data of fig.5. Additionally the bending strength in the absence of any bridging effect is plotted as a dashed line. In a previous study [18] the "macro-crack behaviour" of the same material has been investigated in static bending tests with notched specimens yielding the parameters $\sigma_0=45$ MPa, $\delta_0=1\mu m$. For the natural cracks the maximum friction stresses are distinctly higher. Whilst in macro-crack tests an average value of σ_0 along the macroscopic specimen width of 3.5mm was determined the averaging length for the natural cracks is by a factor of about 10 shorter and more local effects may influence the result.
Figure 91 shows the R-curve (at point A) from strength evaluation as a solid line compared with the R-curve for identical cracks calculated with the bridging parameters derived in [18] (dashed curve) and the "macro-crack R-curve" obtained in [18] (dotted curve). The significant influence of the different values for σ_0 is evident.

In conclusion: As a consequence of bridging interactions it can be concluded that there are deviations from the expected straight line in the Weibull-plot. Such an effect may become pronounced, especially in case of a large scatter of the initial crack size distribution.
It has been shown how the bridging stresses for coarse-grained Al_2O_3 can be estimated from bending strength data. The main intent was to explain a procedure for evaluating the bridging parameters for natural cracks. The absolute results should not be overrated since a number of assumptions (e.g. the initial shape of cracks, the infinite specimen width, the Weibull distributed initial crack sizes) had to be made. Calculations in terms of averaged stress intensity factors show the development of surface cracks until failure providing the strength. In this context two important points must be taken into account:

1. The change of crack shape during crack extension in bending strength tests, i.e. the aspect ratio a/c is not constant!
2. The stress intensity factors at the **two** points A and B of the crack are responsible for crack development and strength.

8. Influence of R-curve effects on subcritical crack growth

8.1 General influence of R-curve effects on lifetimes in static tests

In materials without R-curve behaviour the crack-tip stress intensity factor $K_{I\,tip}$ - responsible for crack growth - is identical with the externally applied stress intensity factor $K_{I\,appl}$. In ceramics with R-curve behaviour the crack tip is shielded by the shielding stress intensity factor. Therefore, the crack tip stress intensity factor results as given by

$$K_{I\,tip} = K_{I\,appl} + K_{I\,shield} \tag{8.1.1}$$

This relation is the basis for understanding R-curve influences on the lifetime behaviour.

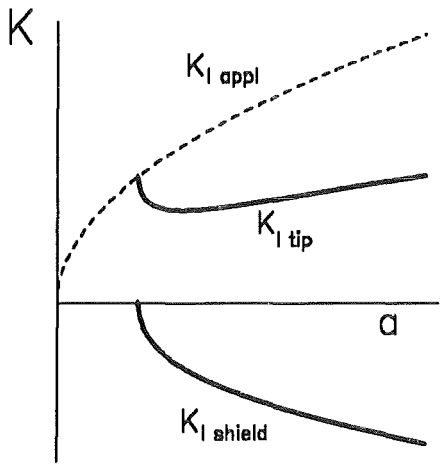

Figure 92. Development of K-values. Development of the stress intensity factors of eq.(8.1.1) in a stable crack growth test.

Whilst stable crack propagation occurs with a constant crack tip stress intensity factor, namely $K_{I\,tip} = K_{I0}$, during subcritical crack growth in a lifetime test under static load, the value of $K_{I\,tip}$ must change with $K_{I\,appl}$ and K_{shield} according to eq.(8.1.1). This behaviour is explained in fig.92.

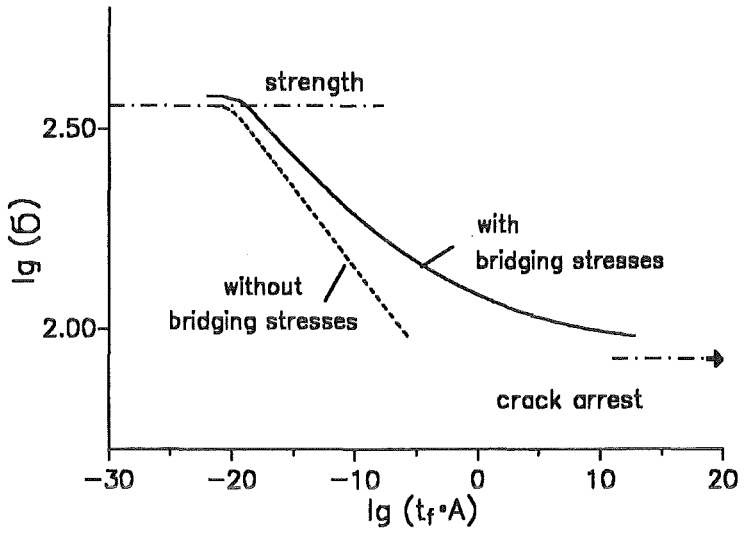

Figure 93. Lifetime. Influence of R-curve effects on lifetimes in static tests [56].

At the beginning of crack extension the crack-tip stress intensity factor decreases significantly with increasing crack length, passes a minimum value and increases again. The applied stress intensity factor $K_{I\,appl}$ (dashed curve) increases monotonically and the difference between these two curves is the shielding stress intensity factor K_{shield}.
In the presence of crack-tip shielding the lifetime t_f results for a given stress σ as

$$t_f = \int_{a_i}^{a_c} \frac{da}{v} = \frac{1}{A} \int_{a_i}^{a_c} \frac{da}{[\sigma Y \sqrt{a} + K_{shield}]^n} \tag{8.1.2}$$

In (8.1.2) a_i is that crack size where slow crack growth starts and a_c is the critical crack size. At the point of failure ($a = a_c$) the crack tip stress intensity factor $K_{I\,tip}$ reaches K_{I0} and, consequently, the subcritical crack growth rate becomes extremely high. Therefore, the integral in eq.(8.1.2) may be extended to infinity without loss of accuracy worth mentioning. Only in case of negligible crack extensions, i.e. $a_c/a_0 \simeq 1$, this approximation will fail. With this assumption made one obtains

$$t_f \simeq \frac{1}{A} \int_{a_i}^{\infty} \frac{da}{[\sigma Y \sqrt{a} + K_{shield}]^n} \tag{8.1.3}$$

The influence of R-curve effects on lifetimes has been computed in [56]. Figure 93 shows the lifetimes for a material without R-curve and a material with strong R-curve behaviour but identical initial crack size distribution and identical subcritical crack growth parameters. As shown in fig. 93, the lifetime curve including shielding effects is flatter than the curve obtained in the absence of crack-tip shielding, i.e. the apparent power law exponent n', defined by lifetimes obtained at different stress levels

$$n' = -\frac{d \log t_f}{d \log \sigma} > n \tag{8.1.4}$$

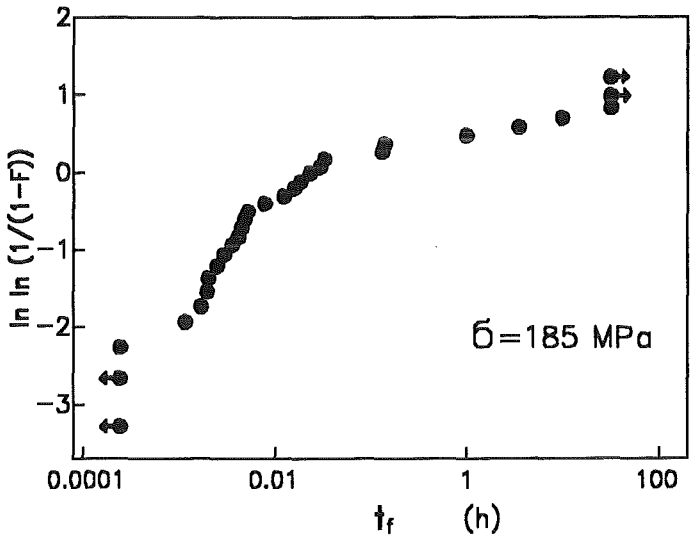

Figure 94. Weibull distribution of lifetimes. Lifetimes measured in a static bending test at 20°C in air for coarse-grained Al_2O_3.

This effect can also be shown analytically. The lifetime in the absence of a shielding effect ($K_{shield} = 0$) results as

$$t_{f(K_{shield}=0)} = \frac{1}{A}\int_{a_i}^{\infty} \frac{da}{[\sigma Y\sqrt{a}\,]^n} = const \cdot \sigma^{-n} \tag{8.1.5}$$

From eq.(8.1.3) differentiation with respect to the stress σ yields

$$\frac{d\,t_f}{d\,\sigma} = -\,n\int_{a_i}^{\infty} \frac{Y\sqrt{a}\;da}{[\sigma Y\sqrt{a} + K_{shield}]^{n+1}} \tag{8.1.6}$$

This can be written by use of the mean value theorem for integrals as

$$\frac{d\,t_f}{d\,\sigma} = -\,n\,\frac{Y\sqrt{a'}}{\sigma Y\sqrt{a'} + K'_{shield}}\,t_f \tag{8.1.7}$$

where the primes indicate a certain crack size in the range $a_i < a' < a_c(=\infty)$.
Introducing logarithmic derivatives yields

$$\frac{d\,\log(t_f)}{d\,\log(\sigma)} = -\,n\,\frac{\sigma Y\sqrt{a'}}{\sigma Y\sqrt{a'} + K'_{shield}} \tag{8.1.8}$$

From eq.(8.1.4) it results for the n-value in presence of an R-curve effect

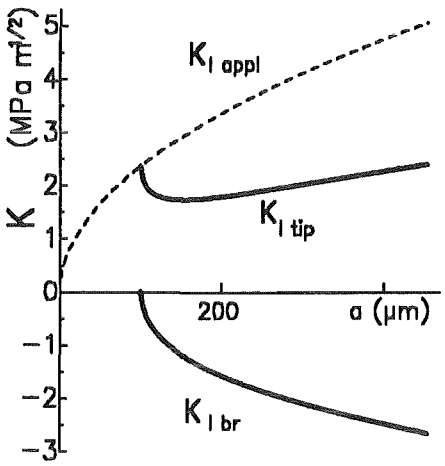

Figure 95. Stress intensity factors. Change of stress intensity factors during crack extension under constant load.

$$n' = n\frac{\sigma Y\sqrt{a'}}{\sigma Y\sqrt{a'} + K'_{shield}} > n \tag{8.1.9}$$

Finally we can conclude

$$n' > n \tag{8.1.10}$$

8.2 A detailled analysis of the influence of bridging interactions

In this section it is illustrated how the bridging interactions in coarse-grained Al_2O_3 will influence the subcritical crack growth and lifetime behaviour of specimens with natural crack populations [57]. Calculations using averaged stress intensity factors - as used for the strength in section 7.1 - show the development of surface cracks until failure. Since spontaneous failure in strength tests is affected by bridging stresses [51],[58], it must be expected that delayed failure due to subcritical crack growth will be influenced, too. This must be the case for alumina [56] [4] as well as for zirconia [9].
In a recent paper [7] lifetime results obtained under constant load have been presented for coarse-grained alumina. In a Weibull-plot a non-linear behaviour was observed which can be seen from fig. 94. As mentioned for the strength behaviour such a behaviour can be also caused, in principle, by a specific flaw population.
In coarse-grained alumina the crack growth resistance increases with increasing crack extension due to friction-like crack-border interactions in the wake of the advancing crack. As a result of these crack surface interactions, the stress intensity factor acting at the crack tip $K_{I\,tip}$ deviates from the externally applied $K_{I\,appl}$ according to eq.(8.1.1)

$$K_{I\,tip} = K_{I\,appl} + K_{Ibr} = K_{I\,appl} - |K_{Ibr}|$$

where $K_{I\,br}$ is the bridging stress intensity factor. This relation is the basis for understanding R-curve influences on lifetime behaviour. For its evaluation one needs the applied stress intensity

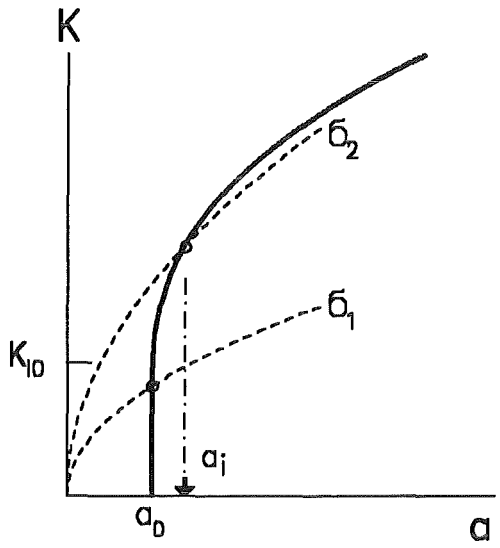

Figure 96. Initial crack size. Definition of initial crack size for a constant-load test.

factor caused by an externally applied load as well as the bridging stress intensity factor. In contrast to the strength computations the abbreviation C is now defined as

$$C = \frac{4 \cdot 1.141(1-\nu^2)K_{I\,tip}\sqrt{a_0}}{YE\pi\delta_0} \quad , \quad Y = 2/\sqrt{\pi} \tag{8.2.1}$$

The occurrence of $K_{I\,tip}$ in the quantity C makes iterative solutions necessary.

8.2.1 Crack propagation under constant load

Surface cracks in ceramic materials caused by surface grinding are commonly assumed to be semi-circular shaped. During crack extension in bending a change of the crack shape must be expected. Therefore, also bridging stress intensity factors for semi-elliptical surface cracks are necessary. In the subsequent considerations the assumption will be made that bridging stress intensity factors for surface cracks can be approximated by the bridging stress intensity factors of embedded cracks with the same aspect ratio.
For numerical computations the same material parameters were chosen as already used in 7.1. All calculations are performed for a specimen thickness W=3.5mm that has been used also in the experimental lifetime tests. The specimen width is assumed to be large so that finite width correction is neither necessary for the bridging stress intensity factor nor for the externally applied stress intensity factor.
Whilst in strength tests crack propagation occurs with a constant crack tip stress intensity factor, namely $K_{I\,tip}=K_{I0}$, the value of $K_{I\,tip}$ must change with $K_{I\,appl}$ and $K_{I\,br}$ according to eq.(8.1.1) during subcritical crack growth in a test performed under static load. This behaviour is schematically explained in fig. 92. The applied stress intensity factor $K_{I\,appl}$ (dashed curve) increases monotonically with crack extension. The bridging stress intensity factor is negative and also increases with crack extension. The sum of these two curves is the crack-tip stress intensity factor $K_{I\,tip}$, which first decreases significantly with increasing crack length, passes a minimum value and increases again.

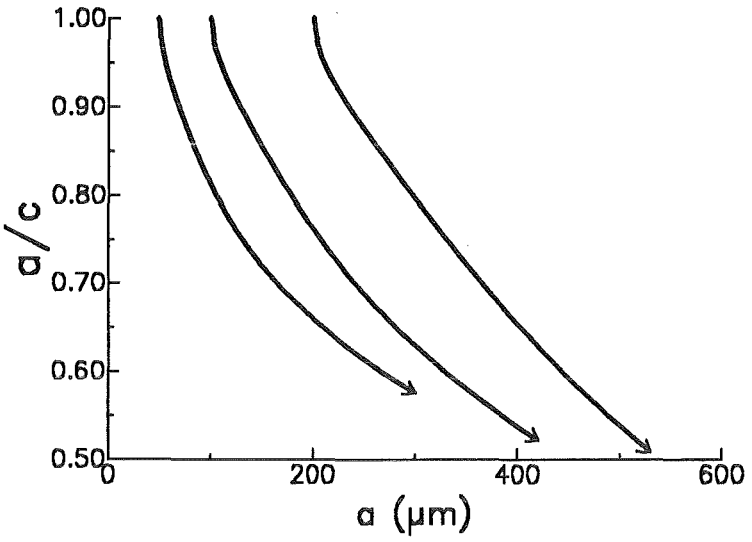

Figure 97. Crack shape. Development of the aspect ratio a/c as a function of the initial crack size a_0 ($N = 30$).

Unfortunately, subcritical crack growth does not start in all cases at the initial crack size. This has to be considered especially for relatively high loads applied. Figure 96 illustrates the problem.

- In case of a low applied stress σ_1 it holds

$$K_{I\,appl,A}\,,\,K_{I\,appl,B} < K_{I0}$$

and, consequently, the crack can propagate only by subcritical crack growth, starting from a_0, c_0.

- In case of a higher stress, $\sigma_2 > \sigma_1$, the crack will extend at the moment of load application up to a crack of dimensions $a' \geq a_0$, $c' \geq c_0$ which are given by the solution of the equations

$$\begin{aligned} \sigma_b Y_A(a'/c',a'/W)\sqrt{a'} - K_{I\,br,A}\Big|_{\Delta a = a' - a_0} &= K_{I0} \\ \sigma_b Y_B(a'/c',a'/W)\sqrt{a'} - K_{I\,br,B}\Big|_{\Delta c = c' - c_0} &= K_{I0} \end{aligned} \qquad (8.2.2)$$

In this case in eq.(8.2.1) the crack-tip stress intensity factor $K_{I\,tip}$ must be K_{I0}.

The crack-growth relation describing subcritical crack growth is assumed to be a power law

$$v = \frac{da}{dt} = \begin{cases} 0 & for \quad K_{I\,tip} < K_{Ith} \\ A(K_{I\,tip})^N & for \quad K_{Ith} < K_{I\,tip} < K_{I0} \\ \rightarrow \infty & for \quad K_{I\,tip} \geq K_{I0} \end{cases} \qquad (8.2.3)$$

where K_{Ith} is the threshold stress intensity factor below which subcritical crack growth does not occur. From theoretical considerations a threshold stress intensity factor for thermally activated bond breaking must occur [59] [60].

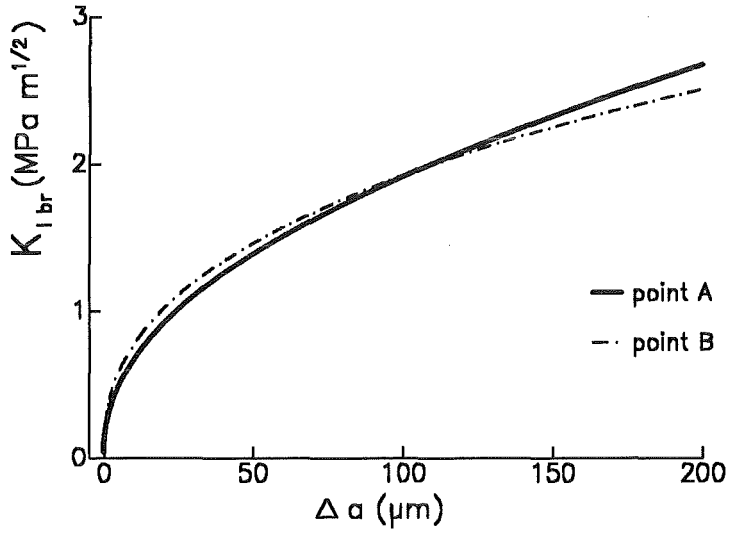

Figure 98. Crack resistance curve. R-curves for the two points A,B computed with $a_0 = 200\mu m$, $\sigma_{bend} = 185MPa$, $N = 30$.

Numerical procedure

Some details of the numerical evaluation of a static lifetime test will subsequently be explained for the special case of $K_{Ith} = 0$. Immediately after load application the crack may have the dimensions a_0, $c_0 = a_0$ (case $\sigma = \sigma_1$ in fig. 96).

Step 1: The stress intensity factors for this situation are

$$K_{I\,appl\,A,B,0} \quad , \quad K_{I\,br\,A,B,0} = 0 \quad , \quad K_{I\,tip\,A,B,0} = K_{I\,appl\,A,B,0}$$

A crack size increment $da = \lambda a_0$, $\lambda \ll 1$ is chosen. The related crack increment dc_0 results from eq.(8.2.3) as

$$dc_0 = (K_{I\,tip\,B,0}/K_{I\,tip\,A,0})^N\, da \tag{8.2.4}$$

and the time increment needed for the crack extension da is

$$dt_0 = \frac{da}{A\, K^N_{I\,tipA,0}}$$

and the new crack dimensions are $a_1 = a_0 + da$; $c_1 = c_0 + dc_0$.

Step 2: The stress intensity factors for the extended crack are

$$K_{I\,appl\,A,B,1} \quad , \quad K_{I\,br\,A,B,1} = f(K_{I\,tip}) \quad , \quad K_{I\,tip\,A,B,1} = K_{I\,appl\,A,B,1} - K_{I\,br\,A,B,1}$$

The next crack increments are

$$da \, , \quad dc_1 = (K_{I\,tip\,B,1}/K_{I\,tip\,A,1})^N\, da$$

and the time increment becomes

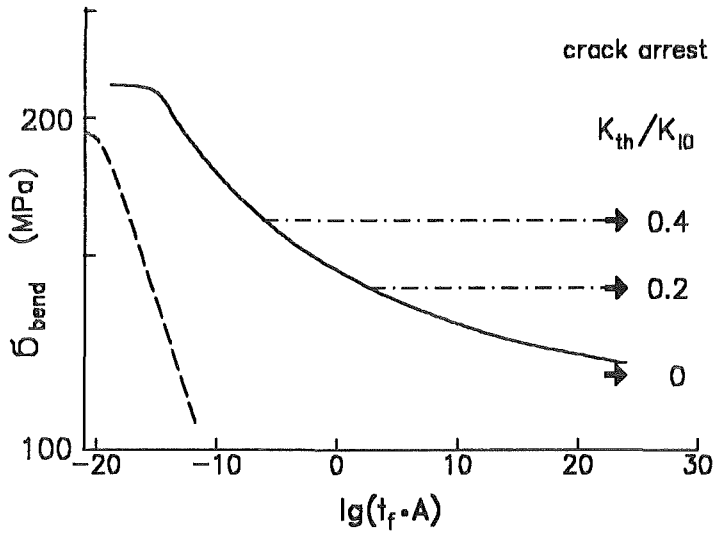

Figure 99. Lifetimes in static tests. Lifetimes in a normalised representation for $N=30$, calculated for a crack of initial size $a_0=200\mu m$; solid curve: with R-curve behaviour, dashed curve: without R-curve effect.

$$dt_1 = \frac{da}{A\, K^N_{I\,tip\,A,1}} \quad , \quad t_1 = t_0 + dt_1$$

It should be noted that $K_{I\,br}$ depends on the crack-tip stress intensity factor $K_{I\,tip}$. There are several possibilities to determine $K_{I\,br}$ and $K_{I\,tip}$. The simplest ones are:

- Replacing the unknown value $K_{I\,tip}$ in eq.(8.2.1) by the value obtained in the preceding step, i.e.

$$K_{I\,br\,A,B,n} = f(K_{I\,tip\,A,B,n-1})$$

  This is recommended above all for very small values of λ.
- The stress intensity factors $K_{I\,br}$, $K_{I\,tip}$ can be obtained from the solution of the implicit equation

$$K_{I\,appl} - K_{I\,tip} - K_{I\,br}(K_{I\,tip}) = 0$$

  which can be found for each step by a zero-routine.

These steps are repeated until $K_{I\,tip}=K_{I0}$ and $dK_{I\,tip}>0$ is fulfilled. The lifetime is given as the sum of all time increments.
In case of $\sigma = \sigma_2$ the initially stable crack development is described by the equations (8.2.2). This system of equations yields the crack dimensions a,c from which subcritical crack growth starts. The further computation is identical with that for $\sigma = \sigma_1$.

Numerical results

In fig.97 the development of the crack shape during a static bending test with 185MPa bending stress is shown for initial crack sizes of $a_0=50$, 100 and $200\mu m$. The principal shape of the curves is identical with that of stable crack extension occurring in bending strength tests. The related R-curves are shown in fig.98 for the crack with $a_0=200\mu m$. The R-curve for point A is plotted as a solid line and the R-curve for the surface point B as a dashed line. Both curves are nearly identi-

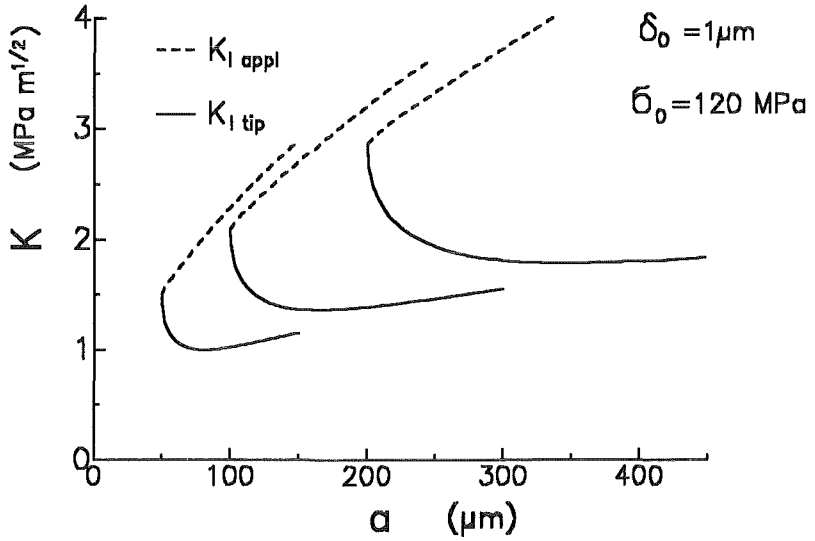

Figure 100. Initial crack size. Influence of the initial crack size a_0 on the applied and crack-tip stress intensity factors.

cal. Figure 99 represents the lifetime t_f as a function of the externally applied bending stress σ_{bend} for a crack of $a_0 = 200\mu m$ and a subcritical crack growth-exponent $N = 30$. Whilst for a material without an R-curve effect a straight line with slope $-1/N$ has to be expected (dashed line) the curve (solid line) deviates from a straight line in case of an R-curve effect due to bridging stresses and the steepness of the curve is significantly lower. This is in agreement with earlier results obtained by the author [18], [4]. The existence of a threshold stress intensity factor $K_{I\,th}$ affects the limit stress value below which crack arrest occurs. The development of the crack-tip stress intensity factor $K_{I\,tip}$ is illustrated in fig.100 for several initial crack sizes. For lifetimes especially the regions around the minimum values of $K_{I\,tip}$ (named $K_{I\,tip,min}$) are of at most importance since crack extension here takes the main part of the whole lifetime. The interdependency of minimum crack-tip stress intensity factor and initial crack size is plotted in fig.101. If a threshold stress intensity factor $K_{I\,th} > 0$ exists, all lifetime tests with $K_{I\,tip,min} \leq K_{I\,th}$ will result in an infinite lifetime since crack arrest must occur.

Finally, the distribution of the lifetimes is shown in fig.102 for the crack size distribution described by eq.(7.1.17) and different $K_{I\,th}$-values selected. Figure 102 represents the results for $N = 20$ and fig.103 for $N = 30$. The solid lines, which describe the lifetime behaviour in the absence of a threshold stress intensity factor, have the same shape as the fitted strength curve in [51]. The influence of a threshold value $K_{I\,th}$ leads to a stronger non-linearity of the lifetime distribution. A sufficient description of the measured lifetime by the calculations can be found for

$$N = 20 \;,\; K_{I\,th}/K_{I0} = 0.5 \;,\; lgA = -10.8 \;\; (A \; in: MPa,s,m) \qquad (8.2.5)$$

With these data the computed lifetime distribution is plotted in fig.104 together with the measured data of fig.93. The only deviation worth mentioning is that the threshold effect does not begin as abruptly as calculated. Also this effect can be understood from the $v - K$ –behaviour plotted in fig.105. The solid lines represent eq.(8.2.3). It can be shown theoretically [59] [60] that the threshold effect is asymptotically reached and the transition from $v > 0$ to $v \to 0$ is smoother than given by eq.(8.2.3). This more realistic behaviour is illustrated by the dashed curve. Having this in mind, the deviations in fig.104 are self-explanatory.

The bridging parameters and the parameters of subcritical crack extension are compared in Table 1 (at the end of this section) with parameters obtained from static tests with specimens containing macrocracks. The bridging stresses obtained from the tests with macrocracks are lower

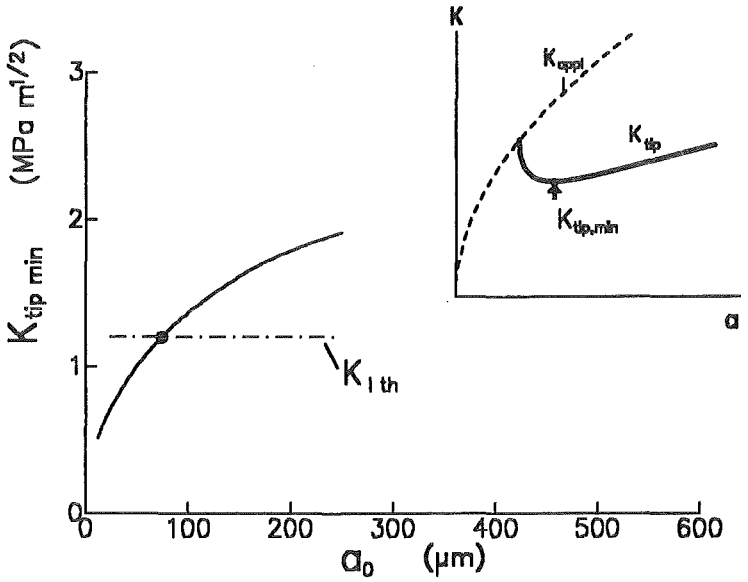

Figure 101. Minimum stress intensity factor. Minimum crack-tip stress intensity factors during crack extension in a constant load test ($\sigma = 185$MPa), (crack arrest situation for $K_{I\,th} = 0.4K_{I0}$ indicated by solid circle).

than those obtained in the tests with microcracks. The parameter N is similar; however, the parameter A is considerably lower for the macrocracks.
In fig.106 the v-K_I-curve obtained from macro-crack measurements [18] is plotted as a dashed line together with the micro-crack relation proposed in this investigation (solid curve). The subcritical crack growth rates for the micro-cracks are significantly lower than the crack velocities obtained with macro-cracks.

8.2.2 Discussion

The evaluation of the lifetime results shows that it is possible to explain the non-linear Weibull-plot by the R-curve effect. The curve in fig.104 of the lifetime distribution and in fig.106 of the $da/dt - K_I$ —relation have been obtained from the bridging stress parameters σ_0 and δ_0 evaluated from the strength distribution. The freely selected parameters are N, A and K_{I0}.
The large discrepancy in the crack-growth rate between micro-cracks and macro-cracks can be reduced if lower values of σ_0 are applied. From fig.107 it can be seen that a reduction in σ_0 from 120 MPa to 100 MPa still leads to a reasonably good description of scatter in lifetime. The corresponding threshold value is 1.75 MPa$\sqrt{m}$. The corresponding growth-rate parameters are $N = 20$, $lgA = -12.8$ leading to a better agreement with the macro-crack behaviour as can be seen from fig.108. However, the crack growth rate is still higher. Therefore, under the assumption made it continues to apply that the bridging stresses for micro-cracks are larger than for macro-cracks and that the crack-growth rate for the same crack-tip stress intensity factor $K_{I\,tip}$ is higher for the micro-cracks. A further decrease in σ_0 for the micro-cracks would yield a lifetime distribution not agreeing with the experimental results.
It cannot be excluded that the assumptions made influence the result. These assumptions are: Weibull distribution without R-curve effects, application of averaged instead of local stress intensity factors, approximation of R-curves of surface cracks by R-curves of embedded cracks.

Considering all these assumptions, nevertheless the cautious conclusion may be drawn that the $da/dt - K_{I\,tip}$ relation of micro-cracks and macro-cracks deviate from each other. There may be different reasons for this effect. Generally, the linear-elastic relations are not fully correct for

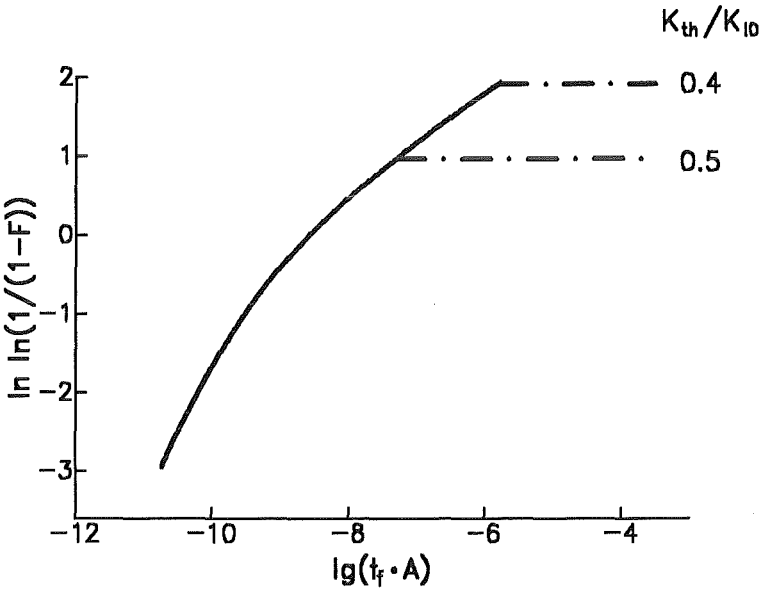

Figure 102. Weibull distribution with threshold. Weibull-distribution of lifetimes under $\sigma_{bend} = 185$MPa, computed for $N = 20$ (dash-dotted lines: influence of a threshold stress intensity factor).

small cracks as can be seen from strength tests. It is also possible that the stress intensity factor of a real flaw/crack-configuration, e.g. a pore with a circumferential crack, deviates from that of a flat crack.

Also the experimental finding of Steinbrech [115] that in stable crack-growth tests small cracks can grow under significantly lower applied stress intensity factors than necessary for macro-cracks may be valid for subcritical crack growth, too.

Test	Crack type	Ref.	N	$lg(A)$, (A in MPa,m,s)	σ_0 (MPa)	δ_0 (μm)
Static tests	micro-cracks	[57]	20	-10.8	120	1
Static tests	macro-cracks	[18]	25	-15.9	46.4	0.95

Table 2. . Comparison of subcritical crack growth with bridging parameters.

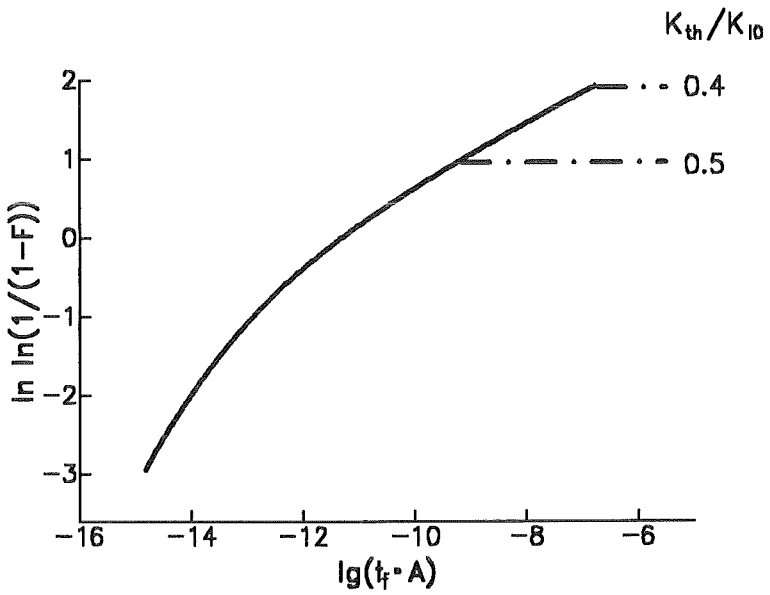

Figure 103. Weibull distribution with threshold. Weibull-distribution of lifetimes under $\sigma_{bend} = 185$MPa, computed for $N = 30$ (dash-dotted lines: influence of a threshold stress intensity factor).

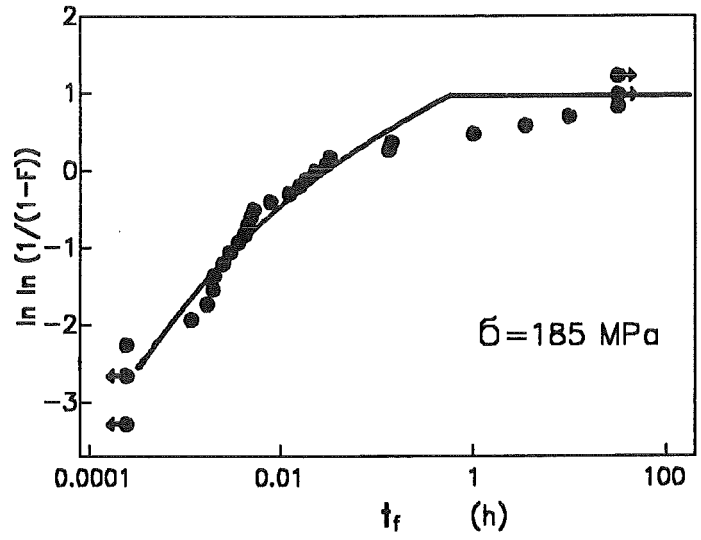

Figure 104. Lifetimes. Lifetimes in static bending tests; circles: measurements from fig.93, solid line: calculated with data set (8.2.2).

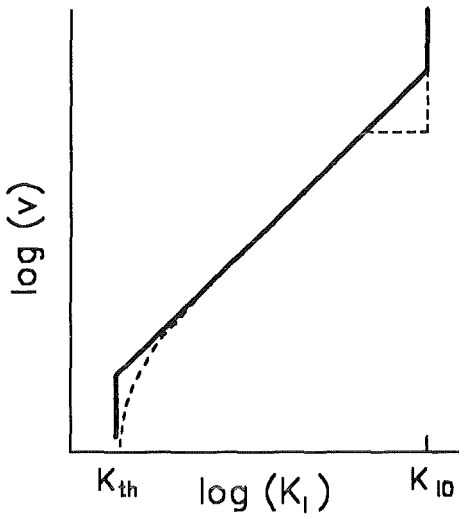

Figure 105. v-K-curve with threshold. Threshold behaviour; solid lines: eq.(8.2.3), dashed curve: realistic behaviour (stress intensity factors in terms of $K_{I\,tip}$).

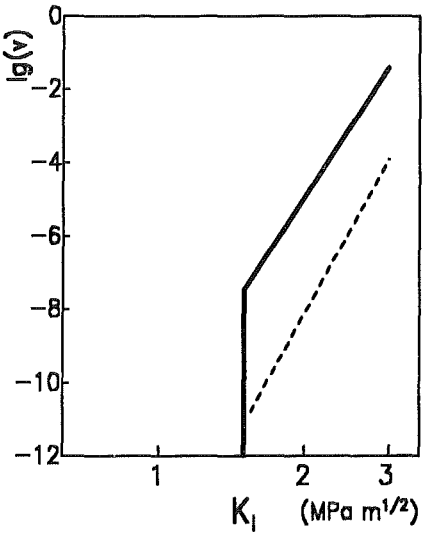

Figure 106. v-K-curve. v-K_I-curves for coarse-grained Al_2O_3; solid curve: obtained from lifetime measurements, dashed curve: macro-crack result from [18] (stress intensity factors in terms of $K_{I\,tip}$).

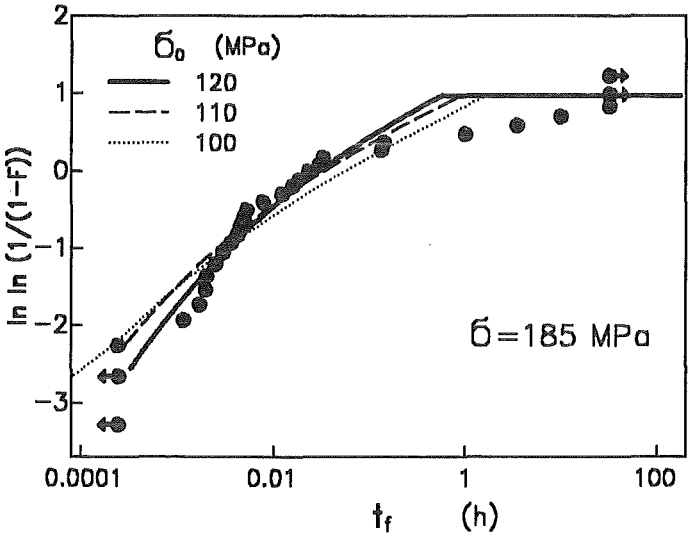

Figure 107. Lifetimes. Influence of the chosen value σ_0 on the lifetime distribution.

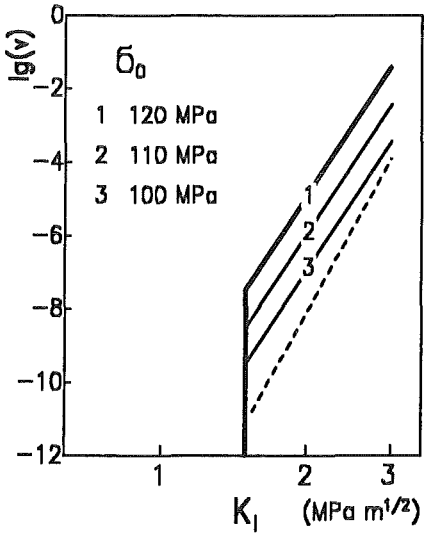

Figure 108. v-K-curve. Influence of the chosen value σ_0 on the v-K_I-curves (stress intensity factors in terms of $K_{I\,tip}$).

9. Influence of R-curve effects on cyclic fatigue

9.1 Experimental facts

Several ceramic materials show the effect of cyclic fatigue. In this section it will be shown that strong R-curve effects can be responsible for this behaviour. In order to prove an effect of cyclic fatigue in a ceramic material, three different types of test are recommended:

1. The comparison of cyclic lifetimes from experiments with predictions from static tests on the basis of K_I-governed subcritical crack growth [61].
2. A second method is the measurement of cyclic lifetimes with very different frequencies but identical upper and lower stresses and identical shape of the amplitude.
   In case of a real fatigue effect the lifetime must decrease with increasing frequency.
3. In the absence of a real cycle effect lifetimes in tests with step-shaped waves should be identical for R=0 and R=-1 and should differ only by a factor of 1/2 for R=1.

Results of tests with specimens containing natural flaws are given in fig.109 [62]. Lifetimes obtained in tests with constant stress are shown in this diagram as open circles. From a least-squares fit $n_s = 40$ was obtained according to $t_f \propto \sigma^{-n}$. The results of the cyclic tests obtained for a frequency of 50Hz and an R-ratio of $R = -1$ are given as solid circles. The slope of the dotted straight line gives an exponent of $n_c = 28$ for a power-law description of cyclic crack growth significantly lower than the value for the static tests. It is obvious that the scatter of the cyclic lifetimes is reduced compared with the static lifetimes. Based on the lifetimes in the constant load tests the cyclic lifetimes were predicted and entered in fig.109 as solid line. The predicted and measured lifetimes are significantly different.

Influence of frequency on cyclic lifetimes: From the lifetime prediction on the basis of subcritical crack growth no influence of the frequency has to be expected. In order to check such an influence cyclic tests were carried out with different frequencies. In fig.110 lifetime results are shown, obtained for a maximum stress of $\sigma_{max} = 175$MPa and frequencies of 0.2, 2, and 20Hz [63]. In addition also static tests are introduced which can be interpreted by a frequency of zero. All static tests yield survival, i.e. lifetimes of more than 200h. The lifetimes in the cyclic tests decrease with increasing frequency. Also this fact is an indication that not only subcritical crack growth may be the reason for failure in cyclic tests.

Influence of the R-ratio: Figure 111 shows cyclic lifetimes of Knoop-damaged specimens obtained with material II. The size of the Knoop-cracks could be measured under the light microscope, and the maximum initial stress intensity factor was calculated.
The tests were carried out with step-shaped pulsating and alternating loads. Since no crack growth under compressive stress intensity factors is possible one should expect identical lifetimes for the R-ratios $R = -1$ and $R = 0$. This is obviously not the case, since the lifetimes under $R = -1$ are significantly lower than under $R = 0$. Static tests should exhibit lifetimes reduced

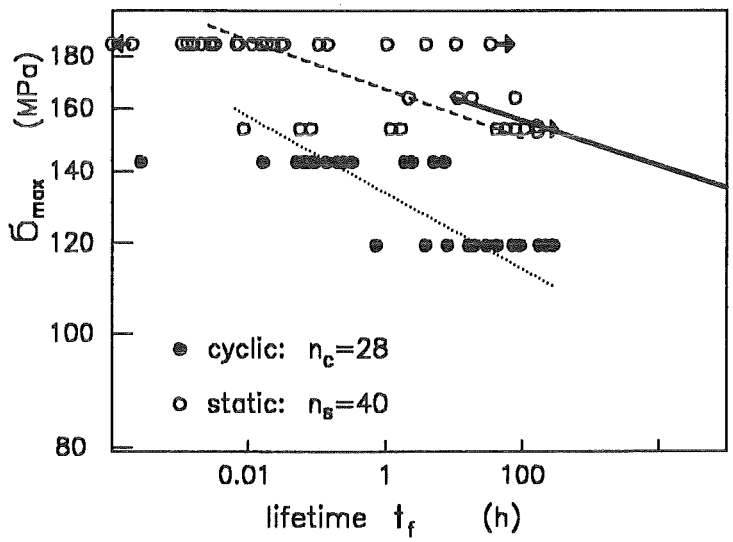

Figure 109. Lifetime measurements and lifetime predictions. Static and cyclic lifetime tests performed on specimens with natural cracks made of coarse-grained Al_2O_3 (material I); solid line: prediction of cyclic lifetimes based on static results.

by a factor of 2 compared with the cyclic ones. In contrast we find significantly higher static lifetimes. These disagreements are a further indication for a real fatigue effect.
In cyclic tests performed with small natural and artificial cracks the following main results were obtained:

1. Lifetimes in cyclic tests are significantly lower than the predictions based on static lifetime tests [64],[65]-[68].

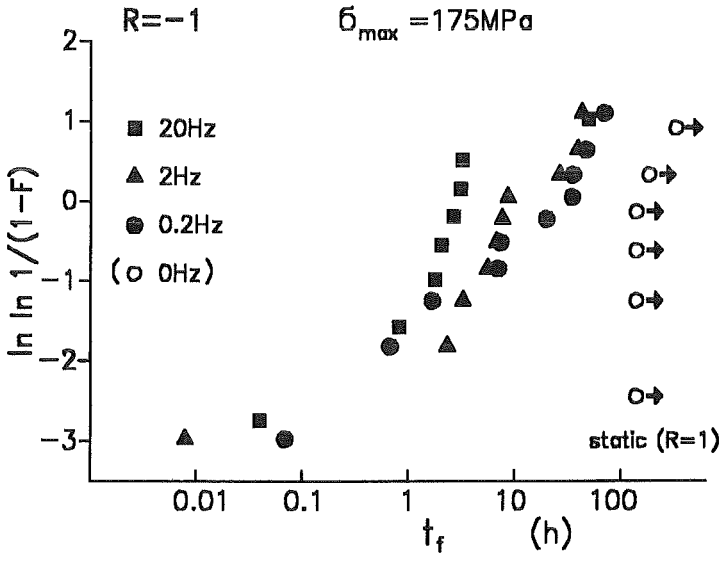

Figure 110. Influence of frequency. Lifetime measurements with specimens containing natural flaws made of material II.

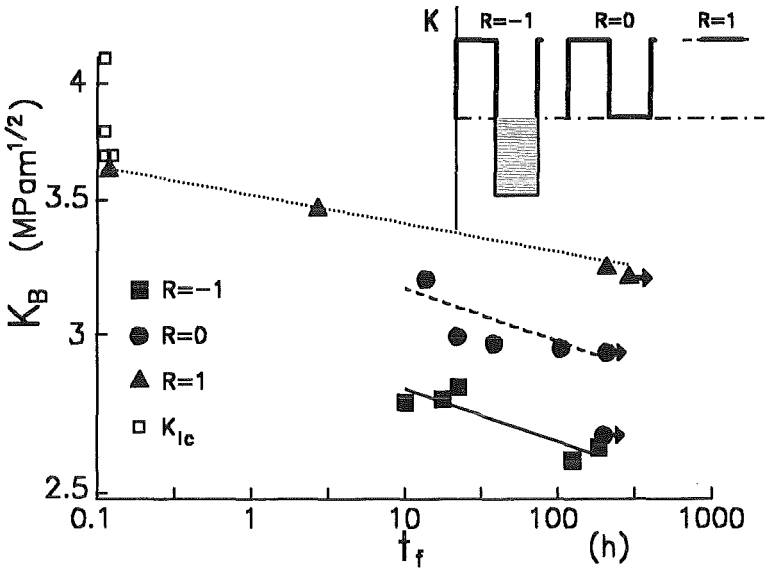

Figure 111. R-ratio. Influence of the R-ratio on the lifetime, Knoop-damaged specimens (material II); open symbols: fracture toughness.

2. In a power law description the exponents n_{cyclic} are obviously lower than the exponents n_{static} resulting in static lifetime tests [62],[64],[65],[66].
3. The scatter of cyclic lifetimes is reduced compared with the scatter in static tests.
4. The influence of cyclic loading mentioned before appears for natural cracks as well as for small artificial Knoop-cracks [64],[62].
5. Materials exhibiting a significant cycle effect also exhibit a pronounced R-curve effect [69].
6. Only a moderate influence of frequency on lifetime can be stated [63].

A model for explanation of cyclic fatigue effects in specimens with small cracks should take these findings into account.

9.2 Theoretical considerations

With the following three assumptions all experimental findings mentioned under items 1.-6. can be explained.

- The mechanisms of crack growth under cyclic load and static loading are identical.
- It is assumed that the fatique behaviour in Al_2O_3 is a direct consequence of the R-curve effect, which is caused by crack surface interactions distributed over the crack.
- These crack surface interactions are assumed to become more and more dissolved with increasing number of cycles [70],[71].

In materials with R-curve the crack tip is shielded by the shielding stress intensity factor K_{Is} and the real stress intensity factor at the crack tip $K_{I\,tip}$ deviates from the applied stress intensity factor $K_{I\,appl}$ as

$$K_{I\,tip} = K_{I\,appl} + K_{Is} \tag{9.2.1}$$

Without any detailed calculation we come to the obvious consequences:

A lifetime prediction for cyclically loaded ceramics becomes complicated in the presence of R-curve effects due to crack bridging interactions. In cyclic tests these crack interactions are assumed to become more and more reduced with increasing number of cycles [22] [23] as has been shown experimentally by in-situ microscopic examinations [22], [23]. In this case the crack tip is exposed to higher loading in cyclic tests than in static tests.
Since for small cracks in coarse-grained Al_2O_3 with $a < 100\mu m$ the maximum crack opening is small compared with δ_0 one can approximate [72]

$$\sigma_{br} \simeq \sigma_0 \tag{9.2.2}$$

In case of cyclic loading the surface interactions may be reduced by the cycles. The number of bridging events will be reduced and in terms of bridging stresses the stress parameter σ_0 will decrease. In order to be able to model the fundamental behaviour we will assume that the decrease of the maximum value of bridging stresses is proportional to the number of cycles (N) and to the actual value of σ_0 which in the integrated form reads

$$\sigma_0 = \sigma_{00} \exp(-\alpha N) \tag{9.2.3}$$

Now we will consider two limit cases.

- **Case 1:** The bridging interactions remain unaffected by the cycles, i.e. $\alpha \to 0$. This case describes also the bridging stress intensity factor for static load. The corresponding limit values for the bridging stress intensity factors results with with $Y = 2/\sqrt{\pi}$

$$K_{I\,br,1} = \frac{2\sigma_{00}}{\sqrt{\pi a}} \sqrt{a^2 - a_0^2} \tag{9.2.4}$$

- **Case 2:** Only a few cycles are necessary to dissolve the crack surface interactions newly created during crack propagation, i.e. $\alpha \to \infty$. This yields

$$K_{I\,br,2} = 0 \tag{9.2.5}$$

Lifetimes:
The influence of cycles on lifetimes becomes obvious by consideration of the limit cases, namely crack surface interactions for static tests and totally vanished crack surface interactions for cyclic tests. For the following considerations a step-shaped load-time history may be chosen

$$\sigma = \left\{ \begin{array}{ll} \sigma_0 & for \quad 0 < t < T/2 \\ -\sigma_0 & for \quad T/2 < t < T \end{array} \right\} \tag{9.2.6}$$

resulting in step-shaped stress intensity factors. Thereby the cyclic problem can be reduced to a static problem. The subcritical crack growth law is given by a power law

$$v = \frac{da}{dt} = \left\{ \begin{array}{ll} A K_{I\,tip}{}^n & for \quad K_{I\,tip} > 0 \\ 0 & else \end{array} \right\} \tag{9.2.7}$$

The lifetime t_f in a static test performed with stress σ results to be

$$t_{f\,static} = \int_{a_i}^{a_c} \frac{da}{v} = \frac{1}{A} \int_{a_i}^{a_c} \frac{da}{[\sigma Y\sqrt{a} - K_{Is}]^n} \tag{9.2.8}$$

where a_i is the initial value of the crack length a and a_c is the crack length at failure. Since the main part of the lifetime results at that state where the denominator of the integrand has its minimum value, the upper integration boundary is without much relevance for the lifetime and can be replaced for instance by infinity.

$$t_{f\,static} = \frac{1}{A} \int_{a_i}^{\infty} \frac{da}{[\sigma Y\sqrt{a} - K_{Is}]^n} \tag{9.2.9}$$

The lifetime for the cyclic limit case of a completely dissolved crack surface interactions ($K_{Is} \to 0$) then results as

$$t_{f\,cycl,\,lim} = \frac{2}{A} \int_{a_i}^{\infty} \frac{da}{[\sigma Y\sqrt{a}\,]^n} = const \cdot \sigma^{-n} \tag{9.2.10}$$

The factor 2 enters eq.(9.2.10) due to the special step-shaped loading profile.
If a time-dependend K_{Is}-value is taken into account a differential equation has to be used instead of eq.(9.2.10) Nevertheless the main result can be obtained by considering eq.(9.2.7) directly. Since K_{Is} is positive the crack growth rate is always

$$v_{static} < v_{cyclic} \quad ,i.e. \quad A(K_{I\,appl} - K_{Is})^n < AK_{I\,appl}^n \tag{9.2.11}$$

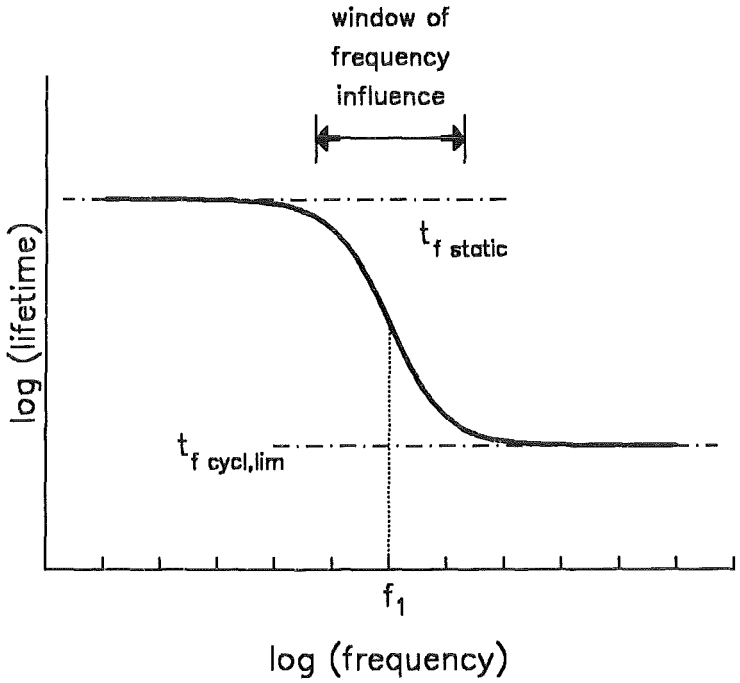

Figure 112. Cyclic lifetimes. Change of lifetime in cyclic tests with frequency (schematically)

and therefore the lifetime in a cyclic test must be lower than predicted from static tests. Due to the high exponents n this effect can become very strong.

n-values:
The n-values of a power law for crack growth can be derived by

$$n = -\frac{d \log t_f}{d \log \sigma} \tag{9.2.12}$$

Especially for the cyclic limit case it results that in this case the n-value becomes trivially identical with the exponent for subcritical crack growth used in eq.(9.2.7). On the other hand the n-value resulting from lifetime measurements in static tests must deviate from the "true value" ($n_{static} > n$) as shown in [4],[56].
From eq.(9.2.9) differentiation with respect to the stress σ yields

$$\frac{d t_f}{d \sigma} = -n \int_{a_i}^{\infty} \frac{Y\sqrt{a}\, da}{[\sigma Y\sqrt{a} - K_{Is}]^{n+1}} \tag{9.2.13}$$

This can be written by use of the mean value theorem for integrals as

$$\frac{d t_f}{d \sigma} = -n \frac{Y\sqrt{a'}}{\sigma Y\sqrt{a'} - K_{Is}'} t_f \tag{9.2.14}$$

where the primes indicate a certain crack size in the range $a_i < a' < a_c (= \infty)$.
Introducing logarithmic derivatives yields

$$\frac{d \log(t_f)}{d \log(\sigma)} = -n \frac{\sigma Y\sqrt{a'}}{\sigma Y\sqrt{a'} - K_{Is}'} \tag{9.2.15}$$

From eq.(9.2.12) it results for the static tests

$$n_{static} = -n \frac{\sigma Y\sqrt{a'}}{\sigma Y\sqrt{a'} - K_{Is}'} \quad n > n \tag{9.2.16}$$

Finally we can conclude

$$n_{static} > n_{cyclic} \tag{9.2.17}$$

Scatter behaviour
Let m_{σ_c} be the Weibull-modulus of the inert strength σ_c and m^* the Weibull-modulus obtained in lifetime tests then it holds

$$m^* = \frac{m_{\sigma_c}}{n-2} \tag{9.2.18}$$

For the static and cyclic lifetime tests it holds

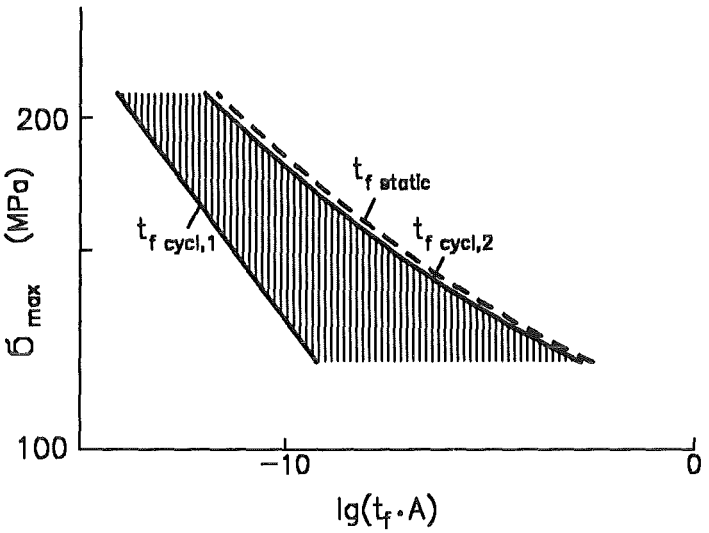

Figure 113. Lifetime prediction. Lifetime predictions for static (dashed line) and cyclic (hatched area) tests calculated with $n=20$, $\sigma_0=100$MPa and a median value of crack distribution of $a_0=100\mu$m;

$$\frac{m^*_{cyclic}}{m^*_{static}} = \frac{n_{static}-2}{n_{cyclic}-2} \tag{9.2.19}$$

As a consequence of eq.(9.2.17) it results

$$m^*_{cyclic} > m^*_{static} \tag{9.2.20}$$

i.e. the scatter of cyclic lifetimes is less than the scatter of static lifetimes.

Influence of frequency

The influence of frequency can easily be understood by a rough estimation. The span of possible lifetimes in cyclic lifetime tests is limited by

$$t_{f\,cycl,lim} \leq t_{f\,cycl} \leq t_{f\,static} \tag{9.2.21}$$

For a frequency $f \to 0$ the static lifetime (apart from the factor 2) will result and for $f \to \infty$ the crack surfaces are instantly free of interactions and the resulting lifetime will be identical with the limit case $t_{f\,cycl,lim}$. The influence of frequency on cyclic lifetime is schematically shown in fig.112. Let f_1 be that frequency where $\log t_f - \log t_{f\,cycl,lim} = 0.5(\log t_{f\,static} - \log t_{f\,cycl,lim})$. This frequency should result a significantly reduced value of K_{Is} during the lifetime test. We can conclude from eqs.(9.2.3) and (9.2.4) as a tendency:

$$K_{Is} \simeq K_{Is0} \exp(-\alpha f t) \tag{9.2.22}$$

If for the frequency f_1 the value of K_{Is} is significantly changed from K_{Is0} during the lifetime it becomes evident - at least for the exponential dependency based on eq.(9.2.3) - that the frequency $f_2 = 10f_1$ approximatively yields the limit case $K_{Is} \simeq 0$ and for $f_3 = 0.1f_1$ no change of K_{Is} due to frequency influences has to be expected ($K_{Is} \simeq K_{Is0}$). With other words: There must be a relative small "window of frequencies" where a significant decrease in lifetime (from $t_{f\,static}$ to $t_{f\,cycl,lim}$) can occure. Outside of this range of frequencies the influence of frequency on lifetime must become

moderate. From previous results we conclude that the coarse-grained 99.6%-Al_2O_3 exhibits a cyclic effect that exceeds the effect expected from subcritical crack growth in static tests. The conspicuous disagreement between predictions based on static lifetimes and the experiments as well as the influence of frequency on the number of cycles to failure are significant indications of this fact.
Figure 113 shows the median values of static lifetimes (dashed line) as predicted by using the data-set

$$n = 20 \ , \quad m = 10 \ , \quad \sigma_{00} = 100MPa \ , \quad a_0 = 100\mu m$$

and the two limit cases of cyclic fatigue (solid lines) computed with eq.(9.2.4) and (9.2.5).
The range where the real cyclic lifetimes have to be expected is hatched. As can be seen from fig.113, the n-value (i.e. the negative reciprocal slope of the curves) is lower for the limit case 2 than for the limit case 1.

10. Influence of R-curve effects on thermal shock behaviour

10.1 General remarks

During thermal shock of ceramic materials crack propagation of initial cracks leads to an increase in crack length. Therefore, the strength after thermal shock is reduced from σ_c to σ_f. This reduction in strength can be described by application of fracture mechanics methods [73]-[77]. The final crack length and thus the strength after the thermal shock depend on

- the size and geometry of the component,
- the thermal shock conditions (temperature of component, temperature of shock medium, heat transfer),
- physical properties of the material which influence the temperature and stress distribution (thermal conductivity, thermal expansion coefficient, heat capacity, density, elastic constants),
- mechanical properties of the material.

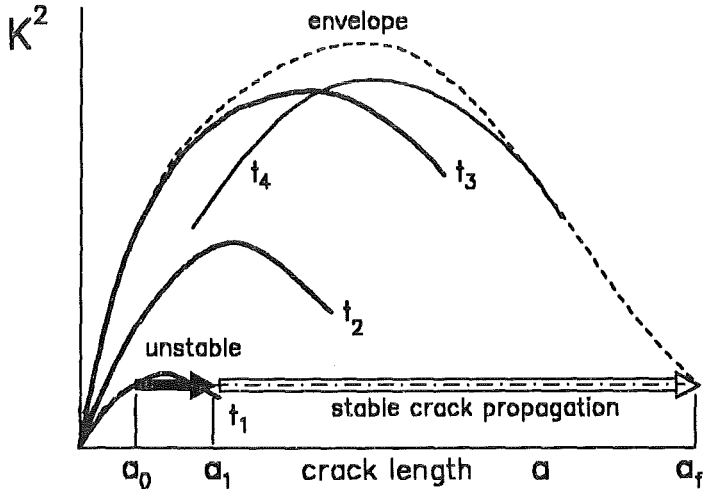

Figure 114. Crack propagation under TS-conditions. Crack propagation under thermal shock conditions for a material without R-curve behaviour; (dash-dotted curve: K_{IR}, solid curves: $K_{I\,appl}$), [78].

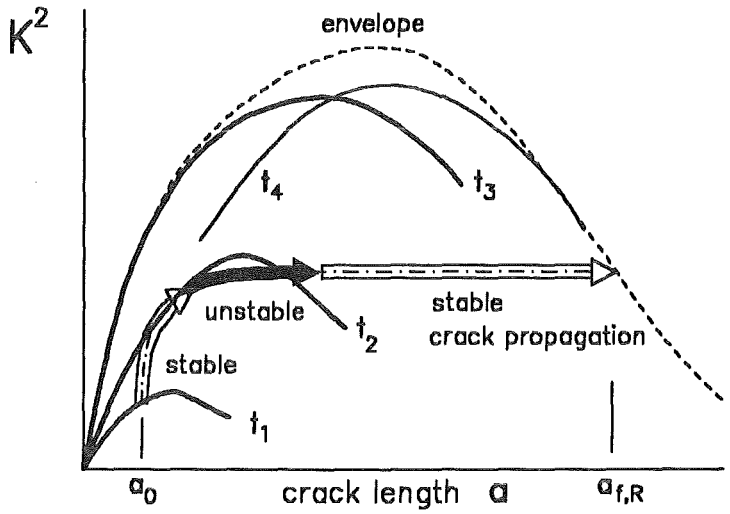

Figure 115. Crack propagation under TS-conditions. Crack propagation under thermal shock conditions for a material with a strong R-curve behaviour; (dash-dotted curve: K_{IR}, solid curves: $K_{I\,appl}$), [78].

One relevant mechanical property is the crack growth resistance. For some materials the crack growth resistance can sufficiently be characterised by the fracture toughness K_{Ic}. For materials whose crack growth resistance increases with crack extension (rising R-curve) the situation is more complicated. A first evaluation can be made under the assumption that crack growth resistance can be described by a unique curve - the relation between K_{IR} and the crack extension $\Delta a = a - a_0$. A more realistic description takes into account that the crack growth resistance curve depends on the actual loading situation and the initial crack length. This has been done in [78]. For the numerical calculations the relation

$$\sigma_{br} = \sigma_0 \exp(-\delta/\delta_0) \tag{10.1.1}$$

was used.
The crack extension during thermal shock can be described by a diagram, in which the stress intensity factor is plotted versus the relative crack length a/W, fig.114. At any time after the thermal shock gets effective, the stress intensity factor first increases with the crack length and then decreases again. All curves have an envelope which also has a maximum in $K_{I\,appl}$. First the situation will be considered of a material with a flat crack growth resistance. A crack of initial length a_0 extends in an unstable mode at time t_0 (black arrow fig.114), when the condition $K_{I\,appl} = K_{I0}$ is fulfilled for the first time. Due to dynamic effects the crack can be driven to a crack length a_1 where $K_{I\,appl}$ is below K_{I0}. Then the crack stops for a moment until $K_{I\,appl}$ reaches K_{I0} again. Afterwards, under the condition $K_{I\,appl} = K_{I0}$, the crack extends in a stable mode (open arrow) until its **final length $a = a_f$, when the** envelope of $K_{I\,appl}$ is reached.
For a rising crack growth resistance curve (see fig.115) the crack follows the points of intersection between the time-dependent stress intensity factors applied, $K_{I\,appl}(a,t)$ and the K_{IR}-curve. Depending on the initial crack length a_0, the shape of the K_{IR}-curve and $K_{I\,appl}(a,t)$, stable crack extension may take place until complete crack arrest or it first may be stable, then unstable and then stable again, as shown in fig.115. A comparison of fig.114 with fig.115 shows that the final crack length a_f is reduced due to the rising crack growth resistance.

10.2 Experimental results

10.2.1 Experimental and theoretical K_{IR}-curves for thermal shock

Schneider et al. [79],[80],[81] measured crack extensions in Al_2O_3 disks under thermal shock loading conditions. The disks were heated in the central part by halogen lamps where the voltage of the lamps increased linearly with time. The details of the experimental set-up are given in [79].

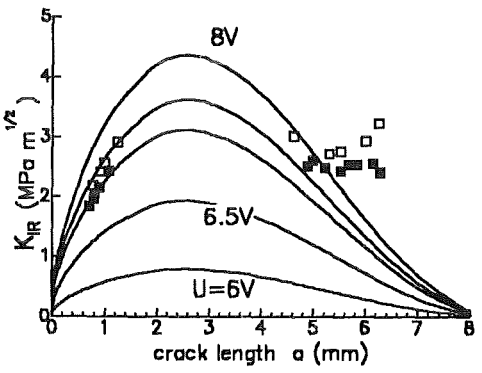

Figure 116. Measured R-curve. Crack growth resistance in a thermal shock test (a_0=0.7mm);(curves: $K_{I\,appl}$).

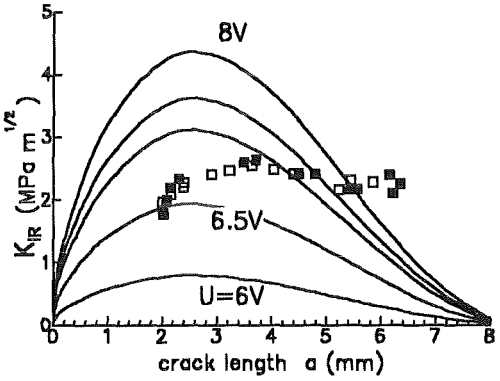

Figure 117. Measured R-curve. Crack growth resistance in a thermal shock test (a_0=1.75mm);(curves: $K_{I\,appl}$).

The applied stress intensity factor as a function of time and the crack length, $K_{I\,appl}\,(a,t)$, has been calculated from the corresponding stress distribution. The results have been plotted in fig.116 and fig.117, where instead of the time the voltage of the lamps is entered as a parameter. The $K_{IR}(a)$ –curve (squares) is obtained from $K_{I\,appl}(a,t)$ and the relation $t(a)$ taken from the experiment:

$$K_{IR}(a) = K_{I\,appl}[a,\, t(a)] \tag{10.2.1}$$

It can be seen that for a large initial crack length the crack extension is stable, whereas for small initial crack length the extension is first stable, then unstable and then stable again. The crack growth resistance curve of the material applied obtained in a three-point bending test with a crack of initial length a_0/W=0.5, is shown in fig.158. From these results σ_0=44 MPa, δ_0=0.25 μm, K_{I0}=2.5 MPa$\sqrt{\text{m}}$ was obtained. In addition to the experimental thermal shock $K_{IR}(a)$ –curve a theoretical $K_{IR}(a)$ –curve can be obtained by inserting a theoretical $t(a)$ in eq.(10.2.1). A theoretical $t(a)$ is given by

$$K_{I\,tip}(a,t) = K_{I0} \tag{10.2.2}$$

The results of $K_{I\,tip}$ in fig.118 and fig.119 were calculated by means of the boundary element program ATHENE [82] as an alternative procedure to the weight function method ([78]). It can be seen in fig.118 and fig.119 that in agreement with the experimental results complete stable crack

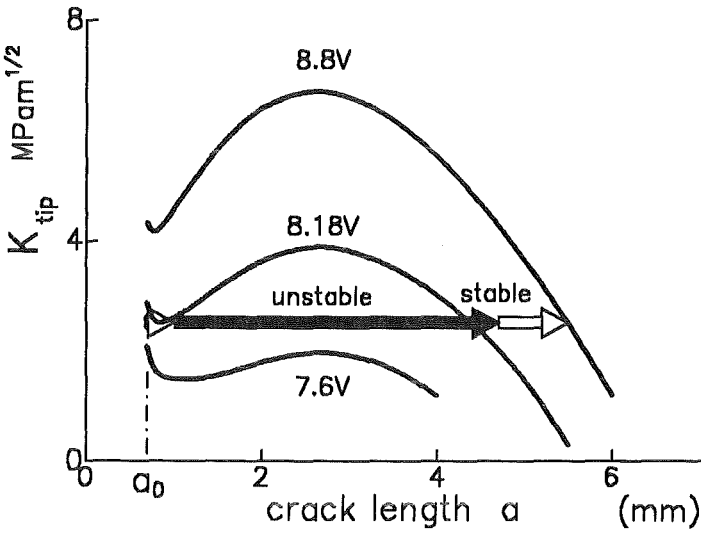

Figure 118. Crack-tip stress intensity factor. $K_{I\,tip}$ during a TS-test ($a_0 = 0.7$mm) [78].

extension is predicted for the longer initial crack length and stable-unstable-stable extension for the small initial crack length. In fig.120 a comparison is shown between the measured and the predicted K_{IR}-curves. This figure also shows the K_{IR}-curve for the bending tests from which the bridging parameters were obtained.
Comparing this curve with that predicted for the thermal shock test the effect of specimen geometry and type of loading can be seen again. Comparison of the predicted with the measured curves makes evident that for both initial crack lengths the trend of the curves (increase - maximum - decrease) is predicted; however, the predicted increase is larger than the measured one. This difference might be caused by a temperature effect. The prediction (see fig.120) was performed with the bridging parameters obtained from a room temperature test, whereas the ther-

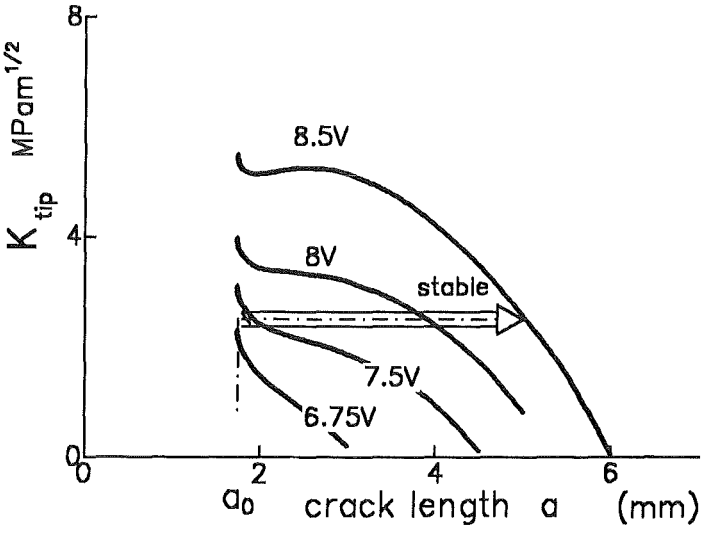

Figure 119. Crack-tip stress intensity factor. $K_{I\,tip}$ during a TS-test ($a_0 = 1.75$mm) [78].

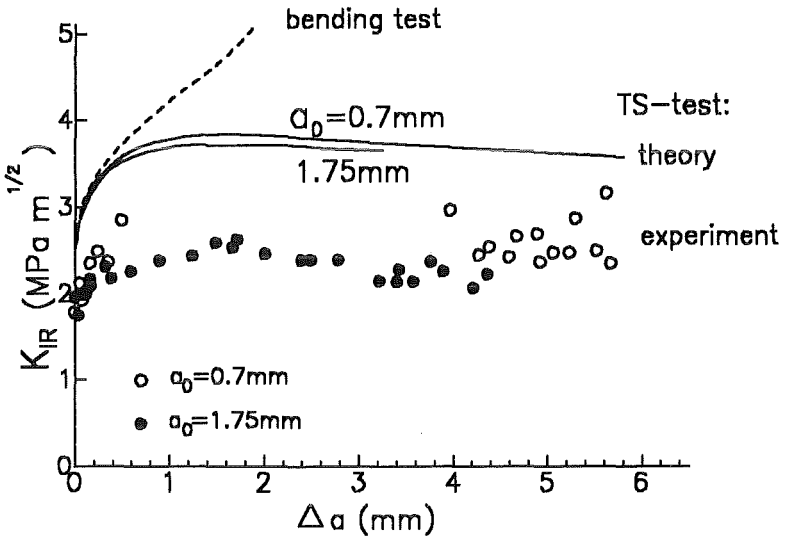

Figure 120. Comparison of R-curves. K_{IR}-curve from controlled bending test compared with predicted K_{IR}-curves for thermal shock tests with different initial crack sizes; TS-curves predicted with bridging parameters σ_0 and δ_0 obtained at room temperature [78].

mal shock crack extension started at about 350°C with a further increase in temperature during crack extension. From the results of Mundry [95], shown in fig.159, a temperature effect of the K_{IR}-curves is obvious. The parameters σ_0 and K_{I0} evaluated from these tests are presented in fig.121. The parameter δ_0 is independent of the temperature.
Figure 122 contains the prediction based on the temperature depending parameters shown in fig.121. For this analysis with temperature dependent material data the K_{I0}-values of fig.121 (solid line) were used. Since no temperature dependent bridging stress parameter σ_0 was available, it has been assumed that its relative change with temperature would be identical with that of material (5) (Table 3) plotted in fig.121.
The theoretical results of fig.122 are in better agreement with the experiments than the results obtained with temperature independent material parameters (fig.120).

10.2.2 Conclusions

The increase of crack growth resistance with increasing crack length caused by bridging interactions at the crack surface depends on the loading conditions as well as on the crack- and specimen geometry. Due to this fact the developed methods to determine the material specific bridging parameters are of high importance.
The investigation of the bridging stresses on the crack propagation under thermal shock conditions shows that the crack development for small crack extensions always proceeds stably. In **case of short initial cracks** the initial stable phase is followed by an instable crack extension phase in the range of intermediate crack lengths which again changes to stable crack propagation for large crack lengths.
The comparison between theoretically predicted and experimentally obtained TS-K_{IR}-curves shows that for coarse-grained Al_2O_3-material the bridging stresses are dependent on temperature. One reason for this effect may be the temperature dependent residual stresses caused by the anisotropy of the Al_2O_3-grains.

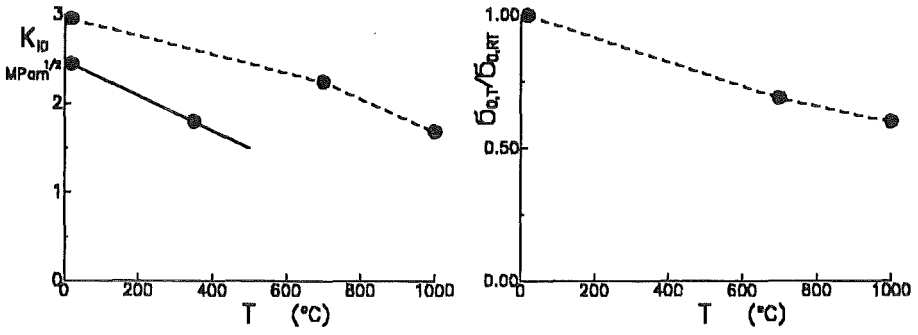

Figure 121. Temperature dependency of R-curve parameters. Results taken from [78]; left figure: Temperature dependence of K_{I0}; dashed line: material (5) (Table 3) evaluated from K_{IR}-curves of fig.159, solid line: results for material (4) taken from measured values in figs.5 and 10. figs.158, 118 and 119 right figure: Temperature dependence of σ_0; material (5) (Table 3) evaluated from K_{IR}-curves of fig.159.

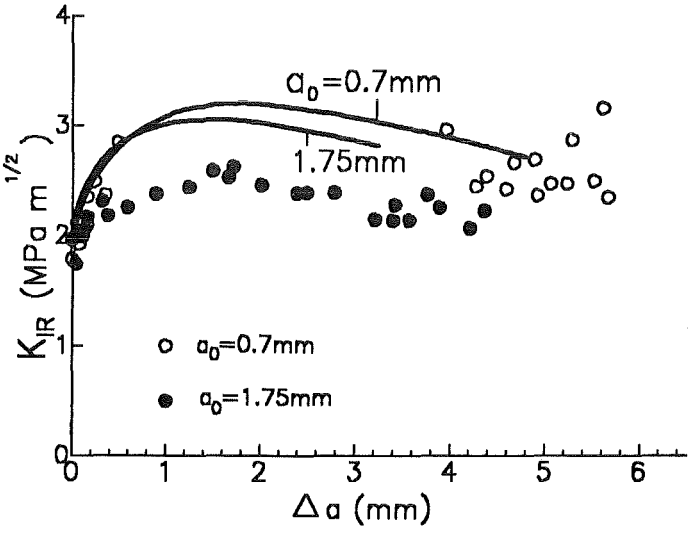

Figure 122. Experimental and theoretical R-curves. Comparison of experimental and theoretical TS-K_{IR}-curves predicted for temperature depending bridging parameters with an identically assumed relative decrease of σ_0 according to the data represented in fig.121.

11. Influence of bridging stresses on Knoop-cracks

Knoop-indentation tests are often performed in order to determine the fracture toughness of ceramic materials. In a number of ceramics the R-curve behaviour affects the development of indentation cracks.

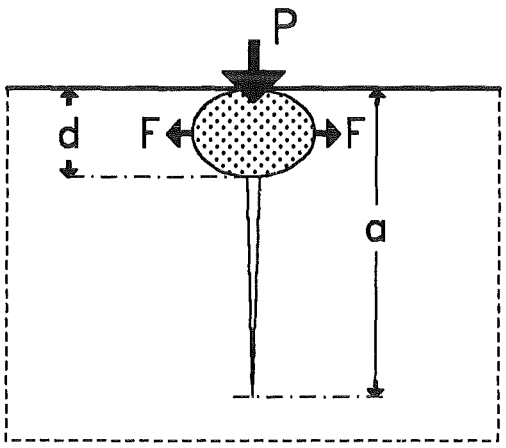

Figure 123. Knoop-indentation. Loading situation during the generation of a Knoop indentation crack.

The cracks generated during Knoop indentation tests (fig.123). are nearly half-penny shaped. In order to allow a simple analysis to be made, the influence of the free surface is neglected and the crack is modelled as one half of a circular embedded crack (fig.124). During the indentation test the Knoop indenter causes wedging stresses σ_w, which are assumed to be constant over a circle with the radius d. Figure 124 illustrates the geometric data and the stresses. For a circular crack, loaded by a stress $\sigma(r)$, the related stress intensity factor is generally given by

$$K_I = \frac{2}{\sqrt{\pi a}} \int_0^a \frac{r\,\sigma(r)\,dr}{\sqrt{a^2 - r^2}} \qquad (11.0.1)$$

The stress intensity factor caused by the wedging stresses σ_w results from eq.(11.0.1) as

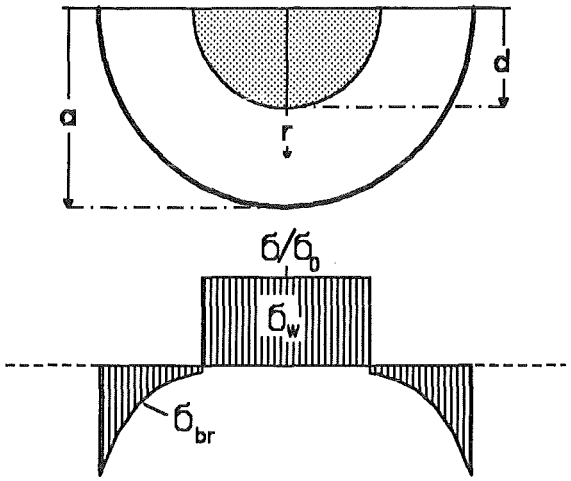

Figure 124. Stresses. Wedging and bridging stresses for a Knoop indentation crack.

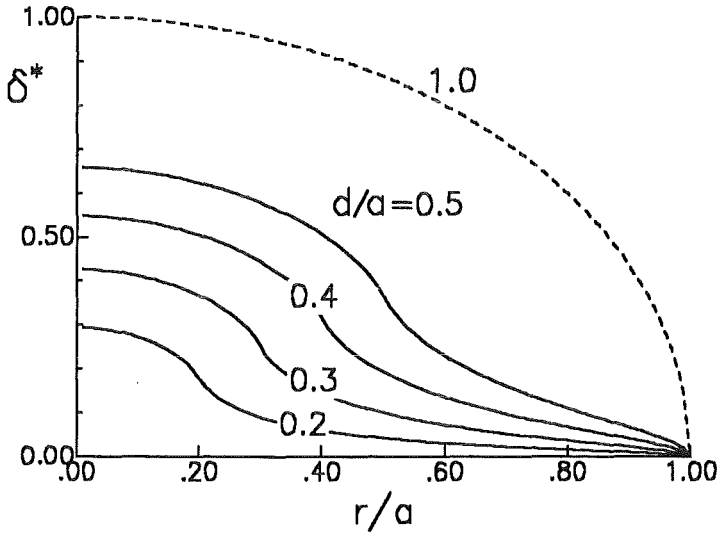

Figure 125. Displacements. COD-field caused by the wedging stresses σ_w for differently chosen wedging areas (d/a = 0.2/0.3/0.4/0.5/1.0).

$$K_{I\,w} = \frac{2}{\sqrt{\pi}}\,\sigma_w \sqrt{a}\left(1 - \sqrt{1 - d^2/a^2}\right) \tag{11.0.2}$$

The crack-opening displacements (COD) for a penny-shaped crack loaded by a stress exclusively dependent on the distance r from the origin can be computed using an integral equation given by Sneddon [83]

$$\delta(r) = \frac{4(1-\nu^2)}{\pi E}\, a \int_{\rho}^{1} \frac{1}{\sqrt{x^2-\rho^2}} \left[\int_{0}^{x} \frac{\rho\, \sigma\, d\rho}{\sqrt{x^2-\rho^2}} \right] dx \quad ; \quad \rho = r/a \tag{11.0.3}$$

where x is a dimensionless integration variable.
The total CODs are superimposed by a part δ_w due to by the wedging stresses and a part δ_{br} due to the bridging stresses

$$\delta_{total} = \delta_w + \delta_{br} \tag{11.0.4}$$

The crack surface displacements due to the constant stresses σ_w are given by [84]

$$\delta_w = \frac{4(1-\nu^2)\, a\, \sigma_w}{\pi E} \cdot f(r/a, a/d) \tag{11.0.5}$$

where $E =$ Young's modulus, $\nu =$ Poisson ratio, and

$$f\left(\frac{r}{a}, \frac{d}{a}\right) = \sqrt{1-(r/a)^2}\left(1-\sqrt{1-(d/a)^2}\right)$$

$$\text{for } r < d \tag{11.0.6}$$

$$+\frac{d}{a}\left[\mathbf{E}(r/d) - E(\arcsin d/a,\, r/d)\right]$$

and

$$f\left(\frac{r}{a}, \frac{d}{a}\right) = \sqrt{1-(r/a)^2}\left(1-\sqrt{1-(d/a)^2}\right)$$

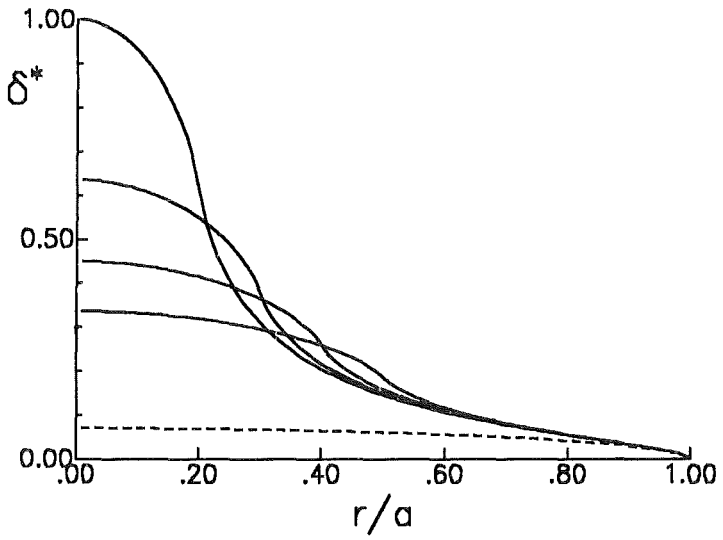

Figure 126. Displacements. COD-field caused by the wedging stresses σ_w for identical stress intensity factors K_{Iw}.

$$+\frac{r}{a}\left[\mathbf{E}(d/r) - E(\arcsin r/a, d/r) - (1 - d^2/r^2)(\mathbf{K}(d/r) - F(\arcsin r/a, d/r))\right] \quad \text{for} \quad r > d \quad (11.0.7)$$

In eqs.(11.0.6) and (11.0.7) F and E are the first and second elliptical integrals and **K** and **E** are the corresponding complete elliptical integrals.
Figure 125 shows the COD-field exclusively caused by the wedging stresses. In this representation the displacements are normalised by

$$\delta^* = \delta \frac{E\pi}{4(1-\nu^2)\, a\, \sigma_w} \quad (11.0.8)$$

In fig.125 the stress σ_w and in fig.126 the wedging stress intensity factor $K_{I\,w}$ were chosen to be constant. It can be seen that the crack-surface profile of the partially loaded crack deviates strongly from the elliptical profile obtained in case of a crack loaded with constant stress over the whole crack area (dashed line: $d/a = 1$). Replacing the total crack-surface displacement by the bridging stresses and use of eq.(11.0.4) yield

$$\delta_0 \ln\left(\frac{\sigma_{br}}{\sigma_0}\right) + \frac{4(1-\nu^2)}{\pi E}\, a \int_\rho^1 \frac{1}{\sqrt{x^2-\rho^2}} \left[\int_0^x \frac{\rho\, \sigma_{br}\, d\rho}{\sqrt{x^2-\rho^2}}\right] dx + \delta_w = 0 \quad (11.0.9)$$

where δ_w is given by eqs.(11.0.5) and (11.0.6), (11.0.7). The solution of this integral equation yields the distribution of the bridging stresses σ_{br} and by application of eq.(11.0.1) the bridging stress intensity factor $K_{I\,br}$ results. In order to solve eq.(11.0.9), one can apply the procedure of successive approximation, which is well known from the numerical treatment of integral equations. The estimation $\sigma_{br} \simeq \sigma_0 \exp(-\delta_w/\delta_0)$ may be used as a starting solution.
From the resulting bridging stress distribution the bridging stress intensity factor $K_{I\,br}$ results according to eq.(11.0.1) as

$$K_{I\,br} = \frac{2}{\sqrt{\pi a}} \int_0^a \frac{r\, \sigma_{br}\, dr}{\sqrt{a^2 - r^2}} \quad (11.0.10)$$

and the total stress intensity factor describing the stress state at the crack tip is

$$K_{I\,tip} = K_{I\,w} + K_{I\,br} \quad , \quad (K_{I\,br} < 0) \quad (11.0.11)$$

Under conditions of stable crack extension (as occurring during generation of a Knoop-crack) the crack-tip stress intensity factor is constant and its value is called K_{I0}

$$K_{I\,tip} = K_{I0} = const. \quad (11.0.12)$$

The total wedging force F is proportional to the indentation load P, i.e.

$$F = \alpha P \quad (11.0.13)$$

where the factor α is a function of geometrical and frictional parameters.
The size of the zone where the wedging stresses act is proportional to the indentation depth and can be expressed by the indentation load P and the hardness H of the ceramic as

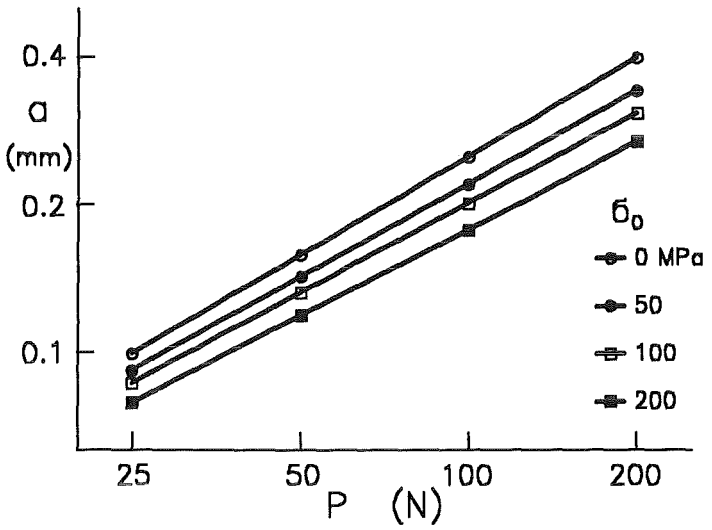

Figure 127. Crack size. Final crack size as a function of the applied indentation load ($\delta_0 = 1\mu m$).

$$d = \beta \cdot \sqrt{P/H} \tag{11.0.14}$$

Consequently the wedging stresses are independent of the indentation load P

$$\sigma_w = \frac{2F}{d^2\pi} = \gamma H \tag{11.0.15}$$

and only dependent on the hardness H of the material.
Expanding the square-root of eq.(11.0.2) into a Taylor series gives an approximation of the wedging stress intensity factor

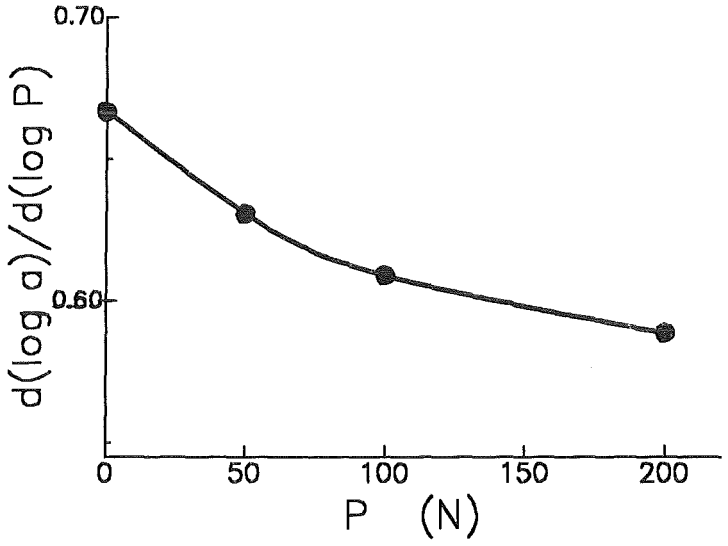

Figure 128. Crack size. Slope of the straight lines in fig.127.

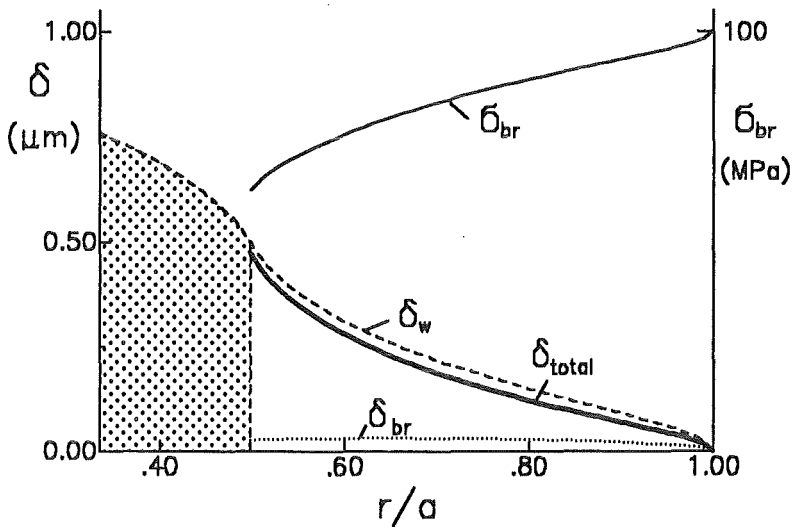

Figure 129. COD-field. Displacements and bridging stresses for a Knoop indentation crack ($a = 0.2$mm, $\delta_0 = 1\mu$m, $P = 100$N).

$$K_{I\,w} \simeq \frac{\sigma_w d^2}{\sqrt{\pi}\, a^{3/2}} = \frac{2}{\pi^{3/2}} \frac{F}{a^{3/2}} \quad \text{for} \quad (d/a)^2 \ll 1 \tag{11.0.16}$$

that is identical with the stress intensity factor for a penny-shaped crack opened by a central pair of forces. Numerical calculations were performed with the parameters:

$$E = 3.6 \cdot 10^5 \text{ MPa}, \quad \nu = 0.2, \quad K_{I0} = 3 \text{ MPa}\sqrt{\text{m}}$$

The wedge size d was chosen as the short diagonal of the Knoop impression [85], [86]. The reference dimensions for Knoop-cracks in Al_2O_3 were taken from [88], [87] as $a \simeq 250\mu$m for $P = 100$N. The bridging parameters σ_0, δ_0 were varied. The computations were carried out for the case that the heavily damaged zone $0 < r < d$ will not transfer cohesive bridging stresses. The results are shown in in fig.127 where the final crack size is plotted as a function of the indentation load P. As can be seen, the final crack size becomes lower with increasing maximum bridging stress σ_0. The mean slopes - represented in fig.128 - decrease with increasing σ_0. Figure 129 shows the displacements and bridging stresses for a Knoop-crack of final crack size $a = 0.2$mm corresponding to an indentation load of $P = 100$ N and bridging parameters $\sigma_0 = 100$ MPa, $\delta_0 = 1\mu$m.
The computations were performed under the condition that the damaged wedging zone will not transfer cohesive bridging stresses.

Conclusion: The presence of bridging stresses has consequences on the generation of cracks by Knoop indentation tests. The following conclusions can be drawn from the present analysis:

- The slope of the $d(\log a)$ *vs* $d(\log P)$ –plot deviates from the theoretical value 2/3.
- Consequently, the value of "K_{Ic}" resulting from measured $\log(a)$ *vs* $\log(P)$ –curves must depend on the indentation load.

DETERMINATION OF R-CURVES AND BRIDGING STRESSES

12. Measurement of R-curves in stable crack growth tests

12.1 Definitions of several stress intensity factors

There is much interest in fracture mechanics of ceramics with a view to determining the R-curves. A number of procedures are possible which yield different $K_{I\,appl}$ values. Several applied stress intensity factors will be defined below:

- Measurements of the true actual crack length a - for instance by use of a travelling microscope - and knowledge of the actual load P or stress $\sigma_{appl} = P/(BW)$ yield the stress intensity factor which is correct in terms of fracture mechanics

$$K_{I\,appl} = \sigma_{appl}\, Y(a) \sqrt{a} \tag{12.1.1}$$

- Very often, the actual crack length is concluded from the global compliance of the specimen, eq.(6.5.1), which increases with increasing crack length. This apparent crack length, denoted by a^*, is smaller than the real one ($a^* < a$). The related stress intensity factor, calculated with a^*,

$$\tilde{K}_{Iappl} = \sigma_{appl}\, Y(a^*) \sqrt{a^*} \tag{12.1.2}$$

  is consequently lower than the stress intensity factor calculated with a:

Combined with the Irwin formula, eq.(6.1.1), the energy release rate allows to define further stress intensity factors. The basis of such evaluations are the load-displacement curves. They can be measured as well as computed with eqs.(6.1.4) and (6.1.5). Computed curves are shown as examples in fig.130 for different crack lengths. The $P - \delta_{LP}$ –curves (or $\sigma_{appl} - \delta_{LP}$ –curves) which would result in a controlled fracture test are found from the curves in fig.130 as the stress-displacement combinations for which the condition $K_{I\,tip} = K_{I0}$ is fulfilled. From fig.130 the values for which K'_{tip} is equal to K'_{I0} were determined. For the following calculations $K'_{I0} = 1$ was chosen. By interpolating the computed points $\sigma_{appl} = f(\delta')$ for the considered discrete crack lengths, the curve of fig.131 results.
The real potential energy which leads to the energy release rate is illustrated in fig.131 as hatched area. The energy release rate resulting from fig.131 is plotted in fig.132. Within the error band of numerical computations we can conclude that - in agreement with eq.(6.2.26) - the energy release rate is constant and the related stress intensity factor equals K_{I0}.

- If we ignore completely the non-linear load-displacement behaviour, we may interpret the hatched area in fig.133 as the change of potential energy ΔU_p.
  The elastic energy and its increment are

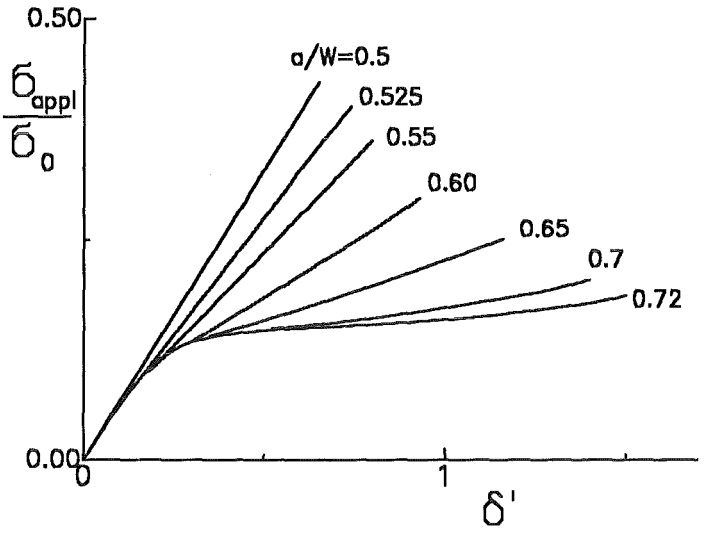

Figure 130. Opening of a bridged crack by externally applied stresses. Load-displacement curves for a crack with bridging interactions according to eqs.(4.1.9) and (4.1.13), $a_0/W=0.5$ (loading: pure tension), abscissa δ' normalised according to eq.(6.5.5).

$$W_{el}=\frac{1}{2}P\delta_{LP} \quad \Rightarrow \quad dW_{el}=\frac{1}{2}(P\,d\delta_{LP}+\delta_{LP}\,dP) \tag{12.1.3}$$

and the work of the external force is

$$dA=P\,d\delta_{LP} \tag{12.1.4}$$

The change of the potential energy is

$$dU_p=dA-dW=\frac{1}{2}\left(P\,d\delta_{LP}-\frac{\delta_{LP}}{P^2}\,dP\right) \tag{12.1.5}$$

Indroducing the global compliance $C=\delta_{LP}/P$ it results

$$dC=\frac{1}{P}\,d\delta_{LP}-\frac{\delta_{LP}}{P^2}\,dP \tag{12.1.6}$$

and eq.(12.1.5) can be rewritten as

$$dU_p=\frac{P^2}{2}\,dC \tag{12.1.7}$$

With the apparent crack length a^* the corresponding energy release rate $\hat{G}$ becomes

$$\hat{G}=\frac{dU_p}{B\,da^*}=\frac{P^2}{2B}\frac{dC}{da^*} \tag{12.1.8}$$

From the compliance formula eq.(6.5.2) we find

$$\frac{dC}{da^*}=\frac{2}{E'B}Y^2(a^*)\,a^* \tag{12.1.9}$$

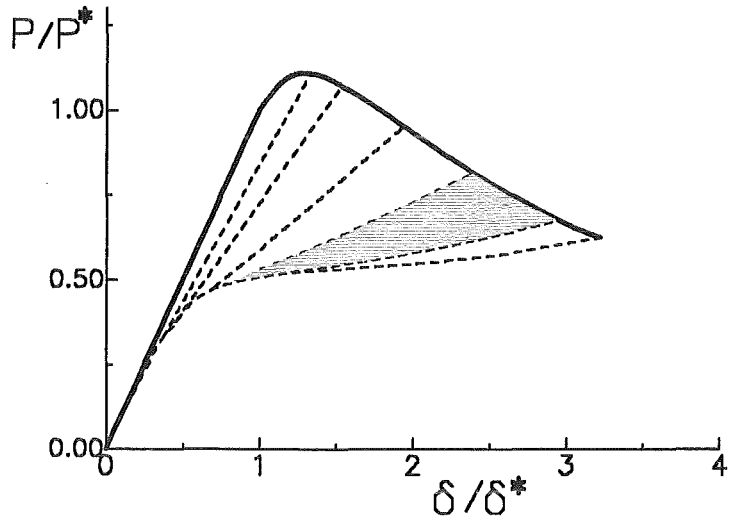

Figure 131. Construction of the load-displacement curve under stable crack growth conditions. Load-displacement curve for a controlled fracture test under tension with $K'_{I0}=1$; $a_0/W=0.5$; hatched area: real potential energy dU_p; $\delta^*=$ displacement where $K_{I\,tip}=K_{I0}$ is reached for the first time.

and the apparent stress intensity factor resulting from the Irwin formula

$$\hat{K}_{Iappl}=\sqrt{E'\hat{G}}=\sigma_{appl}\,Y(a^*)\sqrt{a^*} \tag{12.1.10}$$

is identical with $\tilde{K}_{Iappl}$ defined by eq.(12.1.2).

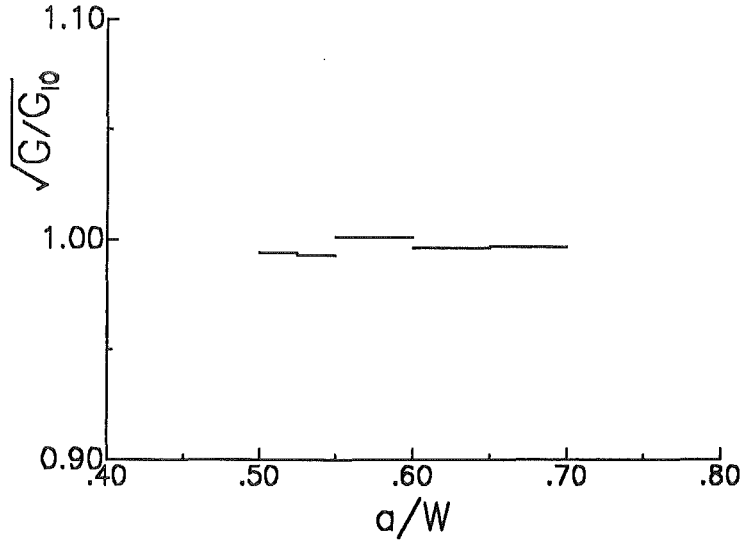

Figure 132. Energy release rate. Averaged energy release rate resulting from the crack increments (shaded areas) of fig.131, computed with eq.(6.2.1).

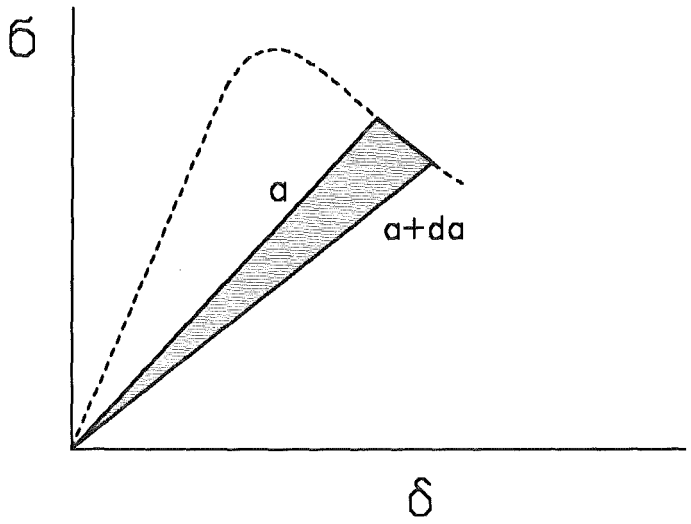

Figure 133. Energy in a controlled fracture test. Definition of the apparent potential energy (schematic).

- A second possibility of defining an energy release rate is to use dU_p/da, applying the physical crack depth a. The potential energy can be expressed by

$$\overline{G} = \frac{dU_p}{B\,da} = W \int_0^{\sigma_{appl,c}} \left(\frac{\partial \delta'_{LP}}{\partial a} \right)_{\sigma_{appl}} d\sigma'_{appl} \qquad (12.1.11)$$

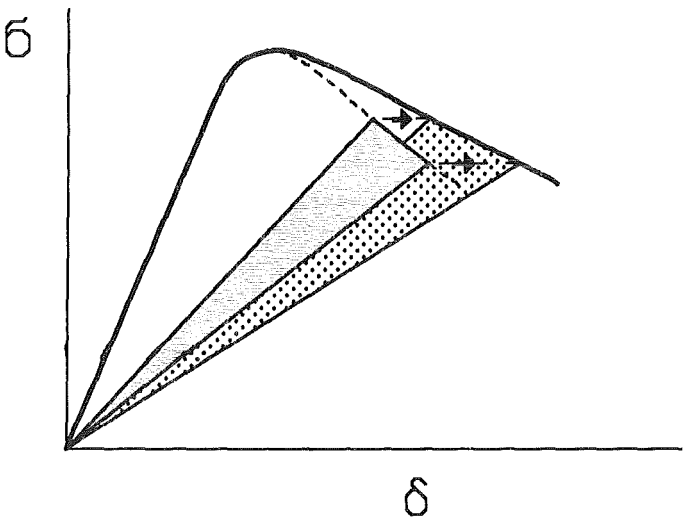

Figure 134. Energy in a controlled fracture test. Increment of apparent potential energy, in case the displacements are shifted until the compliance is in agreement with the compliance of a crack free of bridging interactions (schematic).

For the straight lines in fig.133 it holds

$$\frac{\partial \delta'_{LP}}{\partial a} = \frac{\partial \delta_{LP}}{\partial a} \frac{\sigma'_{appl}}{\sigma_{appl,c}} \tag{12.1.12}$$

Evaluation of the integral gives

$$\overline{G} = \frac{dU_p}{Bda} = \frac{W}{2} \sigma_{appl,c} \left(\frac{\partial \delta_{LP,c}}{\partial a} \right)_{\sigma = const} \tag{12.1.13}$$

and the related stress intensity factor

$$\overline{K}_{appl} = \sqrt{E' \overline{G}} \tag{12.1.14}$$

Since in the general case $da^*/da < 1$ is fulfilled, one has to expect $\overline{K}_{appl} < \hat{K}_{appl}$.

- The slope of the straight lines in fig.134 defines the apparent crack length. If we shift the displacements at a fixed load (or stress applied) to higher values $\vec{\delta}$ (the arrow symbolises the shifted displacements) until the slope of the new straight line is in agreement with the compliance of the unbridged crack, (fig.134), it holds

$$\vec{\delta}_{LP} = P\, C(a) = \sigma_{appl}\, BW\, C(a) \tag{12.1.15}$$

The change of the apparent potential energy is

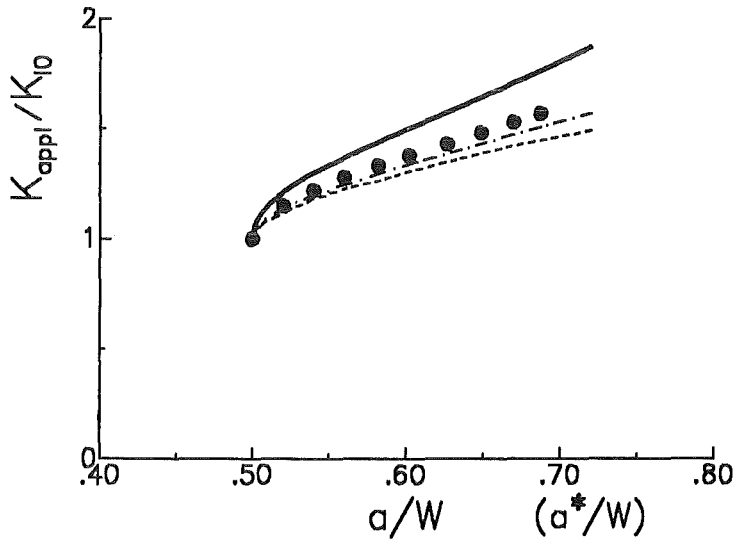

Figure 135. Differently defined R-curves. Comparison of the correct R-curve ($K_{I\,appl}$: solid line) with apparent stress intensity factors resulting from the load-displacement curve: a) $\overline{K}_{appl}$ (dashed curve), b) $\hat{K}_{appl}$ (dash-dotted curve), in addition, the symbols show the apparent stress intensity factor $\hat{K}_{appl}$ plotted versus the apparent crack depth.

$$\frac{d\vec{U}_p}{da} = BW \int_0^{\sigma_{appl,c}} \left(\frac{\partial \vec{\delta}'_{LP}}{\partial a} \right)_{\sigma = const} d\sigma'_{appl} \tag{12.1.16}$$

and the straight lines provide

$$\frac{\partial \vec{\delta}'_{LP}}{\partial a} = \left(\frac{\partial \vec{\delta}_{LP}}{\partial a} \right)_{\sigma_{appl,c}} \frac{\sigma'_{appl}}{\sigma_{appl,c}} \tag{12.1.17}$$

From (12.1.15) we conclude

$$\left(\frac{\partial \vec{\delta}_{LP}}{\partial a} \right)_{\sigma = const} = BW\, \sigma_{appl,c} \frac{\partial C}{\partial a} \tag{12.1.18}$$

Introducing (12.1.17) and (12.1.18) into (12.1.15) yields

$$\frac{d\vec{U}_p}{da} = \frac{1}{2} \sigma^2_{appl} \frac{\partial C}{\partial a} \tag{12.1.19}$$

and with (6.5.2)

$$\vec{G} = \frac{d\vec{U}_p}{Bda} = \sigma^2_{appl}\, Y^2(a)\, a \tag{12.1.20}$$

The related stress intensity factor is

$$\vec{K} = \sqrt{\vec{G}\, E'} = K_{I\,appl} \tag{12.1.21}$$

It is found to be identical with the applied stress intensity factor $K_{I\,appl}$ computed directly from the crack length and load without consideration of the energy.

Finally, the following relation between the differently defined stress intensity factors holds:

$$\overline{K}_{appl} (<) \hat{K}_{appl} = \tilde{K}_{appl} < \vec{K}_{appl} = K_{I\,appl} \tag{12.1.22}$$

Figure 135 gives a comparison of these stress intensity factors.

12.2 Determination of R-curves via compliance

12.2.1 Testing devices

In controlled fracture tests a test arrangement with a very low compliance must be applied. In order to perform such tests with extremely rigid testing devices Maniette et al. [89] proposed a compact tension test in which the fracture mechanics CT-specimen is combined with a parallel spring which allows stable crack propagation. For tension tests with centre- and edge-cracked specimens a testing device proposed by Markowski [90] seems to be appropriate.

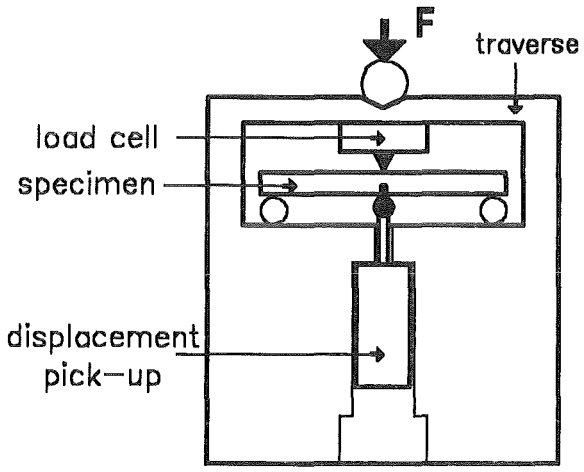

Figure 136. Testing device for R-curve measurements. Simple testing device for stable crack growth measurements [91].

The author used a simple 3-point-bending test arrangement (fig.136). A specimen with a saw-cut of $\simeq 50\mu m$ width is loaded with the externally applied load F. If the compliance of the frame is much lower than the specimen compliance, the fracture test is carried out almost completely displacement controlled. The effective load P acting on the specimen is measured with the load-cell and the displacement is recorded by an inductive displacement pick-up. In order to avoid additional compliances in the inner load circuit, it is recommended to use a load-cell made of quartz. If a testing machine is not available, the modification represented in fig.137 can be applied. In this device the load is generated by a simple screw. Figure 138 shows a typical load vs. displacement curve containing the specimen deformations as well as the roller flattening and remaining elastical deformations of the testing device. The actual crack length can be determined from the change of compliance in the controlled fracture test. Since the compliance is affected by the bridging stresses, an optical crack-length measurement may be of advantage, but the experimental effort drastically increases. In this investigation the compliance method was applied since the R-curves taken from the literature were evaluated with the compliance method, too.

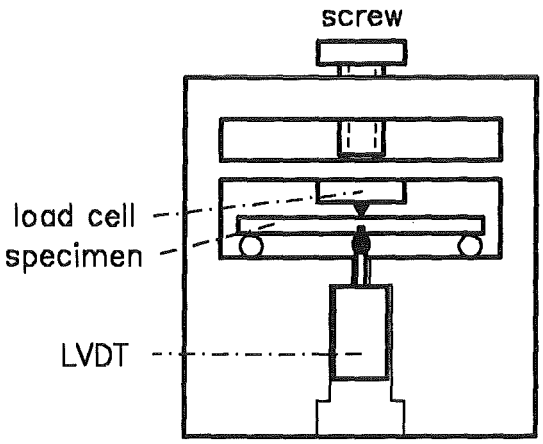

Figure 137. Testing device for R-curve measurements. Modified testing device for use without a testing machine [91].

12.2.2 Evaluation of the load-displacement curve

Figure 138 shows a load-displacement curve obtained for coarse-grained Al_2O_3 as measured. The record was obtained in the loading device represented in fig.136. In order to find the origin for load and displacements and to exclude the non-linear contribution of the Hertzian contact between the specimen and supporting rollers, the straight-line behaviour observed at higher loads has to be extrapolated to zero load (see fig.139). The intersection with the abscissa is the basis for the further evaluations.
Then the linear contribution of the rollers and the elastic deformation of the testing device to the displacements has to be eliminated. Full compliance of the test device with the specimen results from the following contributions:

- The compliance of the uncracked specimen C_0,
- the compliance C_{a_0} caused by the initial crack (or saw-cut) of length a_0,
- the contribution of the crack increment $\Delta a = a - a_0$ after the onset of crack extension, denoted $C_{\Delta a}$, and
- the 'parasitic' compliance C_{par} summarising additional elastic settling and elastic deformations of the supporting rollers and the supporting structure, i.e.

$$C_{meas} = C_0 + C_{a_0} + C_{\Delta a} + C_{par} \tag{12.2.1}$$

For the determination of the R-curve only the displacements according to the compliance

$$C = C_{meas} - C_{par} \tag{12.2.2}$$

are of interest. The parasitic compliance can be determined from the initial straight-line behaviour at $a = a_0$ as

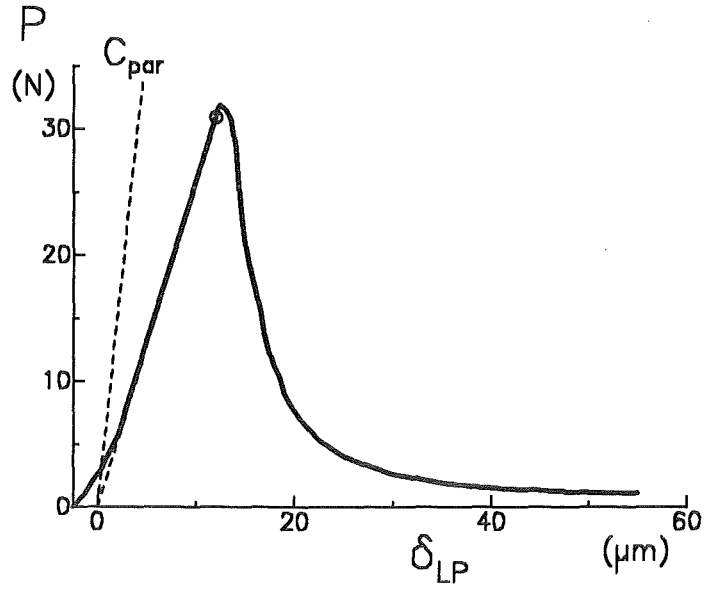

Figure 138. Experimental load-displacement curve. Load-displacement curve for coarse-grained Al_2O_3 measured with the testing device shown in fig.136; the circle indicates the first deviation from the straight line.

$$C_{par} = C_{meas} - C_0 - C_{a_0} \tag{12.2.3}$$

since C_0 and C_{a_0} are known. The compliance of an uncracked bending bar is given by

$$C_0 = \frac{L^2}{W^2 BE}\left[\frac{L}{4W} + \frac{(1+\nu)W}{2L}\right] \tag{12.2.4}$$

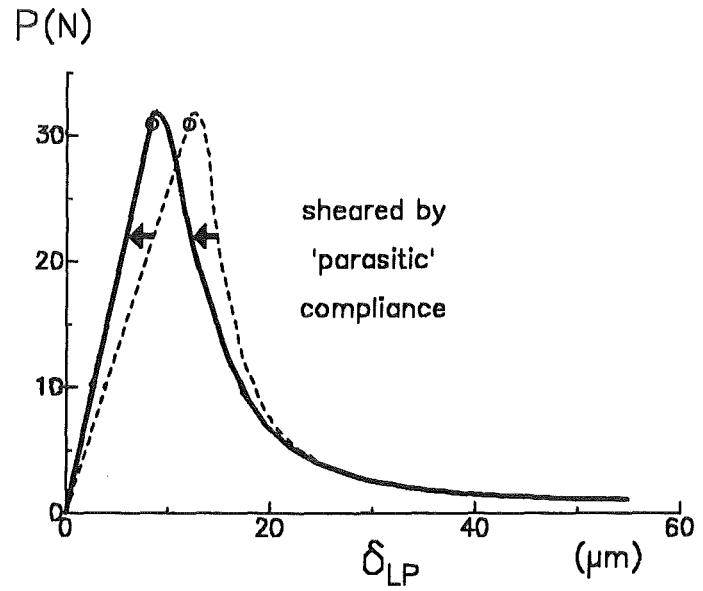

Figure 139. Corrected load-displacement curve. Load-displacement-curve after excluding 'parasitic' compliance.

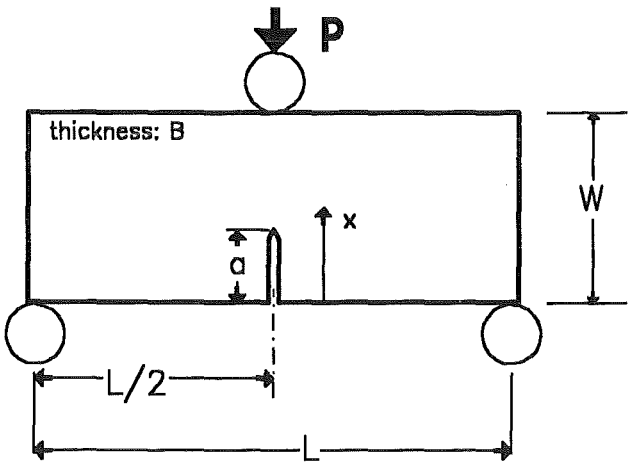

Figure 140. Three-point bending test. Geometrical data.

with $\alpha = a/W$. For the geometric data see fig.140. The contribution of the initial crack (or notch) results as

$$C_{a_0} = \frac{9}{2} \frac{L^2 \pi}{W^2 E B} \int_0^{\alpha} F^2 \, \alpha' \, d\alpha' \qquad (12.2.5)$$

For the calculation of the crack length increment Δa via compliance we can use

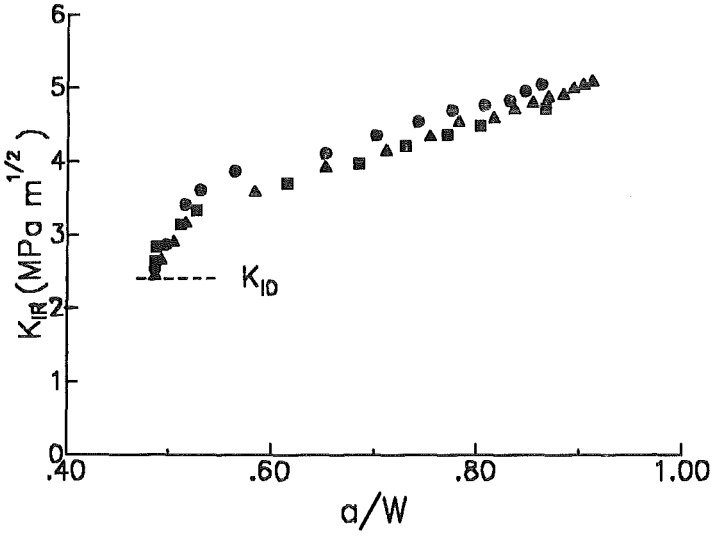

Figure 141. Alumina (batch 1). R-curves measured with the test device (fig.136); coarse-grained Al_2O_3.

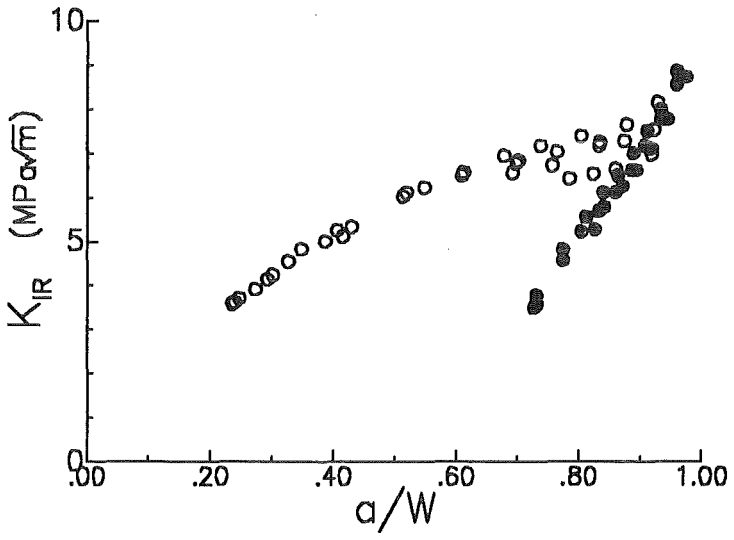

Figure 142. Alumina (batch 2). R-curves measured with the test device (fig.136); coarse-grained Al_2O_3; each symbol comprises four single tests.

$$C_{\Delta a} = \frac{9}{2}\frac{L^2\pi}{W^2EB}\int_{\alpha_0}^{\alpha_0+\Delta\alpha} F^2\,\alpha'\,d\alpha' \qquad (12.2.6)$$

from which $\Delta\alpha$ and Δa may be obtained by a zero routine. The numerical integrations can be avoided by use of polynomial representations of the compliance [92].

$$C_{a_0} = \frac{9}{2}\frac{L^2}{W^2EB}\left(\frac{\alpha}{1-\alpha}\right)^2\sum_{\mu=0}^{5} B_\mu\alpha^\mu \qquad (12.2.7)$$

with the coefficients listed in table 8 in the Appendix. The corrected load-displacement curve is represented in fig.139 as the solid curve. The actual compliance defined as

$$C = \delta_{LP}/P \qquad (12.2.8)$$

then provides the actual crack length and together with the actual load (or the actual bending stress) the applied stress intensity factor $K_{I\,appl}$ can be computed using eq.(4.3.2). The analysis is greatly simplified if explicit stress intensity factor solutions are applied. In the case of 3-point bending it is recommended to use for instance eq.(12.1.2) with the geometric function given by Srawley and Gross [93].

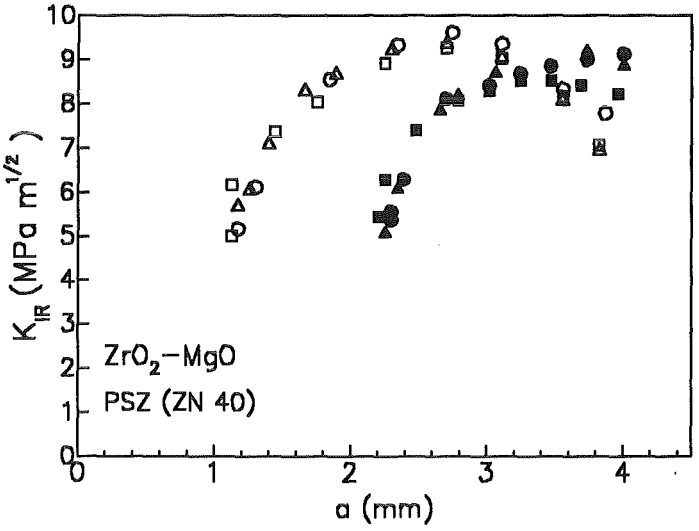

Figure 143. Zirconia. R-curve for MgO-doped zirconia; diferent symbols for different specimens.

12.3 Results for some ceramics

A number of ceramics have been tested and several R-curves obtained through compliance evaluation are plotted in figs.141 -144. The specimens were bending bars with the dimensions: $W = 4.5$mm, $B = 3.5$mm and length $\simeq 45$mm, containing a saw cut of 50μm.
The materials tested were:

- Alumina: two batches of 99.6%Al_2O_3, (Frialit/Degussit, Friedrichsfeld AG, Mannheim) with a mean grain size of 20μm.

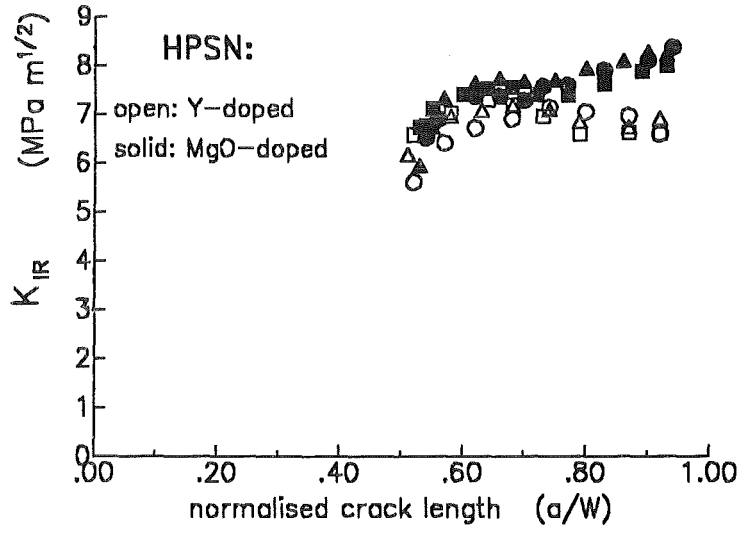

Figure 144. Hot-pressed silicon nitride. R-curves for two types of HPSN.

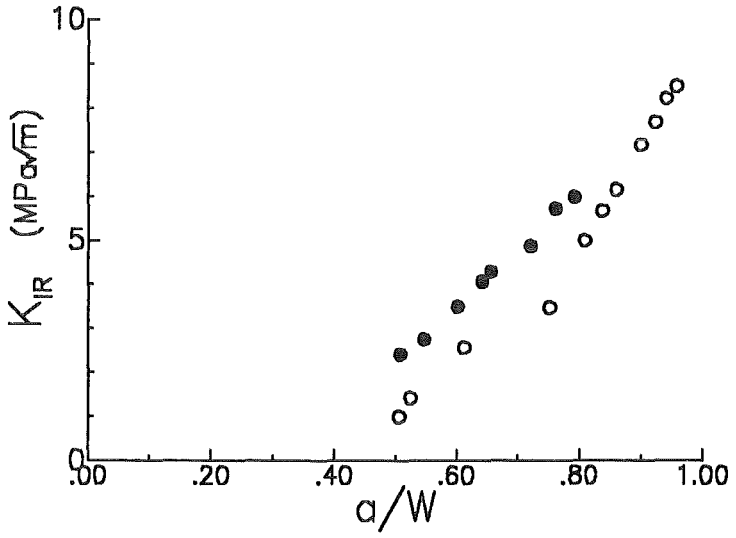

Figure 145. R-curves for CfC. Crack perpendicular to the fiber direction.

- Zirconia ceramics:

  – MgO-doped ZrO_2, PSZ ZN40,
  – Y_2O_3-doped ZrO_2, PSZ ZN100,

  both manufactured by Feldmühle AG, Plochingen, Germany. A controlled fracture test could be carried out only for the MgO-doped material. In case of the PSZ ZN100 fracture was mostly instable and controlled fracture was found only at a relative crack length close to $a/W = 1$.

- Hot-pressed silicon nitride

  – 2.5%-MgO-doped HPSN, NH206, density = 3.20 g/cm^3, Feldmühle AG, Plochingen,
  – Y_2O_3-doped HPSN, NH209, Annawerk, Rödental.

- Carbon-fiber reinforced carbon (CfC), with a saw cut perpendicular to the fiber direction.

It becomes obvious from the two curves for alumina shown in fig.142 that the R-curve is not a material property, but depends strongly on the initial crack size.

12.4 An experimental procedure for the determination of K_{I0}

The stress intensity factor K_{I0} which is characteristic of the onset of crack extension can, in principle, be determined from the load-displacement curve as the first deviation from the initial straight line. Unfortunately, this point is not sharply defined and one has to expect a high margin of uncertainty.
An experimental procedure is proposed which permits a very high resolution of the first deviation from the straight-line behaviour. Figure 146 shows a notched bending bar with two strain gauges at the surface in the compression zone. One of them is applied directly opposite the notch (1), the second (2) at a remote point. Each strain gauge is the active arm of a quarter-bridge circuit. Under bending load the strain gauge (1) will produce a higher signal U_1 than the

other sensor U_2, and the ratio of both signals U_1/U_2 is dependent only on the geometrical conditions and not on the actual load.

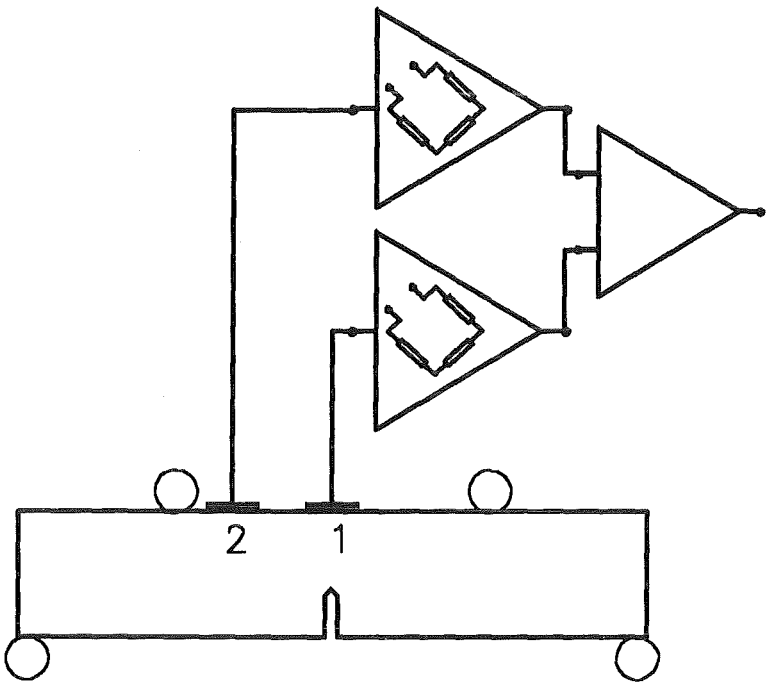

Figure 146. Measurement of the onset of crack extension. A test method for the measurement of K_{I0}; bending specimen with strain gauges.

Both signals are differently amplified in such a way that the output signals become identical. The output signals of the amplifiers are connected in opposition and, consequently, no signal results. By application of a small load the degree of amplification can be adjusted very sensitively. In a fracture test any change of the geometric proportions, for instance of the crack length, is bound to detune the electric circuit and will cause an electrical signal, which may be strongly amplified. In transformation-toughened materials also changes in the size of the transformation zone will affect the signal.

12.5 Proposal for calculation of the R-curve from measured load-displacement curves

12.5.1 Basic considerations

According to the literature, different procedures are applied for determination of R-curves from controlled fracture tests. From a test in which the load is recorded and the crack length is directly observed with a travelling microscope all information is available which is needed to calculate the applied stress intensity factor $K_{I\,appl}$ and to plot the $K_{I\,appl} - \Delta a$ –curve. In many cases, the crack length is obtained indirectly from the specimen compliance which increases with increasing crack length. This method is easy to perform but, unfortunately, in cases of strong R-curve behaviour the results may become wrong, since the reason for the R-curve - for instance the bridging stresses - will affect the compliance, too. Therefore, a procedure will be described in this section which allows the correct R-curve to be determined from a measured load-displacement curve.
The following considerations are based on eq.(4.3.2) which is mostly read from right to left: if a stress distribution along the crack faces is given, a stress intensity factor K_I results. These stresses may be stresses in the uncracked body or real crack surface loadings. But eq.(4.3.2) is a fundamental relationship between crack-surface stresses and the stress intensity factor and can be read also in the inverse direction: any stress intensity factor K_I must be related to a stress distribution σ along the crack line. If this stress distribution is known, all fracture-mechanical consequences are known, too. The real physical reasons of these stresses are actually not of interest and, therefore, we will sum up the real stresses (for instance bridging stresses) and the virtual stresses (for example residual stresses due to phase transformations acting along the crack line after closure of the crack) by the effective stress $\sigma_{shield}(x)$

$$K_{shield} = \int_0^a \sigma_{shield}\, h(x,a)\, dx \tag{12.5.1}$$

We will try to determine in the following section such an effective stress distribution $\sigma_{shield}(x)$ along the crack faces that yields the same load-displacement curve as measured in a real experiment. The stress intensity factor resulting from eq.(12.5.1) then describes the *correct* R-curve.

12.5.2 Application of a power series procedure

The R-curve is fully known when the distribution of the shielding stresses along the crack is known. The distribution of the shielding stresses depends on the actual crack length a and the location x, and a power-series expansion with respect to a and x provides

$$\sigma_{shield}\,(x,a) = \sum_{\mu,\,\nu=0}^{\infty} A_{\mu\nu}(a-x)^{\mu} a^{\nu} \tag{12.5.2}$$

This most general representation is appropriate for all shielding effects. Considering the numerical effort, it may be of advantage to use set-ups in which the real shielding behaviour (if known) is modelled. This will be outlined in Section 12.5.3. Introducing the expansion eq.(12.5.2) into eq.(4.3.5) and taking into account that

$$\sigma = \sigma_{appl} + \sigma_{shield} \tag{12.5.3}$$

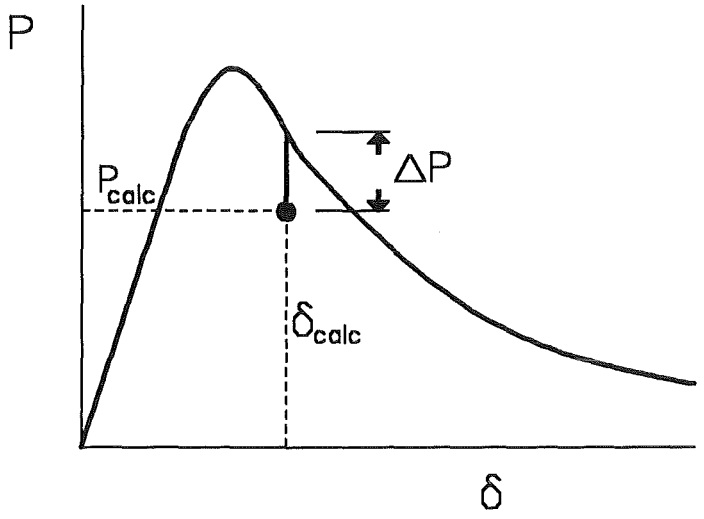

Figure 147. Evaluation of R-curves. Comparison of calculated and measured load-displacement data; illustration for the least-squares procedure.

gives the crack opening displacements

$$\delta = \delta_{appl} + \frac{1}{E'} \sum_{\mu,\nu=0}^{\infty} A_{\mu\nu} \int_0^a \int_{\max(x,x')}^a h(a',x)h(a',x')(a-x')^{\mu} a^{\nu} da'dx' \tag{12.5.4}$$

with

$$\delta_{appl} = \frac{\sigma^*}{E'} \int_0^a \int_{\max(x,x')}^a h(a',x)h(a',x')\left(1 - 2\frac{x'}{W}\right) da'dx' \tag{12.5.5}$$

where σ^* is the outer fiber bending stress. The displacements of the loading points result as [47]

$$\delta_{LP} = \frac{3L}{W^2} \int_0^a \left(1 - 2\frac{x}{W}\right) \delta(x)\, dx \tag{12.5.6}$$

and introducing eq.(12.5.5) into (12.5.6) yields

$$\delta_{LP} = \frac{3L}{E'W^2} \left[\sigma^* \kappa(a) + \sum_{\mu,\nu=0}^{\infty} A_{\mu\nu} \lambda_{\mu\nu}(a) \right] \tag{12.5.7}$$

with

$$\kappa(a) = \int_0^a \left(1 - 2\frac{x}{W}\right) \left[\int_0^a \int_{\max(x,x')}^a h(a',x)h(a',x')\left(1 - 2\frac{x'}{W}\right) da'dx' \right] dx \tag{12.5.8}$$

$$\lambda_{\mu\nu}(a) = \int_0^a \left(1 - 2\frac{x}{W}\right)\left[\int_0^a \int_{\max(x,x')}^a h(a',x)h(a',x')(a-x')^{\mu}\, a^{\nu} da' dx'\right] dx \qquad (12.5.9)$$

The externally applied load is related to the stresses σ_{appl} by

$$P = \frac{2}{3}\sigma^* \frac{BW^2}{L} \qquad (12.5.10)$$

During stable crack growth the shielding stress intensity factor fulfills the condition

$$K_{I\,tip} = K_{I0} = K_{I\,appl} + K_{shield} \qquad (12.5.11)$$

which by use of (12.5.2) in (4.3.2) reads

$$\sum_{\mu,\,\nu=0}^{\infty} A_{\mu\nu}\chi_{\mu}(a) \cdot a^{\nu} W^{\mu+1/2} = K_{I0} - \sigma^* Y_{bend}\sqrt{a} \qquad (12.5.12)$$

with

$$\chi_{\mu}(a) = \int_0^a (a-x)^{\mu} h(x,a)\, dx \qquad (12.5.13)$$

and the geometric function for bending, which is given by

$$Y_{bend} = \frac{1}{\sqrt{a}} \int_0^a \left(1 - 2\frac{x}{W}\right) h(x,a)\, dx \qquad (12.5.14)$$

For calculation of the R-curve the coefficients $A_{\mu\nu}$ have to be determined. This can be done by solving a system of linear equations. Therefore, the number of terms in the power series is restricted to a finite value. If we choose for example as an upper limit $\mu = \nu = n$, we first have to compute the $(n+2)(n+1)/2$ functions for $\lambda_{\mu\nu}(a)$ and $\chi_{\mu}(a)$.
A least-squares procedure will be proposed here for determination of the coefficients. With an arbitrarily given set of $(n+2)(n+1)/2$ coefficients $A_{\mu\nu}$ first the bending stress σ^* is computed with eq.(12.5.12) and then the loading-point displacements are calculated by eq.(12.5.7). In fig.147 the resulting loading-point displacement δ_{LP} for a given value of crack length is introduced. From eqs.(12.5.12) and (12.5.10) the corresponding force P at the loading points is obtained and also entered in fig.147. Both values yield the computed point (P, δ_{LP}). Then the deviation between the calculated load and the measured load is $\Delta P = P_{meas} - P_{calc}$. In a least-squares procedure the best set of coefficients $A_{\mu\nu}$ is determined from the condition

$$\sum_{(N)} (P_{meas} - P_{calc})^2 = minimum \qquad (12.5.15)$$

A computer routine appropriate for such calculations is proposed in the Harwell Subroutine Library (Subroutine VA02A).

12.5.3 Special set-ups reducing the costs of computation

With a view to the practical application of the method described before it must be noted that a great number of terms in eq.(12.5.2) are necessary to approximate the stress distribution sufficiently if steps or steep gradients in the stress distribution occur relatively far away from the crack tip. This may require high numerical efforts, for instance in case of materials with R-curve effects caused by bridging stresses, since in that case a step in the stress distribution occurs at the notch root of the initial saw-cut, i.e. at $x = a_0$.
If **only** bridging stresses are responsible for the R-curve, the set-up in eq.(12.5.2) can be modified as

$$\sigma_{shield}(x,a) = \begin{cases} \sum_{\mu,\nu=0}^{\infty} B_{\mu\nu}(a-x)^{\mu}a^{\nu} & \text{for} \quad x > a_0 \\ 0 & \text{for} \quad x < a_0 \end{cases} \tag{12.5.16}$$

In this case, eq.(12.5.9) has to be replaced by

$$\lambda(a) = \int_0^a \left(1 - 2\frac{x}{W}\right)\left[\int_0^a \int_{\max(x,x' > a_0)}^a h(a',x)h(a',x')(a-x')^{\mu}\, a^{\nu} da' dx'\right] dx \tag{12.5.17}$$

and eq.(12.5.13) by

$$\chi_{\mu}(a) = \int_{a_0}^a (a-x)^{\mu}\, h(x,a)\, dx \tag{12.5.18}$$

For the most general case of shielding stresses a combination of the two limit cases mentioned before is recommended:

$$\sigma_{shield} = \beta\, \sigma_{shield,(x \le a)} + (1-\beta)\, \sigma_{shield,(a_0 \le x \le a)} \quad , \; 0 < \beta < 1 \tag{12.5.19}$$

The parameter β results automatically from the least-squares routine.

12.5.4 Application of step-shaped stress distributions

As described in Section 13.2, the unknown stress distribution may be described by a decomposition into a number of strips with constant stress σ_i. If the border between two strips coincides with a step in stresses, no problems will occur. The stress within one strip may be expanded by

$$\sigma_i = \sum_{\nu=0}^{\infty} C_{i\,\nu} a^{\nu} \tag{12.5.20}$$

Then the crack opening displacements caused by these stresses are

$$\delta(x) = \sum_{i=1}^{N} \sum_{\nu=0}^{M} C_{i\,\nu} a^{\nu}\, \mathbf{g}(x, x_i, x_{i+1}, a) \tag{12.5.21}$$

The further procedure is similar to that in Section 12.5.2.

12.5.5 An example of R-curve determination

12.5.5.1 Some remarks on the fitting procedure

The application of the least-squares procedure described before calls for some experience and will hardly be successful when used for the first time. Two typical problems should be mentioned here. Depending on the arbitrarily chosen starting values, it may be that:

- the calculated loads fit excellently the measured curve, but the result does not fulfill the simple requirement

$$\delta_1 < \delta_2 < \delta_3 < ..... < \delta_N \quad \text{for} \quad a_1 < a_2 < a_3 < ..... < a_N \tag{12.5.22}$$

- the stress distribution in the crack-propagation zone may result, at least partially, as *positive* stresses (note that bridging stresses are negative!).

In order to avoid such curious results, it is recommended to use a weight g_i in the least-squares routine according to

$$\sum_{i=1}^{N} (P_{meas,i} - P_{calc,i})^2 \, g_i = minimum \tag{12.5.23}$$

The weight g_i is for example chosen as $g_i = 1$ in the normal case and will be automatically increased to $g_i = 100$ if in the actual step positive shielding stresses occur or if the condition in eq.(12.2.1) is violated.
The effort in numerical computations can be reduced if the controlled fracture test is interrupted at a certain crack length which, can be measured easily under the light microscope. Since the related load and displacement are known, a very high weight can be applied in eq.(12.2.2) to satisfy this additional condition.

12.5.5.2 Results

As an example of the procedure described before the load-displacement curve, fig.148, obtained for coarse-grained Al_2O_3 in a four-point bending test will be analysed. The load-displacement curve sheared by the initial compliance (and only containing the contribution of the crack extension Δa) is given in fig.149. In order to allow simple computations to be made, the coefficients $\lambda_{\mu\nu}(a)$, $\kappa(a)$ and $\chi_\mu(a)$ were computed for a number of different crack lengths and entered in Table 9 in the Appendix. If additional crack lengths are necessary - and the direct evaluation of the integrals seems to be too difficult - these tables may be interpolated with respect to a/W by cubic splines. For the least-squares procedure the special set-up in eq.(12.5.16) was applied. The integrals $\lambda_{\mu\nu}$, χ_μ, κ and Y were evaluated for 12 different crack lengths selected, namely for **a/W=0.505, 0.51,0.52,0.53,0.54,0.55,0.56,0.575,0.60,0.625,0.65,0.675,0.70** and 0.725.
The least-squares procedure ended up with the set of the first 10 coefficients $A_{\mu\nu}$ with $\mu + \nu \leq 3$ which were used to calculate the load-displacement curve. In fig.150 the result is shown as open squares together with the measured curve. The resulting R-curve is shown in fig.151 as the solid line. An evaluation based on the compliance method, i.e. on eq.(12.5.7) in the simplified form

$$\delta_{LP} = \frac{3L}{E'W^2} \sigma^* \kappa(a) \tag{12.5.24}$$

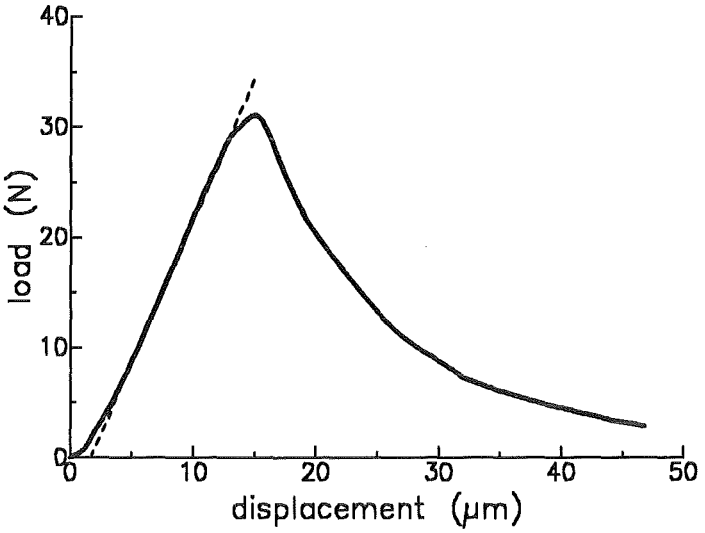

Figure 148. Measured load-displacement curve. Load-displacement curve for coarse-grained Al_2O_3 (batch 2).

yields the apparent R-curve plotted additionally as circles in fig.151. In the first range of crack extension, $0.5 \leq a/W \leq 0.6$, the two results are nearly identical. At larger crack extensions the apparent R-curve is significantly lower as has been expected from the calculations made in Section 12.1 and plotted in fig.135. A second specimen of the same coarse-grained Al_2O_3 was tested in a controlled fracture test and suspended after a certain amount of crack propagation. The actual physical crack length was measured after fracture. Therefore, one may put a droplet of ink into the initial notch after unloading and break the specimen when the ink is dry. The actual stress intensity factor computed with the load at the moment of unloading for the real crack

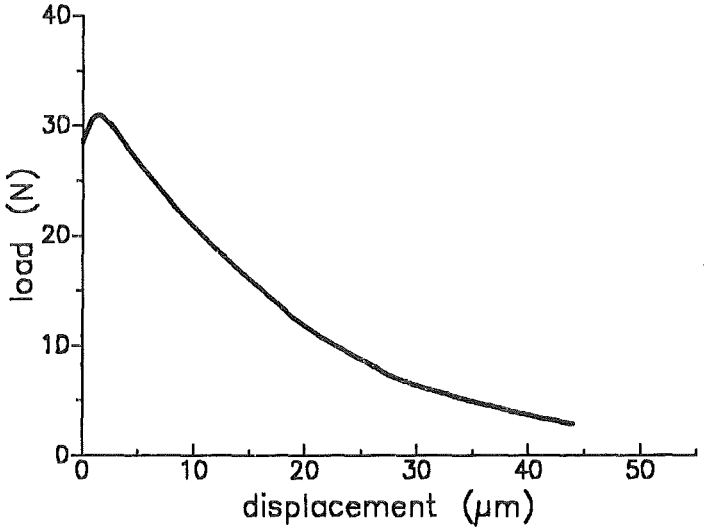

Figure 149. Sheared load-displacement curve. Load-displacement curve after exclusion of the 'parasitic' compliance, the compliance of the unnotched specimen, and the compliance of the crack with initial crack length a_0. (chosen for demonstration of the method proposed in Section 12.5.2).

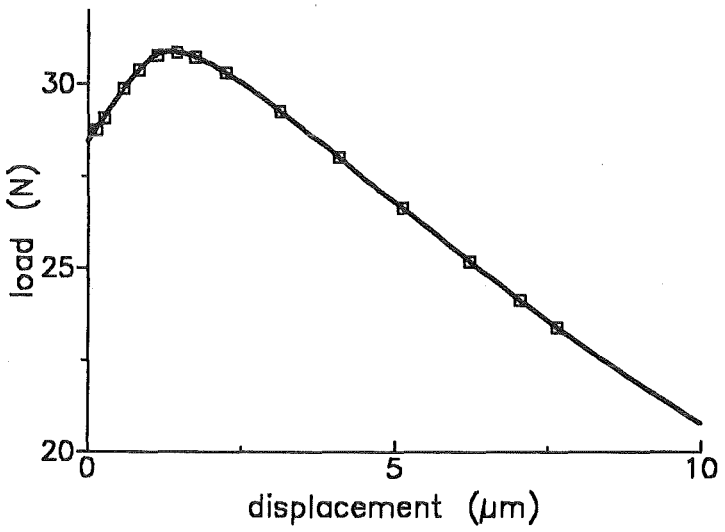

Figure 150. Comparison between calculated and measured load-displacement curves. Comparison of the calculated load-displacement curve obtained with the procedure described in section 12.5.2 (squares) with the measured curve (solid line).

length is entered as a solid square in fig.151. It becomes obvious from the dotted line that this value is consistent with the general trend of the computed R-curve represented by the solid line. The apparent R-curve value resulting from an evaluation via compliance is given by the open square which is in agreement with the circles, taking into account the scatter of several specimens. The shielding stresses, calculated with eq.(12.5.2) are shown in fig.152.

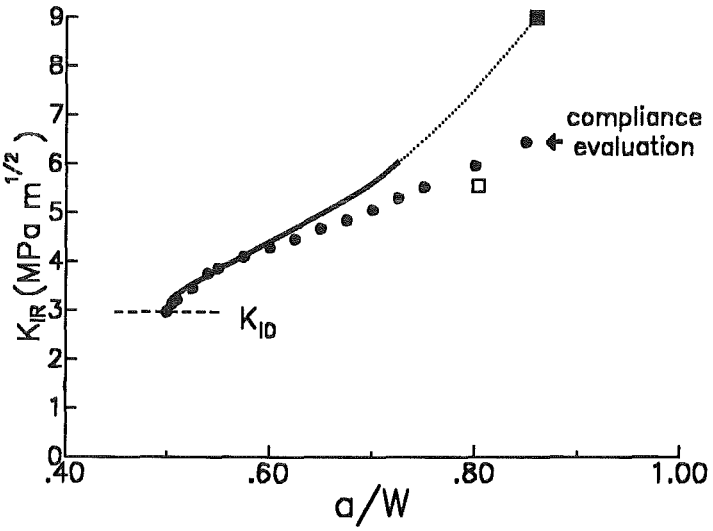

Figure 151. Comparison of R-curves. Comparison of the R-curve obtained with the procedure of in section 12.5.2 (solid line) with the R-curve based on the linear-elastic compliance (circles); solid square: unloaded specimen with measured crack length, open square: unloaded specimen with compliance evaluation.

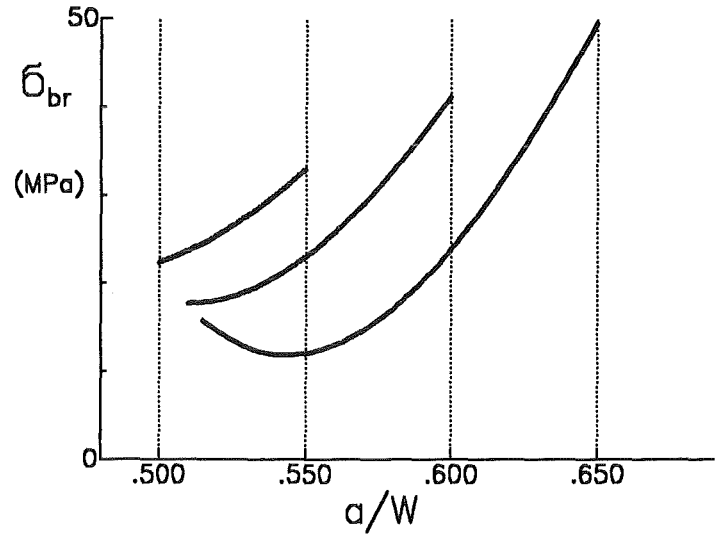

Figure 152. Stress distribution in the crack propagation zone. Stresses for crack extensions of $\Delta a/W = 0.05, 0.1$ and 0.15.

In principle, it is possible to derive the bridging-stress relation by computing the local crack opening displacements using eq.(12.5.4) and relating it to the stresses obtained by eq.(12.5.2). It should be mentioned that only a rough estimate of the relation $\sigma_{br} = f(\delta)$ can be expected although the global loading-point displacements and, consequently, the R-curve were sufficiently approximated. The reason is the limited number of coefficients $A_{\mu\nu}$ available for the representation of the x-dependency of the stress distribution. In our case, the stress distribution along the crack-propagation line is described only by a polynomial of 3rd degree that cannot represent complicate stress distributions in detail. On the other hand, one should have in mind that for δ_{LP}

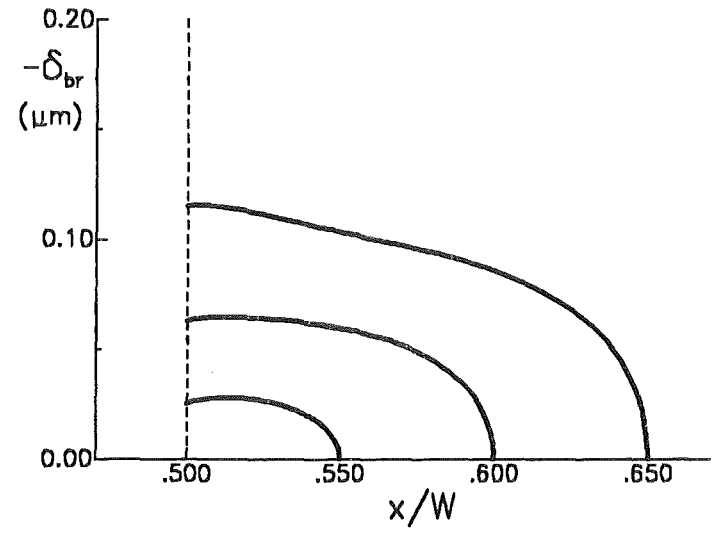

Figure 153. Shielding displacements. Displacements caused by the shielding stresses for different crack sizes.

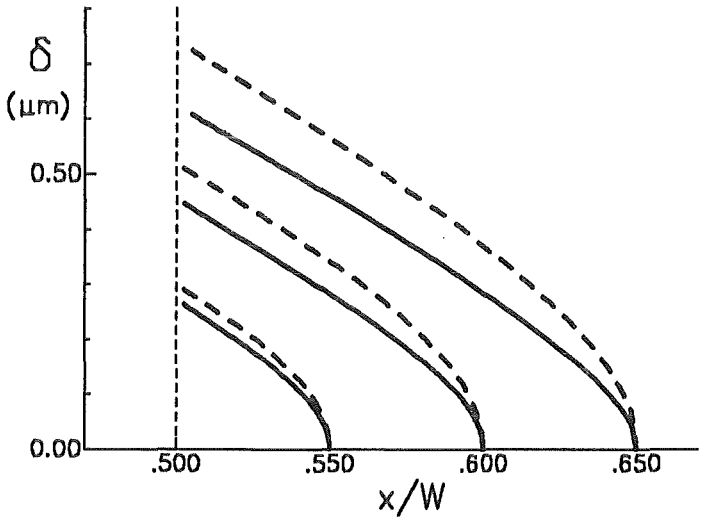

Figure 154. Applied and total displacements. Dashed lines: displacements caused by the applied stresses. Solid lines: total displacements as the superposition of applied and shielding stresses.

and K_{shield} only integrated and, hence "smoothed" stresses influence the result. Nevertheless, the author tried to evaluate $\sigma_{br} = f(\delta)$. In a first step, the displacements caused by the shielding stresses were computed with eq.(12.5.5) and represented in fig.153. In addition, the displacements due to the applied stresses were computed, eq.(12.5.7), and entered as dashed curves in fig.154. The total displacements obtained by superposition of the "applied displacements" and the "shielding displacements" are traced as solid lines. Finally, the shielding-stress relation results by plotting the shielding stresses versus the total displacements, as shown in fig.155.

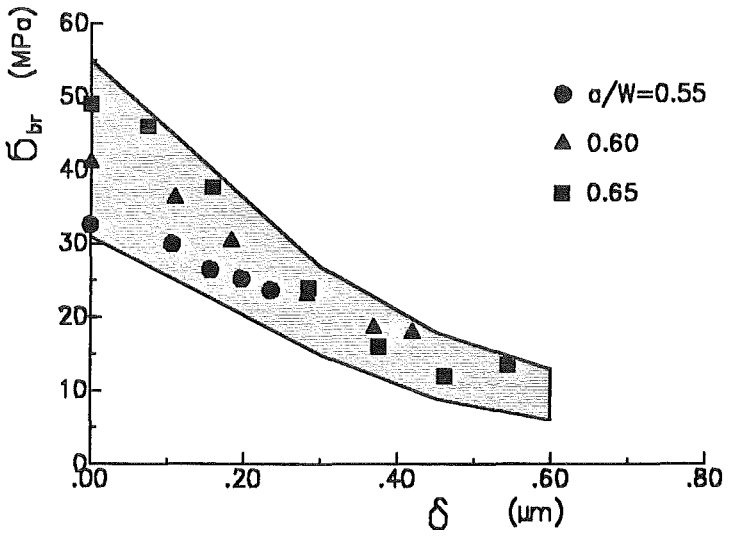

Figure 155. Shielding stresses. Shielding -(bridging)-stresses as a function of total displacement.

12.6 Determination of crack resistance by optical crack length measurement

The procedure described before was developed to determine the R-curve for the case that only the load-displacement curve has been recorded during a controlled fracture test. The determination of the bridging-stress relation by the previous analysis needs much numerical effort and is associated with an unknown margin of uncertainty.
The evaluation of the bridging stresses becomes much easier if the crack length has been measured simultaneously with a microscope. It will be explained in this section how such information can be used to derive the bridging-stress relation.

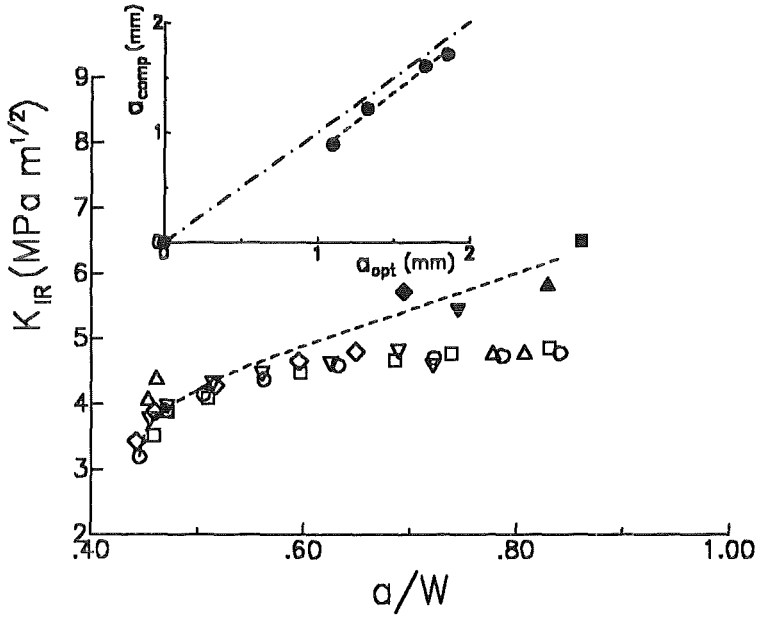

Figure 156. R-curve for Al_2O_3. R-curves for coarse-grained Al_2O_3 (batch 1). Open symbols: evaluation via compliance for one single specimen. Closed symbols: optical crack-length evaluation after suspending four specimens at different crack lengths.

In fig.156 R-curves are shown for five different specimens made from coarse-grained Al_2O_3 (batch 1). Four of the tests were interrupted after different amounts of crack propagation and broken after introducing a droplet of ink into the crack region. The optically measured crack lengths yield the K_{IR}-values represented by the closed symbols, whilst the R-curve data derived via compliance are represented by the open symbols. The insert in fig.156 shows the differences between crack lengths obtained by optical and by compliance procedures.
The bridging stresses can be obtained also from the crack-resistance curves based on the physically correct crack length a_{opt}. Before starting the numerical analysis, the R-curve data obtained by optical crack length measurement may be "smoothed" to reduce the scatter caused by the different specimens. The mean curve is given by the dashed line. If this curve has been determined, we can use the same procedure as described in Section 12.5, apart from the special considerations mentioned in Subsection 12.5.5.1. Consequently, the computation becomes much easier.

13. Methods for the determination of bridging stresses

13.1 Determination of bridging stress parameters for a given relation

A first possibility to determine the bridging relation is to prescribe the type of relation and to determine its parameters. The procedure will be outlined with R-curves from the literature. The observed R-curves (or K_{IR} –curves) have often been described by a relation between the bridging stress intensity factor $K_{I\,br}$ and the crack extension Δa, i.e. $K_{I\,br} = f(\Delta a)$. This would be an appropriate description if the R-curve were a material property. It has been concluded from experimental results [12] and theoretical considerations [19], [94] that the R-curve is not a material property but must depend on the specimen geometry, the initial crack length, the type of loading (tension, bending), the conditions of crack propagation (constant load test, stable crack growth test), and the initial value of the stress intensity factor in a constant load test. Due to this fact the increase in crack resistance must be characterised directly by the bridging law $\sigma_{br} = f(\delta)$ which relates the bridging stresses σ_{br} to the crack surface displacements δ.
In the following considerations the special bridging relation from section 4.1 is used

$$\sigma_{br} = \sigma_0 \exp(-\delta/\delta_0) \tag{13.1.1}$$

In order to make the procedure easier the basic relations - given already in earlier sections - are here listed once more. The bridging stresses are responsible for the bridging stress intensity factor $K_{I\,br}$

$$K_{I\,br} = \int_0^a h\left(\frac{x}{a}, \frac{a}{W}\right)\sigma_{br}(x)\,dx \tag{13.1.2}$$

The externally applied stresses σ_{appl} give rise to the applied stress intensity factor $K_{I\,appl}$

$$K_{I\,appl} = \int_0^a h\left(\frac{x}{a}, \frac{a}{W}\right)\sigma_{appl}(x)\,dx \tag{13.1.3}$$

The effective stress intensity factor $K_{I\,tip}$ (describing the stresses at the crack tip) results from the principle of superposition as

$$K_{I\,tip} = K_{I\,appl} - |K_{Ibr}| \tag{13.1.4}$$

A negative sign is used for K_{Ibr} because the compressive bridging stresses are used as positive values. Finally, the crack surface displacements can be calculated by

$$\delta(x) = \frac{1}{E'} \int_0^a \int_{\max(x,x')}^a h(a',x)h(a',x')[\sigma_{appl}(x') - \sigma_{br}(\delta(x'))]da'dx' \qquad (13.1.5)$$

The procedure of evaluating the stress intensity factors $K_{I\,br}$ and $K_{I\,tip}$ contains the following steps:

1. Solution of the integral equation (13.1.5) for the given applied stresses and the bridging stresses described by eq.(13.1.1). The result is the distribution of the displacements $\delta(x)$.
2. Introducing δ in eq.(13.1.1) yields the bridging stresses σ_{br}.
3. Inserting the bridging stresses in eq.(13.1.2) gives the bridging stress intensity factor $K_{I\,br}$, and from the applied stresses the related applied stress intensity factor $K_{I\,appl}$ can be obtained using eq.(13.1.3).
4. The crack tip stress intensity factor $K_{I\,tip}$ finally results from eq.(13.1.4).

In [18] this procedure was performed for bending load and different a_0/W. In order to reduce the efforts of computation the resulting stress intensity factors were tabulated in the form

$$K'_{I\,appl} = f(K'_{I\,tip}, a/W, \delta'_0) \qquad (13.1.6)$$

where the stress intensity factors are normalised with respect to the maximum bridging stress σ_0 and the specimens width W as

$$K'_I = K_I/(\sigma_0\sqrt{W}) \qquad (13.1.7)$$

The values of δ_0 were scaled by

$$\delta'_0 = \frac{E'}{\sigma_0 W}\,\delta_0 \qquad (13.1.8)$$

Parabolic interpolation of the tabulated data allows to determine the stress intensity factors for a range of relevant values of $K_{I\,appl}$, a/W and δ_0.
The weight-function based procedure described above is applied to determine the parameters (σ_0, δ_0) of the bridging stress relation from experimental data measured by the author and from K_{IR}-curves available in the literature.

13.1.1 Determination of parameters for the bridging stress relation

The bridging stresses can be obtained from a test performed under increasing load on a cracked specimen. The test results are usually presented as $K_{I\,appl}$ versus crack extension Δa. In a stable crack-growth test the crack-tip stress intensity factor $K_{I\,tip}$ fulfills the condition of crack propagation

$$K_{I\,tip} = K_{I0} \qquad (13.1.9)$$

where K_{I0} corresponds to the initial value of the K_{IR}-curve measured at $\Delta a = 0$ (see fig.2). If $K_{I\,appl}$ is known, theoretical K_{IR}-curves follow as a function of $K_{I\,tip}$

$$K_{IR,calc} = K_{I\,appl}(K_{I\,tip}, a/W, \delta_0)\Big|_{K_{I\,tip} = K_{I0}} \qquad (13.1.10)$$

or with the function f in eq.(13.1.6)

$$K_{IR,calc} = \sigma_0\sqrt{W}\ f(K_{I0}/\sigma_0\sqrt{W}\ , a/W, \delta_0) \qquad (13.1.11)$$

considering the normalisation (13.1.7) for K_I. Due to the approximately square-root shaped K_{IR}-curves for $\Delta a \to 0$, the value K_{I0} can hardly be measured in a stable crack growth test. Therefore, very often the value of K_{I0} has also to be considered as an unknown parameter.
In order to determine the unknown parameters σ_0, δ_0, K_{I0}, a least-squares procedure can be applied. The procedure is described by the following steps:

1. Starting with a first estimation of the parameters the normalised stress intensity factor $K'_{I\,tip}$ is computed by

$$K'_{I\,tip} = K_{I0}/(\sigma_0\sqrt{W}) \qquad (13.1.12)$$

2. Parabolic interpolation of tables in [18] using bicubic splines for a/W, $K'_{I\,tip}$ and cubic splines for δ'_0 yields the K_{IR}-curve from eq.(13.1.11) for the actual parameter set σ_0, δ_0, K_{I0}.
3. The least-squares routine compares the calculated R-curve with the experimental R-curve and determines the sum of squares according to

$$S^2 = \sum (K_{IR,calc} - K_{IR,exp})^2 \qquad (13.1.13)$$

The routine changes the parameter set (σ_0, δ_0, K_{I0}) as long as a minimum of S^2 is reached. In this way, the best parameter set in least-squares terms is determined. For practical use the Harwell-Routine VA02A may be recommended.

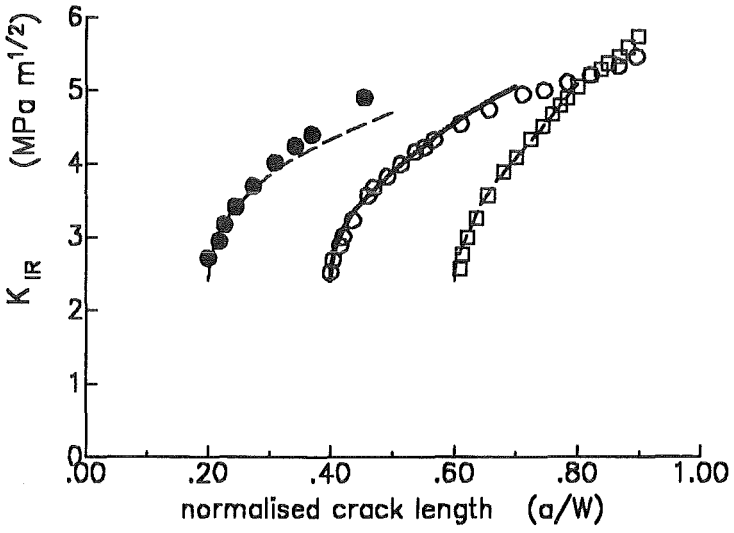

Figure 157. R-curves for alumina. R-curves measured by Steinbrech et al. [12] compared with curves calculated with the parameters from the least-squares procedure, (solid curve: fitted R-curve, dashed curves: predicted R-curves).

A series of R-curve data for coarse-grained Al_2O_3 has been given by Steinbrech et al. [12]. The original data expressed by energy release rates were converted with (E=360GPa, ν=0.22) into K_{IR} data. Figure 157 shows the data measured with specimens of W=7mm thickness. As the result of the fitting-procedure performed with the data for a_0/W=0.4 it was found:

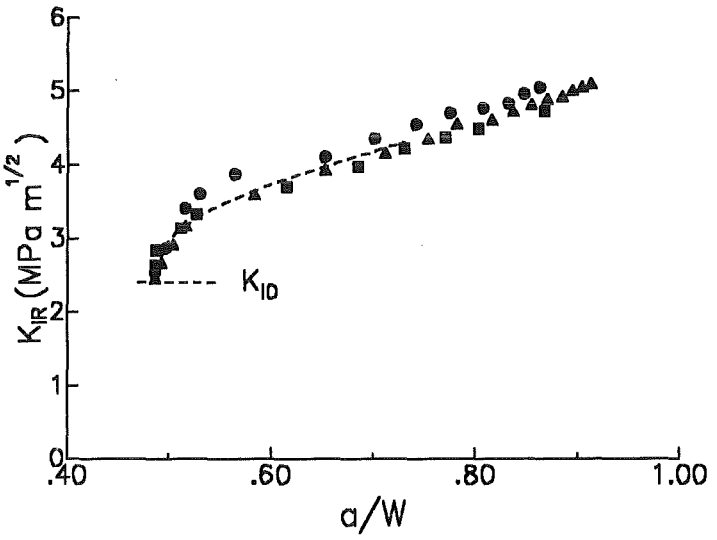

Figure 158. R-curve for alumina. R-curves represented in fig.158, compared with curves calculated with the parameters from the least-squares procedure, (dashed curve: fitted R-curve).

$$\sigma_0 = 42MPa \ , \ \delta_0 = 0.41\mu m \ , \ K_{I0} = 2.4MPa\sqrt{m}$$

The fitting curve corresponding to these parameters is plotted as a solid line in fig.157. By use of this parameter set also the R-curves for $a_0/W = 0.2$ and 0.6 were calculated. The results are introduced in fig.157 as dashed lines. The agreement is excellent for $a_0 = 0.6$, and also for $a_0/W = 0.2$ the experimental results can be described well. But for large crack extension deviations are evident.

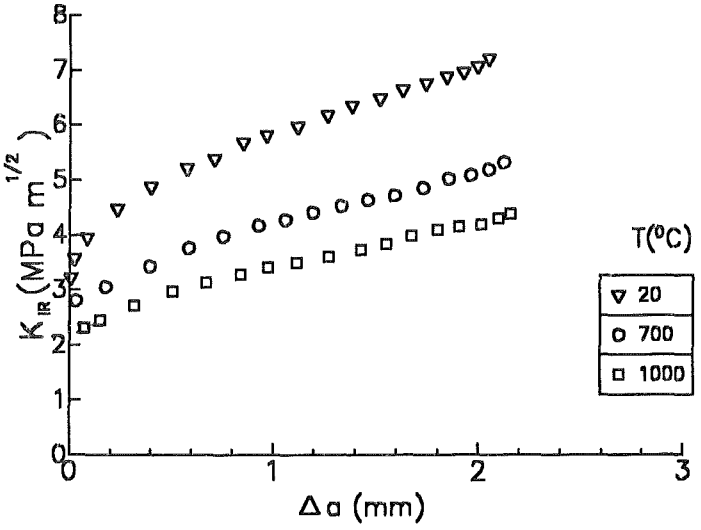

Figure 159. R-curves at elevated temperatures. R-curves for Al_2O_3 at different temperatures measured by Mundry [95].

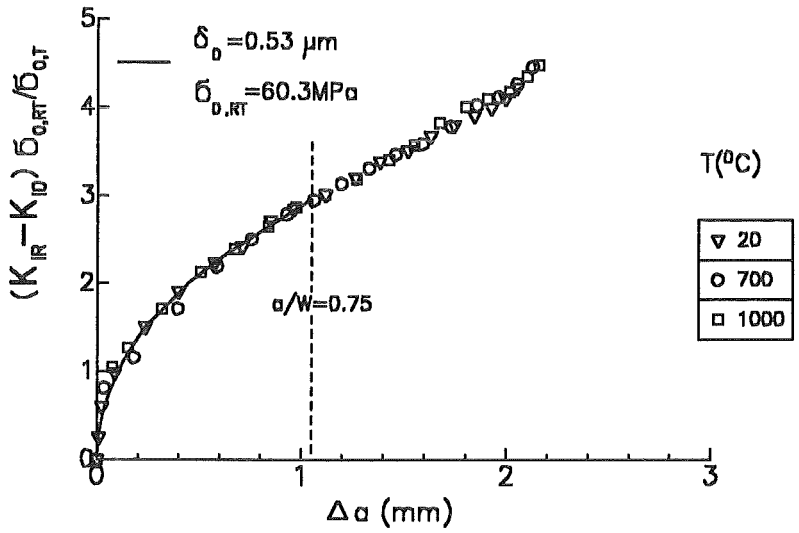

Figure 160. Normalised master-curve. R-curves of fig.159 in a normalised representation, compared with curves calculated with the parameters from the least-squares procedure (solid curve).

R-curve measurements made on coarse grained Al_2O_3 at elevated temperatures were reported by Mundry [95]. The material (AF997, Desmarquest) showed a mean grain size of 16μm. After recalculation in terms of stress intensity factors using the Young's moduli 368GPa for room temperature, 335GPa for 700°C and 278GPa for 1000°C ([95]), the R-curves in fig.159 were obtained.

Method	Grain size (μm)	σ_0 (MPa)	δ_0 (μm)	K_{I0} ($MPa\sqrt{m}$)	n	lgA^*	fig.162
$K_{I\,appl} - \Delta a$ [12] [18]	17	42	0.41	2.5			(1)
$da/dt - K_{I\,appl}$ [18]	20	46.4	0.95		25	-2.97	(2)
strength distribution [51]	20	120	1				
$da/dt - K_{I\,appl}$ [18]	3.2(i)	88.8	0.224		25	-0.7	(3)
$K_{I\,appl} - \Delta a$ [72]		44	0.25	2.5			(4)
$K_{I\,appl} - \Delta a$ [72] [95]	16	60.3	0.53	2.95			(5)

Table 3. Fracture mechanical data. Numbers in the last column refer to fig.162; (*i*) this material shows an inhomogeneous grain size distribution with maximum grains of $\simeq$25μm grain size.

The fitting-procedure was applied under the assumption that δ_0 is independent of temperature. The room-temperature data were found to be

$$\sigma_0 = 60.3MPa \;,\; \delta_0 = 0.53\mu m \;,\; K_{I0} = 2.95MPa\sqrt{m}$$

Figure 160 shows the data for all temperatures in a normalised representation. In addition, the curve computed with the fitted bridging parameters is shown in fig.160. The agreement is very good. The temperature dependencies of σ_0 and K_{I0} are shown in fig.161. Both fracture mechanical parameters decrease with increasing temperature. The nearly linear decrease of the maximum bridging stresses σ_0(T) indicates that there is a contribution to σ_0 due to temperature de-

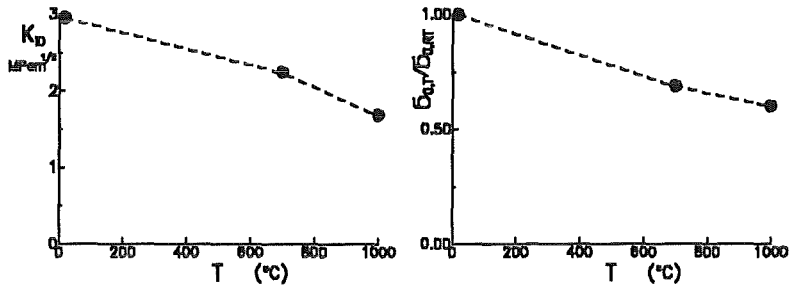

Figure 161. R-curve parameters. Stress intensity factor K_{I0} for the onset of stable crack propagation and maximum bridging stress σ_0 vs. temperature.

pendent internal stresses which are caused by the anisotropy of the thermal expansion coefficient in Al_2O_3. The reduction of internal stresses between the grains may also be responsible for the decreasing K_{I0}.

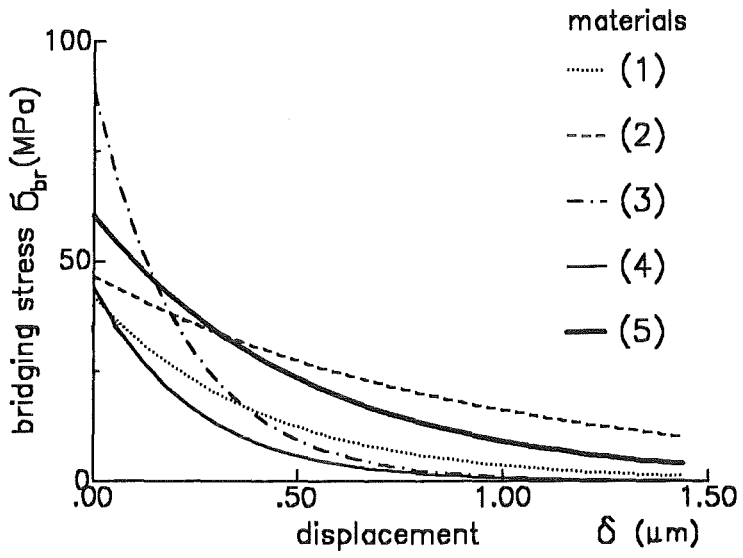

Figure 162. Bridging relations. Bridging relations from macrocracks (numbers refer to Table 3)

13.1.2 Evaluation of bridging parameters from constant load tests

The relationship between crack growth rate and stress intensity factor can be determined by applying a load to specimens with macrocracks and measuring the crack growth directly or indirectly from the change of the compliance of the specimens. Other methods are using specimens with natural flaws applying indirect fracture mechanics methods to obtain the $da/dt - K_I$-relation. Assuming a power-law relation between da/dt and K_I

$$\frac{da}{dt} = AK_I^n = A^*\left(\frac{K_I}{K_{Ic}}\right)^n \qquad (13.1.15)$$

the parameters A (or A^*) and n can be obtained from the experimentally obtained relation between the fracture stress and the loading rate (dynamic bending test) or from the relation between lifetime and stress. A modified lifetime method which does not require the assumption of a power law was developed in [96].
It was shown by several authors [97], [98], [99], [100], that discrepancies between results from specimens with macrocracks and from specimens with natural flaws can occur. This behaviour can be related to the increase in crack growth resistance with increasing crack extension.
In this section results of crack growth measurements for alumina from specimens with macro- and microcracks are compared. From the results the crack growth resistance curve is evaluated.
The tests with macrocracks were performed with single-edge-notched specimens of size 3.5x4.5x50mm. The notch in the center of the specimen was prepared with a diamond saw. The notch depth was 2.245±0.01mm, the notch width 50μm. The specimens were loaded in three-point bending with a constant load P. The distance of the loading rollers was 45mm. The tests have been performed at room temperature in normal air environment for material I and in water for material II.
The time dependent displacement δ was measured as shown in fig.163 in the center of the specimen. For some tests the crack length was also measured at the surface using a travelling microscope. It was observed that immediately after load application several cracks developed simultaneously. After some crack extension only one of them continued to propagate.
The tests with specimens containing natural flaws were obtained from the scatter of the lifetime of tests with constant load applying the modified lifetime method [96]. The results represent the initial crack growth rate of natural cracks at the beginning of a constant load test. The details of the evaluation are published elsewhere [7],[101]. Here only the final results are reported.

3. Experimental results and data evaluation
An example of the change of the displacement $\Delta\delta$ with time is shown in in fig.163. The general trend is first a decrease in the displacement rate $d\Delta\delta/dt$ and a steep increase before final fracture. In some specimens with low loads crack arrest was observed. From the displacement the crack length a and from the crack length a the stress intensity factor K_I was calculated.
In a first approximation the crack length has been evaluated by linear-elastic analysis from the compliance neglecting the effect of R-curve.
In fig.163. the change in the crack length Δa_{comp} obtained from the change of the compliance with time is plotted versus the optically measured length of the dominating crack Δa_{opt} for a specimen with a load corresponding to an initial stress intensity factor of $K_{Ii}/K_{Ic}=0.8$. For small Δa the compliance method leads to an overestimation and for larger Δa to an underestimation of the optically measured crack length. This behaviour is in agreement with measurements reported by Hübner and Jillek [2].
The overestimation could result from the development of several small cracks shortly after load application. The underestimation obviously is related to crack border interactions leading to the R-curve behaviour as described in section 4.
In the used procedure the two methods were combined. Direct observation of the crack tip location in longer time steps together with the continuously recorded displacements in the load line provide all information necessary to determine v-K-curves.

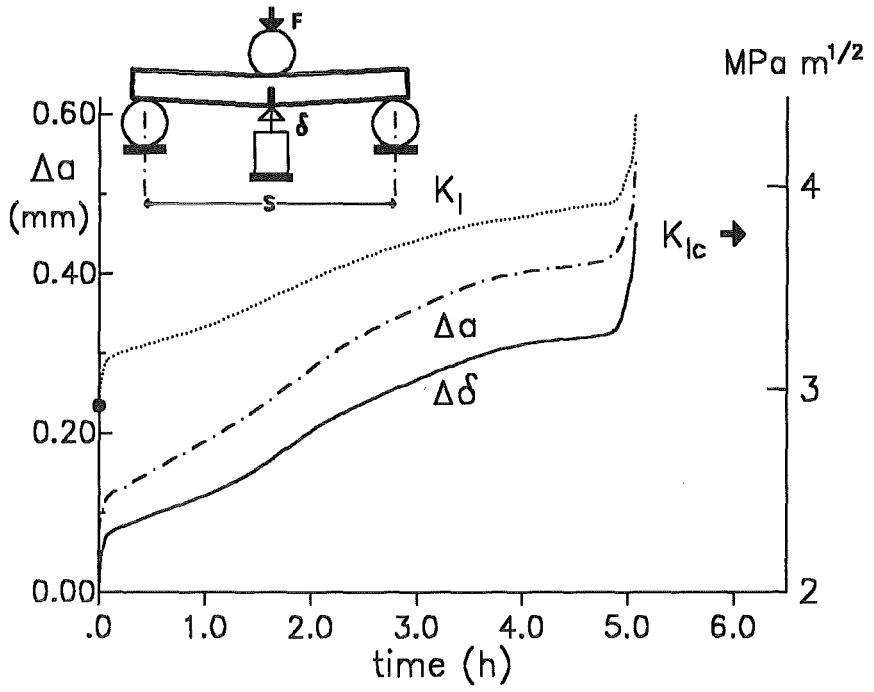

Figure 163. Constant load test. Displacement measurements in constant load tests with notched bending bars.

The fracture toughness obtained from 4-point-bending tests with a saw cut of 50μm width (SENB) is introduced in order to show that the stress intensity factors $K_{I\,appl}$ occuring in the static tests can be significantly higher than the "fracture toughness".
In fig.165 $da/dt - K_{I\,appl}$-curves for different applied stresses are plotted with the crack length obtained from a_{comp}. Two typical types of $da/dt - K_I$-curves can be seen. Tests with low initial stress intensity factors show first a decrease of the crack growth rate with increasing crack length and therefore increasing $K_{I\,appl}$. The crack growth rate drops by several orders of magnitude within a small amount of crack extension. After a large range with nearly constant crack growth rate the crack growth rate increases until final fracture. For the lowest K_{Ii} crack arrest was observed.
Cracks starting with a high initial stress intensity factor K_{Ii} (caused by a higher load applied) exhibit an approximatively constant crack growth rate until an increase to final fracture.
Figure 164 also contains the results of tests with natural cracks from [7]. These results can be described by eq.(13.1.15) with $A^* = 5 \cdot 10^{-4}$m/s, n = 38.6.
Results of crack growth measurements for alumina from specimens with macrocracks are reported in [20]. Two commercially available materials were investigated:

- material I : 99.6%-Al_2O_3 $K_{Ic} = 3.3MPa\sqrt{m}$, average grain size 20μm.
- material II: 99.6%-Al_2O_3 (hipped) $K_{Ic} = 4MPa\sqrt{m}$; this material shows an inhomogeneous grain size distribution with a mean grain size of 3.2μm and maximum grains of $\simeq$25μm size.

The results reported in [20] were obtained with single-edge notched specimens, 3.5x4.5x50mm in size, loaded in three-point bending with a constant load. The notch in the center of the specimen was prepared with a diamond saw. The notch depth was 2.245$\pm$0.01mm, the notch width 50μm.
In figs.165 and 166$da/dt - K_{I\,appl}$-curves are plotted for different stresses applied. Two types of $da/dt - K_I$-curves can be seen. First, a decrease of the crack growth rate with increasing crack length and therefore increasing $K_{I\,appl}$ is obvious. The crack growth rate drops by several orders of magnitude within a small amount of crack extension. After a large range with a nearly constant crack growth rate the crack growth rate increases until final fracture. For the lowest K_{Ii} for both materials crack arrest was observed.

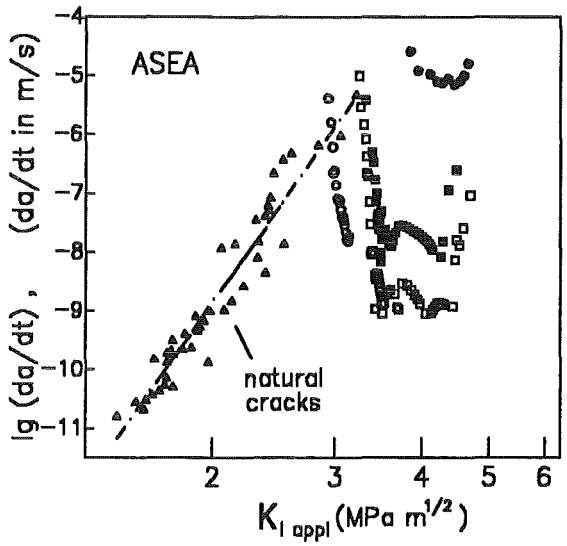

Figure 164. Natural cracks compared with macro-cracks. v-K-curves for material II; triangles: specimens with natural flaw population, other symbols: macro-cracks.

Whilst in case of stable crack extension the value $K_{I\,tip}$ is known, the crack-tip stress intensity factor changes during crack propagation in constant load tests.
In order to determine the parameters σ_0, δ_0 from constant load tests, also a least-squares procedure is applied. The treatment is outlined for the special case that the subcritical crack growth is described by a power law relation

$$v = \frac{da}{dt} = AK_I^n = A^*(K_I/K_{Ic})^n \tag{13.1.16}$$

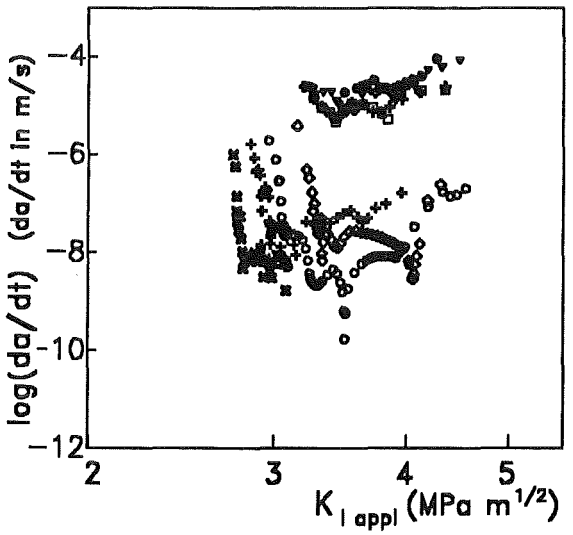

Figure 165. v-K-curves for alumina. $v - K_I$ –curves for specimens with macrocracks from static bending tests (material I) [20]; $K_{Ii} = 2.72/2.96/3.06/2.82/3.20/3.21/3.25 MPa\sqrt{m}$.

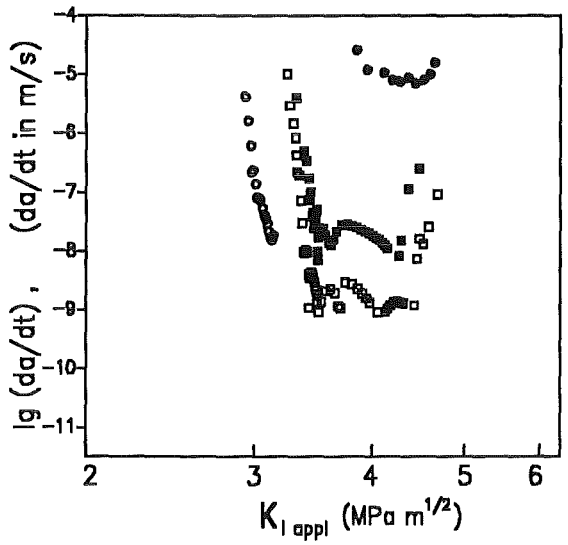

Figure 166. v-K-curves for alumina. $v - K_I$ –curves for specimens with macrocracks from static bending tests (material II) [20]; ($K_{Ii} = 2.93/3.25/3.32/3.85 MPa\sqrt{m}$).

- The procedure starts with an estimated initial combination of parameters (σ_0, δ_0, A^*, n). For any data point ($K_{I\,appl}$, a/W) the crack-tip stress intensity factor $K_{I\,tip}$ is calculated, and using eq.(13.1.16) the subcritical crack growth rate v_{calc} is calculated.

- The calculated (v_{calc}) and the measured crack growth rates v_{meas} are intercompared and the sum of squares is determined by

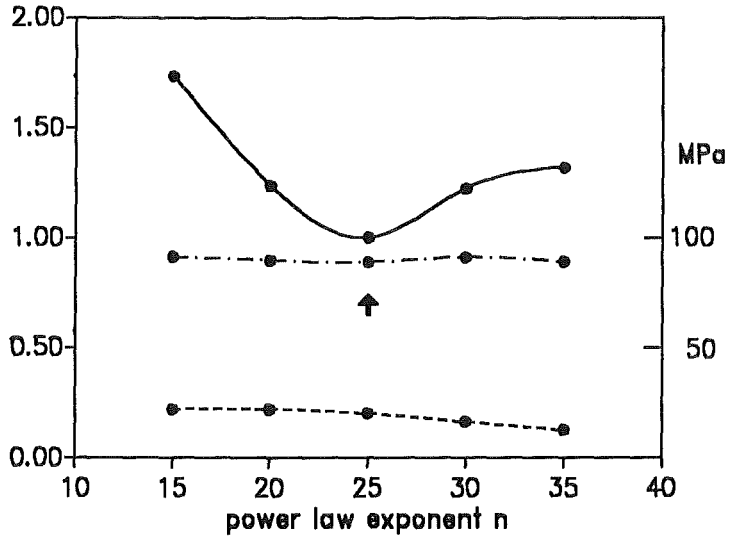

Figure 167. Fit-data. Least-squares results for fixed exponents n; S^2/S^2_{min} (solid curve, left hand scale), δ'_0 (dashed curve, left hand scale), σ_0 (dash-dotted, right hand scale): material II.

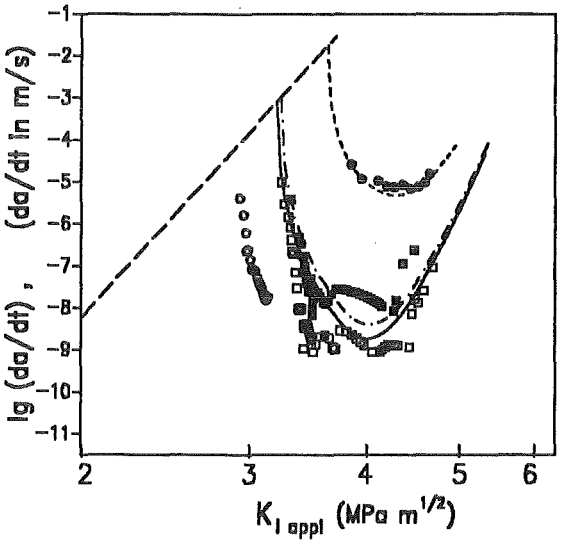

Figure 168. Comparison between measurement and fit. $v - K_{I\,appl}$ –curves for material II calculated with the fitted parameter set (dashed straight line: $v = f(K_{I\,tip})$).

$$S^2 = \sum (\log(v_{calc}) - \log(v_{meas}))^2 \qquad (13.1.17)$$

- Further treatment by a least-squares procedure is similar to that for stable crack propagation apart from the fact that now a set of 4 parameters are determined.

The result of calculation is:

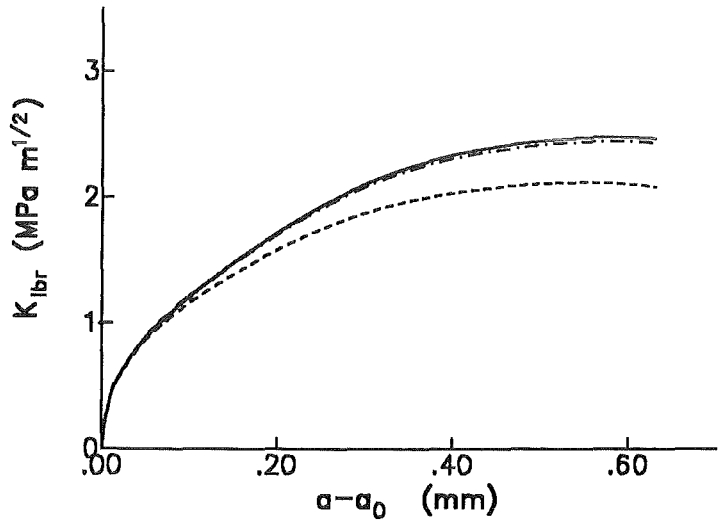

Figure 169. R-curve. R-curves for material II calculated with the fitted parameter set and $K_{II} = 4MPa\sqrt{m}$ (lines as in fig.19).

material I: $\sigma_0 = 46.4MPa$, $\delta_0 = 0.95\mu m$, $\log A^* = -2.97$, $n = 25$

material II: $\sigma_0 = 88.8MPa$, $\delta_0 = 0.224\mu m$, $\log A^* = -0.7$, $n = 25$

In earlier investigations the subcritical crack growth behaviour of natural cracks was determined for material I [7] and material II [101] by application of a modified lifetime method [96] ignoring possible R-curve effects. The result was $n = 38$ for material I and $n = 20$ for material II. The discrepancies in the n-values for the macro-cracks may be caused either by fundamental differences in the subcritical crack growth behaviour of natural, small cracks compared with artificial macro-cracks or/and by intolerable influences of the R-curve on the evaluation procedure for the natural cracks.

To check the accuracy of the parameters determined (σ_0, δ_0, A^*, n), the least-squares sums S^2 - normalised to the minimum value S^2_{min} - are plotted in in fig.167 for a number of power law exponents n. The dashed line represents δ'_0 and the dash-dotted curve shows σ_0.
In fig.168 the $v - K_{I\,appl}$ —curves - calculated with the bridging parameters of material II - are plotted for several initial stress intensity factors K_{Ii}. The dashed straight line describes the power law relation $v = AK_{tip}^n$. Finally, fig.169 shows the R-curve calculated with the fitted material data.
$v - K_I$ —curves vor specimens with natural flaw population were obtained with the modified lifetime method. A power law is found with an exponent of $n = 19$. Obviously the crack growth behaviour is - in terms of $K_{I\,appl}$ as the abscissa - strongly different from that of the macroscopic cracks (see fig.164). This is a significant indication for an R-curve influence, at least in case of the macro-cracks.

13.2 Determination of bridging stresses from crack profiles

In order to determine the relation between bridging stresses σ_{br} and the crack opening displacement (COD) δ, $\sigma_{br} = f(\delta)$, one can evaluate the CODs observed during stable crack propagation. Such evaluations were performed by Rödel et al. [23] on coarse-grained alumina with the "Round-Compact-Tension" specimen (RCT). In their computations they used a Barenblatt relation between bridging stresses and crack opening displacements. In [102], it has been shown how the fracture-mechanics weight-function method can be applied to evaluate the bridging-stress relation from displacement measurements without the restrictions imposed by the Barenblatt model. As an example of interest the results of Rödel et al. will be considered below.

13.2.1 The weight function method

The determination of bridging stresses from COD-measurements can be done by application of the weight function method. The basic relations are repeated here once more. For any given stress distribution $\sigma(x)$ in the uncracked component the stress intensity factor K_I for a crack of depth a results in

$$K_I = \int_0^a h(x, a)\sigma(x)\, dx \quad , \tag{13.2.1}$$

where h is the weight function. As shown by Rice [29], the weight function is related to the CODs of a reference load case (subscript r) and the related reference stress intensity factor

$$h(x, a) = \frac{E'}{K_{Ir}} \frac{\partial}{\partial a} \delta_r(x, a) \tag{13.2.2}$$

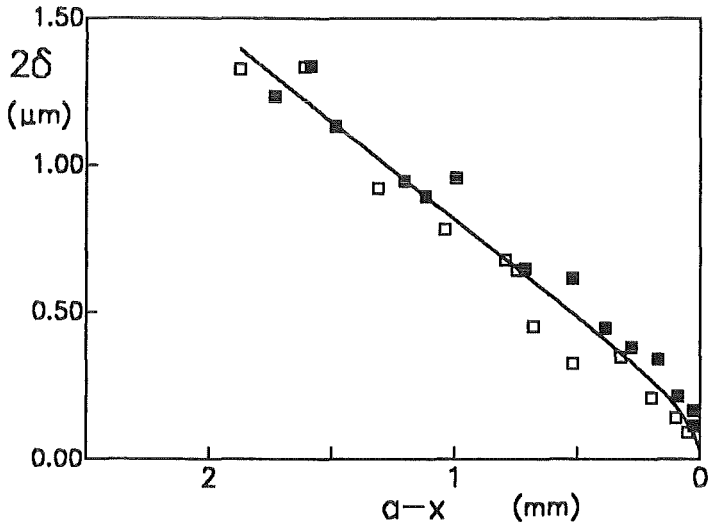

Figure 170. Profile of a crack in alumina. COD measurements from Rödel et al. [23] for $K_{I\,appl}=4.6\text{MPa}\sqrt{\text{m}}$ (symbols: two data-sets of the same specimen), and least-squares fit according to (13.2.6) with $N=2$, (solid line).

where $E' = E/(1-\nu^2)$ is the plane strain Youngs modulus (ν = Poisson's ratio). From eqs.(13.2.1) and (13.2.2) the crack surface displacements can be calculated from the stress distribution by [19]

$$\delta(x) = \frac{1}{E'} \int_0^a \int_{\max(x,x')}^a h(a',x)h(a',x')\,\sigma(x')\,da'dx' \qquad (13.2.3)$$

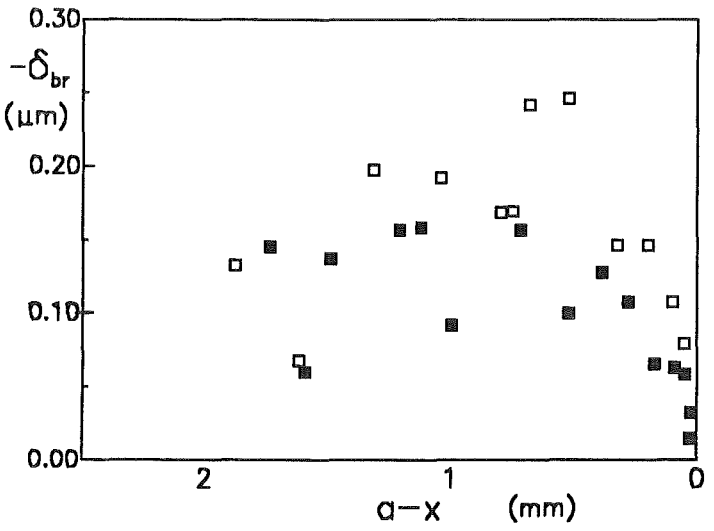

Figure 171. Bridging displacements. Bridging-displacements δ_{br} in the crack propagation zone.

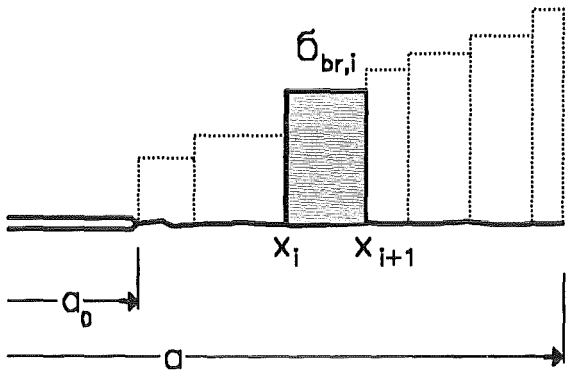

Figure 172. Prescribed type of stress distribution. The strip-loaded crack.

where x is the coordinate where the displacement is computed and x' is the location where the stress σ acts. If the externally applied stress σ_{appl} as well as bridging stresses σ_{br} act on the crack surfaces the total crack opening displacements result as

$$\delta(x) = \delta_{appl} + \delta_{br} = \frac{1}{E'}\int_0^a \int_{\max(x,x')}^a h(a',x)h(a',x')[\sigma_{appl}(x') + \sigma_{br}(x')]da'dx' \tag{13.2.4}$$

$$= \frac{1}{E'}\int_x^a K_{I\,appl}(a')h(a',x)\,da' + \frac{1}{E'}\int_0^a \int_{\max(x,x')}^a h(a',x)h(a',x')\sigma_{br}(x')da'dx'$$

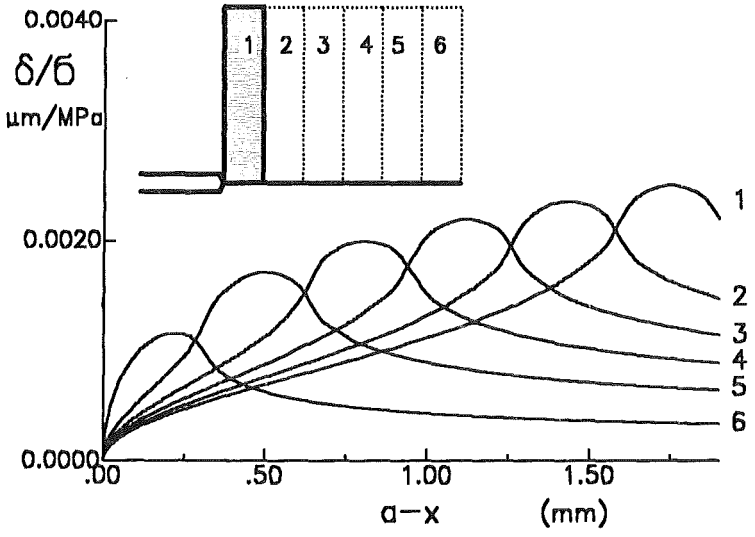

Figure 173. Bridging stresses. Influence function $g(x, x_i, x_{i+1}, a)$ for the strip partition given in the insert.

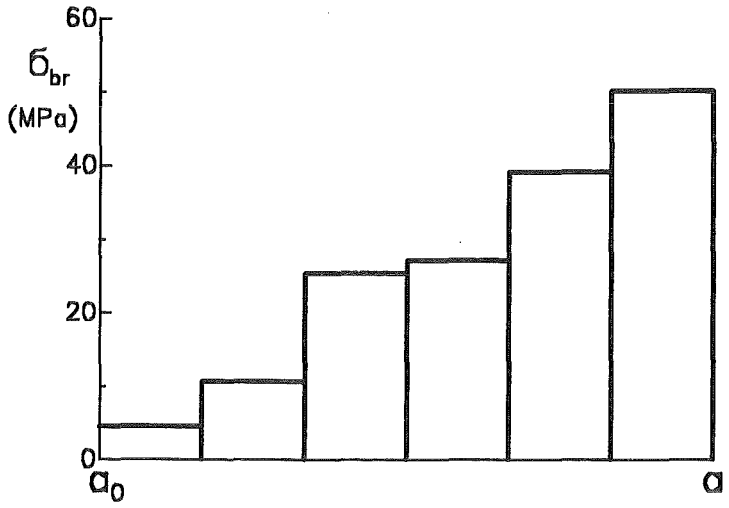

Figure 174. Displacements caused by strip loads. Distribution of bridging stresses along the crack-propagation line.

This relation is the basis for the evaluation of bridging stresses from crack opening profiles. The weight function for the RCT-specimen is given in [103] and the stress intensity factor solution has been derived by Newman [104].

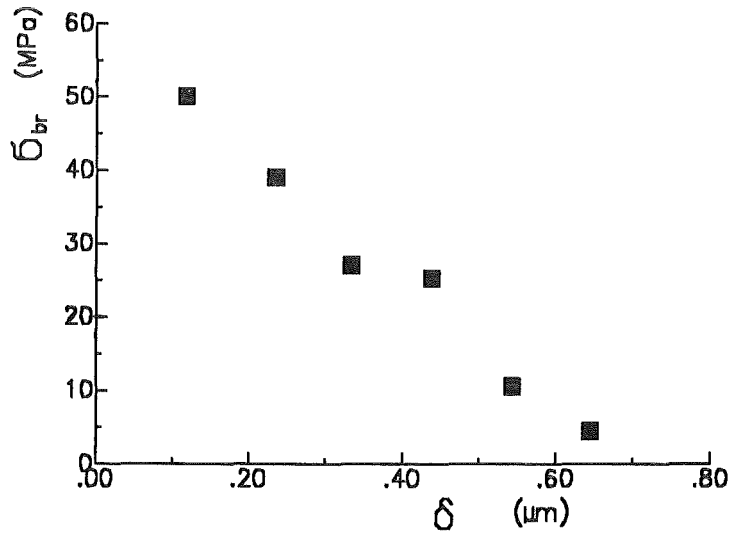

Figure 175. Bridging stresses. Bridging stresses as a function of the displacements at the centre of the strips.

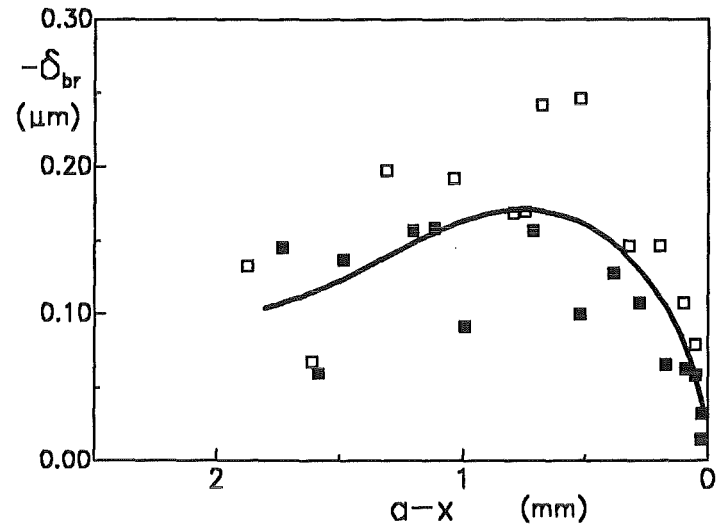

Figure 176. Bridging displacements. Comparison of the result of the power series procedure with the bridging displacements from fig.171.

13.2.2 Fracture mechanical evaluation of COD-measurements

In fig.170 the crack opening profile measured by Rödel et al. [23] is plotted versus the distance $\xi = a - x$ from the crack tip. The material investigated was a hot-pressed alumina with a grain size of 11μm. The RCT-specimens had a diameter of $D = 100$ mm, a thickness $t = 1$ mm and an initial starter crack size of $a_0 \simeq 20$ mm. The elastic constants were $E = 400$ GPa and $\nu = 0.25$. From the data of fig.170 one can easily determine the crack-tip fracture toughness K_{I0}, i.e. the crack-tip stress intensity factor in case of stable crack propagation. Since the near-tip displacements are square-root-shaped [1]

$$\delta_{tip} = \sqrt{\frac{8}{\pi}} \frac{K_{tip}}{E'} \sqrt{a - x} \tag{13.2.5}$$

we can express the CODs by a least-squares fit according to

$$\delta = \sum_{n=0}^{N} B_n \left(1 - \frac{x}{a}\right)^{n+1/2} \tag{13.2.6}$$

where the coefficient B_0 is related to the crack-tip fracture toughness K_{I0} by

$$K_{tip} = K_{I0} = \sqrt{\pi/8} \frac{E'}{\sqrt{a}} B_0 \tag{13.2.7}$$

A 3-terms fit ($N = 2$) to the data of fig.170 results in mrom a 3-terms fit ($N = 2$) it results

$$\delta_{br} = 0.2884\sqrt{a - x} + 0.11857(a - x)^{3/2} + 0.000297(a - x)^{5/2} \tag{13.2.8}$$

(δ_{br} in μm, a, x in mm) and, consequently, it results from eq.(13.2.7) $K_{I0} = 2.4\text{MPa}\sqrt{\text{m}}$. The fitting curve is entered in fig.170 as a solid line.

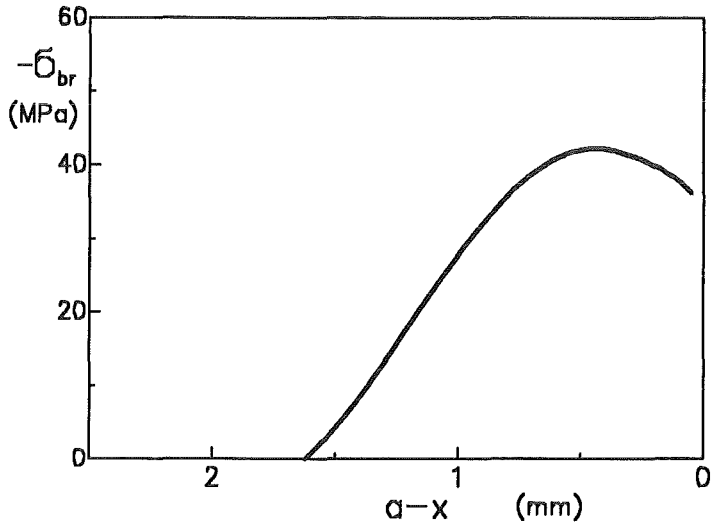

Figure 177. Bridging stresses. Distribution of bridging stresses along the crack propagation line.

The numerical computation of bridging stresses may be based on eq.(13.2.4) written in the form

$$\delta_{br} = \delta_{measured} - \frac{1}{E'} \int_x^a K_{I\,appl}(a')h(a', x)\, da' \qquad (13.2.9)$$

where the first term on the right hand side is known from the displacement measurements (fig.170) and the second can be computed from [103] and [104].
The bridging displacements resulting from (13.2.9) are plotted in fig.171. Using these data one can now determine the bridging stress distribution in the crack propagation zone by solving the integral equation

$$\frac{1}{E'} \int_0^a \int_{\max(x,x')}^a h(a',x)h(a', x')\, \sigma_{br}(x')\, da'dx' = \delta_{br} \qquad (13.2.10)$$

13.2.3 Numerical procedures for the evaluation of crack profile measurements

There are several procedures known to evaluate σ_{br} from the integral equation (13.2.10). The most familiar method is to devide the interval $a_0 \leq x \leq a$ in N intervals of same width $\Delta x = (a - a_0)/N$. Then the integrations are replaced by sums leading to a system of N linear equations. The solution yields a number of N stress values corresponding to the N intervals. Since the weight function is singular for $x' \rightarrow a'$, the number of intervals must be very high.

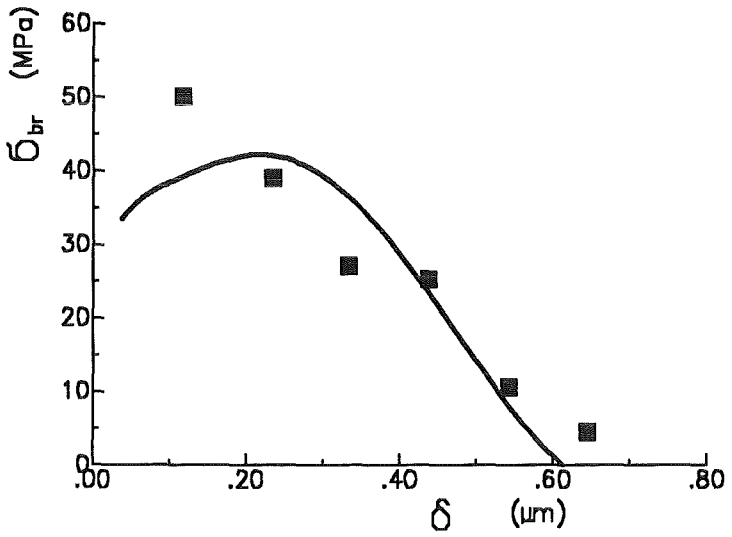

Figure 178. Bridging stresses. Bridging stresses as a function of crack opening displacement; (squares: results from fig.

13.2.3.1 Decomposition of the stress distribution by strips of finite width

A simple possibility of solving eq.(13.2.10) will be outlined. We divide the range of crack propagation, $a_0 \leq x \leq a$, into N (not necessarily identical) strips with constant bridging stress in a strip. In fig.172 the i-th strip with the bridging stress $\sigma_{br,i}$ is illustrated. The profile of the bridging displacements caused by the bridging stresses in the i-th strip is given by

$$\delta_{br,i}(x) = \sigma_{br,i}\,\frac{1}{E'}\int_{\max(x,x_i)}^{a} h(a',x)\left[\int_{x_i}^{a_{\min}} h(a',x')dx'\right]da' = \sigma_{br,i}\,\mathbf{g}(x, x_i, x_{i+1}, a) \qquad (13.2.11)$$

where

$$a_{\min} = \min(a', x_{i+1}) \qquad (13.2.12)$$

After analytical evaluation of the inner integral in (13.2.11) the function **g** can be expressed as

$$\frac{\delta_{br,i}(x)}{\sigma_{br,i}} = \mathbf{g}(x, x_i, x_{i+1}, a) = \sqrt{\frac{2}{\pi}}\,\frac{1}{E'}\int_{\max(x,x_i)}^{a} h(a',x)\sqrt{a'}\left\{2\left(\sqrt{1-\frac{x_i}{a'}} - \sqrt{1-\frac{a_{\min}}{a'}}\right)\right.$$

$$\left. + \sum_{\nu,\mu=0}^{4} \frac{A_{\nu\mu}}{\mu+3/2}\,\frac{(a'/W)^{\nu}}{(1-a'/W)^{3/2}}\left[\left(1-\frac{x_i}{a'}\right)^{\mu+3/2} - \left(1-\frac{a_{\min}}{a'}\right)^{\mu+3/2}\right]\right\}da' \qquad (13.2.13)$$

The total bridging displacement field can be composed by

$$\delta_{br}(x) = \sum_{i=1}^{N} \sigma_{br,i}\,\mathbf{g}(x, x_i, x_{i+1}, a) \qquad (13.2.14)$$

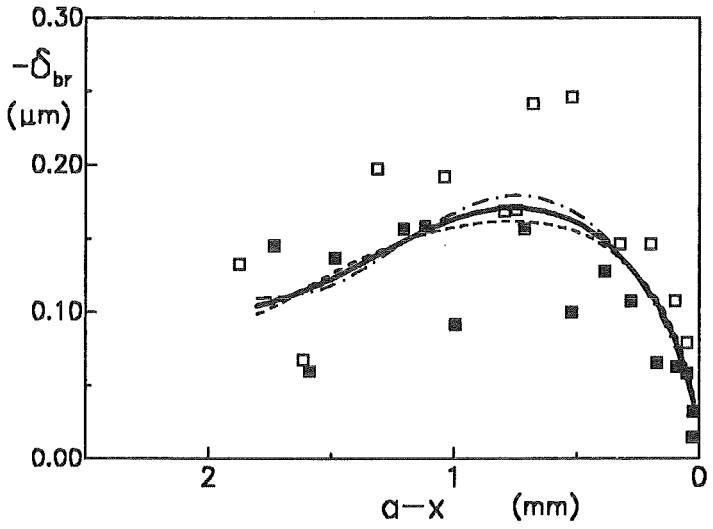

Figure 179. Bridging stresses. Bridging stresses as a function of crack opening displacement.

The function **g**, defined by eq.(13.2.11), is an influence function which describes the displacements resulting from a strip-shaped stress with $\sigma = 1$MPa. Figure 173 illustrates this influence function for a special choice of strip partition. If now at N locations the crack opening displacements are known and the N functions $\mathbf{g}(x, x_i, x_{i+1}, a)$ have been determined, we obtain a system of N linear equations from which the unknown N values of $\sigma_{br,i}$ result.
In a fitting-procedure the unknown set of stresses σ_i was determined. The resulting stress distribution is shown in fig.174. Figure 175 finally shows the bridging stresses as a function of the crack surface displacements δ. For the displacements in fig.175 the values in the centres of the strips were used. In principle, the number of strips can be increased. But for the present data the relative high scatter (see representation in fig.171) would not allow the stresses to be determined with higher accuracy.

13.2.3.2 Power-series expansion of the stress distribution

A second possibility consists in using a power-series representation of the bridging stress distribution. If we assume that the bridging stress is given by an adequately smooth function of the displacement, the related Taylor-series reads

$$\sigma_{br}(\delta) = \sum_{n=0}^{\infty} \frac{1}{n!} \frac{\partial^n \sigma_{br}}{\partial \delta^n} \Big|_{\delta=0} \delta^n \qquad (13.2.15)$$

Since the near-tip COD-field is always square-root shaped, $\delta \propto \sqrt{a-x}$, the general stress vs. displacement relation must be of the type

$$\sigma_{br} = \sum_{n=0}^{\infty} D_n \left(1 - \frac{x}{a}\right)^{n/2} \qquad (13.2.16)$$

and cannot contain integer exponents only. Introducing eq.(13.2.16) into (13.2.10) results in an infinite system of linear equations

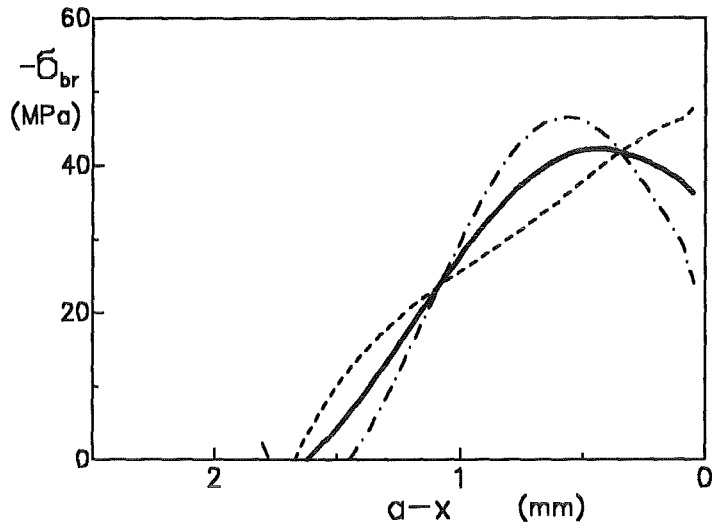

Figure 180. Bridging stresses. Bridging stresses as a function of crack opening displacement.

$$\sum_{n=0}^{\infty} D_n E_n(a,x) = \delta_{br} \tag{13.2.17}$$

where

$$E_n(a,x) = \frac{1}{H}\int_0^a \int_{\max(x,x')}^a h(a',x)h(a',x')\left(1-\frac{x'}{a}\right)^{n/2} da'dx' \tag{13.2.18}$$

For practical use a truncation of the infinite series (13.2.16) after the term $n = N$ is recommended

$$\sigma_{br} = \sum_{n=0}^{N} D_n\left(1-\frac{x}{a}\right)^{n/2} \tag{13.2.19}$$

The unknown (N+1) coefficients D_n can then be determined from a least-squares fit of the data in fig.171, represented by the dashed curve. Consequently, the bridging stress distribution is known from (13.2.19).
This procedure was applied also to the data shown in fig.171. As the result of the least-squares fit the bridging displacements, according to eq.(13.2.17), are entered as the solid line in fig.176. The related bridging-stress distribution $\sigma_{br} = f(a-x)$ is represented in fig.177 and, finally, the bridging-stress relation $\sigma_{br} = f(\delta)$ resulting from combining fig.170 with fig.177 is shown in fig.178.

Sensitivity of the procedure: A short study of sensititvity is given in figs.179 to 181. For the fitting procedure resulting in figs.176 to 178 all data points had the same weight. In a modified evaluation the data points with $a-x>1$mm entered the analysis with the weight 1.5 and the other data points with the weight 1. The results of the least-squares procedure are represented as the dashed curves in figs.179 to 181. In another case the inverse distribution of the weights was chosen, i.e. weight=1 for the data points with $a-x>1$mm and weight=1.5 for the data points closer to the crack tip. These results are indicated by the dash-dotted lines. One can conclude that a small deviation in the bridging displacements of fig.179 will have a significant influence on the bridging stresses.

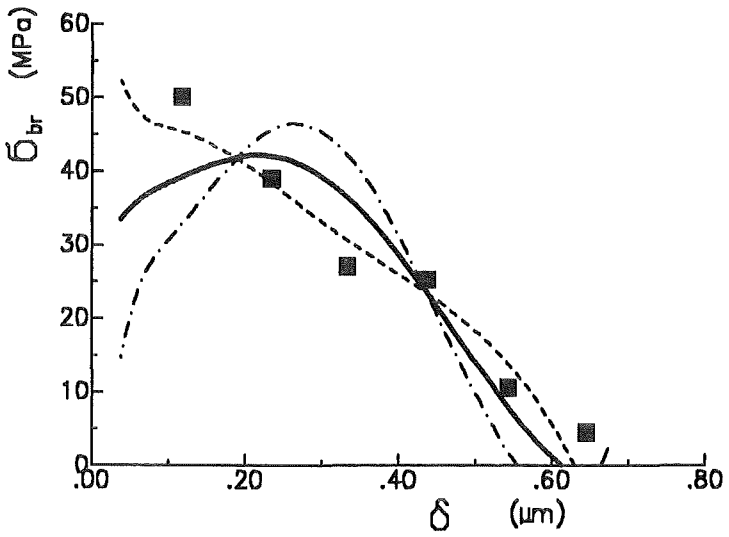

Figure 181. Bridging stresses. Bridging stresses as a function of crack opening displacement.

These differences make obvious that a very high experimental accuracy - leading to a low scatter in the function $\sigma_{br} = f(a - x)$ - is necessary for application of the COD-procedures. Such high accuracies can be reached, for instance, by moire interferometry.

13.2.3.3 Choice of special set-ups

A third procedure with the numerical expenditure significantly reduced is the application of specially chosen functions for the σ_{br} versus $(a - x)$ dependency. In [23] a set-up of type

$$\sigma_{br} = \sigma_{br,max}(1 - \beta(a - x))^{\gamma} \tag{13.2.20}$$

has been chosen, with the two free parameters β and γ determined from the measured displacements by a least-squares procedure. A small disadvantage of this method might be that

- the number of degrees of freedom is limited,
- the unknown dependency $\sigma_{br} = f(x/a)$, which, in principle, should be determined has to be prescribed, and, therefore, the bridging relation $\sigma_{br} = f(\delta)$ is restricted, as can easily be shown for the set-up (13.2.20).
  The Taylor-expansion of eq.(13.2.20) at $x = a$ yields the leading terms

$$\sigma_{br}/\sigma_{br,max} = 1 - \beta\gamma(a - x) + \frac{1}{2}\beta^2\gamma(\gamma - 1)(a - x)^2 \ldots\ldots \tag{13.2.21}$$

  and since $\delta \propto \sqrt{a - x}$ for $x \to a$, the resulting relation $\sigma_{br} = f(\delta)$ must start with

$$\sigma_{br} = \sigma_{br,max}\left(1 + c\delta^2 \ldots\ldots\right) \tag{13.2.22}$$

  Since the linear term in the expansion is not present, a linear dependency $\sigma_{br} = f(\delta)$ cannot result due to the special type of set-up chosen.
  In fig.182 the results of fig.175 are compared with the results of Rödel et al. [23] based on the simplified relation, eq.(13.2.20). This shows that in the specific case the approach of Rödel et al. is sufficiently accurate.

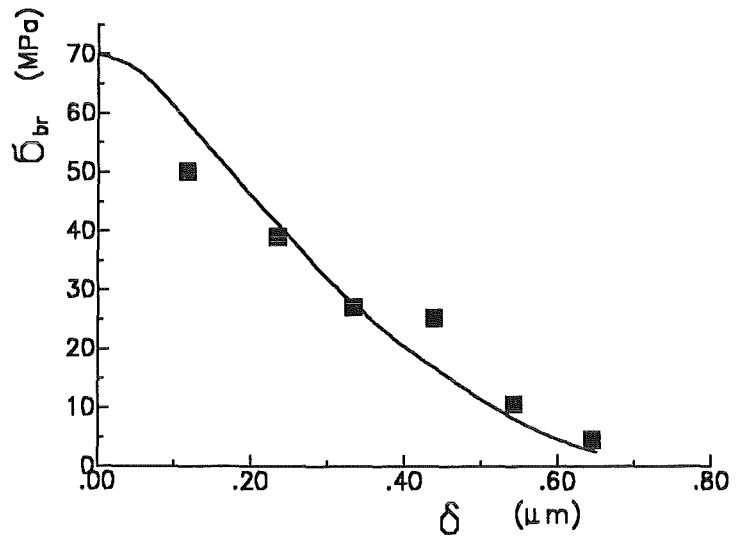

Figure 182. Bridging-stress relation. Comparison of the result of fig.175 with the result obtained by Rödel et al. [23] (curve).

13.2.4 Discussion of results

Several bridging-stress relations $\sigma_{br} = f(\delta)$ are used in the literature. Mai and Lawn [24] proposed a relation

$$\sigma_{br} = \left\{ \begin{array}{ll} \sigma_0(1 - \delta/\delta_0)^m & \text{for } \delta/\delta_0 < 1 \\ 0 & \text{for } \delta/\delta_0 > 1 \end{array} \right\} , \; m = 0,1,2,... \qquad (13.2.23)$$

If we assume that the characteristic displacement for which the bridging stresses vanish is Γ −distributed [18], it results for $m = 0$:

$$\sigma_{br} = \sigma_0 \left(1 + \frac{\delta}{\delta_0} \right) \exp(-\delta/\delta_0) \qquad (13.2.24)$$

and for $m = 1$:

$$\sigma_{br} = \sigma_0 \exp(-\delta/\delta_0) \qquad (13.2.25)$$

A fitting procedure was applied in order to be able to describe by these formulas the results of fig.175. Figure 183 shows the results for eq.(13.2.23) with $m = 1$ (dotted curve: $\sigma_0 = 59$MPa, $\delta_0 = 0.69\mu$m), for eq.(13.2.24) (solid line: $\sigma_0 = 58.6$MPa, $\delta_0 = 0.19\mu$m), and, finally, for eq.(13.2.25) (dashed line: $\sigma_0 = 75$MPa, $\delta_0 = 0.32\mu$m). The best representations seem to be given by eq.(13.2.23) with $m = 1$ and eq.(13.2.24).
For various Al_2O_3-ceramics parameters for eq.(13.2.25) were compiled in [78]. These data which were found in the ranges $40\text{MPa} < \sigma_0 < 120\text{MPa}$ and $0.22\mu\text{m} < \delta_0 \leq 1\mu\text{m}$ are in good agreement with the parameters found here.

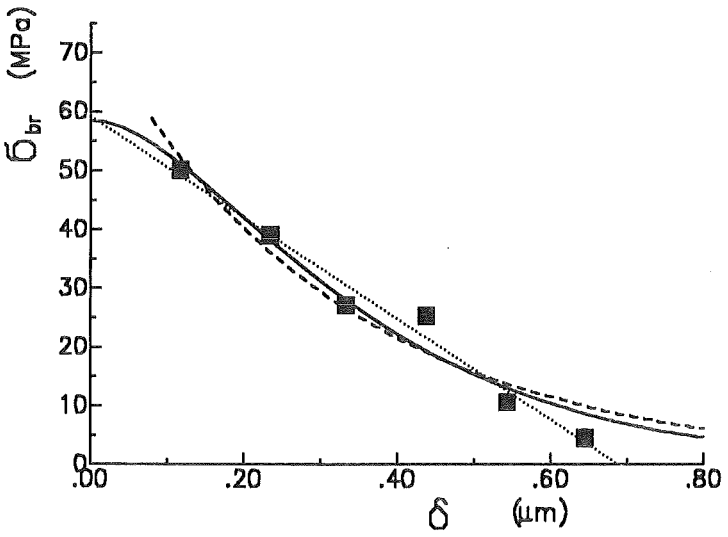

Figure 183. Bridging-stress relation. Fitting of several bridging-stress relations to the results of fig.175.

13.2.4.1 Evaluation of displacements obtained by Yu and Kobayashi

As mentioned before a high accuracy is necessary for the evaluation of the bridging-stress relation from displacement measurements. Such high accuracies can be reached, for instance, by moire interferometry. In [105] Yu and Kobayashi presented displacement measurements performed with specimens machined from SiC_W/Al_2O_3 and by application of moire interferometry. The cross-section of the specimen is shown in fig.184. A Chevron notch was prepared to create a sharp crack. In the bending bars a crack was generated by the single-edge-precrack-beam (SEPB) method, and the specimen was then loaded in a 3-point bending arrangement. The measured displacements are entered as squares in fig.185. The displacements of a crack without bridging effects were computed in [105] using the FE-method and entered as solid line in fig.185. According to $\delta_{br}(x) = \delta(x) - \delta_{appl}$, the displacements caused by the bridging stresses were computed and entered in fig.186. The result shows very little scatter, and by application of a smoothing procedure the curve plotted in fig.186 is obtained. Application of the procedure based on the power-series representation yields the bridging stresses depending on the distance from the crack tip (fig.187). The power series was truncated after 8 terms (N=7) and after 10 terms (N=9). As the result, the bridging stress (averaged over the whole thickness of the bending bar) is plotted. Finally, one obtains from figs.186 and 187 the bridging-stress relation plotted in fig.188. The characteristic shape of the $\overline{\sigma}_{br} - \delta$ –curve is in both cases the same. The real relation $\sigma_{br} - \delta$ is described in the range outside the Chevron notch.
From fig.188 we may conclude that the type of bridging relation is similar to that of eqs.(4.1.9) and (4.1.13) represented in fig.12.

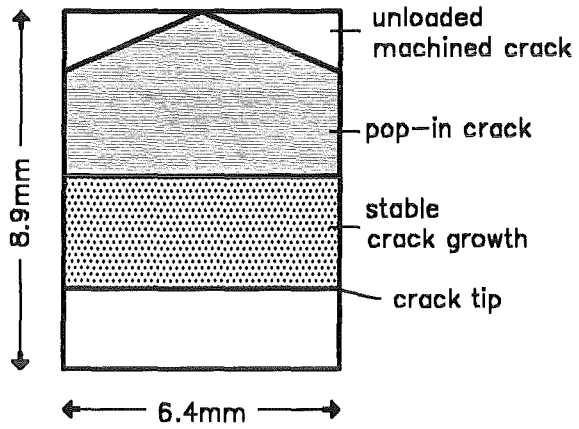

Figure 184. Specimen used by Yu and Kobayashi. The shaded area indicates the range of pre-cracking.

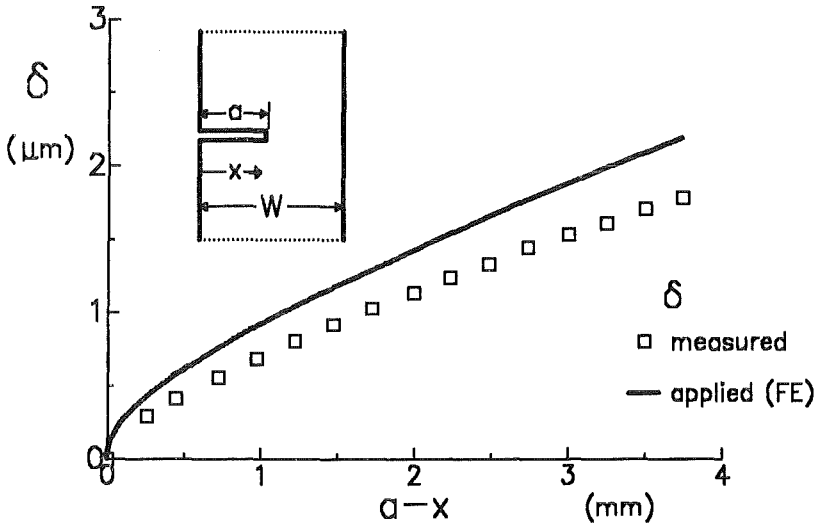

Figure 185. COD-measurements by a moire-technique. Measured displacements (squares) and displacements of the material free of bridging interactions (solid line), given by Yu and Kobayashi [105].

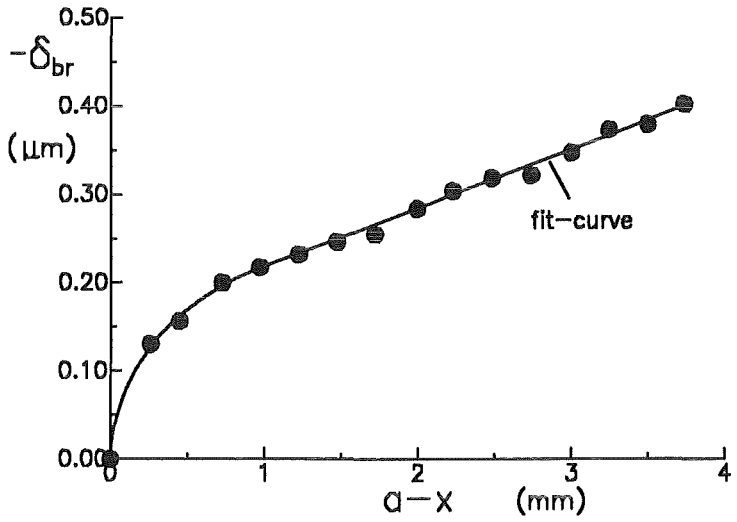

Figure 186. Bridging displacements. Displacements δ_{br} caused by the bridging stresses in the crack propagation zone.

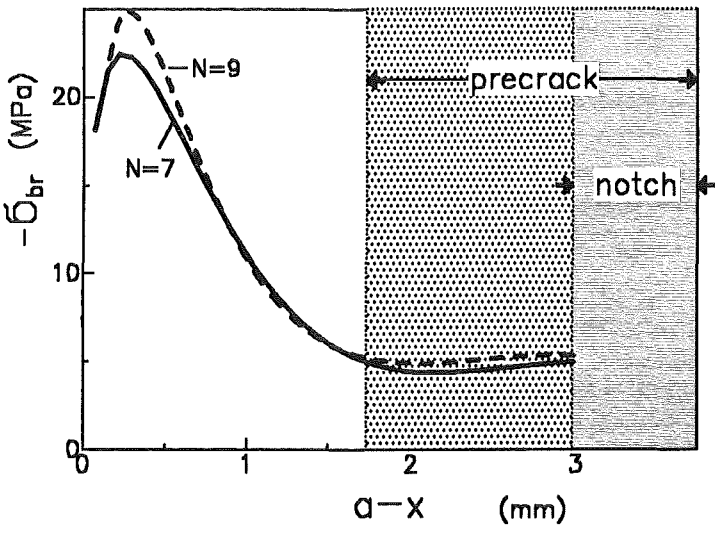

Figure 187. Bridging relation. Bridging stress as a function of the location $(a - x)$; shaded areas indicate the regions where the Chevron notch and the precrack extend.

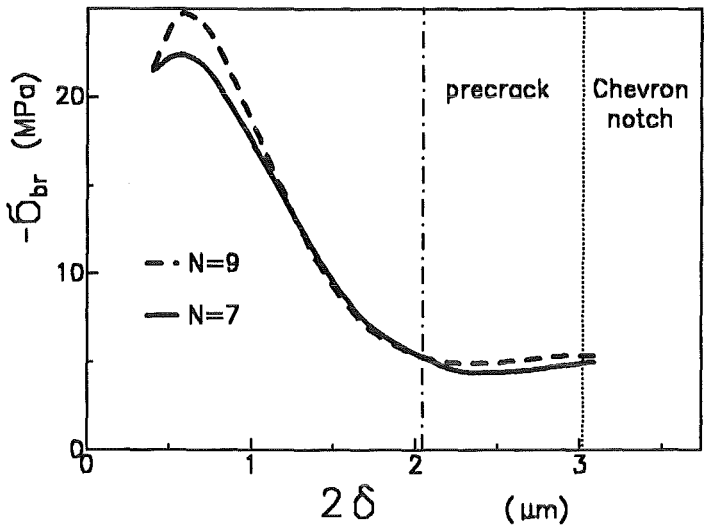

Figure 188. Bridging relation. Bridging stress as a function of crack opening displacement.

14. Different R-curves for macroscopic and microscopic cracks?

14.1 Experimental findings

As shown recently, beside macro-cracks also micro-cracks exhibit a rising crack resistance behaviour [115]. Results obtained by Steinbrech and Schmenkel [115] for coarse-grained Al_2O_3 are plotted in fig.189 (after some re-evaluation [106]) as energy release rates versus crack extension Δa. For the extensions up to 1mm of the macro-cracks no effect of initial crack length can be seen.

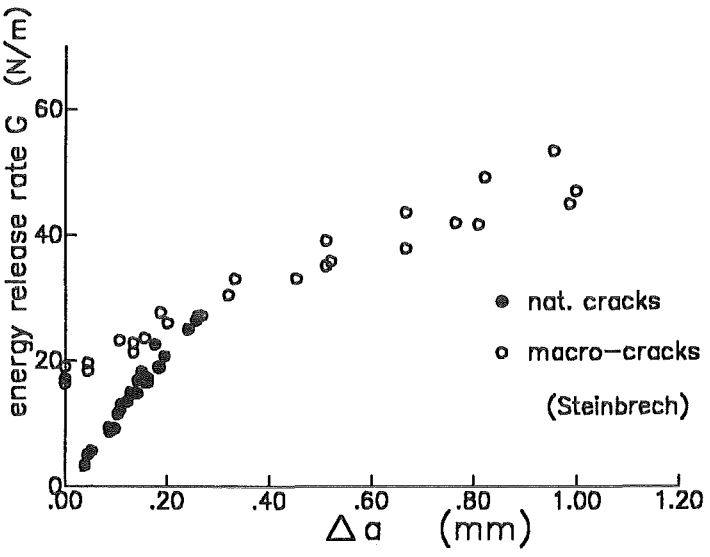

Figure 189. Macro- and micro-crack R-curves. R-curves for alumina obtained by Steinbrech [115].

The micro-crack results are strongly different from the macro-crack results obtained with SENB-specimens. It is amazing that the initially applied energy release rate - necessary to initiate stable crack extension - is extremely low compared with the macro-crack value G_{I0} and that the slope of the micro-crack curve is very high. An interpretation of this behaviour has been given in [106] based on residual stresses due to thermal mismatch. In the following the main features of this analysis will be explained and in addition the influence of subcritical crack growth will be considered.

Al_2O_3 shows a significant anisotropy of thermal expansion coefficient. Measurements on single crystals of Al_2O_3 yield [107]

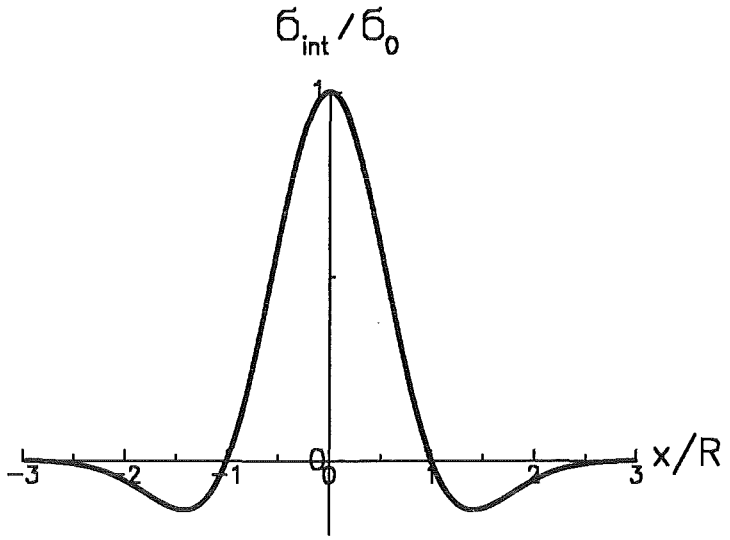

Figure 190. Residual stresses. Distribution of self-balanced residual stresses caused by thermal mismatch.

$$\alpha_{parallel\ to\ c-axis} \simeq 6.6 \cdot 10^{-6}/gradC \quad , \quad \alpha_{orthogonal\ to\ c-axis} \simeq 5.4 \cdot 10^{-6}/gradC$$

In a polycrystalline material the c-axis is randomly orientated. It is a simple consequence of statistics that clusters of grains must exist where the resulting averaged component of the c-axis is significantly different from the overall mean value of 1/3. Such a cluster is the reason for a local stress field. Starting from a stress-free state at sintering temperature, local mismatching of the thermal extension coefficient generates stresses during the cooling phase. Such a localized stress source will be called a "stress nest" here.
Since also the orientations of the clusters are randomly distributed, the macroscopic mean value of the thermal stresses must vanish. It is clear that the interaction of "stress nests" will complicate a theoretical treatment. To simplify the problem only one single stress nest will be considered in the following.

14.2 Fracture-mechanical model

In order to allow a fracture-mechanical analysis to be made the self-balanced internal stresses in a stress nest are modelled by

$$\sigma_{int} = \sigma_0\left[1 - (r/R)^2\right] \exp\left[-(r/R)^2\right] \qquad (14.2.1)$$

Figure 190 illustrates the stress distribution. σ_0 is the maximum stress and R represents a characteristic dimension of the stress nest. A circular crack with radius a situated in the sphere of influence of $\sigma(r)$ then exhibits a stress intensity factor

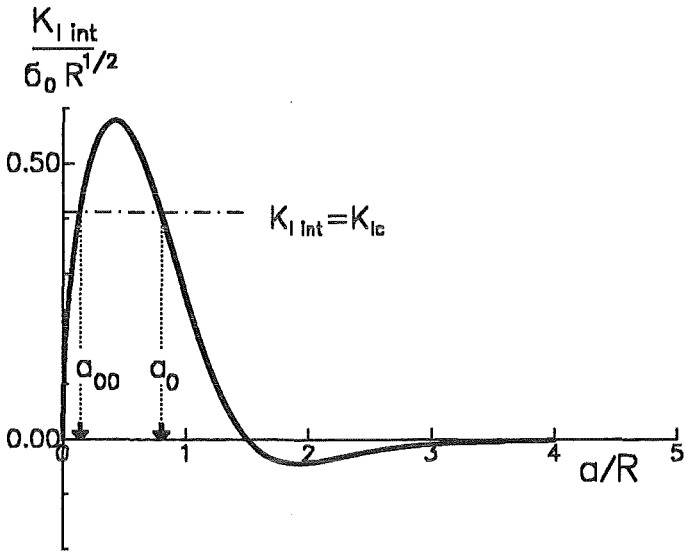

Figure 191. Residual stress intensity factor. Stress intensity factor for a crack in a residual stress field

$$K_I = \frac{2}{\sqrt{\pi a}} \int_0^a \frac{\sigma(r)\, r}{\sqrt{a^2 - r^2}}\, dr \tag{14.2.2}$$

which reads after integration

$$K_{I\,int} = \frac{\sigma_0}{\sqrt{\pi}} \sqrt{a} \left[1 + \left(\frac{R}{a} - 2\frac{a}{R} \right) \mathbf{F}(a/R) \right] \tag{14.2.3}$$

where the subscript "int" means the stress intensity factor caused by internal stresses, and **F** is Dawson's integral

$$\mathbf{F}(x) = e^{-x^2} \int_0^x \exp(t^2)\, dt \tag{14.2.4}$$

The stress intensity factor $K_{I\,int}$ is plotted in fig.191 as a function of the normalized crack size a/R. The maximum value

$$(K_{I\,int})_{max} = \sigma_0 \sqrt{R}\ 0.5764 \tag{14.2.5}$$

appears at $a/R = 0.4273$, and for $a/R > 1.5$ the stress intensity factor $K_{I\,int}$ is negative.
After sintering crack nuclei of size a_{nucl} may be present. These defects may be pores with annular cracks or wedge cracks at the triple points of the grains. The following treatment of circular cracks can also be performed for these crack types and also for surface cracks. The behaviour will in principle be the same as for circular cracks.
In case that the maximum internal stress intensity factor is higher than the fracture toughness K_{Ic} all crack nuclei in the range of

$$a_{00} < a_{nucl} < a_0 \tag{14.2.6}$$

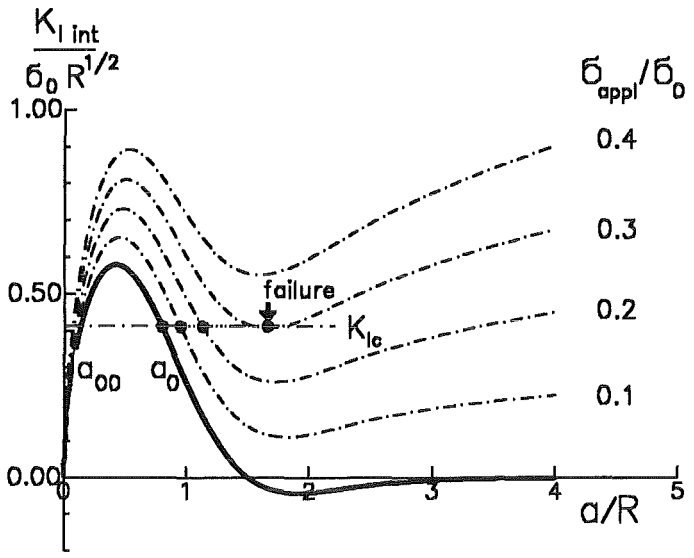

Figure 192. Total stress intensity factor. Residual stress intensity factor superposed with the applied stress intensity factor.

will grow during the cooling phase which results in a final crack size a_0. The crack size limits a_{00} and a_0 are given by the two solutions of

$$K_{Ic} = \frac{\sigma_0}{\sqrt{\pi}} \sqrt{a} \left[1 + \left(\frac{R}{a} - 2\frac{a}{R} \right) \mathbf{F}(a/R) \right] \tag{14.2.7}$$

14.3 Materials without subcritical crack extension

After cooling down from the sintering temperature to room temperature the thermally induced micro-cracks with the crack size a_0/R are highly stressed, i.e. the micro-crack is in a state with $K_I = K_{Ic}$, and it holds

$$K_{Ic} = \frac{\sigma_0}{\sqrt{\pi}} \sqrt{a_0} \left[1 + \left(\frac{R}{a_0} - 2\frac{a_0}{R} \right) \mathbf{F}(a_0/R) \right] \tag{14.3.1}$$

This fact is of high importance to all fracture-mechanics considerations.
By combining eqs.(14.2.3) and (14.3.1) the unknown stress σ_0 can be eliminated and it results

$$K_{I\,int} = \sqrt{\frac{a/R}{a_0/R}} \frac{1 + \left(\frac{R}{a} - 2\frac{a}{R} \right) \mathbf{F}(a/R)}{1 + \left(\frac{R}{a_0} - 2\frac{a_0}{R} \right) \mathbf{F}(a_0/R)} K_{Ic} \tag{14.3.2}$$

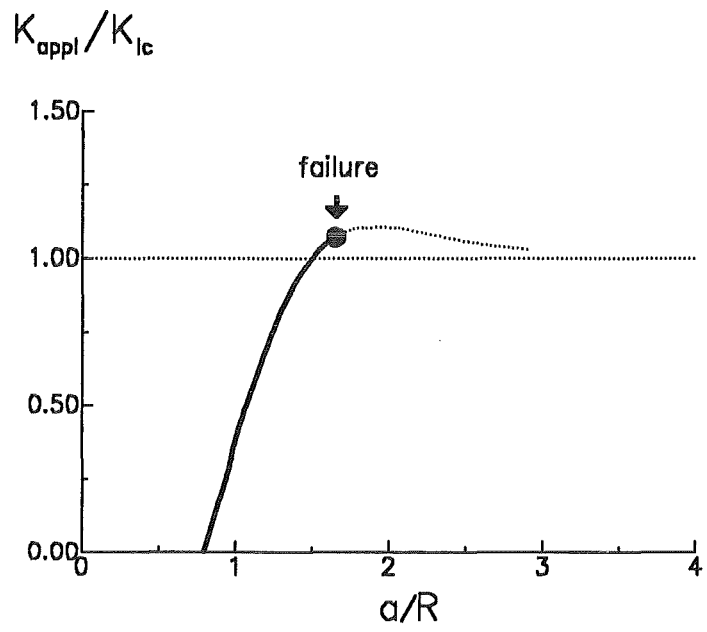

Figure 193. Applied stress intensity factor. $K_{I\,appl}$ vs crack size resulting from fig.192.

14.3.1.1 Stable crack growth for K_{Ic} = const.

In a test with externally applied stress σ_{appl} the external stress intensity factor

$$K_{I\,appl} = \frac{2}{\sqrt{\pi}} \sigma_{appl} \sqrt{a} \qquad (14.3.3)$$

is superimposed to the internal stress intensity factor $K_{I\,int}$. In order to avoid interactions of the

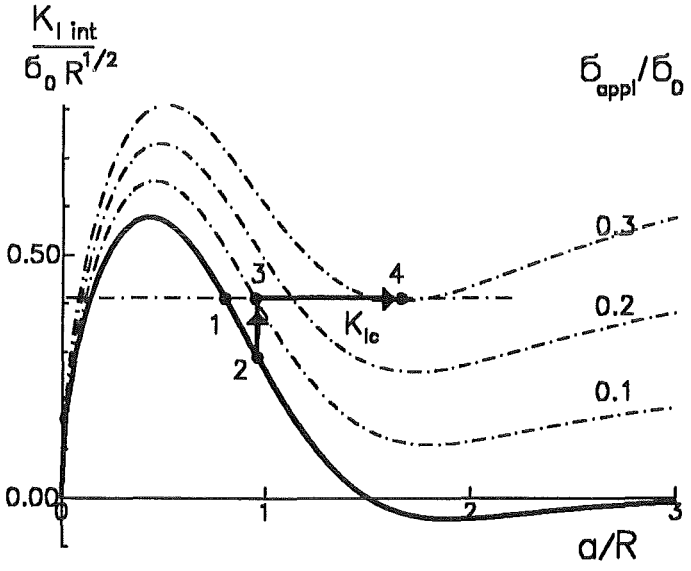

Figure 194. Crack development in presence of subcritical crack growth. Influence of subcritical crack growth before fracture test.

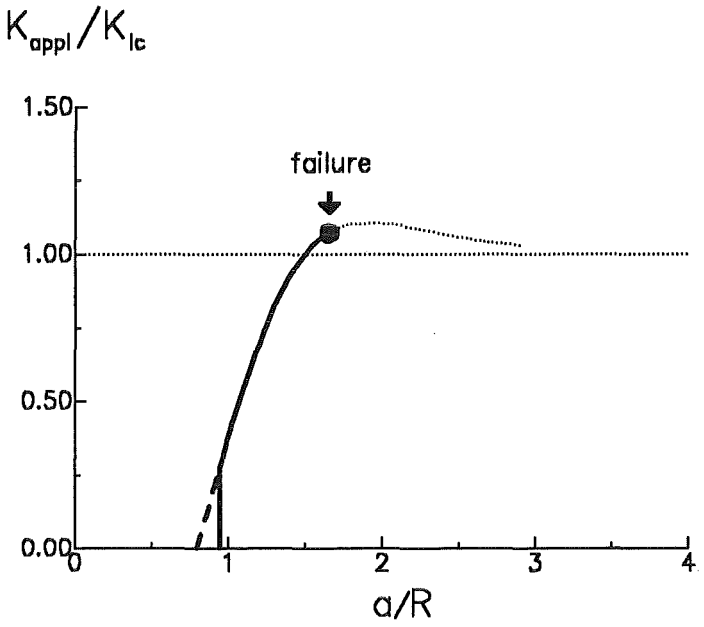

Figure 195. Applied stress intensity factor. Influence of subcritical crack growth before fracture test.

two stresses the internal stress σ_{int} is assumed to be a remote stress. This simplification leads to the total stress intensity factor acting at the crack tip

$$K_{I\,total} = K_{I\,int} + K_{I\,appl} = K_{I\,tip} \tag{14.3.4}$$

In fig.192 the total stress intensity factor $K_{I\,total}$ is represented for several values of the ratio σ_{appl}/σ_0. If the external stress σ_{appl} is increased, stable crack growth occurs. The condition for crack growth is

$$K_{I\,total} = K_{Ic} \tag{14.3.5}$$

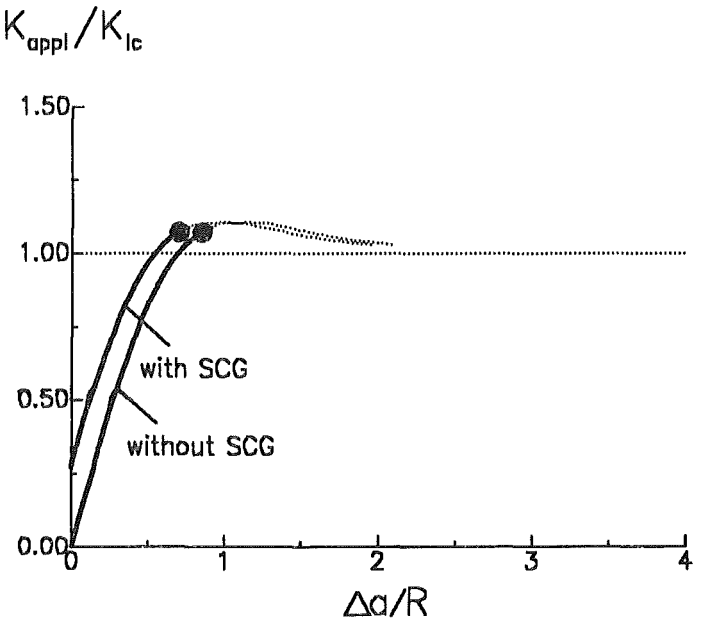

Figure 196. R-curves. Influence of subcritical crack growth on the R-curve.

Figure 192 is a graphical representation of the crack extension $\Delta a = a - a_0$, obtained from the intersections of the $K_{I\,total}$-curves with the horizontal line describing $K_{I\,total} = K_{Ic}$. At the point marked by an arrow, where $K_{I\,total}$-a/R exhibits a horizontal tangent, failure occurs.
The stress intensity factor $K_{I\,appl}$ can be calculated from eq.(14.3.4), too. Figure 193 shows the stress intensity factor $K_{I\,appl}$ as a function of the crack length a. Failure will occur in a strength test at the location indicated by an arrow.
The rough fracture-mechanical model explains the behaviour of small cracks. Extremely low energy release rates are necessary to initiate stable crack propagation. Also the strong increase in stress intensity factors $K_{I\,appl}$ with Δa is in agreement with the experimental results.

14.4 Materials with subcritical crack extension

In the presence of subcritical crack growth - which is strongly pronounced for alumina in normal air - the crack may extend during and after the cooling-down phase at stress intensity factors $K_I < K_{Ic}$. This behaviour is illustrated in fig.194. During subcritical crack growth the residual stress intensity factor decreases along the $K_{I\,int} - a/R$ —curve, starting from point 1. At the moment when the fracture test is performed, the residual stress intensity factor is assumed to coincide with point 2. Then, in the bending test at first the externally applied load has to be increased to the level $K_I = K_{Ic}$ which is reached at point 3. The further crack development is the same as for materials without subcritical crack growth provided that the bending test is peformed within a short interval so that additional subcritical crack growth may be neglected. The development of the applied stress intensity factor $K_{I\,appl}$ with the crack length is shown in fig.195. Finally, fig.196 shows the R-curve, namely the applied stress intensity factor $K_{I\,appl}$ as a function of crack extension Δa for both cases.
In conclusion it can be stated:
If a material contains thermally induced microcracks, these cracks are - in the absence of subcritical crack growth - in a state with $K_I = K_{Ic}$. This fact makes plausible that stable crack propagation is possible at the lowest loadings applied externally.
It has been shown that the experimental result of stable crack growth of small cracks - which occurs at very low external loads - can be explained by internal stresses caused by anisotropy of the thermal expansion coefficients of alumina.
In the presence of subcritical crack growth the R-curve starts at a higher stress intensity factor, but the following curve is identical to that obtained in the absence of subcritical crack growth.

15. References

[1] H. Tada, P.C. Paris, G.R. Irwin "The stress analysis of cracks handbook", Del Research Corporation (1986).

[2] H. Hübner, W. Jillek, Sub-critical crack extension and crack resistance in polycrystalline alumina, J. Mater. Sci. **12**(1977)117-125.

[3] K. Kendall, N. McN. Alford, S.R. Tan, J.D. Birchall, Influence of toughness on Weibull modulus of ceramic bending strength, J. Mater. Res. **1**(1986)120-123.

[4] T. Fett, D. Munz, Influence of R-curve effects on lifetimes for specimens with natural cracks, in 'Fracture Processes in Concrete, Rock and Ceramics', edited by J.G.M. van Mier, J.G. Rots, A. Bakker, Vol.1, 365-374, E&FN Spon, London.

[5] R.F. Cook, D.R. Clarke, Fracture stability, R-curves and strength variability, Acta Metall. **36**(1988)555-562.

[6] D.K. Shetty, J.S. Wang, Crack stability and strength distribution of ceramics that exhibit rising crack-growth-resistance (R-curve) behaviour, J. Amer. Ceram. Soc. **72**(1989)1158-1162.

[7] T. Fett, D. Munz, Static and cyclic fatigue of ceramic materials, in: 'Ceramics Today - Tomorrow's Ceramics', Ed. P. Vincezini, Elsevier Science Publishers B.V., 1991, 1827-1835.

[8] T. Fett, D. Munz, G. Thun, Influence of frequency on cyclic fatigue of coarse-grained Al_2O_3, J. Mater. Sci. Letters **12**(1993) 220-222.

[9] J. Proß, Unterkritisches Rißwachstum in gefügeverstärkten Keramiken, Thesis, University of Stuttgart, 1992.

[10] R. Knehans, R.W. Steinbrech, Memory effect of crack resistance during slow crack growth in notched Al_2O_3 bend specimens, J. Mater. Sci. Letters, **1**(1982),327-329.

[11] R.W. Steinbrech, R. Knehans, W. Schaarwächter, Increase of crack resistance during slow crack growth in Al_2O_3 bend specimens, J. Mater. Sci., **18**(1983),265-270.

[12] R. Steinbrech, A. Reichl, W. Schaarwächter,J. Amer. Ceram. Soc. **73**(1990),2009-2015.

[13] E.K. Beauchamp, S.L. Monroe, Effect of crack-interface bridging on subcritical crack growth in ferrites, J. Amer. Ceram Soc. **72**(1989),1179-1184.

[14] D.G. Jensen, V. Zelizko, M.V. Swain, Small flaw static fatigue crack growth in Mg-PSZ, J. Mater. Sci. Letters **8**(1989),1154-1157.

[15] A. Okada, N. Hirosaki, M. Yoshimura, Subcritical crack growth in sintered silicon nitride exhibiting a rising R-curve, J. Amer. Ceram. Soc. **73**(1990),2095-2096.

[16] P.L. Swanson, C.J. Fairbanks, B.R. Lawn, Y. Mai, B.J. Hockey, Crack-interface grain bridging as a fracture resistance mechanism in ceramics: I Experimental study on alumina, J. Amer. Ceram. Soc. **70**(1987),279-289.

[17] T. Fett, D. Munz, Crack growth in ceramics with R-curve behavior (in German), in: Festschrift E. Macherauch, Werkstoffkunde, DGM 1991, 375-384.

[18] T. Fett, D. Munz, Evaluation of R-curves in ceramic materials based on bridging interactions, KfK-Report 4940, Kernforschungszentrum Karlsruhe, 1991.

[19] T. Fett, D. Munz, Evaluation of R-curve effects in ceramics, J. Mater. Sci. **28**(1993)742-752.

[20] T. Fett, D. Munz, Subcritical crack growth of macro-cracks in alumina with R-curve-behaviour, J. Amer. Ceram. Soc. **75**(1992)958-63.

[21] G. Vekinis, M.F. Ashby, P.W.R. Beaumont, R-curve behaviour of Al_2O_3 ceramics, Acta metall. mater. **38**(1990),1151-1162.

[22] H. Frei, G. Grathwohl, New test methods for engineering ceramics - in-situ microscopy investigation, Ceramic Forum International, cfi, **67**(1991), 27-35.

[23] J. Rödel, J.F. Kelly, B.R. Lawn, In situ measurements of bridged crack interfaces in the scanning electron microscope, J. Amer. Ceram. Soc. **73**(1990),3313-3318.

[24] Y. Mai, B.R. Lawn, Crack-interface grain bridging as a fracture resistance mechanism in ceramics: II. Theoretical fracture mechanics model, J. Amer. Ceram. Soc. **70**(1987),289.

[25] T. Fett, D. Munz, Influence of crack-surface interactions on stress intensity factor in ceramics, J. Mater. Sci. Letters **9**(1990),1403-1406.

[26] H.G. Hahn, Bruchmechanik, B.G. Teubner, Stuttgart 1976.

[27] R.H. Dauskardt, Cyclic fatigue-crack growth in grain bridging ceramics, J. of Engng. Mater. and Techn. **115**(1993)244-251.

[28] H. Bueckner, A novel principle for the computation of stress intensity factors, ZAMM **50**(1970),529-546.

[29] J. R. Rice, Int. J. Solids Structures **8**(1972)751-758

[30] T. Fett, C. Mattheck, D. Munz, On the calculation of crack opening displacement from the stress intensity factor, Engng. Fract. Mech. **27**(1987)697-715.

[31] P.C. Paris, Document D2-2195, The Boeing Company, 1957.

[32] B.R. Lawn, Physics of fracture, J. Amer. Ceram. Soc. **66**(1983),83-91.

[33] T. Fett, "Stress intensity factors and weight functions for the edge cracked plate calculated by the Boundary Collocation Method", KfK-Report 4791, Kernforschungszentrum Karlsruhe, 1990.

[34] T. Fett, D. Munz, Stress intensity factors for circular cracks with crack surface interactions due to bridging stresses, Int. J. Fract. **55**(1992)R73-R79.

[35] R.M. McMeeking, A.G. Evans, Mechanics of transformation toughening in brittle materials, J. Amer. Ceram. Soc. **65**(1982)242-46.

[36] B. Budiansky, J.W. Hutchinson, J.C. Lambropoulos, Continuum theory of dilatant transformation toughening in ceramics, Int. J. Solids Structures **19**(1983)337-355.

[37] M.L. Williams, J. Appl. Mech. **24**(1957)109-114.

[38] T. Fett, Weight function for an edge crack for tractions at arbitrary location in the body, to be published in Engng. Fract. Mech.

[39] J.D. Eshelby, Determination of the elastic field of an ellipsoidal inclusion and related problems, Proc. R. Soc., London, Ser. A, **241.**(1957)376-396.

[40] D.M. Stump, B. Budiansky, Crack-growth resistance in transformation-toughened ceramics, Int. J. Solids Structures **25**(1989)635-646.

[41] J.C. Amazigo, B. Budiansky, Steady-state crack growth in supercritically transforming materials, Int. J. Solids Structures **24**(1988)751-755.

[42] J.W. Hutchinson, On steady quasi-static crack growth, Harvard University Report DEAP S-8, 1974.

[43] W. Kreher, W. Pompe, Internal stresses in heterogeneous solids, Akademie-Verlag, Berlin, 1989.

[44] D.M. Stump, B. Budiansky, Finite cracks in transformation-toughened ceramics, Acta metall. **37**(1989)3297-3304.

[45] T. Fett, D. Munz, Stress intensity factors and weight function solutions, KfK-Report 5290, Kernforschungszentrum Karlsruhe, 1994.

[46] H.L. Ewalds, R.J.H. Wahnhill, Fracture Mechanics, Edward Arnolds (Publishers) Ltd, London, 1984.

[47] T. Fett, D. Munz, Fracture mechanical treatment of bridging stresses, KfK-Report 5256, Kernforschungszentrum Karlsruhe, 1993.

[48] D. Broek, Elementary Engineering Fracture Mechanics, Martinus Nijhoff Publishers, 1986, Dordrecht.

[49] A.G. Evans, R.M. McMeeking, On the toughening of ceramics by strong reinforcements, Acta metall. **34**(1986)2435-2441.

[50] T. Fett, Influence of bridging stresses on specimen compliances, J. Mater. Sci. Letters **10**(1991),1211-1216.

[51] T. Fett, D. Munz, Estimation of bridging interactions for natural cracks from bending strength of coarse-grained Al_2O_3, to be published in J. of the Am er. Ceram Soc..

[52] J.C. Newman, I.S. Raju, An empirical stress-intensity factor equation for the surface crack, Engng. Fract. Mech. **15**(1981),185-192.

[53] T.A. Cruse, P.M. Besuner, J. of Aircraft **12**(1975)369-375.

[54] T. Fett, C. Mattheck, D. Munz, Approximate weight functions for 2D and 3D problems, J. Engng. Analysis **6**(1989),48-62.

[55] T. Fett, The crack opening displacement field of semi-elliptical surface cracks in tension for weight functions applications, Int. Journ. of Fracture 36(1988),55-69.

[56] T. Fett, D. Munz, Subcritical crack growth of macro- and microcracks in ceramics, Fracture Mechanics in Ceramics Vol.9, 1992, 219-233.

[57] T. Fett, D. Munz, Influence of bridging interactions on the lifetime behaviour of coarse-grained Al_2O_3, J. Europ. Ceram. Soc. **12**(1993)131-138.

[58] S.J. Bennison, B.R. Lawn, Flaw tolerance in ceramics with rising crack resistance characteristics, J. Mater. Sci. **24**(1989)3169-3175.

[59] E.R. Fuller, R.M. Thomson, Lattice theories of fracture, in: Fracture Mechanics of Ceramics IV, Plenum Press (1978) 507-548.

[60] T. Fett, A fracture-mechanical theory of subcritical crack growth in ceramics, Int. J. Fract. **54**(1992),117-130.

[61] Evans, A.G., Fuller, E.R., Crack propagation in ceramic materials under cyclic loading conditions, Metall. Trans. **5** (1974)27-33.

[62] T.Fett, G. Martin, D. Munz, G. Thun, Determination of da/dN-ΔK-curves for small cracks in alumina in alternating bending tests, J. Mater. Sci. **26**(1991) 3320-3328.

[63] T.Fett, D. Munz, G. Thun, Influence of frequency on cyclic fatigue of coarse grained Al_2O_3, **12**(1993)220-222.

[64] T. Fett, D. Munz, Cyclic fatigue of aluminum oxide in bending, Proc. of the MECC Maastricht, June 1989, Vol.3, 3.195-3.199.

[65] T. Kawakubo, "Static and cyclic fatigue in ceramics", MRS-Conference, Tokyo, 1988.

[66] T. Kawakubo, K. Komeya, "Static and cyclic fatigue behavior of a sintered silicon nitride at room temperature", J. Amer. Ceram. Soc. **70**(1987)400-405.

[67] A. Weddigen, G. Grathwohl, Ermüdung keramischer Werkstoffe, in: Mechanische Eigenschaften keramischer Konstruktionswerkstoffe (Ed. G. Grathwohl) DGM-Verlag, Oberursel 1993, 149-160.

[68] T. Fett, D. Munz, G. Thun, Zyklische Ermüdung an grobkörnigem Aluminiumoxid, in: Mechanische Eigenschaften keramischer Konstruktionswerkstoffe (Ed. G. Grathwohl) DGM-Verlag, Oberursel 1993, 167-172.

[69] G. Grathwohl, Mat.-wiss. u. Werkstofftech. **19**(1988).113-124.

[70] H. Frei, G. Grathwohl, Beitr. Elektronenmikroskop. Direktabb. Oberfl. **22**(1989),71-77.

[71] S. Lathabai, J. Rödel, B.R. Lawn, Cyclic fatigue from frictional degradation at bridging grains in alumina, J. Amer. Ceram. Soc. **74**(1991) 1340-1348.

[72] T. Fett, D. Munz, Differences between static ans cyclic fatigue effects in alumina, J. Amer. Ceram. Soc. **12**(1993)352-354.

[73] A.G. Evans, E.A. Charles, J. Amer. Ceram. Soc. **60**(1977)22-28.

[74] M.V. Swain, Fract. Mech. Cer. Vol.**6**(1983)355-359.

[75] H.A. Bahr, H. Bahlke, M. Kuna, H. Liesk, Theor. Appl. Fract. Mech. **8**(1987)33-39.

[76] H.A. Bahr, U. Bahr, H. Bahlke, H. Maschke, A Petzold, H.J. Weiß, Multiple crack propagation under thermal load, in: Thermal Shock and Thermal Fatigue Behavior of Advanced Ceramics, ed. by G.A. Schneider and G. Petzow, Kluwer Academic Publishers, Dordrecht 1993, 143-153.

[77] M.V. Swain, J. Amer. Ceram. Soc. **73**(1990)621-628.

[78] H.A. Bahr, T. Fett, I. Hahn, D. Munz, I. Pflugbeil, Fracture mechanics treatment of thermal shock and the effect of bridging stresses, in: Thermal Shock and Thermal Fatigue Behavior of Advanced Ceramics, ed. by G.A. Schneider and G. Petzow, Kluwer Academic Publishers, Dordrecht 1993, 105-117.

[79] G.A. Schneider, F. Magerl, I. Hahn, G. Petzow, Unstable and stable crack propagation and R-curve behavior in thermally shocked discs, in: Thermal Shock and Thermal Fatigue Be-

havior of Advanced Ceramics, ed. by G.A. Schneider and G. Petzow, Kluwer Academic Publishers, Dordrecht 1993, 229-244.

[80] I. Hahn, R-Kurvenverhalten von Keramiken unter transienten thermischen Belastungen, Thesis, University of Stuttgart (1992).

[81] F. Magerl, G.A. Schneider, G. Petzow, Thermal fatigue and subcritical crack growth in ceramics, in: Thermal Shock and Thermal Fatigue Behavior of Advanced Ceramics, ed. by G.A. Schneider and G. Petzow, Kluwer Academic Publishers, Dordrecht 1993, 407-418.

[82] H. Maschke, A boundary integral equation method for the problem of multiple, interacting cracks in anisotropic materials, in: E. Czoboly(ed.), Failure Analysis - Theory and Practice, Proc. 7th European Conference on Fracture, Budapest, Hungary, EMAS U.K.,pp.161-167.

[83] I.N. Sneddon, Proc. of the Royal Soc., London, A 187(1946),229.

[84] T. Fett, Crack opening displacement of a penny-shaped crack in an infinite body loaded by internal pressure over a circular area, Int. J. Fract. **20**(1982),R135-R138.

[85] B.R. Lawn, M.V. Swain, J. Mater. Sci. **10**(1975),113.

[86] M.G. Mendiratta, J.J. Petrovic, J. Mater. Sci. **11**(1976)973.

[87] G. Ziegler, D. Munz, Bruchwiderstandsmessungen an Al_2O_3 und Si_3N_4 mit der Knoop Härteeindrück-Technik, Ber. Deutsch. Keram. Ges. (DKG) **56**(1979),128-131.

[88] G. Ziegler, M. Majdic, Quantitative Auswertung der Rißgeometrie in keramischen Werkstoffen, Beitr. elektronenmikroskop. Direktabb. Oberfl. **11**(1978),137-144.

[89] Y. Maniette, M. Inagaki, M. Sakai, Fracture toughness and crack bridging of a silicon nitride ceramic, J. Europ. Ceram. Soc. **7**(1991)255-263.

[90] W. Markowski, Ein neues Prinzip der Werkstoffprüfmaschine, Materialprüfung **32** (1990) 144-148.

[91] T. Fett, G. Thun, Vorrichtung zur Durchführung von kontrollierten Biegebruchversuchen, German device patent G9207089.2

[92] T. Fett, An analysis of the three-point bending bar by use of the weight function method, Engng. Fract. Mech. **40**(1991)683-686.

[93] J.E. Srawley, B. Gross, Side-cracked plates subject to combined direct and bending forces, ASTM STP 601, Philadelphia, 1976.

[94] T. Fett, D. Munz, Influence of initial crack size, specimen size and loading type on R-curves caused by bridging stresses, Int. J. Fract. **49**(1991),R21-R30.

[95] G. Mundry, Gefüge, Bruchmodus und Rißwiderstandsverhalten von Aluminiumoxidkeramik unterschiedlicher Silizium- und Magnesiumoxidgehalte, Fortschrittsberichte VDI, Reihe 18, Nr.95, (in German).

[96] T. Fett, D. Munz , Commun. of the Amer. Ceram Soc. 68,(1985) C213-C215.

[97] T.E. Adams, D.J. Landini, C.A. Schumacher, R.C. Bradt, Micro- and macrocrack growth in alumina refractories, Amer. Ceram. Soc. Bull., **60**(1981)730-735.

[98] B.J. Pletka, S.M. Wiederhorn, A comparison of failure predictions by strength and fracture mechanics techniques, J. Mater. Sci. **17**(1982)1247-1268.

[99] K. Chen, Y. Ko, Slow crack growth in silica, high alumina, alumina-chromia, and zircon brick, Amer. Ceram. Soc. Bull. **67**(1988)1228-1234.

[100] T. Fett, D. Munz, Lifetime evaluation of ceramic materials, J. Europ. Ceram. Soc. **6**(1990)67-72.

[101] T.Fett, K. Keller, D. Munz, NAGRA, Technical Report 85-51(1985), Baden, Switzerland.

[102] T. Fett, Evaluation of the bridging relation from COD-measurements by use of the fracture mechanical weight function, to be published in J. Amer. Ceram. Soc.

[103] T. Fett, A weight function for the RCT-specimen, Int. J. Fract./Rep. Curr. Res. **63**(1993) R81-R85.

[104] J.C. Newman, Int. J. Fract **17**(1981)567-78.

[105] C.T. Yu, A.S. Kobayashi, Fracture process zone in SiC_w/Al_2O_3, ASTM-Meeting 93, Cocoa-Beach.

[106] T. Fett, D. Munz, Why can microcracks in ceramics propagate at extremely low stress intensity factors?, J. Mater. Sci. Letters **11**(1992)257-260.

[107] E. Ryshkewitch, Oxide Ceramics, Academic Press, New York 1960.

[108] T. Fett, Engng. Fract. Mech. **42**(1992)435-44.

[109] H.J. Petroski, J.D. Achenbach, Engng. Fract. Mech. **10**(1978)257-66

[110] T. Fett, Engng. Fract. Mech. **39**(1991)905-914, Corrigendum **42**(1992)1051.

[111] X.R. Wu, Int. J. Fract. **48**(1991)179-192.

[112] P. Morawietz, C. Mattheck, D. Munz, Int. J. Num. Math. Engng. **21**(1985)1487-1497.

[113] X. Niu, G. Glinka, Engng. Fract. Mech. **26**(1987)701-706.

[114] M. Sakai, J. Yoshimura, Y. Goto, M. Inagaki, R-curve behavior of a polygranular graphite: Microcracking and grain bridging in the wake region, J. Amer. Ceram. Soc. **71**(1988),609-616.

[115] R. Steinbrech, O. Schmenkel, Crack-resistance curves for surface cracks in Alumina, Comm. J. Amer. Ceram. Soc. **71**(1988),C271-C273.

[116] T. Fett, Crack opening displacement of a penny-shaped crack in an infinite body loaded by internal pressure over a circular area, Int. J. Fract. **20**(1982),R135-R138.

[117] T. Fett, D. Munz, Subcritical crack growth of macro- and microcracks in ceramics, Proc. of "Fracture Mechanics of Ceramics", **9**(1992) 219-233, Plenum Press, New York.

[118] Z. Knesl, A criterion of V-notch stability, Int. J. Fract. **48**(1991),R79-R83.

[119] F. Kroupa, Z. Knesl, Criteria for crack propagation at ceramic interfaces, Proc. Int. Conf. Engineering Ceramics 92, Smolenice Castle, Oct. 1992, M. Haviar Ed..

[120] E. Kullig, H. Riesch-Oppermann, T. Winkler, A. Brückner-Foit, A stochastic model simulating the development of irregular crack patterns in thermal fatigue, ESIS ECF10 Structural Integrity, Vol.1, 1994, pp.603-614.

[121] D. Munz, Y.Y. Yang, Stresses near the free edge of the interface in ceramic-to-metal joints, J. Europ. Ceram. Soc. **13**(1994) 453-460.

[122] O.T. Iancu, T. Fett, D. Munz, A fracture mechanical treatment of free edge stress singularities applied to a brazed ceramic/metal compound, Int. J. Fract. **46**(1990) 159-172.

[123] M. Tilscher, A. Brückner-Foit, D. Munz, unpublished results.

[124] M. Busch, M. Heinzelmann, H.G. Maschke, A cohesive zone model for the failure assessment of V-notches in micromechanical components, to be published in Int. J. Fract./Reports of Current Research.

[125] M.L. Williams, J. Appl. Mech., **19**(1952) 526-528.

[126] T. Fett, A weight function for cracks ahead of sharp notches, submitted to Int. J. Fract./Rep. of Curr. Res.

Appendix A. Weight functions

A.1 Weight function for remote tractions

Stress intensity factors for cracks exposed to any loading can be calculated using the weight functions method. In most cases of practical interest the crack surface weight function is applied. If a stress distribution $\sigma(x)$ acts on the crack surfaces of a one-dimensional crack of depth a , the effective stress intensity factor K_I is given by [28]

$$K_I = \sigma^* \sqrt{\pi a}\, F = \int_0^a h(x,a)\sigma(x)\, dx \qquad (A.1.1)$$

where σ^* is a characteristic stress value of the stress distribution $\sigma(x)$, e.g. the stress acting near the plate surface. The weight functions h(x,a) used in eq.(A.1.1) are known for most types of crack.
But the weight function method is not restricted to crack surface loadings. In its more general formulation it is also possible to apply the procedure to tractions which act at any given contour in the body (fig.197).

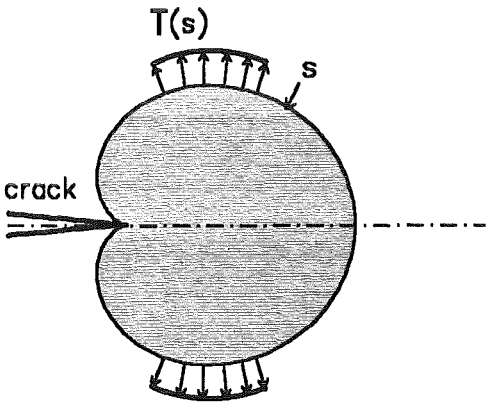

Figure 197. Remote tractions. Symmetrical tractions along a surface (s) at the crack tip.

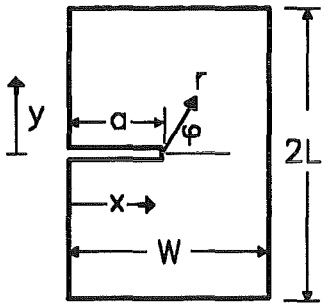

Figure 198. Geometrical data. Edge-crack in a plate.

Such weight functions are of special interest in computation of R-curves in ceramics when phase transformations occur in the crack-tip region [35]. In this more general case one can write

$$K_I = \int h(s,a)T(s)\,ds \tag{A.1.2}$$

where $T(s)$ are tractions over a surface s. As shown by Rice [29][1] the weight function can be related to the displacements u_r^T of a reference loading case (subscript r) which act in the direction of the tractions $T(s)$ of the actual loading case:

$$h(s,a) = \frac{E'}{K_{Ir}} \frac{\partial}{\partial a} u_r^T(s,a) \tag{A.1.3}$$

For the plane strain module E' it holds $E/(1-\nu^2)$ with E=Young's modulus and ν=Poisson's ratio. Obviously eq.(A.1.3) covers also the crack face weight function when the surface s is chosen to be the crack surface. In order to determine the weight function for a crack/component configuration we have to determine the displacement field of the reference load case as well as the related stress intensity factor. The computation of weight functions can be done by determination of the displacements around the crack tip, which are fully known if we succeed in the determination of the Airy stress function as outlined in [38]. After use of the stress function, the displacements result as

$$\begin{aligned} \boldsymbol{u} = \frac{1+\nu}{E} \sum_{n=0}^{\infty} A_n r^{n+1/2} \frac{n+3/2}{n-1/2} [(n+4\nu-5/2)\cos(n-1/2)\varphi - (n-1/2)\cos(n+3/2)\varphi] \\ + \frac{1+\nu}{E} \sum_{n=0}^{\infty} A_n^* r^{n+1} [(n+4\nu-2)\cos n\varphi - (n+2)\cos(n+2)\varphi] \end{aligned} \tag{A.1.4}$$

$$v = \frac{1+\nu}{E} \sum_{n=0}^{\infty} A_n r^{n+1/2} \frac{n+3/2}{n-1/2} [(n-1/2)\sin(n+3/2)\varphi - (n-4\nu+3/2)\sin(n-1/2)\varphi]$$

$$+ \frac{1+\nu}{E} \sum_{n=0}^{\infty} A_n^* r^{n+1} [(n+2)\sin(n+2)\varphi - (n-4\nu+4)\sin n\varphi] \qquad (A.1.5)$$

The cartesic components of the displacements are

$$u_x = u\cos\varphi - v\sin\varphi$$
$$u_y = u\sin\varphi + v\cos\varphi \qquad (A.1.6)$$

and the components of the weight function are given by

$$h_x = \frac{E'}{K_r}\frac{\partial u_x}{\partial a}$$
$$h_y = \frac{E'}{K_r}\frac{\partial u_y}{\partial a} \qquad (A.1.7)$$

The practical evaluation of the derivatives in eq.(5.1.24) can be performed as

$$\frac{du_x}{da} = \frac{\partial u_x}{\partial r}\frac{dr}{da} + \frac{\partial u_x}{\partial \varphi}\frac{d\varphi}{da} + \frac{\partial u_x}{\partial A_n}\frac{dA_n}{da} + \frac{\partial u_x}{\partial A_n^*}\frac{dA_n^*}{da}$$
$$\frac{du_y}{da} = \frac{\partial u_y}{\partial r}\frac{dr}{da} + \frac{\partial u_y}{\partial \varphi}\frac{d\varphi}{da} + \frac{\partial u_y}{\partial A_n}\frac{dA_n}{da} + \frac{\partial u_y}{\partial A_n^*}\frac{dA_n^*}{da} \qquad (A.1.8)$$

with

$$\frac{dr}{da} = -\cos\varphi \quad , \quad \frac{d\varphi}{da} = \frac{\sin\varphi}{r} \qquad (A.1.9)$$

The first coefficients of a 20-terms representation are listed in Table 4 for A_n and in Table 5 for A^*_n. In order to allow cubic interpolations the tabulated data are normalised according to

$$\tilde{A}_n = A_n(1-\alpha)^\beta \quad , \quad \alpha = a/W \qquad (A.1.10)$$

$$\tilde{A^*}_n = A^*_n(1-\alpha)^\beta \qquad (A.1.11)$$

	n=0	1	2	3	4	5	6	7	8	9
α	$\beta=1.5$	2.5	3.5	3.5	3.5	3.5	3.5	3.5	3.5	3.5
0.25	0.0829	0.0215	0.0533	0.0439	-0.152	0.2830	-0.203	-0.573	4.0130	1.7727
0.30	0.0850	0.0267	0.0448	0.0229	-0.074	0.1661	-0.169	-0.092	1.3618	0.5719
0.40	0.0873	0.0329	0.0320	0.0115	-0.004	0.0422	-0.046	0.1080	0.0102	-0.386
0.50	0.0882	0.0356	0.0245	0.0149	0.0168	0.0289	0.0175	0.0351	-0.027	-0.013
0.60	0.0884	0.0366	0.0209	0.0227	0.0334	0.0474	0.0628	0.0874	0.0912	0.0669
0.65	0.0883	0.0367	0.0200	0.0276	0.0453	0.0718	0.1111	0.1600	0.1854	0.1300
0.70	0.0883	0.0367	0.0196	0.0338	0.0631	0.1147	0.1972	0.2719	0.2514	0.1229
0.75	0.0883	0.0367	0.0195	0.0419	0.0923	0.1910	0.3335	0.4077	0.2831	0.0796
0.80	0.0884	0.0367	0.0197	0.0535	0.1386	0.3058	0.5152	0.5868	0.3903	0.1148
0.85	0.0897	0.0381	0.0208	0.0694	0.1934	0.4198	0.6598	0.6837	0.4087	0.1052
0.90	0.0919	0.0409	0.0206	0.0800	0.2272	0.4622	0.6465	0.5762	0.2837	0.0524

Table 4. . Coefficients $\tilde{A}_n$ for a 20-terms polynomial representation.

	n=0	1	2	3	4	5	6	7	8	9
α	$\beta=2$	3	4	4	4	4	4	4	4	4
0.25	0.02300	-0.0370	-0.0922	0.09128	0.00272	-0.3372	0.96039	-1.6678	-4.3971	-0.2444
0.30	0.00967	-0.0425	-0.0586	0.05902	-0.0383	-0.0982	0.35271	-0.6572	-1.3918	-0.0750
0.40	-0.0109	-0.0423	-0.0248	0.01192	-0.0262	0.00452	0.00300	-0.1321	0.21273	0.1835
0.50	-0.0248	-0.0361	-0.0147	-0.0061	-0.0194	-0.0134	-0.0210	-0.0061	0.03872	0.0005
0.60	-0.0333	-0.0298	-0.0125	-0.0155	-0.0254	-0.0331	-0.0483	-0.0589	-0.0507	-0.0181
0.65	-0.0359	-0.0275	-0.0126	-0.0197	-0.0336	-0.0529	-0.0823	-0.1087	-0.0989	-0.0306
0.70	-0.0377	-0.0259	-0.0130	-0.0247	-0.0473	-0.0875	-0.1412	-0.1648	-0.1159	-0.0297
0.75	-0.0387	-0.0249	-0.0135	-0.0312	-0.0701	-0.1400	-0.2131	-0.2064	-0.1060	-0.0212
0.80	-0.0395	-0.0248	-0.0143	-0.0406	-0.1013	-0.2005	-0.2823	-0.2515	-0.1207	-0.0214
0.85	-0.0436	-0.0291	-0.0167	-0.0531	-0.1326	-0.2477	-0.3223	-0.2668	-0.1227	-0.0232
0.90	-0.0556	-0.0361	-0.0165	-0.0544	-0.1299	-0.2202	-0.2540	-0.1860	-0.0773	-0.0149

Table 5. . Coefficients $\tilde{A}^*_n$ for a 20-terms polynomial representation.

A.2 Weight function for the RCT-specimen

Round-Compact-Tension (RCT) specimens can be used in fracture mechanics of ceramics to determine the bridging stresses between the crack faces from COD-measurements ([23],[102]). The related procedure needs knowledge of the fracture mechanical weight function.
Weight functions are known for the special case of a disc, which is identical with the RCT-specimen with load application holes of negligible diameter. Such a weight function for the edge cracked circular disc was derived in [108]. As a consequence of Saint-Venant's theorem the

differences between the disc and the RCT-specimen have only to be expected to occur near the load application holes, i.e. for $x \simeq 0$ (fig.199).
In order to take into account the influence of the real geometry the weight function of the RCT-specimen will be derived. The weight function can be derived from CODs of a reference load case and the related reference stress intensity factor according to eq.(4.3.3) The crack-opening displacements can be expressed by a power-series representation

$$\delta = \sum_{n=0}^{\infty} C_n \left(1 - \frac{x}{a}\right)^{n+1/2} \qquad (A.2.1)$$

with the coefficients C_n dependent on the relative geometry.

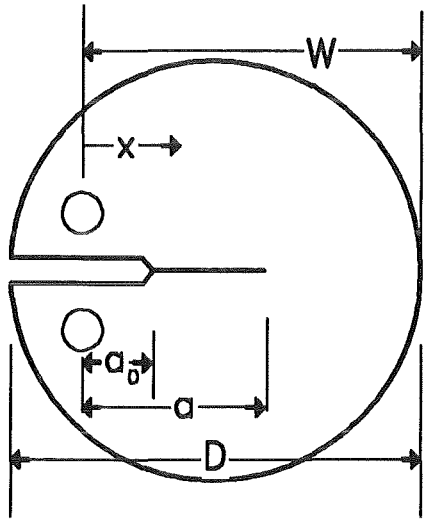

Figure 199. RCT-specimen. Geometrical data of the Round-CT-specimen (RCT).

For the specially chosen test specimen (RCT-specimen, see (fig.199) Newman [104] determined stress intensity factors and COD at different locations of the crack surface. The stress intensity factor solution of Newman [104] can be written as

$$K_I = \sigma_0 \sqrt{W}\, F_I \;, \quad \sigma_0 = \frac{P}{Wt} \;, \quad F_I = \frac{(2+\alpha)(0.76 + 4.8\alpha - 11.58\alpha^2 + 11.43\alpha^3 - 4.08\alpha^4)}{(1-\alpha)^{3/2}} \qquad (A.2.2)$$

(t = thickness, P = load applied). This information and some crack mouth conditions allow a number of coefficients in (A.2.1) to be determined:

1. **The crack-tip field is** related to the stress intensity factor by [109]

$$\delta\,(x \to a) = \left(\frac{8}{\pi}\right)^{1/2} \frac{K_{Ir}}{E'} \sqrt{a - x} \qquad (A.2.3)$$

2. As could be shown for an edge crack the second and third derivatives must vanish ([54] [110]):

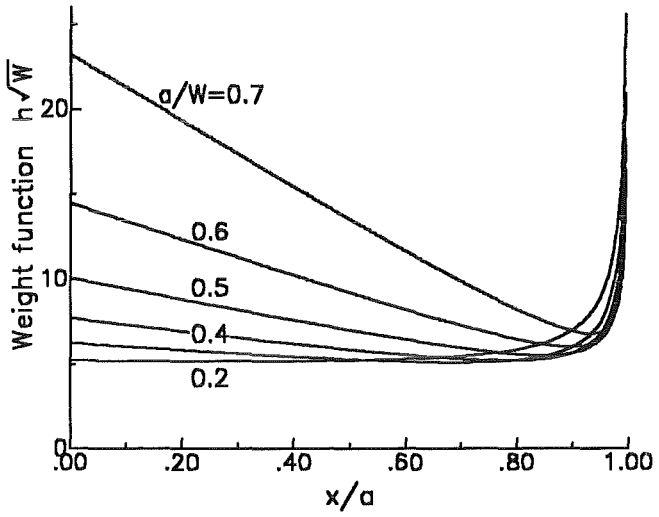

Figure 200. RCT-specimen. Weight function for the RCT-specimen.

$$\frac{\partial^2 \delta}{\partial x^2} = 0 \quad , \qquad \frac{\partial^3 \delta}{\partial x^3} = 0 \quad , \quad \text{for } x = W - D \tag{A.2.4}$$

3. The COD-field of eq.(A.2.1) must fulfill the special displacements obtained in [104] by BE-computations ([111]). In [104] the crack opening displacements are given at the load-line (i.e. $x = 0$) and at the crack mouth (i.e. $x = W - D$).

This procedure and its modifications are well established in the literature and successfully applied in numerous investigations ([109]-[113]). The results for the RCT-specimen are represented in Table 6 and illustrated in fig.200.
Table 6 shows the weight function values in a representation which lends itself easily to interpolation by bicubic splines

$$h = \sqrt{\frac{2}{\pi a}} \, \frac{g(x/a, a/W)}{\sqrt{1 - x/a}\,(1 - a/W)^{3/2}} \tag{A.2.5}$$

Using the data from Table 6 the weight function can be expressed within $\pm 1\%$ accuracy by the approximation formula

$$h = \sqrt{\frac{2}{\pi a}} \, \frac{1}{\sqrt{1 - x/a}\,(1 - a/W)^{3/2}} \left[\left(1 - \frac{a}{W}\right)^{3/2} + \sum_{\mu,\,\nu\,=\,0}^{4} A_{\nu\mu} (1 - x/a)^{\mu+1} \left(\frac{a}{W}\right)^{\nu} \right] \tag{A.2.6}$$

with coefficients $A_{\nu\mu}$ listed in Table 7.

a/W	x/a=0.0	0.2	0.4	0.6	0.8	0.9	0.95	1.0
0.2	2.081	1.848	1.603	1.337	1.044	0.885	0.801	0.716
0.25	2.305	1.972	1.642	1.314	0.984	0.818	0.734	0.650
0.3	2.501	2.085	1.686	1.303	0.936	0.759	0.672	0.586
0.35	2.673	2.185	1.725	1.294	0.894	0.705	0.614	0.524
0.4	2.830	2.277	1.761	1.286	0.854	0.654	0.558	0.465
0.45	2.985	2.367	1.797	1.279	0.815	0.604	0.504	0.408
0.5	3.151	2.464	1.837	1.273	0.778	0.557	0.453	0.354
0.55	3.338	2.577	1.886	1.272	0.742	0.510	0.403	0.302
0.60	3.551	2.708	1.943	1.273	0.707	0.465	0.355	0.253
0.7	3.997	2.975	2.055	1.267	0.632	0.376	0.265	0.164
0.8	4.062	2.966	1.995	1.175	0.531	0.283	0.179	0.089

Table 6. Weight function for the RCT-specimen. Normalised representation g(x/a,a/W) according to eq.(A.2.5).

ν	$\mu=0$	1	2	3	4
0	2.826	-5.865	0.8007	-0.2584	0.6856
1	-10.948	48.095	-3.839	1.280	-6.734
2	35.278	-143.789	6.684	-5.248	25.188
3	-41.438	196.012	-4.836	11.435	-40.140
4	15.191	-92.787	-0.7274	-7.328	22.047

Table 7. Weight function for the RCT-specimen. Coefficients $A_{\nu\mu}$ for eq.(A.2.6).

A.3 Averaged bridging stress intensity factors for an embedded elliptical crack

The averaged stress intensity factors for the elliptical crack loaded by constant crack surface stresses, i.e. $\delta_0 \to \infty$ can be calculated with eq.(7.1.2). The crack opening displacements of an embedded elliptical crack loaded by a constant stress σ - for instance the stress σ_0 - is used as the exactly known reference COD-field [1]

$$v = \frac{\sigma_0}{E'} \frac{2a}{\mathbf{E}(k)} \sqrt{1 - \rho^2/r^2} \qquad (A.3.1)$$

where $\mathbf{E}(k)$ is the complete elliptical integral of the second kind with the modulus $k = \sqrt{1 - a^2/c^2}$ (for ρ and r see fig.85). It results from eq.(7.1.2)

$$\overline{K}_{br,\,ellipse,\,A} = \frac{4\sigma_0\sqrt{a}}{\overline{Y}_A \pi \mathbf{E}(k)} \int_0^{\pi} \Big[\sin^2\varphi \sqrt{1 - a_0^2/r^2} \; +$$

$$+\frac{1}{3}\left(\cos^2\varphi+\frac{1}{(c/a)^2-1}\frac{\mathbf{E}(k)-\mathbf{K}(k)}{\mathbf{E}(k)}\right)\left(1-a_0^2/r^2\right)^{3/2}\Bigg]d\varphi \qquad (A.3.2)$$

$$\bar{K}_{br,\,ellipse,\,B}=\frac{4\sigma_0\sqrt{a}}{\bar{Y}_B\pi\mathbf{E}(k)}\int_0^{\pi}\Big[\cos^2\varphi\sqrt{1-a_0^2/r^2}\;-$$

$$-\frac{1}{3}\left(\cos^2\varphi+\frac{1}{(c/a)^2-1}\frac{\mathbf{E}(k)-\mathbf{K}(k)}{\mathbf{E}(k)}\right)\left(1-a_0^2/r^2\right)^{3/2}\Bigg]d\varphi \qquad (A.3.3)$$

where $\mathbf{K}(k)$ is the complete elliptical integral of second kind with the modulus k. The reference stress intensity factors (subscript r) are described by the geometric functions

$$\bar{Y}_A=\sqrt{\frac{4}{3\mathbf{E}(k)}\left(2+\frac{1}{c^2/a^2-1}\frac{\mathbf{E}(k)-\mathbf{K}(k)}{\mathbf{E}(k)}\right)} \qquad (A.3.4)$$

$$\bar{Y}_B=\sqrt{\frac{4}{3\mathbf{E}(k)}\left(1-\frac{1}{c^2/a^2-1}\frac{\mathbf{E}(k)-\mathbf{K}(k)}{\mathbf{E}(k)}\right)} \qquad (A.3.5)$$

A.4 Coefficients for the compliance polynomials

	B_0	B_1	B_2	B_3	B_4	B_5
L/W = 2	1.7046	-6.251	13.924	-18.867	14.073	-4.3928
4	1.7950	-5.9908	12.452	-16.161	11.609	-3.508
8	1.8787	-5.9556	11.742	-14.669	10.200	-2.9972
16	1.9210	-5.9329	11.368	-13.894	9.4753	-2.7354
32	1.9424	-5.9220	11.185	-13.524	9.1344	-2.6138
∞	1.9638	-5.9091	10.991	-13.128	8.7669	-2.4818

Table 8. Coefficients for the compliance formula. Coefficients B_μ for eq.(12.2.7).

A.5 Integrals for the evaluation of load-displacement curves

The integrals used in section 12.5 can be determined numerically in each step of the evaluation. But since three integrations are required and since the integrals can be used for any specimen again it makes sense to tabulate them. In the following tables numerical values are entered. Note, that the crack lengths are normalized on the specimens width W, i.e. relative crack lengths $\alpha = a/W$ are used.

ν	μ	$\alpha = 0.51$	0.525	0.55	0.575	0.60	0.625	0.65
0	0	2.079E-3	8.721E-3	2.735E-2	5.607E-2	9.705E-2	1.537E-1	2.310E-1
0	1	1.249E-5	1.314E-4	8.270E-4	2.554E-3	5.919E-3	1.177E-2	2.133E-2
1	0	1.060E-3	4.579E-3	1.504E-2	3.224E-2	5.823E-2	9.606E-2	1.502E-1
0	2	8.919E-8	2.350E-6	2.965E-5	1.376E-4	4.263E-4	1.062E-3	2.316E-3
1	1	6.369E-6	6.897E-5	4.548E-4	1.468E-3	3.551E-3	7.356E-3	1.386E-2
2	0	5.407E-4	2.404E-3	8.270E-3	1.854E-2	3.494E-2	6.004E-2	9.768E-2
0	3	6.932E-10	4.575E-8	1.156E-6	8.060E-6	3.334E-5	1.040E-4	2.724E-4
1	2	4.549E-8	1.234E-6	1.631E-5	7.915E-5	2.558E-4	6.639E-4	1.505E-3
2	1	3.248E-6	3.621E-5	2.502E-4	8.443E-4	2.131E-3	4.598E-3	9.018E-3
3	0	2.757E-4	1.262E-3	4.550E-3	9.705E-3	2.096E-2	3.752E-2	6.345E-2

Table 9. Coefficients for the stress distribution in the bridging zone. Coefficients $\lambda_{\mu\nu}/W^{2+\nu+\mu}$ for eq.(12.5.17).

ν	μ	$\alpha = 0.675$	0.70	0.725	0.75	0.775	0.80	0.825	0.85
0	0	3.364E-1	4.805E-1	6.799E-1	9.598E-1	1.362E0	1.955E0	2.867E0	4.342E0
0	1	3.641E-2	5.973E-2	9.555E-2	1.506E-1	2.363E-1	3.721E-1	5.941E-1	9.738E-1
1	0	2.271E-1	3.364E-1	4.929E-1	7.198E-1	1.055E0	1.564E0	2.365E0	3.690E0
0	2	4.623E-3	8.690E-3	1.568E-2	2.753E-2	4.762E-2	8.199E-2	1.422E-1	2.515E-1
1	1		4.181E-2	6.927E-2	1.130E-1	1.831E-1	2.976E-1	4.901E-1	8.277E-1
2	0		2.355E-1	3.574E-1	5.399E-1	8.178E-1	1.251E0	1.951E0	3.137E0
0	3	6.354E-4	1.367E-3	2.779E-3	5.430E-3	1.034E-2	1.946E-2	3.660E-2	6.984E-2
1	2		6.083E-3	1.137E-2	2.065E-2	3.690E-2	6.560E-2	1.173E-1	2.138E-1
2	1	1.659E-2	2.927E-2	5.022E-2	8.473E-2	1.419E-1	2.381E-1	4.043E-1	7.035E-1
3	0	1.035E-1	1.648E-1	2.591E-1	4.049E-1	6.338E-1	1.001E0	1.610E0	2.666E0

Table 10. Coefficients for the stress distribution in the bridging zone. Coefficients $\lambda_{\mu\nu}/W^{2+\nu+\mu}$ for eq.(12.5.17).

μ	$\alpha = 0.51$	0.525	0.55	0.575	0.60	0.625	0.65
0	1.649E-1	2.743E-1	4.240E-1	5.709E-1	7.293E-1	9.081E-1	1.116E0
1	5.638E-4	2.433E-3	7.076E-3	1.701E-2	3.049E-2	4.974E-2	7.663E-2
2	3.419E-6	3.745E-5	2.512E-4	8.197E-4	1.993E-3	4.127E-3	7.734E-3
3	2.457E-8	6.783E-7	9.208E-6	4.555E-5	1.490E-4	3.886E-4	8.798E-4
4	1.918E-10	1.331E-8	3.640E-7	2.718E-6	1.192E-5	3.904E-5	1.065E-4

Table 11. Coefficients for the stress distribution in the bridging zone. Coefficients $\chi_\mu/W^{\mu+1/2}$ for eq.(12.5.18).

μ	$\alpha = 0.675$	0.70	0.725	0.75	0.775	0.80	0.825	0.85
0	1.363E0	1.663E0	2.034E0	2.503E0	3.111E0	3.922E0	5.044E0	6.670E0
1	1.137E-1	1.646E-1	2.344E-1	3.310E-1	4.662E-1	6.593E-1	9.426E-1	1.375E0
2	1.355E-1	2.266E-2	3.668E-2	5.807E-2	9.072E-2	1.410E-1	2.200E-1	3.479E-1
3	1.809E-3	3.476E-3	6.369E-3	1.124E-2	1.939E-2	3.300E-2	5.597E-2	9.565E-2
4	2.564E-4	5.649E-4	1.166E-3	2.295E-3	4.367E-3	8.128E-3	1.469E-2	2.760E-2

Table 12. Coefficients for the stress distribution in the bridging zone. Coefficients $\chi_\mu / W^{\mu+1/2}$ for eq.(12.5.18).

$\alpha = 0.51$	0.525	0.55	0.575	0.60	0.625	0.65	
0.6155	0.6748	0.7876	0.9213	1.0813	1.2746	1.5107	
$\alpha = 0.675$	0.70	0.725	0.75	0.775	0.80	0.825	0.85
1.8032	2.1711	2.6799	3.2607	4.0930	5.2522	6.9360	9.5215

Table 13. Coefficients for the stress distribution in the bridging zone. Coefficients κ / W^2 for eq.(12.5.8).

$\alpha = 0.5$	0.51	0.525	0.55	0.575	0.60	0.625	0.65
1.5009	1.5332	1.5850	1.6818	1.7938	1.9240	2.0766	2.2572
$\alpha = 0.675$	0.70	0.725	0.75	0.775	0.80	0.825	0.85
2.4733	2.7353	3.0580	3.4630	3.9830	4.6697	5.6088	6.9529

Table 14. Geometric function Y for 4-point bending. Y computed with eq.(12.5.14).

Appendix B. Strength of uncracked bodies

B.1 Failure of brittle materials under singular stresses

The model of bridging interactions in the wake of a crack is not only applicable to interprete the R-curve behaviour of ceramics. Also the failure behaviour of brittle materials in the vicinity of stress singularities may be treated with this model.

B.1.1 Assessment of singular stresses

Singular stresses in components may be caused by geometrical discontinuities (sharp notches) or material discontinuities (bonded dissimilar materials, corners of grains). Due to these singular stresses, the component may fail. It is difficult to establish a failure criterion for such components. Several possibilities will be listed below

- Knesl [118][119] proposed to assume that the material fractures if a mean normal stress, averaged over a certain length, exceeds a critical value (see also [120],[121]). It is self-evident that this criterion depends on the characteristic length itself.

For brittle materials the failure may be caused by pre-existing cracks near the notch tip. Then fracture mechanics can be applied

- A small single semi-elliptical surface crack, located in the stress singularity, has been considered in [122]. Failure was predicted for the case that the stress intensity factor reached the fracture toughness.
- Tilscher et al. [123] make use of the fact that natural cracks exist in the neighbourhood of a stress singularity. By application of multiaxial Weibull statistics failure can be predicted.

Also, if no real crack exists at the interface, the failure of the highly stressed material near a stress singularity may be treated in terms of fracture mechanics.

- Busch et al. [124] propose a cohesive zone model. A virtual crack of prescribed length $a = 20\text{nm}$ at the tip of a sharp V-notch is considered which is bridged by molecular forces. A critical crack mouth opening is assumed as condition for failure.

Failure in the absence of pre-existing cracks will be described here by use of the weight function method. In order to simplify the problem, we consider failure of the interface to be caused by stresses normal to the interface line. The intact material near a stress concentrator responsible for singular stresses is described by an interface along the prospective crack as a crack which is bridged by "bridging stresses". The procedure will be outlined by the example of a sharp notch at the surface of a component. Therefore, we model the prospective failure line (dashed line in fig.201) as a crack of length $a \to \infty$ which is (in the absence of an applied stress) completely bridged.

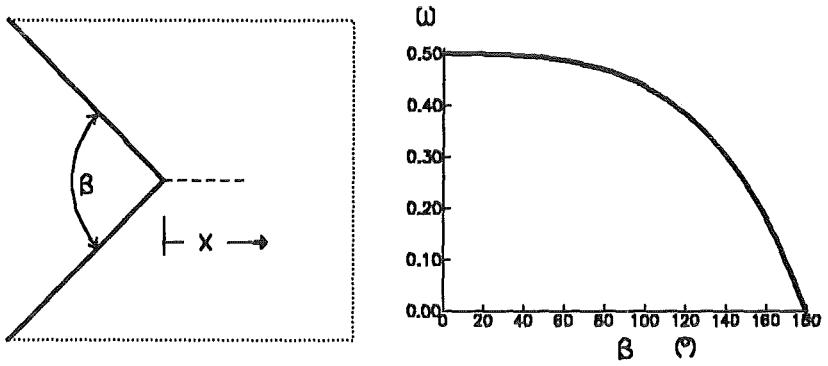

Figure 201. . Sharp notch in a semi-infinite body and stress exponent ω.

Under symmetrical loading (e.g. load perpendicular to the dashed line in fig.201) by external forces the normal stresses along the prospective crack line in the uncracked component are given for small distances from the notch tip $x \ll L$ (see fig.202) by

$$\sigma_{appl} = \frac{A_I}{\sqrt{2\pi}\, x^{\omega}} \qquad (B.1.1)$$

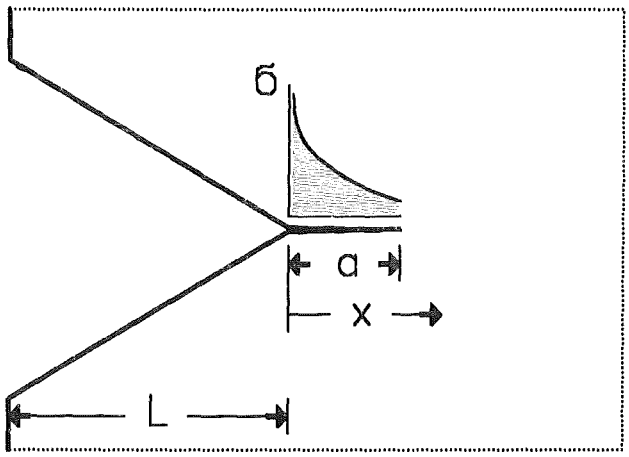

Figure 202. . Sharp notch in a body with a small crack at the tip; singular stresses at the notch tip caused by an external loading.

where ω is the first solution of [37]

$$\sin 2(\omega - 1)\alpha + (\omega - 1) \sin 2\alpha = 0 \qquad (B.1.2)$$

with $\alpha = \pi - \beta/2$. The first root is limited by $0 < \omega \leq 1/2$ for $\pi/2 > \alpha \leq \pi$. Figure 201 shows the dependency $\omega = f(\beta)$. A_I is called the notch stress intensity factor. In the following considerations we will restrict the coordinate x to the vicinity of the notch tip which might be on the order of a few interatomic distances

$$x \ll a \ll L \qquad (B.1.3)$$

Nevertheless, it is assumed that continuum mechanics is applicable.

B.1.2 Bridging stress model and crack opening displacement

We model the interface as two separated bodies, continuously connected by bonds, which bridge the gap along the intersection line. Similar to [124]we assume that the material will fail if a critical displacement is reached. Therefore, we model the bridging stresses as

$$\sigma_{br} = \begin{cases} \sigma_0 \dfrac{\delta}{\delta_1} & \text{for} \quad \delta < \delta_1 \\ \sigma_0 & \text{for} \quad \delta_1 < \delta \leq \delta_2 \\ 0 & \text{for} \quad \delta_2 < \delta \end{cases} \qquad (B.1.4)$$

(see fig.203). δ is the displacement of the bonding partners which is interpreted as the crack opening displacement of the apparent crack. It should be noted that for materials with a non-linear stress-strain behaviour - as for instance described by eq.(B.1.4) - no real stress singularity can occur. The maximum stresses must be $\sigma_{max} \leq \sigma_0$. In this sense, our model is a hybrid model assuming unlimited linear-elastic material behaviour in the whole material except the prospective failure line where eq.(B.1.4) is assumed to be valid.
It must be ensured that for the completely bridged "pseudo-crack" no additional stress singularity by the crack appears. If this were the case also ahead of the virtual crack tip, then the bonds in this region must also be stretched and have to be considered as part of the bridged crack, etc.. In order to avoid a stress singularity ahead of the tip of the assumed crack, we have to ensure that the total stress intensity factor K_I, composed of the externally applied stress intensity factor $K_{I\,appl}$ and the bridging stress intensity factor K_{br}, must vanish

$$K_I = K_{I\,appl} + K_{br} = 0 \qquad (B.1.5)$$

For a given stress distribution $\sigma(x)$ in the uncracked component the stress intensity factor results as [28]

$$K_I = \int_0^a h(a,x)\, \sigma(x)\, dx \qquad (B.1.6)$$

where $h(a,x)$ is the fracture mechanics weight function. The condition given by eq.(B.1.5) reads in terms of the weight function

$$\int_0^\infty h(a,x)\, [\sigma_{appl}(x) + \sigma_{br}(x)]\, dx = 0 \qquad (B.1.7)$$

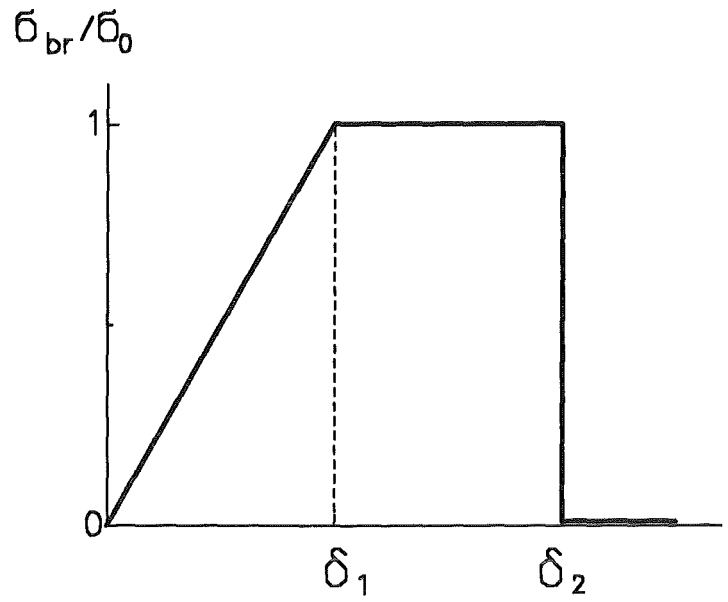

Figure 203. . Bridging stress relation.

In our special case the relevant notch stresses are concentrated close to the mouth of the apparent crack, i.e. $x \ll a$. Equation (B.1.7) then reads

$$h(a,0)\int_0^\infty [\sigma_{appl}(x) + \sigma_{br}(x)]\,dx = 0 \qquad (B.1.8)$$

which is satisfied only if

$$\int_0^\infty [\sigma_{appl}(x) + \sigma_{br}(x)]\,dx = 0 \qquad (B.1.9)$$

i.e. if the normal forces are in equilibrium. The displacements of crack surfaces loaded by stresses are

$$\begin{aligned}\delta(x) &= \frac{1}{E'}\int_x^a h(a', x)\,da' \int_0^{a'} h(a', x')[\sigma_{appl}(x') + \sigma_{br}(x')]\,dx' \\ &= \frac{1}{E'}\int_x^a h(a', x)[K_{appl}(a') + K_{br}(a')]\,da'\end{aligned} \qquad (B.1.10)$$

In eq.(B.1.10) x is the coordinate with the displacement computed and x' is the location where the stress σ acts.

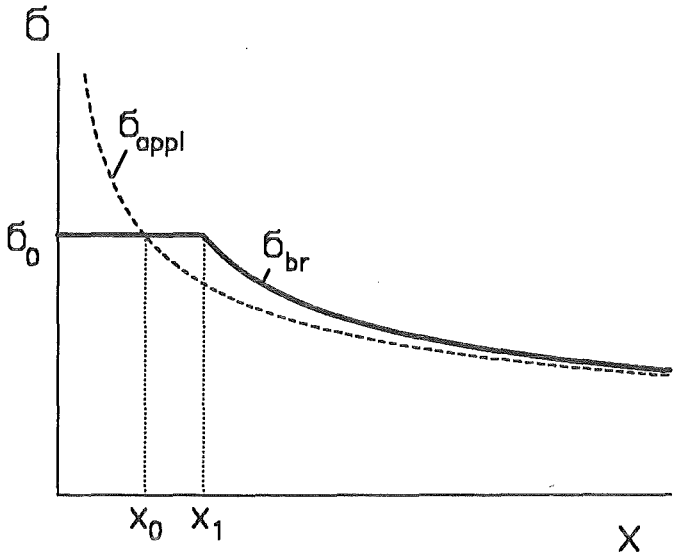

Figure 204. . Stresses along an infinitely long apparent crack.

B.1.3 Numerical treatment

One possibility to determine the stresses and crack opening displacements from the solution of the integral equation (B.1.10) is the application of successive approximations. Unfortunately, the procedure will not lead to convergence. As a second possibility we may expand the unknown bridging stresses in eq.(B.1.10) by appropriate power series expansions with respect to x and have to determine the unknown coefficients by solving a system of nonlinear equations.
In order to ensure a priori the asymptotic behaviour of the bridging stresses for $x \to \infty$, we expand the bridging stress distribution for $x \geq x_1$ in an asymptotic series

$$\sigma_{br}(x) = \sum_{n=0}^{\infty} \frac{A_{I\,n}}{\sqrt{2\pi}\,(x-c)^{n+\omega}} \qquad (B.1.11)$$

with the unknown parameters A_{In}, $n > 0$ and c.
As an example, we consider a situation at a sharp notch as shown in fig.202 with a notch opening angle β. For such sharp notches a three-terms weight function is given in [126] that reads

$$h(x,a) = \sqrt{\frac{2}{\pi a}}\left[\frac{1}{\sqrt{1-\rho}} + B_1\sqrt{1-\rho} + B_2(1-\rho)^{3/2}\right] \qquad (B.1.12)$$

with tabulated coefficients B_1, B_2 for distinct values of β amenable to interpolation. In this case, the applied stress intensity factor reads

$$K_{I\,appl} = A_I\sqrt{\frac{a}{\pi}}\; a^{-\omega}\,\Gamma(1-\omega)\left(\frac{1}{\Gamma(3/2-\omega)} + \frac{1}{2}\frac{B_1}{\Gamma(5/2-\omega)} + \frac{3}{4}\frac{B_2}{\Gamma(7/2-\omega)}\right) \qquad (B.1.13)$$

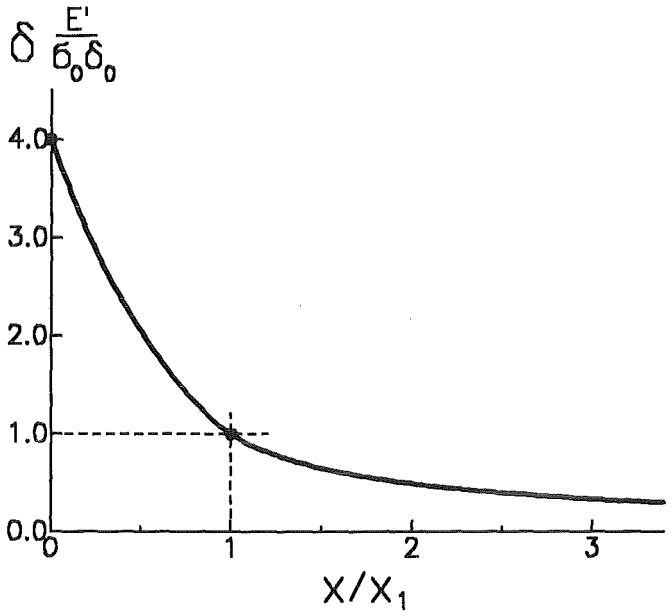

Figure 205. . Crack-opening displacements of an apparent crack of infinite length under notch-stress loading for $\omega = 0.45$ (second approximation); $\delta_2/\delta_1 = 4$.

B.1.3.1 First approximation

As a first approximation we restrict the series extension to the first term with the coefficient $A_{I0} = A_I$. For small applied stresses, leading to $\delta_1 < \delta < \delta_2$ at $x = 0$, the condition $\sigma = \sigma_0$ at $x = x_1$ and the equilibrium condition

$$\int_0^\infty \frac{A_I}{\sqrt{2\pi}\, x^\omega}\, dx = \sigma_0 x_1 + \int_{x_1}^\infty \frac{A_I}{\sqrt{2\pi}\, (x - x_1 + x_0)^\omega} \qquad (B.1.14)$$

yield

$$x_1 = \frac{1}{1-\omega} x_0 \qquad c = x_1 - x_0 \quad \text{with} \quad x_0 = \left(\frac{A_I}{\sqrt{2\pi}\, \sigma_0} \right)^{1/\omega} \qquad (B.1.15)$$

The resulting bridging stresses are entered in fig.8 for this first approximation. It should be noted that in this first rough estimation no properties of the special bridging stress relation, eq.(B.1.4), have been entered.

B.1.3.2 Second approximation

In a second approximation we will include the term with $n = 1$ in eq.(B.1.11). From the condition $\sigma(x_1) = \sigma_0$ and the condition of equilibrium we obtain a system of two non-linear equations

$$\frac{A_I}{\sqrt{2\pi}\, (x_1 - c)^\omega} + \frac{A_{I1}}{\sqrt{2\pi}\, (x_1 - c)^{\omega+1}} = \sigma_0 \qquad (B.1.16)$$

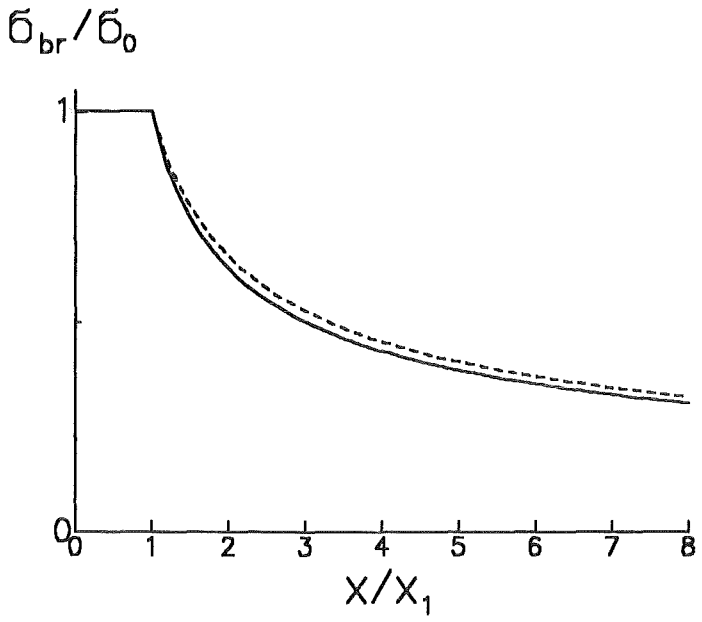

Figure 206. . Bridging stresses in first and second approximation; solid line: first approximation, dashed line: second approximation, computed with $\omega = 0.45$, $\delta_2/\delta_1 = 4$.

$$\frac{A_I}{\sqrt{2\pi}\,(1-\omega)}(x_1-c)^{1-\omega} - \frac{A_{I1}}{\sqrt{2\pi}\,\omega}(x_1-c)^{-\omega} = \sigma_0 x_1 \qquad (B.1.17)$$

that provides x_1 and c. If we introduce the following (normalised) parameters:

$$A_I^* = \frac{A_I}{\sqrt{2\pi}\,\sigma_0 \delta_1^{\omega}} \quad , \quad A_{I1}^* = \frac{A_{I1}}{A_I \delta_1} \qquad (B.1.18)$$

we find

$$A_I^* = \tilde{A}_I \left(\frac{E'}{\sigma_0}\right)^{\omega} \quad , \quad A_{I1}^* \propto \frac{E'}{\sigma_0} \qquad (B.1.19)$$

with the numerical coefficients $\tilde{A}_I$ listed in Table 2 for several ratios δ_2/δ_1 and different values of ω. For the numerical computations a finite crack has to be used. In order to fulfill the restriction $a \gg x_1$ sufficiently, $a = 200x_1$ was chosen. The coefficients for the weight function are listed in Table 16.

δ_2/δ_1	$\omega = 0.374$	$\omega = 0.425$	$\omega = 0.45$	$\omega = 0.50$
2.5	0.905	0.87	0.845	0.82
3	(0.985)	0.95	0.937	0.92
4		(1.10)	1.09	1.08
5			1.22	1.21

Table 15. . Parameters $\tilde{A}_I$ defined by eq.(B.1.19); values in brackets: extrapolations.

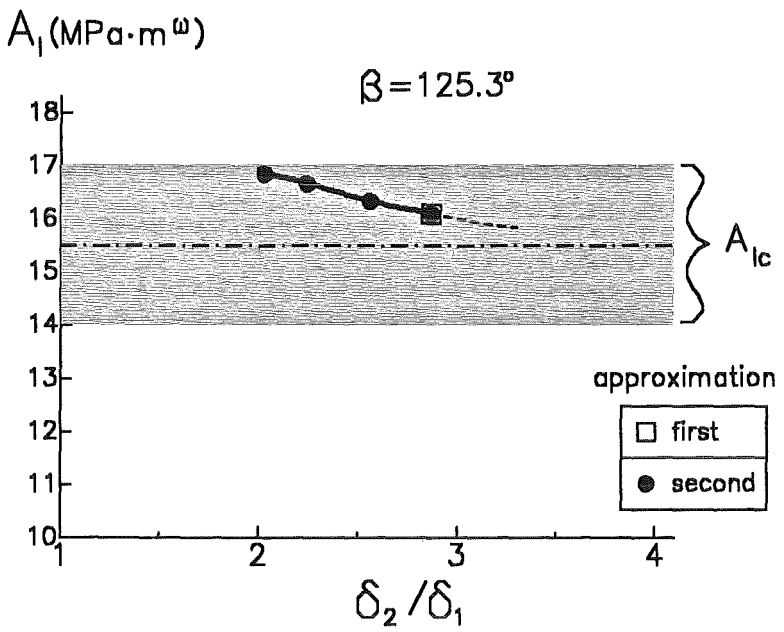

Figure 207. . Influence of the ratio δ_2/δ_1 of the critical notch stress intensity factor A_I; open square: first approximation, circles: second approximation, shaded area: scatter-band of experiments carried out by Busch et al. [124] with single-crystalline silicon ($\beta = 125.3°$).

ω	B_1	B_2
0.500	0.0	0.0
0.450	0.030	0.080
0.425	0.075	0.088
0.374	0.175	0.093

Table 16. . Parameters B_1, B_2 for the weight function eq.(B.1.12) interpolated from data given in [126].

The resulting crack opening displacements are plotted in fig.205 and the bridging stress distribution is shown in fig.206 together with the first approximation.

B.1.3.3 Failure behaviour

Failure condition

Due to the crack opening displacements, the bonds between the crack faces may exceed the maximum tolerable distance δ_2 and a real material separation will occur. This state is reached when the notch stress intensity factor A_I reaches a critical value, namely

$$A_{Ic} = A_I^* \sqrt{2\pi}\, \sigma_0 \delta_1^\omega = \tilde{A}_1(\omega) \sqrt{2\pi}\, \sigma_0 \left(\frac{E'}{\sigma_0} \delta_1 \right)^\omega \qquad (B.1.20)$$

If the notch opening angle is $\beta = 0$, we have a crack and the notch stress intensity factor is identical with the fracture toughness K_{Ic}, i.e.

$$K_{Ic} = \tilde{A}_I(1/2) \sqrt{2\pi}\, \sigma_0 \left(\frac{E'}{\sigma_0} \delta_1 \right)^{1/2} \qquad (B.1.21)$$

and by combination of eqs.(B.1.20) and (B.1.21) we find a relation between the notch stress intensity factor and the fracture toughness K_{Ic} which enables us to predict the critical notch stress intensity factor on the basis of the fracture toughness

$$A_{Ic} = \tilde{A}_I(\omega)\sqrt{2\pi}\,\sigma_0^{1-2\omega}\left(\frac{K_{Ic}}{\tilde{A}_I(1/2)\sqrt{2\pi}}\right)^{2\omega} \qquad (B.1.22)$$

Practical example

In order to compute the notch intensity factor A_I for a real material, we apply the relations derived before to single-crystalline silicon with $\beta = 125.26°$. This material was examined by Busch et al [124] using the Boundary Element Method. As result of analytical calculations, taking into account the anisotropic behaviour, they report an exponent $\omega = 0.374$. This value deviates slightly from the value for isotropic material ($\omega = 0.366$) resulting from eq.(B.1.2). Busch et al. [124] also report the experimental notch stress intensity factor $A_{Ic} = 15.5$ MPa m^{ω} with a deviation of $\pm 10\%$, the elastic constants for the (111) planes $E = 187$GPa and $\nu = 0.4$, and the fracture toughness $K_{Ic} = 0.9$ MPa$\sqrt{m}$. The correct value $\omega = 0.374$ will be used below in the computation of the stress state, but isotropic material behaviour is assumed in the calculation of failure behaviour. The coefficients for the weight function can be derived by interpolation from the data reported in [126]. They are entered in table 1. The parameter σ_0 results from the condition that the initial slope of the bridging relation agrees with the macroscopic elastic behaviour, i.e.

$$\delta_1/\sigma_0 = d/E \qquad (B.1.23)$$

($d = 0.312$nm lattice distance), and from the condition that the bridging stresses must yield the correct specific surface energy 2γ:

$$2\gamma = \sigma_0\delta_1\left(\frac{\delta_2}{\delta_1} - \frac{1}{2}\right) = \frac{1-\nu^2}{E}K_{Ic}^2 \qquad (B.1.24)$$

Consequently, one obtains

$$\sigma_0 = \left[\frac{K_{Ic}^2(1-\nu^2)}{d\,(\delta_2/\delta_1 - 1/2)}\right]^{1/2} \qquad (B.1.25)$$

which is necessaryto evaluate eq.(B.1.22). The critical notch stress intensity factors are plotted in fig.207 with the ratio δ_2/δ_1 as the parameter. The open square represents the solution of the first order approximation with the result $A_{Ic} = 16.1$ MPam$^{0.374}$. The solid circles give the results of the second order approximation. The experimental results of Busch et al. [124] are represented as a shaded band. Good agreement between computations and experiments is obvious. The numerical results are within the scatter-band of the experiments.

B.2 Nomenclature

a = crack depth
A prefactor of power law of subcritical crack growth, work done by external forces, area
A = deepest point of a surface crack, series coefficients
b = width of a bridging element
B = surface point of a surface crack, series coefficients, thickness
C = compliance, series coefficients
c = half crack width of a surface crack
D = diameter, series coefficients
E = Young's modulus, incomplete elliptical integral
$E' = E/(1-\nu^2)$ = Youngs modulus in plane strain
E = complete elliptical integral of second kind
Ei = exponential integral
F = geometric function for stress intensity factors $F = Y/\sqrt{\pi}$, elliptical integral, failure probability
G = shear modulus
G = energy release rate (in notation of [49])
h = weight function, switch-on function, length of a bridging element
H = hardness
J = J-integral
k = modulus for elliptical integrals
K = stress intensity factor
K = complete elliptical integral of first kind
m = Weibull modulus
n = exponent of power law of subcritical crack growth
n = normal vector on the contour line of the transformation zone
p = pressure
P = force
r = radius, radial coordinate
R = Ratio of minimum and maximum load in cyclic tests, crack resistance
s = contour line of transformation zones
S = crack area, roller distance
T = surface tractions
u = displacement in x-direction
U = elastically stored energy
v = displacement in y-direction, crack growth rate
V = Volume between crack faces
W = thickness of a component, energies
x = coordinate with origin at the surface of a component
Y = geometric function for stress intensity factors $Y = F\sqrt{\pi}$
Z = Westergaard stress function

α = relative crack depth
χ = definite integral
δ = crack opening displacements
ε = length of the phase transformation zone
$\eth$ = virtual change
κ = definite integral
λ = definite integral, coefficient in bridging relation
μ = coefficient of friction, running index
ν = Poisson's ratio, running index
ω = width of the phase transformation zone
φ = angle, complex stress function
Φ = Airy's stress function

ψ = complex stress function
ρ = radial coordinate
σ = normal stress
σ^* = characteristic stress
τ = shear stress

Subscripts
0 : initial value
appl : applied
b : bending
br : bridging
c : critical, characteristical
f : failure, fracture
i : initial value
int : internal
LP : loading point
meas : measured
p : potential
res : residual
shield : shielding
tip : effective at crack tip
total : total
w : wedge